Free-Boundary Simulations of ITER Advanced Scenarios

THÈSE N^O 5808 (2013)

PAR

Karim BESSEGHIR

Not to be absolutely certain is, I think, one
of the essential things in rationality.
— Bertrand Russell

Abstract

The successful operation of ITER advanced scenarios is likely to be a major step forward in the development of controlled fusion as a power production source. ITER advanced scenarios raise specific challenges that are not encountered in presently-operated tokamaks.

In this thesis, it is argued that ITER advanced operation may benefit from optimal control techniques. Optimal control ensures high performance operation while guaranteeing tokamak integrity. The application of optimal control techniques for ITER operation is assessed and it is concluded that robust optimisation is appropriate for ITER operation of advanced scenarios. Real-time optimisation schemes are discussed and it is concluded that the necessary conditions of optimality tracking approach may potentially be appropriate for ITER operation, thus offering a viable closed-loop optimal control approach.

Simulations of ITER advanced operation are necessary in order to assess the present ITER design and uncover the main difficulties that may be encountered during advanced operation. The DINA-CH&CRONOS full tokamak simulator is used to simulate the operation of the ITER hybrid and steady-state scenarios. It is concluded that the present ITER design is appropriate for performing a hybrid scenario pulse lasting more than 1000s, with a flat-top plasma current of 12MA, and a fusion gain of $Q \cong 8$. Similarly, a steady-state scenario without internal transport barrier, with a flat-top plasma current of 10MA, and with a fusion gain of $Q \cong 5$ can be realised using the present ITER design.

The sensitivity of the advanced scenarios with respect to transport models and physical assumption is assessed using CRONOS. It is concluded that the hybrid scenario and the steady-state scenario are highly sensitive to the L-H transition timing, to the value of the confinement enhancement factor, to the heating and current drive scenario during ramp-up, and, to a lesser extent, to the density peaking and pedestal pressure.

Keywords: tokamak, ITER, optimal control, real-time optimisation, advanced scenarios, hybrid scenario, steady-state scenario, free-boundary, DINA, CRONOS.

Résumé

Le succès de la réalisation de scénarios avancés pour le tokamak ITER consituera probablement une avancée majeure dans l'optique de développer la fusion contrôlée comme source d'énergie. Toutefois, la réalisation des scénarios avancés pour ITER soulève des défis spécifiques qui n'ont pas encore été abordés dans les tokamaks actuellement en opération.

Cette thèse soutient l'idée que la réalisation de scénarios avancés pour ITER peut grandement bénéficier de l'apport de techniques provenant du domaine du contrôle optimal. Le contrôle optimal est une méthode d'automatique qui permet d'utiliser les capacités du tokamak de manière presque optimale tout en garantissant son intégrité.

Diverses techniques de contrôle optimal et leur application sont évaluées et il est conclu que l'optimisation robuste est adaptée pour l'opération d'ITER. Des algorithmes d'optimisation en temps réel sont présentés et discutés. Il ressort de cette discussion que le contrôle optimal d'ITER en boucle fermée peut être réalisé par le truchement de l'approche de contrôle optimal qui consite à réguler les conditions nécessaires d'optimalité.

Cette thèse traite aussi de la simulation des scénarios avancés d'ITER. Il est nécessaire de simuler l'opération des scénarios avancés d'ITER afin d'évaluer si la conception du tokamak est adaptée à l'opération de tels scénarios. De plus, la simulation des scénarios avancés d'ITER permet de révéler les difficultés principales que leur opération risque de présenter.

Le simulateur à frontière libre DINA-CH&CRONOS est utilisé afin de simuler le scénario hybride et le scénario état-stationnaire d'ITER. Cette thèse conclut que la conception d'ITER est appropriée pour la réalisation d'un scénario hybride possédant un courant plasma maximum de 12MA et restant en régime hybride pour une durée d'au moins 1000s, avec un gain de fusion de $Q = 8$. La conception d'ITER est aussi adaptée pour la réalisation d'un scénario état-stationnaire possédant un courant plasma maximum de 10MA et atteignant l'état stationnaire avec un gain de fusion $Q = 5$.

La sensibilité des scénarios avancés par rapport aux modèles de transport choisis est estimée à l'aide du simulateur à frontière imposée CRONOS, ainsi que leur sensibilité par rapport à diverses importantes hypothèses physiques. Il est conclu que le scénario hybride et le scénario état-stationnaire sont extrêmement sensibles au timing de la transition L-H, à la valeur du facteur d'amélioration du confinement, au scénario de chauffage et d'induction externe de courant durant la phase initiale des scénarios, ainsi qu'au piquage du profil de densité et à la pression du piédestal dans une moindre mesure.

Mots clés : tokamak, ITER, contrôle optimal, optimisation en temps réel, scénarios avancés, scénario hybride, scénario état-stationnaire, frontière libre, DINA, CRONOS.

Preface

The present thesis sits on the fence of tokamak control and tokamak modelling. These two subjects are typically studied by separate scientific communities between which the communication is sometimes difficult. This work tries to bridge these two domains by presenting the concepts of tokamak control and tokamak modelling in a manner and in a vocabulary that are hopefully accessible to both communities. This choice reflects a reality encountered during this work, in which close collaboration with control experts and tokamak modelling experts was necessary.

The subject of this thesis is the simulation of the operation of ITER scenarios from the perspective of tokamak control and free-boundary modelling.

This thesis was initially devoted to the exploration of optimal control techniques and their implementation in the framework of tokamak operation. Indeed, it is the author's opinion that scenario development must be automated for ITER. Such automation may be achieved via the application of optimal control techniques which hits two birds with one stone in that they guarantee tokamak integrity while automating close-to-optimal operation.

The development of optimal control techniques in the framework of tokamak operation does not necessarily necessitate the use of full tokamak simulators. However, the author had at his disposal an extremely powerful tool in the DINA-CH&CRONOS full tokamak simulator for the development of which considerable effort had been invested. In this context, it is easy to understand that when the opportunity appeared in December 2010 to use DINA-CH&CRONOS to its full capability in a Fusion for Energy (F4E) grant as part of an international consortium, the decision was made to momentarily put aside the development of optimal control techniques for tokamak operation to concentrate on full tokamak simulations of the ITER hybrid and steady-state scenarios.

It was originally intended to focus back on the development of optimal control techniques for tokamak operation as soon as the full tokamak simulations of the ITER hybrid and steady-state scenarios had been completed. However, these required far more effort than anticipated. After the completion of the F4E grant, a decision had to be made regarding the work to be undertaken in the last months of this thesis. The two possibilities consisted of either pursuing the exploration and development of optimal control techniques for tokamak operation or to refine the ITER hybrid scenario and steady-state scenario simulations.

It was decided to continue the development of the ITER full tokamak simulations for the following reasons. Firstly, the next step in the exploration of optimal control for tokamak operation involved the study of real-time optimisation (RTO) techniques. RTO is still a subject of research

in the control community and the exploration of such techniques for tokamak operation might have required significantly more time than available. Secondly, the full tokamak simulations of the ITER hybrid and steady-state scenarios suffered from several weaknesses that needed to be addressed. Finally, this choice was also made with the perspective of capitalising on the effort investment made in the development of DINA-CH&CRONOS.

The present thesis therefore consists of an exploratory study of optimal control techniques for ITER operation and the discussion of full tokamak simulations of the ITER hybrid and steady-state scenarios. Both subjects have in common the operation of ITER from a tokamak control perspective.

Contents

Contents

1 Introduction

Fusion reactions routinely occur in the universe. They are one of the major processes providing the necessary energy for stars to sustain their burn and prevent their gravitational collapse [1]. The goal of controlled fusion research is to perform fusion reactions and collect the released energy for commercial use. In that perspective, controlled fusion research mainly focuses on fusion reactions that yield an important amount of energy and occur with a high probability at relatively low respective speed of the reactants. A candidate satisfying these requirements is the fusion of the $^2_1$H and $^3_1$H hydrogen isotopes (respectively called deuterium D and tritium T) in the following process:

$$^2_1\text{H} + ^3_1\text{H} \quad \longrightarrow \quad ^4_2\text{He}(3.5\text{MeV}) + n(14.1\text{MeV}).$$
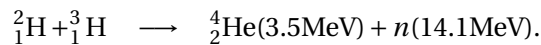
A more detailed calculation of the released energy in this reaction is provided in Appendix A.

1.1 Motivation for fusion-powered reactors

Developing controlled fusion reactors is a stimulating and possibly largely rewarding objective. In order to assess their economical and environmental feasibility, several features of hypothetical controlled fusion reactors must be assessed:

1. The abundance of reactants;

2. The reactant consumption;

3. The power production flexibility and reliability;

4. The risks associated with byproducts and wastes;

5. Technical and proliferation risks;

6. Other features.

These features are discussed throughout this paragraph.

1.1.1 Abundance of reactants

The most prominent candidate reactants for controlled fusion are deuterium and tritium because their interaction has a high cross-section at low relative velocities. Assuming that future controlled fusion reactors will consume deuterium and tritium, it is important to assess their availability.

- Deuterium constitutes ~0.015% of the extremely abundant hydrogen isotopes [2]. Its availability is high, although it should be emphasised that the extraction of deuterium requires energy that must be accounted for in the controlled fusion reactors overall energetic efficiency.

- Tritium, which is a radioactive isotope with a half-life of ~12.26 years, does not naturally exist but can be produced in several different ways. Among them, two mechanisms stand out:

  - Tritium is the product of a nuclear reaction between a neutron and any natural isotope of lithium ($^6_3$Li or $^7_3$Li). Lithium is an abundant resource, especially in the seas [3].

  - Tritium is a product of nuclear fission in some presently-operated fission reactors, such as the CANDU fission reactors [4].

  The present reserves of tritium are relatively scarce. In fact, they are estimated to peak at 27kg in the late 2020s and will decay at a 5.47% rate per year. However, controlled fusion reactors may be able to breed large quantities of tritium by taking advantage of the highly energetic neutron produced by the deuterium-tritium fusion.

  Using controlled fusion to breed tritium can be achieved by surrounding the controlled fusion reactor with a lithium-coated or lithium-enriched blanket that will not only collect the neutron energy, but also breed tritium [5]. This hits two birds with one stone because it provides a collector for the energy of the neutrons, and saves the energy that would otherwise have been required to produce tritium another way. Nonetheless, a baseline amount of tritium is required to start the reactor.

  Assuming that each deuterium-tritium fusion reaction breeds at least one tritium atom, the high availability of lithium would thus guarantee high availability of tritium. However, the extraction of lithium also requires energy that must be accounted for in the controlled fusion reactor overall energetic efficiency.

To conclude on the abundance of reactants, one may say that both deuterium and tritium appear to be abundant, given the caveat that controlled fusion reactors must be able to breed tritium from collisions between highly energetic neutrons and lithium isotopes.

1.1.2 Reactant consumption

In order to estimate the controlled fusion technology energy production potential, it is important to assess the reactant consumption rate of a hypothetical controlled fusion reactor.

The Leibstadt (Switzerland) fission reactor produced ~9.5TWh of energy for 8094h of operation in 2011 [6]. This theoretically requires about 412kg of $^{235}_{92}$U. In 2011, the Leibstadt fission reactor consumed about 980kg of this reactant, corresponding to a net power production efficiency of about 42% [7]. A hypothetical controlled fusion reactor consuming deuterium and tritium with perfect net power production efficiency would theoretically require ~40.8kg of deuterium and ~61.1kg of tritium to produce a similar amount of energy. However, the actual amount of fuel consumed will depend on the reactor net power production efficiency.

In order to assess the efficiency of a hypothetical controlled fusion reactor, it is necessary to emphasise the following. A controlled fusion reactor will most probably produce electric energy by heating water, i.e. via a process similar to those used in fission and fossil fuel power plants. The efficiency of this process is dependent on the effective power density of the collector. In a controlled fusion reactor, the highly energetic neutrons produced by the fusion reaction are not only electrically neutral, but they also possess a very high velocity. As a result, they barely interact with other particles. Collecting their energy therefore requires large quantities of material. The neutrons' energy being spread amongst a very large collector, the power density is therefore decreased. Hence, a controlled fusion reactor may reach a lower level of efficiency than fission or fossil fuel power plants.

When evaluating the energetic efficiency of future controlled fusion power plants, it is thus safer to remain conservative. With the ad hoc hypothesis that the actual net power production efficiency of a hypothetical fusion reactor is 50%, this corresponds to ~91.6kg of consumed deuterium and ~122.2kg of consumed tritium per year of operation. These amounts of consumed reactants are comparable to fission reactors, and much smaller than fossil fuels reactors.

1.1.3 Power production flexibility and reliability

In principle, controlled fusion reactors will be capable of operating at any time during day or night, independently of weather conditions. In that sense, their flexibility is similar to that achieved by fission or fossil fuel reactors, with the caveat that tokamaks and inertial fusion facilities are intrinsically pulsed controlled fusion reactors.

This flexibility is one of the major advantages that presently-operated fission and fossil fuels power plants possess over solar- and wind-powered energy production facilities. Indeed, one of the major problems regarding solar-powered energy is the fact that the sun only shines 12 hours a day on average thus necessitating efficient energy storage methods to provide power on the grid during nighttime. Similarly, wind-powered energy production has the major drawback that wind strength is essentially not controllable and hardly predictable in the long

term. Energy storage is thus also necessary for windmill farms.

It is sometimes argued that energy could be stored using hydroelectric dams, but this reasoning has three major weaknesses. Firstly, pumping water from a low-altitude lake to a high-altitude artificial lake is an energetically costly process. Hence, such storage would diminish the overall efficiency of solar- or wind-powered energy production. Secondly, the creation of artificial lakes requires the flooding of large areas and the drying out of others. A massive increase in the number of hydroelectric dams may thus have a major impact on populations and on the environment. Finally, the availability of natural hydroelectric storage is scarce. In fact, even a mountainous country such as France may not possess enough natural sites in order to store enough energy for nighttime consumption if all the electricity were produced using solar- and wind-powered energy production facilities [8].

The power production flexibility and reliability of controlled fusion reactors therefore provides them with a competitive advantage.

1.1.4 Risks associated with byproducts and wastes

The products of the deuterium and tritium fusion reactions are neutrons and helium atoms:

- **Neutrons**
  The highly energetic neutrons produced during fusion of deuterium and tritium cannot be easily collected because of their high velocity and their subsequent low probability of interaction with a collector. However, a thick blanket of material around the reactor guarantees the absorption of the major part of the highly energetic neutrons.

  As mentioned earlier, it is envisaged to use these highly energetic neutrons in order to breed tritium by using a lithium-coated or lithium-enriched blanket.

  At the end of the lifecycle of a fusion reactor, the components of the reactor within the blanket and the blanket itself may be nuclearly activated by the neutron bombardment. The amount of activated material will however remain small and an appropriate choice of material may decrease the half-life of these radioactive wastes to much shorter durations that fission reactor nuclear wastes.

- **Helium**
  Helium is a noble gas, meaning that it does not interact with other molecules. Helium is naturally present on Earth in extremely small quantities. Although, to the author's knowledge, no study supports nor contradicts this hypothesis, its effect on health and environment is commonly assumed to be less harmful than nuclear fission wastes or fossil fuel combustion byproducts.

Fusion reactor byproducts and wastes are therefore likely to be less harmful to health and the environment than fission and fossil fuels reactor byproducts and wastes.

1.1.5 Technical and proliferation risks

In fission reactors, technical failure to control the chain reaction that is triggered by the fission of the fuel may result in catastrophic scenarios, such as the melting of the core. Melted uranium or plutonium being extremely corrosive, radioactive material is eventually released in the atmosphere if not well contained. This scenario infamously happened in the fission power plant of Chernobyl in 1986.

A similar scenario in a hypothetical controlled fusion reactor would consist of the loss of tritium containment and its release in the atmosphere. The fact that tritium is a radioactive element raises safety concerns. Tritium may bind to an OH radical to form an HTO radioactive water molecule. Such a molecule may be absorbed in the human body in which it possesses a 4-7 days biological half-life [9]. Even though this short biological half-life excludes long term biological accumulation, the effect of HTO ingestion or inhalation may potentially be harmful.

Nonetheless, it should be stated that the confinement of tritium is technologically much simpler and less subject to risks than that of uranium or plutonium, because tritium is neither corrosive, nor is its breeding subject to any chain reaction.

Controlled fusion is almost unaffected by proliferation risks. With the notable exception of inertial confinement reactors (see 1.2.2), controlled fusion is a declassified research field since the 1950s. The technology used in this research domain is hardly transferable to fission.

1.1.6 Other features

- **Maturity**
  Although fusion reactions have already been observed in controlled fusion reactors, controlled fusion technology is not mature yet. The principal challenge that remains to be tackled is power production efficiency. At present, no controlled fusion reactor has demonstrated a higher power production than the power consumed for operation.

- **Tritium**
  Most of the weaknesses of hypothetical controlled fusion reactors arise from the fact that tritium is used as a fuel. It should be emphasised that tritium is presently envisaged as a reactant mainly due to its high fusion rate with deuterium at low relative velocities. There exist several other feasible fusion reactions, such as deuterium-deuterium fusion, but they all have a lower fusion rate than deuterium-tritium reactions for low relative velocities.

- **Cost**
  At the end of the day, the success of fusion-powered energy production will be determined by the cost of the produced energy. This will rely on three critical points, namely the reactor efficiency, the in-house capability of breeding tritium via neutron bombardment of lithium atoms, and the future prices of deuterium and lithium.

1.1.7 Conclusion

This paragraph discussed the potential of controlled fusion reactors. In summary, they benefit from the advantages of fission reactors, but with considerably lower health and proliferation risks. In a time when fossil fuel resources become scarce and fission reactors are under considerable political and popular pressure, the development of a new energy source such as controlled fusion may have a significant added value.

1.2 Technical features of controlled fusion reactors

In view of developing controlled fusion as an energy source, let us now discuss possible technical approaches for the design and operation of controlled fusion reactors.

1.2.1 The plasma state

The amount of power produced by a fusion-powered reactor is directly proportional to the fusion reaction rate. If we consider a gas with a deuterium particle density n_D and a tritium particle density n_T, the fusion reaction rate per unit volume $\mathcal{R}$ is given by

$$\mathcal{R} = n_D n_T \langle \sigma v \rangle,$$

where σ is the collision cross-section between deuterium and tritium, v is their relative speed, and $\langle \cdot \rangle$ denotes an average over the deuterium and tritium velocity distribution functions. The $\langle \sigma v \rangle$ factor is maximised when the deuterium-tritium gas effective temperature reaches an optimal value. In the case of deuterium-tritium collisions, and assuming that the deuterium and tritium distribution functions are Maxwellian, it is maximised for a temperature of the order of $\sim 70 \text{keV} \cong 8 \cdot 10^8 \text{K}$. The $\langle \sigma v \rangle$ factor quickly decreases if the achieved gas temperature is significantly lower.

Therefore, the achievement of a high fusion reaction rate is performed when a dense gas of deuterium and tritium is raised to an extremely high temperature. In these conditions, the deuterium-tritium gas changes phase and is in the state of *plasma*, meaning that a significant fraction of the plasma-constituting electrons is no longer bound to the plasma-constituting ions.

The fact that the deuterium-tritium gas used for controlled fusion becomes a plasma at

such high temperatures comes as an non-negotiable reality rather than a choice. No other known fusion reaction can achieve a similar reaction rate at a lower temperature. Therefore, controlled fusion research is bound to deal with plasmas.

1.2.2 Plasma confinement

In order to achieve controlled fusion, a major challenge is to confine an extremely hot and dense plasma within a vacuum vessel.

The simplistic approach that consists of confining the hot deuterium and tritium plasma in a simple vacuum vessel, for example made of stainless steel, does not hold. As the plasma contacts the walls of the vacuum vessel, the plasma cools down and the energy provided for its heating is lost in the vacuum vessel walls without enabling the occurrence of many fusion reactions. On top of that, such a contact between the plasma and the vacuum vessel may damage the vessel and release impurities in the plasma.

A more complex plasma confinement scheme is therefore required. There are three well-understood plasma confinement schemes:

- **Gravitational confinement**
  The easiest plasma confinement scheme consists of letting the plasma confine itself by its own gravitational collapse. This is the kind of confinement observed in stars. The obtained equilibrium is a hydrostatic equilibrium, in which the gravitational collapse is exactly compensated by the radiative pressure.

  Such a confinement scheme is inapplicable to controlled fusion because the critical mass of fuel required is extremely high.

- **Inertial confinement**
  Another approach to plasma confinement consists of simultaneously driving a large number of highly energetic deuterium and tritium atoms at the same point. The goal of this approach is to trigger a high number of fusion reactions by drastically increasing n_D and n_T at a point in space and time.

  Experimentally, such confinement is achieved by collapsing a finely-designed pellet containing deuterium and tritium. The collapse is performed by applying a high isotropic pressure on the pellet normally using lasers. One of the main difficulties in this approach consists of guaranteeing the isotropy of the pellet and of the applied pressure in order to ensure that all the deuterium and tritium reach the same point at the same time.

  Successful experiments have been reported since 1974 [10] and recently, the National Ignition Facility (NIF) started operating in the United States [11]. It should be however stated that this research field has military applications. Only scarce data is available to the public because most of the technical design and experimental results remain classified.

- **Magnetic confinement**

  Electrically charged particles are subject to magnetic pressure. Equivalently, charged particles essentially follow magnetic field lines. This is the theoretical basis for the magnetic confinement approach.

  In a controlled fusion plasma, a large fraction of the plasma constituting atoms are ionised. The magnetic confinement approach aims at taking advantage of that fact by applying magnetic pressure on the plasma to confine it within a vacuum vessel. Designing a device with a specific geometry and a specific magnetic field topology may guarantee plasma confinement.

Most, if not all civil controlled fusion programs focus on magnetic confinement.

1.2.3 Plasma magnetic confinement

Magnetic confinement may be performed in several different manners, of which two important branches are stellarators and tokamaks.

- **Stellarators**

  A stellarator is a vacuum vessel isomorphic to a torus, in which a helical magnetic field is externally applied by coils surrounding the vacuum vessel. The helical magnetic field guarantees plasma confinement.

  There are several stellarators in activity (for example TJ-II in Madrid, Spain [12]) and under construction (W7-X in Greifswald, Germany [13]).

  Stellarators are steady-state devices by design. Unlike tokamaks, stellarators do not need the presence of plasma current for operation. This renders stellarators attractive in view of developing a controlled fusion reactor because their steady-state property guarantees continuous energy production. However, stellarators historically suffered from a significantly lower performance than tokamaks, which partly explains their lower popularity in the controlled fusion research community.

- **Tokamaks**

  A tokamak consists of a torus-shaped vacuum vessel in which a vertical magnetic field and a toroidal magnetic field (i.e. along the torus axis) are externally applied by coils surrounding the vacuum vessel. Tokamaks rely on externally generated plasma current in order to achieve the helical magnetic field configuration necessary for plasma confinement.

  The plasma current is generated via a transformer action (see 1.3.2). This makes tokamaks intrinsically pulsed devices, which is a serious drawback in view of using tokamaks as controlled fusion reactors. Nonetheless, the popularity of tokamaks can be explained by the fact that they historically demonstrated the best performance amongst all controlled fusion devices.

Tokamaks are the subject of a large part of the civil controlled fusion programs and of this thesis. Their technical operating scheme is exposed in more details in 1.3.

There exists several other less popular controlled fusion devices using a magnetic confinement approach, such as Z-pinch devices (for example, Imperial College London's MAGPIPE device [14]), θ-pinch devices [15], srew-pinch devices [16], mirror machines (used, for example, by the TriAlpha company [17]), and other plasma confinement devices. All these devices have a lower performance than tokamaks.

1.3   Tokamaks

This paragraph describes the basic technical features and operating scheme of a tokamak.

- Tokamak geometry;

- Tokamak equilibrium basic principles;

- Heating and current drive.

1.3.1   Tokamak geometry

A tokamak is an electromagnetic device whose primary purpose is to magnetically confine a hot and dense plasma. It consists of multiple essential parts schemed in Figure 1.1.

The plasma is contained in a torus-shaped vacuum vessel. The first wall, i.e. the plasma-facing wall, is usually made of low atomic number Z material in order to minimise the effects of impurities within the plasma. The vacuum vessel is typically made of conducting material. The vacuum vessel is surrounded by three sets of coils. Firstly, the vertical coils surrounding the torus-shaped vacuum vessel are called toroidal field (TF) coils, because they generate a magnetic field aligned with the axis of the toroidal vacuum vessel. Secondly, the flat horizontal coils at the centre of the torus-shape vacuum vessel are called the central solenoid (CS) coils. Their role is to induce an electromotive force (emf), known as the *loop voltage V_{loop}*, within the plasma in order to generate plasma current. They also contribute to the plasma column positioning and shaping. Finally, the flat horizontal coils outside and on top of the torus are called the poloidal field (PF) coils, because they generate a magnetic field perpendicular to the toroidal direction. The PF coils are mainly used for positioning and shaping the plasma column, as well as guaranteeing its vertical stability. The CS coils also generate poloidal magnetic field and the frontier between CS coils and PF coils is blur. In this thesis, the set of CS and PF coils is referred to as the PF system coils. Multiple plasma data measurement systems (also called plasma diagnostics) also surround formerly- and presently-operated tokamaks but are not displayed in Figure 1.1.

A cylindrical coordinate system (R, ϕ, Z) is commonly used to describe the torus. Its origin is
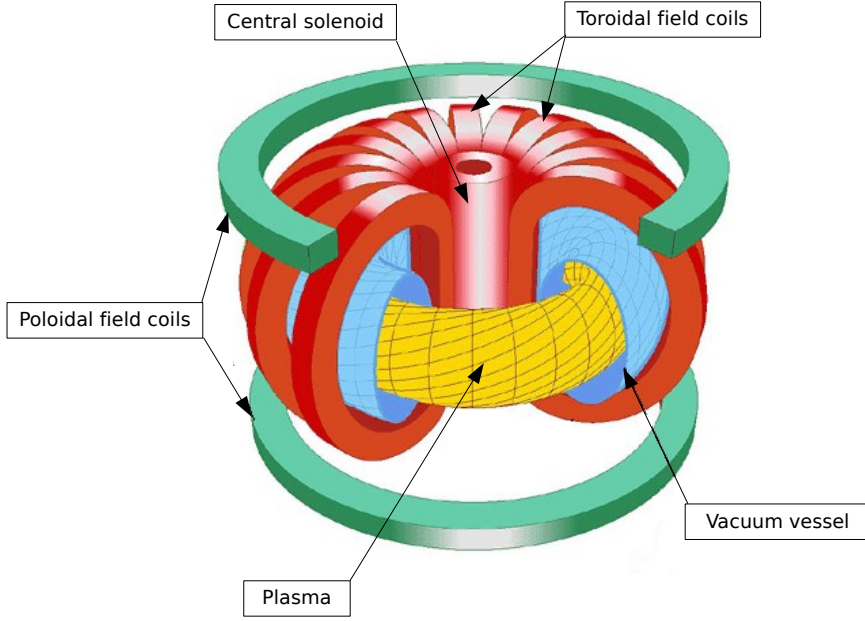
Figure 1.1: Schematic view of a tokamak.

at the intersection of all the torus symmetry planes.

Because tokamaks essentially present the same features independently of the toroidal angle ϕ, they are often displayed in a poloidal cross-section, i.e. a ϕ=const. cross-section (see Figure 1.2). Disregarding the toroidal dimension of the torus neglects important physical features, such as the toroidal magnetic field ripple that is due to the spacing between the TF coils. The poloidal cross-section representation should therefore always be remembered as a simplification of the three-dimensional reality.

When a plasma is present in the vacuum vessel, it is common to introduce a second coordinate system (r, θ) displayed in Figure 1.3. The origin of this coordinate system is the plasma axis, which is defined in Chapter 2.

For further reference, we define the *plasma current weighted centroid* as follows:

$$R_{\mathrm{mag}} := \frac{1}{I_p} \int\limits_{S_{\mathrm{plasma}}} R\, \mathbf{j}_{\mathrm{tor}}(R, Z) \cdot \mathbf{dS} \qquad Z_{\mathrm{mag}} := \frac{1}{I_p} \int\limits_{S_{\mathrm{plasma}}} Z\, \mathbf{j}_{\mathrm{tor}}(R, Z) \cdot \mathbf{dS},$$

where $\mathbf{j}_{\mathrm{tor}} = \mathbf{j}_\phi = \mathbf{j} \cdot \hat{\mathbf{e}}_\phi$ is the toroidal plasma current density at the toroidal angle ϕ=const., S_{plasma} is the plasma cross-section at ϕ=const., and I_p is the total toroidal plasma current. I_p
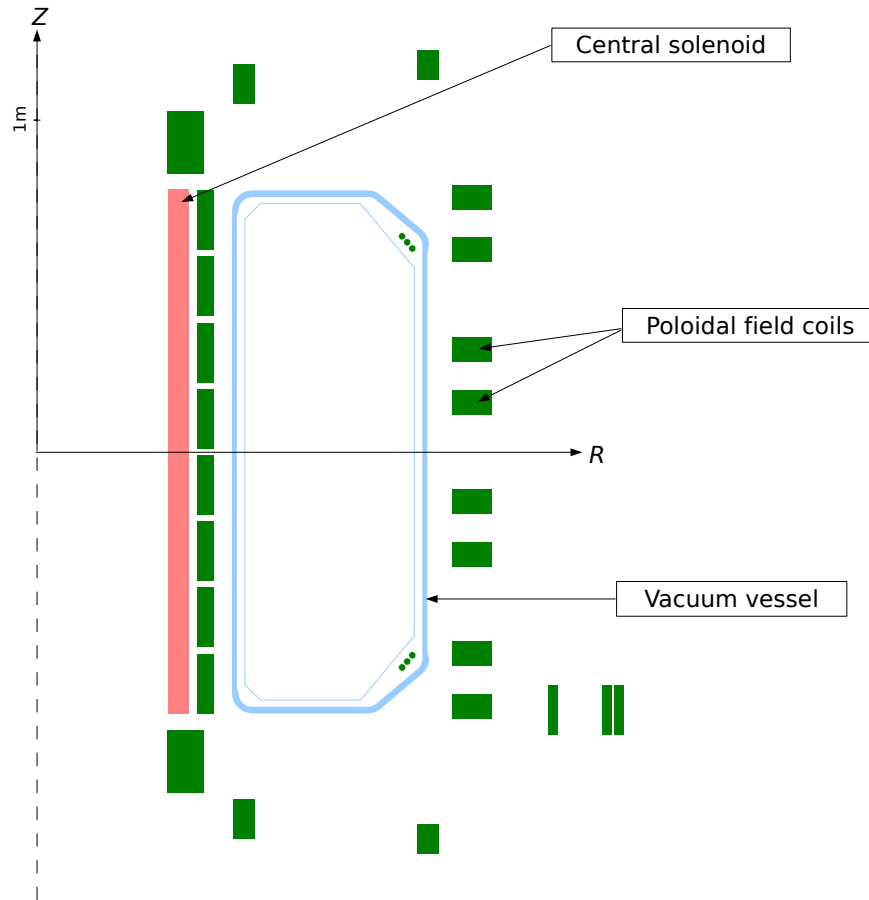
Figure 1.2: Schematic poloidal cross-section of the Tokamak à Configuration Variable (TCV). The R and Z cylindrical coordinates axes are labelled and the ϕ coordinate is not displayed. The TF coils are usually not displayed in poloidal cross-section representations.

will be referred to as the *plasma current*, with the definition:

$$I_p := \int\limits_{S_{\text{plasma}}} \mathbf{j}_{\text{tor}}(R, Z) \cdot \mathbf{dS}.$$

This definition is valid for any ϕ=const. poloidal cross-section.

1.3.2 Tokamak equilibrium basic principles

This paragraph describes the basic features of a tokamak equilibrium and its functioning principles.
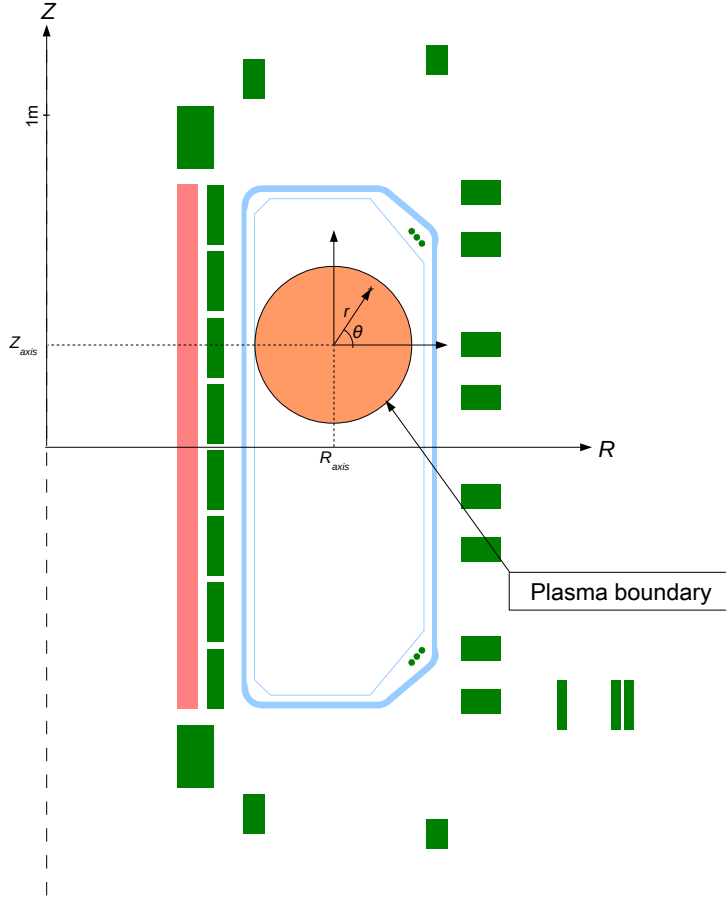
Figure 1.3: Poloidal representation of a hypothetical plasma within the TCV vacuum vessel. The origin of the (r, θ) coordinate system is the plasma axis.

Poloidal magnetic field and plasma current

Let us assume the presence of a plasma within the vacuum vessel. If the TF coils are loaded with a constant current, they generate a constant toroidal magnetic field in the plasma. Because of the torus-shaped configuration of the ensemble of the TF coils, the amplitude of this toroidal magnetic field decreases as $B_\phi(R) \sim \frac{1}{R}$. The toroidal magnetic field being higher for the region in which R is small, this region of a tokamak poloidal cross-section is called the high field side (HFS). Conversely, the region of large R is called the low field side (LFS).

The plasma electrons and ions roughly follow the toroidal magnetic field lines but also drift across the toroidal magnetic field because of its topology. This drift is vertical and charge-dependent. If only a toroidal magnetic field and no other magnetic field were applied in the plasma, the plasma ions would drift in the direction opposite to the plasma electrons, thus generating a strong vertical electric field. This electric field would, in turn, drive the plasma particles to drift horizontally towards the vacuum vessel wall. In such a configuration, the

plasma would be quickly lost. A different magnetic field configuration is thus necessary for plasma confinement.

Applying a magnetic field in the $\hat{\mathbf{e}}_\theta$ direction is a crucial step towards a solution to this challenge. In a tokamak, this poloidal magnetic field is generated by externally driving a toroidal plasma current I_p. The addition of this poloidal magnetic field creates a helical component to the magnetic field lines and provides a viable topological configuration of the magnetic field for plasma confinement [18].

The plasma current is generated as follows. The PF system coils act as the primary of a transformer, the secondary being the plasma. By modifying the PF system coil currents, the poloidal magnetic flux, which is the magnetic flux defined on the surface displayed in Figure 1.4, is modified and a toroidal loop voltage is induced in the plasma. A plasma current is then generated because the plasma is conducting.
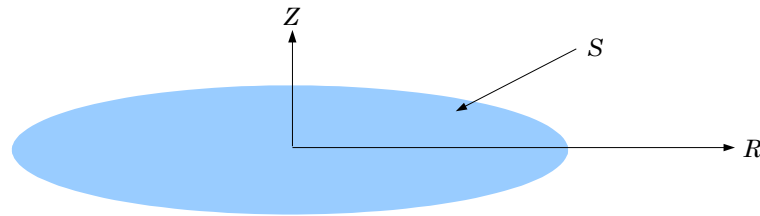
Figure 1.4: Definition of the poloidal magnetic flux.

The presence of a plasma current implies several features specific to tokamaks:

- **Heating**
  Inducing a current within the plasma provides a significant heating source. Because the plasma is resistive, it may be heated via the Joule effect. This heating mechanism is also known as *Ohmic heating*. Historically, Ohmic heating is one of the main reasons for the success of tokamaks because it enabled the achievement of higher temperatures than other plasma confinement concepts.

- **Reliability of breakdown**
  The presence of a loop voltage within the vacuum vessel assists the generation of a plasma, by providing energy to charged particles within the plasma and helping the breakdown process.

- **Tokamak pulses**
  The tokamak concept requires that plasma current be driven within the plasma. Because the maximum current load in a coil is bounded, the PF system coils can only provide a finite amount of volt-seconds to the plasma. This means that tokamaks are intrinsically pulsed devices.

As further exposed in Chapter 5, it is possible to design and perform steady-state toka-mak operating schemes that enable the plasma current to be sustained with no externally driven emf. Theoretical and experimental evidence already demonstrated the feasibility of such schemes.

Tyre tube force

Let us assume the existence of a circular plasma within a vacuum vessel with a boundary pressure p. Let us assume that p is constant over the plasma boundary. This pressure applies a radial force on the plasma column (see Figure 1.5). The radial force applied on the internal
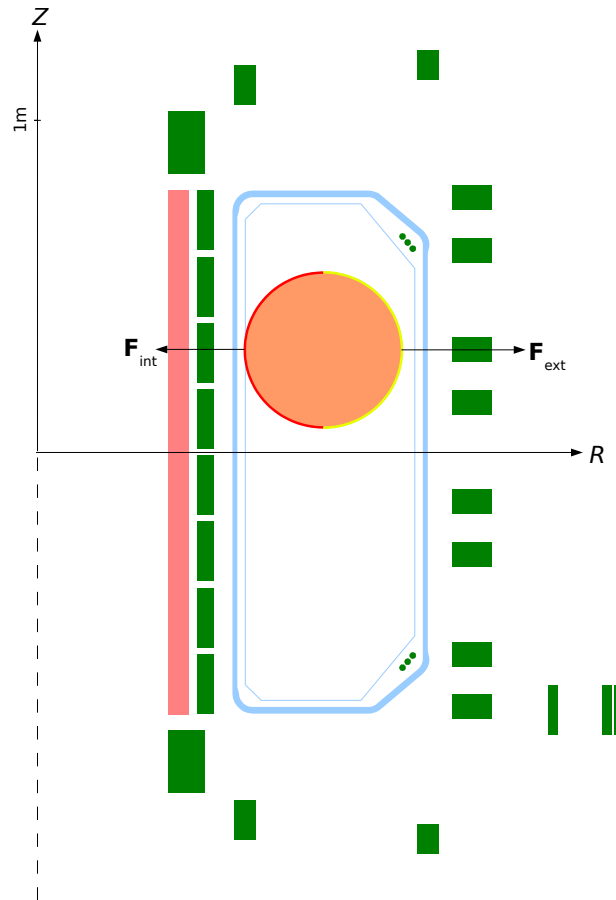
Figure 1.5: Schematic poloidal cross-section of TCV with a hypothetical plasma within the vacuum vessel. The tyre tube force is represented.

and external surfaces are respectively given by:

$$\mathbf{F}_{\text{int}} = -pS_{\text{int}}\hat{\mathbf{e}}_R \qquad \mathbf{F}_{\text{ext}} = pS_{\text{ext}}\hat{\mathbf{e}}_R,$$

where $S_{\text{int}} = 2\pi a(\pi R - 2a)$ is the internal surface and $S_{\text{ext}} = 2\pi a(\pi R + 2a)$ is the external surface of the toroidal plasma column boundary, and a the so-called *minor radius* of the plasma, meaning the radius of the circular cross-section of the plasma column.

Because $S_{\text{int}} < S_{\text{ext}}$ for the plasma boundary as well as for all the isobaric concentric internal plasma surfaces, there exists a net radial force, called the *tyre tube force*, pushing the plasma column in the $+\hat{\mathbf{e}}_R$ direction.

Hoop force

There exists another radial force on the plasma column, known as the *hoop force*. It arises from the following.

Because $S_{\text{int}} < S_{\text{ext}}$, it would seem at first sight that the magnetic pressure due to the magnetic field generated by the plasma current results in a radial force opposite to the tyre tube force. However, the following effect must be taken into account. The plasma current on the opposite side of the torus also generates a poloidal magnetic field. This extra poloidal magnetic field strengthens the poloidal magnetic field close to the torus axis (small R) and weakens the poloidal magnetic field far from the torus axis. This is displayed in Figure 1.6. As a result, the
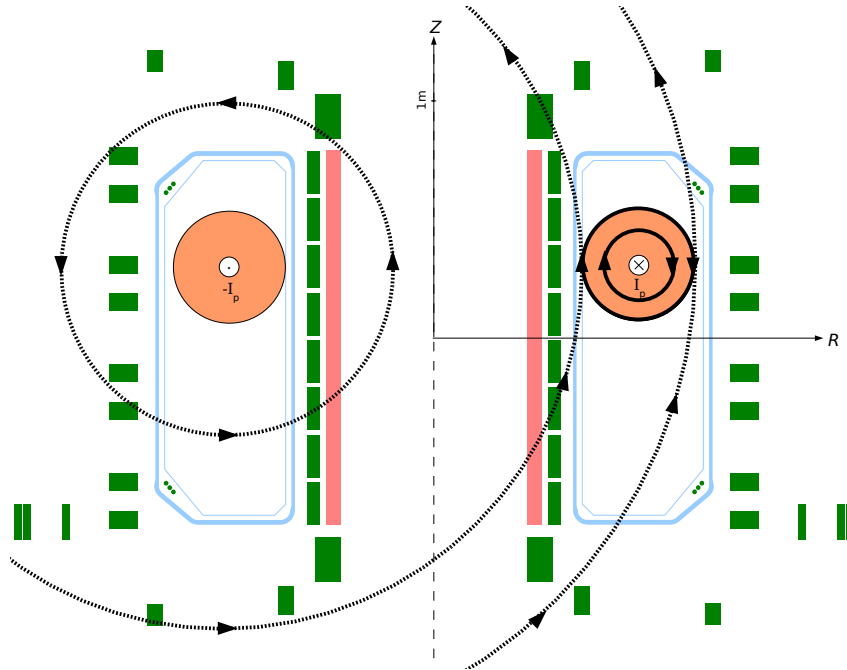
Figure 1.6: Schematic representation of the effect of the opposite poloidal cross-section on the poloidal magnetic field.

direction of the resulting radial force applied on the plasma column by the magnetic pressure depends on the intensity difference between the inner and outer poloidal magnetic fields, as

well as the size of the plasma inner and outer surface.

Poloidal field coils and vertical magnetic field

In a tokamak, the tyre tube force and the hoop force are compensated by an externally applied magnetic field. This magnetic field $\mathbf{B}_V$ is vertical and is applied by the PF coils pushing the plasma towards the HFS thanks to the Lorentz force. This is displayed in Figure 1.7.
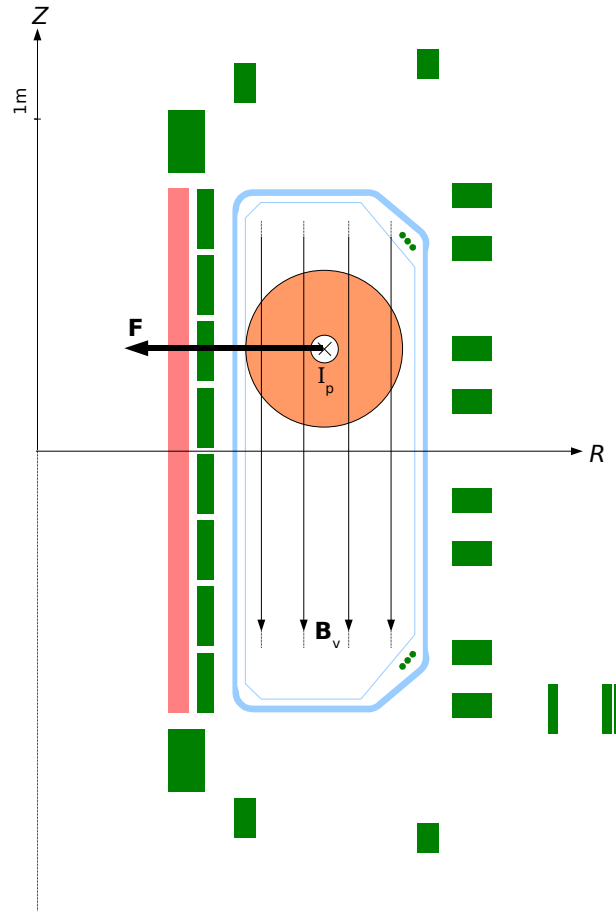
Figure 1.7: Schematic representation of the effect of a vertical magnetic field $\mathbf{B}_V$.

Plasma elongation

The PF coils provide extra degrees of freedom in order to impose a desired magnetic field topology and enable new features such as the shaping of the plasma column. Introducing a radial component to the vertical magnetic field elongates or compresses the plasma column, as displayed respectively in Figure 1.8 and Figure 1.9.
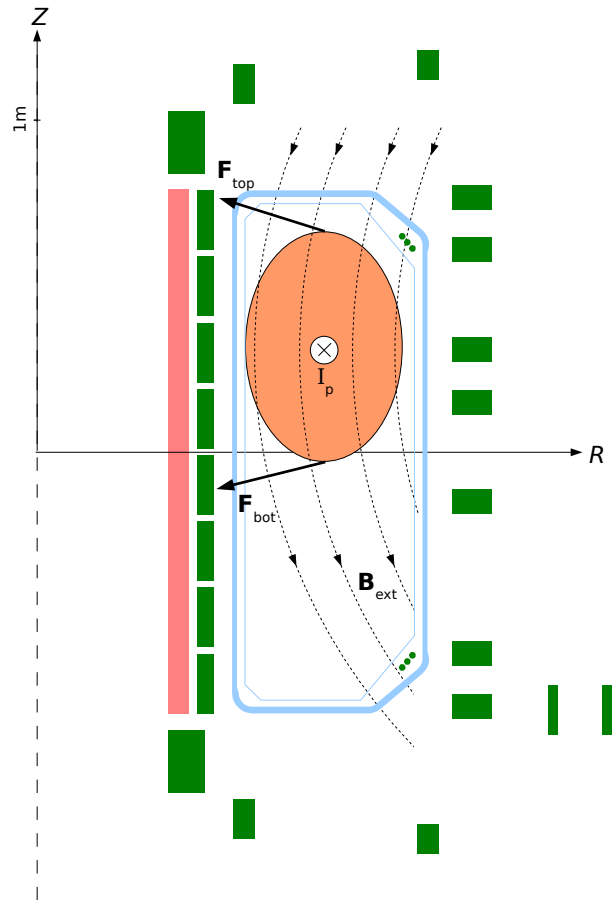
Figure 1.8: Effect of a specific magnetic field configuration on the plasma shape.

The elongation κ of a supposedly elliptic plasma is defined as the ratio of its vertical axis to its horizontal axis, namely,

$$\kappa = \frac{b}{a},$$

where a is the horizontal radius of the elliptic plasma and b its vertical radius.

$\kappa < 1$ means that the plasma is compressed, $\kappa > 1$ means that the plasma is elongated, and $\kappa = 1$ means that the plasma is circular.

Vertical stability

Elongated plasmas are of high interest, because they reach higher performance (see 1.6). However, the magnetic field configuration necessary to elongate the plasma column renders it vertically unstable. This can be heuristically explained as follows.
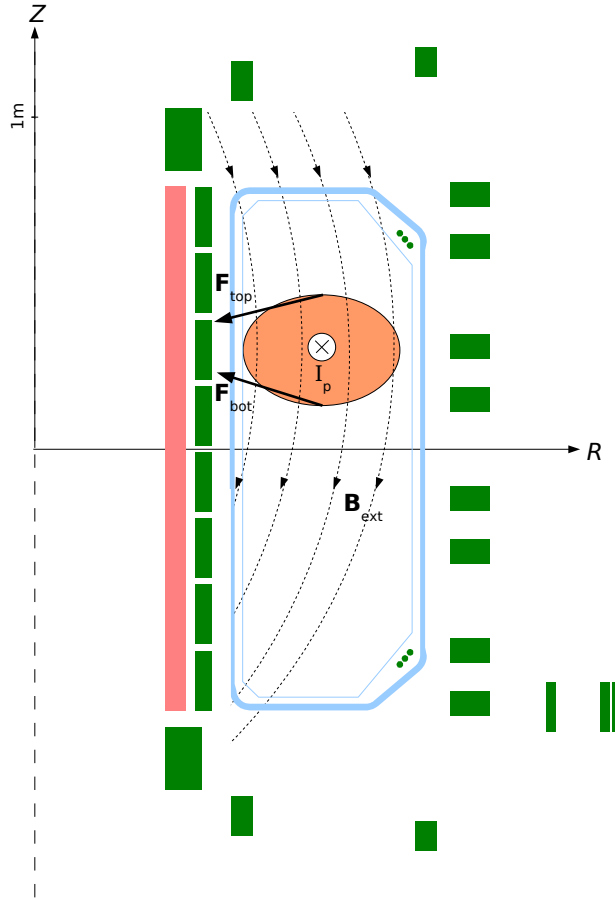
Figure 1.9: Effect of a specific magnetic field configuration on the plasma shape.

Let us assume that the plasma column is a rigid filament located at $(R_{\mathrm{mag}}, Z_{\mathrm{mag}})$. Except for the filament, the vacuum vessel can be considered as empty. Assuming the absence of a time-varying electric field, Ampère's law in the vacuum is given by

$$\nabla \times \mathbf{B} = \mathbf{0}. \tag{1.1}$$

In general, the magnetic field can be given as

$$\mathbf{B} = \begin{pmatrix} B_R \\ B_\phi \\ B_Z \end{pmatrix}.$$

The second component of (1.1) can be written as

$$\frac{\partial B_Z}{\partial R} - \frac{\partial B_R}{\partial Z} = 0, \tag{1.2}$$

which is valid for any (R, Z) in the vacuum vessel, except on the plasma filament.

Assuming $B_R(R_{\text{mag}}, Z_{\text{mag}}) > 0$, there is a vertical component to the Lorentz force applied on the plasma filament

$$F_Z = -2\pi R_{\text{mag}} \cdot I_p \cdot B_R(R_{\text{mag}}, Z_{\text{mag}}) \tag{1.3}$$

The gradient of the vertical component of the Lorentz force is obtained by differentiating (1.3) with respect to the plasma column vertical position

$$\frac{\partial F_Z}{\partial Z} = -2\pi R_{\text{mag}} \cdot I_p \cdot \frac{\partial B_R}{\partial Z}. \tag{1.4}$$

Substituting (1.2) in (1.4), we have

$$\frac{\partial F_Z}{\partial Z} = -2\pi R_{\text{mag}} \cdot I_p \cdot \frac{\partial B_Z}{\partial R}. \tag{1.5}$$

There are three possible situations:

- $\dfrac{\partial B_Z}{\partial R} < 0$

  This is the situation displayed in Figure 1.8. In that case, the vertical force moving the plasma column vertically increases as the plasma column moves. This situation is **unstable**.

- $\dfrac{\partial B_Z}{\partial R} > 0$

  This is the situation displayed in Figure 1.9. In that case, the vertical force moving the plasma column vertically decreases as the plasma column moves. This situation is **stable**.

- $\dfrac{\partial B_Z}{\partial R} = 0$

  In this case, the vertical force applied on the plasma column is independent of the plasma column position within the vacuum vessel. This situation is **marginally stable**.

The time constant of the elongated plasma column vertical instability is short, typically of the order of 0.1s for ITER and as fast as 0.3ms for TCV. Operating tokamaks with elongated plasmas therefore requires specific attention, as exposed in 1.5.

1.3.3 Heating and current drive

Plasma heating

Assuming plasma confinement is achieved, it is important to keep in mind that an intermediate goal of controlled fusion research remains to obtain a fusion reaction rate $\mathcal{R}$ as high as possible. As stated in 1.2.1, the fusion reaction rate per unit volume quickly increases with the achieved deuterium and tritium temperatures and is maximised for temperatures of the order of ~70keV. Achieving such high temperatures necessitates plasma heating.

In a tokamak, a fraction of the plasma heating is provided by the plasma current, via Ohmic heating (see 1.3.2). However, there are several additional external heating mechanisms used in presently-operated tokamaks. Some of the most common external heating methods are as follows:

- **Electron Cyclotron Resonance Heating (ECRH)**
  Charged particles roughly perform a cyclotron motion around a magnetic field line. For electrons, the cyclotron motion pulsation is given by

  $$\omega_{\text{ce}} = \frac{eB}{m_e},$$

  where e is the electron elementary charge, B is the intensity of the magnetic field, and m_e is the electron elementary mass.

  The idea behind ECRH systems consists of injecting electromagnetic waves at frequencies that are close to or harmonics of the electron cyclotron resonant frequency. The wave energy is transferred to the electrons, which results in an increase of their kinetic energy and, in turn, of an increase of the electron temperature. The energetic electrons transfer energy to ions via collisions, which increases the ion temperature.

  As seen in 1.3.2, the toroidal magnetic field strength $B_\phi(R)$ decreases as $\sim \frac{1}{R}$. Thus, by choosing an appropriate ECRH frequency, there will be an R=const. surface at which the wave energy will mostly be absorbed. This feature enables localised heating of the plasma, which is a precious asset for tokamak operation.

  Thanks to the wave properties, there is no evanescent region between the ECRH antennae and the plasma. The ECRH antennae may thus be placed far from the plasma. This enables the implementation of steering-mirrors for wave-vector orientation, allowing real-time modifications of the ECRH power deposition location.

- **Ion Cyclotron Resonance Heating (ICRH)**
  The functioning principle of the ICRH systems is identical to that of the ECRH systems, with the exception that ICRH systems typically heat the plasma impurities, also called *minorities*. The minorities then transfer energy and momentum to the plasma deuterium and tritium ions. ICRH systems also enable localised heating, but the minorities density profile is often unknown and difficult to control.

The ICRH antennae must be close to the plasma (close to the cut-off density) in order to ensure efficient plasma-wave coupling because the region between the ICRH antennae and the plasma is evanescent for the wave. As a result, the ICRH antennae are in a more hostile environment and real-time geometric steering of the power deposition location is not implemented.

- **Neutral Beam Injection (NBI)**
  The principle behind NBI heating consists of injecting highly energetic neutral atoms in the plasma. These atoms will then collide with the plasma particles and transfer their energy and momentum to the plasma. As a result, NBI systems can contribute to the plasma heating.

The combined effects of Ohmic heating and the additional heating systems enable the achievement of high plasma temperatures.

Plasma current drive

By design, a tokamak drives a plasma current by generating a loop voltage within the plasma using the PF system coils (see 1.3.2). However, there are several additional methods for externally driving plasma current. Some of the most common additional current drive approaches are as follows:

- **Electron Cyclotron Current Drive (ECCD)**
  Plasma current can be driven by an ECRH antenna if the wave vector possess a non-zero toroidal component. Plasma current arises from the transmission of wave energy to electrons. This energy transfers preferrably occurs for electrons moving in the same toroidal direction as the wave vector [18]. As a result, a net plasma current is driven.

- **Neutral Beam Injection (NBI)**
  Injecting highly energetic neutral particles with a non-zero toroidal component may drive a plasma current via the momentum transfer ocurring in collisions between the plasma-constituting particles and the neutral particles under certain conditions exposed in Chapter 2.

- **Lower Hybrid Current Drive (LHCD)**
  As ECCD systems, LHCD systems drive plasma current by transferring energy from an electromagnetic wave to the plasma electron via the lower-hybrid resonance. The wave-particle interaction occurs preferentially with electrons travelling in the same toroidal direction as the wave vector.

There exists another important source of non-inductive current drive provided by the plasma itself. This additional current drive source is known as the *bootstrap current*. This current

arises from the presence of a pressure gradient between the plasma centroid and the plasma boundary. It is exposed in greater details in 2.1.7.

The combined effects of the non-inductive current drive systems and the bootstrap current can provide a significant fraction of the plasma current. In fact, plasma pulses in which no current is externally driven have been performed on TCV [19].

Heating and current drive synergy

The plasma resistivity η decreases as the plasma temperature increases. In fact, [20] indicates that for singly charged ions, the plasma resistivity can be estimated by

$$\eta = 2.8 \cdot 10^{-8} \cdot T_e^{-3/2} [\Omega\text{m}], \tag{1.6}$$

where T_e is the electron temperature in keV.

Therefore, heating the plasma decreases its resistivity. If, at the same time, a non-zero loop voltage is present within the plasma, the plasma current can be increased as a direct effect of the plasma heating. Heating the plasma may thus provide a contribution to current drive.

On the other hand, externally driving plasma current increases the intensity of Ohmic heating within the plasma. As a result, non-inductive current drive may also contribute to plasma heating.

1.4   Tokamak operation and scenarios

1.4.1   Tokamak operation

As exposed in 1.3.2, tokamaks are intrinsically pulsed controlled fusion devices. Hence, there is a finite sequence of events occurring before, during, and after a plasma pulse. The following describes a non-exhaustive sequence of events necessary for operating a tokamak:

1. **Glow discharge conditioning**
   Glow discharge treatments are commonly used for wall conditioning of high vacuum devices. They aim at removing the impurities from the vessel surface and minimise the particle-induced desorption [21]. In a tokamak, glow discharge conditioning is performed in order to minimise the impurity fraction in the plasma.

2. **Vacuum pumping**
   Before a plasma discharge, a high vacuum is maintained within the vacuum vessel in order to minimise the level of impurities. Efficient vacuum systems are thus required for tokamak operation.

3. **TF coil loading**
   Current is loaded onto the TF coils in order to provide a toroidal magnetic field in the vacuum vessel.

4. **CS coil loading**
   Before the plasma pulse, the CS coil currents are loaded. Their fast modification will induce the loop voltage necessary for tokamak operation.

5. **Gas pre-fill**
   A gas of the desired plasma-composing particles is then injected in the vacuum vessel via the action of a gas valve.

6. **Breakdown**
   The currents in the CS coils are rapidly modified, thus generating an emf in the gas-filled vacuum vessel.

   There exists a small fraction of ionised atoms in the neutral gas filling the vacuum vessel. These electrons and ions are accelerated thanks to the loop voltage induced by the modification of the CS coil currents. In turn, these accelerated electrons and ions ionise other neutral particles by collision. These collisions trigger an avalanche of ionisations and generate a plasma. This process is known as a breakdown.

   There exist a minimum threshold loop voltage below which the accelerated ions and electrons recombine too quickly to trigger the avalanche reaction. The generated loop voltage must be greater than this minimum threshold.

   In tokamaks, it is common to assist the breakdown via the action of heating systems in order to save volt-seconds. The breakdown can typically be assisted by heating the partly ionised gas via ECRH [22].

7. **Ramp-up**
   At this point, the produced plasma is cold, small, and carries a low plasma current. The plasma current must be raised to higher values to heat the plasma. In that perspective, a strong loop voltage is applied via the PF system coils, which also help position and shape the plasma column.

8. **Flat-top**
   When the plasma current reaches a predetermined value, it is normally maintained constant. To achieve that, the loop voltage in the plasma is decreased, but remains non-zero to compensate the resistive losses. The plasma shape is also typically kept unchanged.

   Because a non-zero loop voltage must be maintained within the plasma, the achievable plasma pulse duration at a given plasma current depends on the volt-seconds that the PF system coils can provide.

   The flat-top phase is usually a quasi-steady-state period of a plasma pulse. In a controlled fusion tokamak, most fusion reactions will occur during flat-top.

9. **Ramp-down**
   After the flat-top phase, the plasma current is brought down to lower values in a phase called ramp-down. Ramping the plasma current down also lowers the plasma temperature. Typically, the plasma elongation and minor radius are also decreased during ramp-down.

   The necessity of a ramp-down phase is explained as follows:

   - **Protection against large emfs in the coils**
     If the plasma current were abruptly dropped, the sudden change in plasma current would induce large emfs in the PF system coils and in the conducting vacuum vessel walls. Because all the coils and the vacuum vessel dwell in intense magnetic fields, inducing such large emfs in these components may damage them by the onset of large Lorentz forces. Thus, a sudden change in plasma current threatens tokamak integrity.

   - **Protection of plasma facing components**
     An abrupt plasma current decrease may result in the loss of control of the plasma column position and shape. In turn, this may lead to high power depositions in sensible areas of the vacuum vessel, e.g. on heating, current drive, or plasma diagnostic facing components. This may result in subsequent damage to these components.

   The plasma current ramp-down must therefore be performed in a controlled manner.

10. **Termination**
    At the end of ramp-down, the plasma is cold and ceases to be ionised. At this point, the plasma terminates, and the ions and electrons contained within the vacuum vessel recombine. This is supported by the fact that, at termination, there is no loop voltage in the vacuum vessel to enable the avalanche reaction which led to the breakdown.

    After the plasma termination, the PF system coil currents are brought back to zero.

1.4.2 Scenarios

As exposed in the previous section, tokamak operation consists of a long and complex sequence of events that needs to be finely timed. The information necessary for performing a plasma pulse is summarised in a *scenario*.

Tokamak scenarios are imagined or projected sequences of events for tokamak operation. Each tokamak pulse is the implemented result of a scenario and the same scenario can be used for several tokamak pulses. Scenarios can be materialised in different manners depending on subjective choices made by the tokamak operator, as well as the objective of the plasma pulse. For example, a tokamak scenario can be expressed by providing the following parameters:

- The desired plasma current waveform $I_{p,\mathrm{ref}}(t)$;

- The desired plasma shape parameters waveforms $R_{\mathrm{mag,ref}}(t), Z_{\mathrm{mag,ref}}(t), a_{\mathrm{ref}}(t), \kappa_{\mathrm{ref}}(t)$, etc.;

- The desired PF system coil current waveforms;

- The heating and current drive power waveforms $P_{\mathrm{ECRH}}(t), P_{\mathrm{NBI}}(t)$, etc.;

- The desired line-averaged electron density waveform $\bar{n}_{e,\mathrm{ref}}(t)$.

The tokamak scenarios can be sorted into classes. Typically, they are divided in three classes:

- **Ohmic scenarios**

  Ohmic scenarios consist of tokamak scenarios that do not use additional heating and current drive for operation, but only rely on the plasma current induced by the PF system coils for operation.

  This class of scenarios is not very flexible. It does not allow the development of drastically different operating schemes, even though the achieved performance can change from one Ohmic scenario to the other.

- **Inductive scenarios**

  Inductive scenarios rely on Ohmic heating and inductively driven plasma current, but also on additional heating and current drive sources, such as ECRH, ECCD, ICRH, etc. They typically reach higher performance than Ohmic scenarios. Moreover, several new degrees of freedom are accessible thanks to the availability of the additional heating and current drive sources. This renders inductive scenarios more flexible than Ohmic scenarios.

- **Advanced scenarios**

  Advanced scenarios consist of inductive scenarios in which the heating and current drive source are used in a more sophisticated manner that provides significantly higher neutron fluence per plasma pulse. Advanced scenario research aims at providing a candidate scenario for steady-state operation in a fusion power plant [23].

  The division between inductive scenarios and advanced scenarios is somewhat artificial. Throughout this thesis, advanced scenarios are distinguished from inductive scenarios by the fact that the ramp-up phase of advanced scenarios affects the plasma evolution for durations significant with respect to the tokamak plasma current diffusion characteristic time, which is not the case for inductive scenarios.

  Advanced scenarios are extremely sensitive to small differences in the ramp-up phase. This will be investigated in greater details in Chapter 5.

Advanced scenarios are important for controlled fusion research, because they aim at enabling higher neutron fluence per plasma pulse and possibly steady-state tokamak operation. They may thus provide a solution to the challenge that is the inherent pulsed nature of tokamaks, which would be a major step towards making tokamaks viable controlled fusion reactors.

1.5 Tokamak control

During tokamak operation, there is a significant number of events that must occur in a finely-timed sequence. However, tokamak operators can only act on a small number of fully controllable variables known as the *actuators*. A non-exhaustive list of tokamak actuators could consist of the following:

- Demand gas valve voltages;

- Demand TF coil power supply voltages;

- Demand PF system power supply voltages;

- Demand heating and current drive powers.

To perform a plasma pulse, the operator must provide a scenario in the form of a set of desired waveforms, also called *controlled variable references* or simply *references*, as exposed in 1.4.2. These references must be translated into demand gas valve voltages, demand TF coil power supply voltages, demand PF system power supply voltages, and demand heating and current drive powers, i.e. into actuator signals.

1.5.1 Pre-programming

Translating references $y_{\text{ref}}(t)$ into actuator signals $u(t)$ can be performed by analytic or numeric tokamak models. These models can be run before the plasma pulse and the calculated actuator signals can then be implemented on the tokamak to perform the desired plasma pulse in a scheme called *pre-programming*.

A schematic illustration of tokamak operation using a pre-programming approach is provided in Figure 1.10.
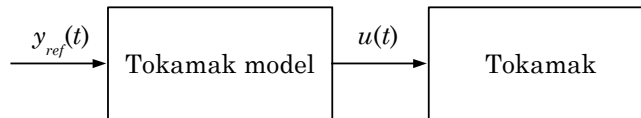
Figure 1.10: Schematic illustration of pre-programming. $y_{\text{ref}}(t)$ are the references as a function of time, $u(t)$ are the actuators signals as a function of time.

On its own, a pre-programming approach is *not* appropriate for tokamak operation for the following reasons:

- **Disturbances**

  Tokamaks are subject to unpredictable or inaccurately modelled disturbances. Such disturbances can arise from the plasma activity, the fraction of impurities within the plasma, the temporary or definitive failure of actuators, or several other causes.

  Disturbances can have a significant effect on the tokamak evolution. Failure to account for disturbances may result in the implementation of an inappropriate plasma pulse. In most cases, unmanaged disturbances lead to an uncontrolled plasma termination.

- **Imperfect modelling**

  A tokamak is a non-linear dynamical system to which there exists no known general analytical solution. All the models presently used for tokamak operation only possess a limited range of validity and suffer from non-negligible modelling inaccuracies. Moreover, the more precise the tokamak model, the more time it requires to simulate the tokamak evolution.

  Hence, translating a given plasma scenario into pre-programmed actuator signals is an imperfect process.

- **Irreproducibility of pulses**

  Tokamak evolution is highly sensitive to a large set of sometimes uncontrollable external influences. It is therefore arguably impossible to perform two identical pulses.

  Relying only on a pre-programming approach for reproducing plasma pulses may therefore lead to the implementation of pulses that greatly differ from one another.

- **Imperfect actuators**

  As any technological piece of equipment, the tokamak actuators are imperfect. For example, the PF system power supplies are subject to an operational delay, they may saturate when a too large absolute voltage demand is made, and they only approximately provide the demand voltage because power supplies rely on the switching of thyristors for providing DC voltage. As a result, using a pre-programming approach with imperfect actuators may lead to undesired tokamak behaviour.

- **Time scales**

  In a plasma pulse, the time scales of some plasma phenomena are extremely short. A human operator cannot possibly react to the tokamak evolution and adapt the actuators signals *on-the-fly*, i.e. during a plasma pulse.

  Hence, a pre-programming scheme using a human feedback is not appropriate for tokamak operation.

- **Vertical instability**

  Let us imagine that the scenario requires an elongated plasma. Paragraph 1.3.2 demonstrated that elongated plasmas are vertically unstable. Therefore, even slight discrepancies between the pre-programmed magnetic field configuration and its actual implementation during the plasma pulse may lead to the occurrence of a plasma column vertical displacement event (VDE).

1.5.2 Feedforward control

A more flexible scheme consists of enabling on-the-fly creation of the actuator demand signals on the basis of the references, also known as *feedforward control*. Feedforward control provides extra flexibility to the tokamak operator to adapt the scenario on-the-fly. Pre-programming is a special case of feedforward control.

Feedforward control applied on its own is not appropriate for tokamak control, for the same reasons detailed in the previous section. A more complex approach is therefore necessary for achieving reliable tokamak operation.

1.5.3 Feedback control

In order to reliably operate a tokamak, it is necessary to implement an automated mechanism that accounts for tokamak disturbances on-the-fly. This mechanism must automatically account for modelling and actuator imperfections as well. Finally, such an automated mechanism ought to react quickly, with a time constant much shorter than the effect it tries to control.

The feedback control research domain provides a solid theoretical and experimental background for the development of such automated feedback control mechanisms.

During operation, raw data, also known as the *system outputs*, is acquired by the plasma diagnostics. This raw data is then treated using analytical or computer-based algorithms to provide reconstructed or estimated data that can be directly compared with the references. These signals are known as the *measured outputs* $y(t)$. Given these definitions, a tokamak feedback control mechanism performs the following scheme:

1. The measured outputs $y(t)$ are subtracted from the corresponding references $y_{\mathrm{ref}}(t)$ at a given time t. This difference is also known as the *measured error*, or simply the *error* $e(t)$. It should be noted that a class of control algorithms is directly fed by both the measured outputs $y(t)$ and the references $y_{\mathrm{ref}}(t)$ [24], but such algorithms are not implemented in this thesis.

2. The error is fed to a control algorithm, which computes the actuators signals $u(t)$ that need to be demanded to the actuators on-the-fly.

3. The tokamak reacts to the demand actuator signals and its behaviour is measured by plasma diagnostics systems.

4. The measured outputs $y(t)$ are estimated or reconstructed on-the-fly by the diagnostic systems. They are then subtracted to the corresponding references.

5. The scheme starts again at point 1.

Such a feedback control mechanism is also called a *closed-loop* control scheme. A schematic representation of the action of a closed-loop control scheme is provided in Figure 1.11.
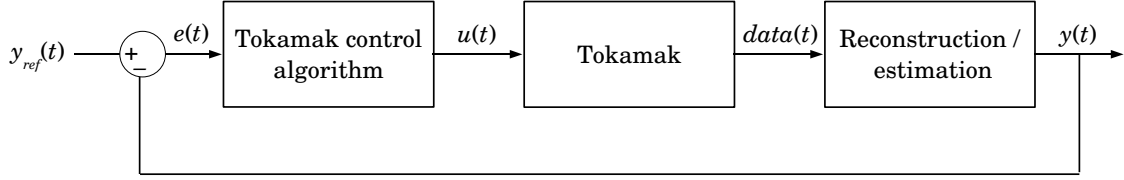
Figure 1.11: Schematic illustration of a tokamak closed-loop control scheme. $y_{\text{ref}}(t)$ are the references, $u(t)$ are the actuator signals as a function of time, and $y(t)$ are the estimated or reconstructed measured outputs.

Such a closed-loop control mechanism provides an automated solution to the challenges raised by tokamak operation. The disturbances, imperfect modelling, irreproducibility of pulses, and imperfect actuators are theoretically and practically treated as measured errors. Feedback control schemes can react quickly, depending on the data reconstruction scheme and the reactivity of actuators. Finally, the vertical instability challenge can be tackled by providing feedback control of the vertical position and speed of the plasma column.

It must also be stated that similar feedback control algorithms have been applied for a long time in a vast number of domains, from aeronautics to chemical engineering. Feedback control techniques have been applied to tokamaks since the 1960s [25].

1.5.4 Tokamak control engineering

Feedback and feedforward control

Pure feedback control schemes can only achieve mediocre performance when applied on tokamaks. Indeed, neglecting to use feedforward control combined with feedback control results in a large activity of the feedback controllers. The demand signals provided by the feedback controllers are large because the feedback control algorithm is responsible for both reference tracking and regulation. In turn, the actuator demand signals can sometimes exceed the capabilities of the actuators. To prevent actuator saturation or even unstable behaviour, it is usually necessary to decrease the aggressiveness of the feedback controllers, thus diminishing their effectiveness [26].

Combining feedback control with feedforward control greatly improves the control scheme performance. Such combination possesses the advantage of feedforward control in that the control system provides rough estimates of the demand actuator signals. At the same time, disturbances can be accounted for in a more aggressive manner via feedback control.

Tokamak control features

Since the first implementations of combined feedforward and feedback control schemes on tokamaks, both the improvement in computer performance and the increased accuracy of tokamak models opened new perspectives for tokamak control. Firstly, the number of measured outputs in real-time has increased, which enabled new reference tracking capabilities. Secondly, the improved computer performance allowed much more sophisticated control algorithms to be implemented. Finally, the recently developed and more subtle advanced tokamak scenarios necessitate precise implementation and efficient control schemes. The scope of tokamak control has thus widened. As a result, tokamak control schemes must now track and regulate more measured outputs with higher precision, and with essentially the same number of actuators.

Although combined feedforward and feedback control schemes can be very efficient, they have limitations inherent to tokamaks and to control theory:

- **Actuator limitations**
  Although the imperfection of actuators can be accounted for in some control algorithms, actuator limitations such as saturations, delays, or inaccuracies decrease the efficiency of the control scheme.

- **Measured output estimation or reconstruction**
  The performance of a control scheme depends on the precision of the measured output estimation or reconstruction. Uncertainty in the measured outputs directly passes on as a decrease of the efficiency of the control scheme.

  When tokamak protection is at stake, there exist control algorithms known as *robust control* schemes that guarantee that operation remains on the 'safe' side with regard to measured output uncertainty or other features (for example, large disturbances). Robust control schemes are less efficient than more aggressive control schemes.

- **Validity range**
  In order to implement a combined feedforward and feedback control scheme for tokamak operation, two tokamak models must be developed. Firstly, the feedforward control model must be able to estimate the actuator signals that must be demanded according to the references. Secondly, the feedback control model must be able to estimate the actuator signals that must be demanded according to the measured error. These models ought to converge faster than the time scale of the tokamak behaviour it is modelling because they must provide estimations on-the-fly, except for pre-programming.

  Hence, tokamak control models must remain simple in order provide fast computation of the appropriate actuator demands. However, simple models cannot simulate the full complexity of tokamaks. Therefore, simple tokamak models possess a limited validity range, and when tokamaks reach a state outside of the validity range, the control scheme may fail.

- **Infeasibility of scenarios**
  Some scenarios are not feasible given a specific tokamak and its associated actuator set. For example, the reference plasma current may be too high to be achieved, or the reference shape may be inappropriate for the tokamak magnetic configuration. In such cases, the control system fails to successfully implement the scenario.

Although not perfect, combined feedforward and feeback control schemes are extremely useful tools for tokamak operation.

1.5.5 Definition of control

Since the 1990s, the tokamak control community vocabulary has evolved in an ambiguous manner regarding control. In some cases, 'to control' means 'to have an effect on'. In the author's opinion, that definition is somewhat vague. For example, current and pressure profile 'control' has been reported, when really only the timing of the L-H transition is modified, thus affecting the current density and pressure profile evolutions [27]. Another example is the reported 'control' of the Neoclassical Tearing Modes (NTMs) using sawtooth 'control' [28]. In this case, 'sawtooth control' should be understood as pre-programmed sawtooth frequency control, whereas 'NTM control' means that NTMs are *avoided* using the feedforward sawtooth frequency control technique.

In control theory, *control* is defined as 'the use of algorithms and feedback in engineered systems' [29] and the goal of a control system is to 'make the controlled system behave in a desired way by manipulating the plant actuators'. The more specific objectives of a control system are to *regulate* the controlled system, i.e. to counteract the effect of disturbances, and to *track* a reference, i.e. to keep the system evolution close to a pre-determined reference [30].

Throughout this thesis, the term 'control' will refer to the control theory definition in order to avoid confusion. A system variable will be considered 'controlled' if it can be brought from an arbitrary starting state to a given objective state in a finite time and using finite actuator signals, provided that the objective state is attainable. In that sense, the use of the term 'control' in this thesis can be associated with what is sometimes obscurely known as 'real-time control' in the tokamak operation community.

1.6 Tokamak performance

There are several ways to define the performance of a tokamak plasma pulse. In most cases, the success or failure of a plasma pulse is subjectively determined by the tokamak operator who estimates whether the pulse objective was achieved. However, performance can be defined in a more formal manner. Such a definition ought to encapsulate the long-term goal of using tokamaks as controlled fusion devices and must enable the comparison between plasma pulses on the same or on different tokamaks. This paragraph discusses possible metrics for

assessing the performance of a tokamak plasma pulse.

1.6.1   Fusion gain

The performance of a controlled fusion reactor can be defined as the ratio between the net power produced by the plant and the required power necessary for operation, i.e.

$$\zeta = \frac{P_{\text{net}}}{P_{\text{consumed}}},$$

where P_{net} is the net produced power, and P_{consumed} the consumed power for operation. This ratio must be $\zeta > 1$ for controlled fusion reactors.

This metric is inappropriate for evaluating the performance of presently performed plasma pulses because no tokamak has ever usefully collected fusion power. P_{net} depends on unknowns factors such as the efficiency of the neutron collector, the blanket coolant, and several other characteristics specific to hypothetical controlled fusion reactors. On the other hand, P_{consumed} can already be estimated, but its value depends on tokamak-dependent factors such as the resistivity of the TF, CS, and PF coils, the efficiency of the voltage power supplies, the efficiency of the heating and current drive systems, and the efficiency of the control systems.

It is of more interest to define a performance criterion that can be compared between tokamaks and between plasma pulses. Such a criterion can be given by the fusion gain Q defined as:

$$Q = \frac{P_{\text{fus}}}{P_{\text{boundary}}}, \tag{1.7}$$

where P_{boundary} the total amount of external power provided at the plasma boundary (Ohmic power and additional power) and P_{fus} is the fusion power produced in the plasma, i.e.

$$P_{\text{fus}} = \int_V \mathscr{R} \, dV \cdot 17.6\text{MeV} = 17.6\text{MeV} \cdot \int_V n_D n_T \langle \sigma v \rangle dV,$$

where V is the plasma volume and 17.6MeV is the amount of energy produced by one fusion reaction.

Significant fusion gain has already been obtained. The best performance was achieved by the Joint European Torus (JET) tokamak in 1999, where $Q = 0.95 \pm 0.17$ was transiently achieved [31].

It should be stated that achieving $Q > 1$ does not directly imply that the tokamak is producing more net power than it consumes. In fact, Q is simply a scale indicating tokamak performance. Achieving $\zeta > 1$, which would denote higher net power production than power consumption, is only attained for higher values of Q.

1.6.2 Energy confinement time

Another possible expression of tokamak performance is given by the so-called *Lawson criterion* [32]. Let us assume a plasma with a of 50% deuterium and 50% tritium composition ($n_D = n_T = \frac{n}{2}$) raised at a temperature T. The plasma has a volume V. Let us also assume that this plasma loses power as:

$$P_{\text{loss}} = P_{\text{Brehms}} + \frac{W}{\tau_E},$$

where

$$P_{\text{Brehms}} = 4.8 \cdot 10^{-37} \int_V n^2 T^{1/2} dV \qquad T \text{ in [keV]}$$

is the power radiated by Brehmsstrahlung [20], $W = 3 \int_V n T dV$ is the plasma energy, and τ_E is the characteristic energy confinement time.

Let us now assume that all the helium fusion products ^4_2He (also known as α-particles) stay within the plasma and contribute to its heating. The α-particle plasma self-heating power is given by:

$$P_\alpha = \int_V \frac{1}{4} n^2 \langle \sigma v \rangle \mathscr{E}_\alpha dV,$$

where $\mathscr{E}_\alpha = 3.5\text{MeV}$ is the energy carried by the α-particle fusion product.

The Lawson criterion consists of a simple power balance criterion. It requires that the plasma heating power be greater than the power loss in order to sustain the plasma. In other words,

$$P_\alpha + P_{\text{additional heating}} \geq P_{\text{Brehms}} + \frac{W}{\tau_E}.$$

Assuming that there is no additional heating ($P_{\text{additional heating}} = 0$) and that the Brehmsstrahlung power is negligible compared to the plasma characteristic power loss, this inequality can be expressed as

$$\mathscr{E}_\alpha \tau_E \int_V n^2 \langle \sigma v \rangle dV \geq 12 \int_V n T dV \tag{1.8}$$

In the ~10-20keV temperature range, the $\langle \sigma v \rangle$ parameter for deuterium-tritium fusion reactions scales as [18]:

$$\langle \sigma v \rangle \cong 1.1 \cdot 10^{-24} T^2 \qquad T \text{ in [keV]}.$$

Assuming that the plasma density and temperature are higher at the plasma axis than at the plasma boundary, and assuming that the density and temperature profiles are parabolic, the

Lawson criterion for plasma ignition can be expressed as

$$\hat{n}\hat{T}\tau_E \geq 5\cdot 10^{21}\,\mathrm{m}^{-3}\,\mathrm{keV\,s}, \tag{1.9}$$

where $\hat{n}$ is the plasma density at the plasma axis and $\hat{T}$ is the plasma temperature at the plasma axis.

The left-hand-side of inequality (1.9) can be considered as a metric for tokamak performance. It increases as the energy confinement time τ_E for given peak value of plasma temperature and density. Thus, τ_E can be considered itself as an indicator of tokamak performance.

1.6.3 Limits to tokamak performance

It is possible to choose either Q or $nT\tau_E$ as a metric for plasma pulse performance. Whichever the choice, performance is in fact limited for a given tokamak by the following factors:

- **Greenwald density limit**
  Both the fusion gain Q and the Lawson factor $nT\tau_E$ increase when the plasma density increases. A simple approach to improve tokamak performance could thus simply consist of increasing the plasma density. Unfortunately, there is a maximum density that a tokamak plasma can sustain for a given plasma current I_p and a given plasma shape. This critical density is known as the *Greenwald density limit* $\bar{n}_G$ [33]

$$\bar{n}_G = \gamma\frac{I_p}{\pi a^2}, \tag{1.10}$$

  where $\bar{n}_G$ is expressed in $[10^{20}\mathrm{m}^{-3}]$, I_p is expressed in [MA], a is expressed in [m], and $\gamma = 1$ $[\mathrm{m}^{-1}\,\mathrm{MA}^{-1}]$. This density limit is expressed as a line-averaged density.

  Tokamak performance is restrained by the Greenwald density limit. However, increasing the plasma current enables the achievement of a higher density and, in turn, improves the tokamak performance.

- **Troyon β-limit**
  Improving tokamak performance can be achieved by increasing plasma pressure $p = nT$. However, there exists a semi-empirical limit restraining the maximum pressure achievable in a particular magnetic configuration known as the *Troyon limit*.

  In order to express the Troyon limit, it is necessary to scale the plasma pressure with respect to the magnetic configuration. Such a scaling is provided by the definition of the dimensionless parameter β

$$\beta = \frac{2\mu_0 \int_V p\,dV}{\int_V B^2\,dV}, \tag{1.11}$$

  where V is the plasma volume. The numerator of the definition of β thus corresponds

to the volume averaged plasma pressure, while the denominator corresponds to the volume averaged magnetic pressure.

The Troyon limit is then expressed as [34, 35]:

$$\beta < C_{\text{Troyon}} \frac{\mu_0 I_p}{a B_\phi}. \tag{1.12}$$

where $C_{\text{Troyon}} = 2.0 - 3.0$, with β expressed in [%], I_p expressed in [MA], a expressed in [m], and B_ϕ expressed in [T].

Hence, performance cannot be straightforwardly improved on a given tokamak, but theoretical and empirical limits exist.

1.6.4   Energy confinement time scaling law

It is important to understand how the tokamak performance scales with respect to parameters that can be acted upon. In that perspective, scaling laws for the energy confinement time have been compiled using data from several hundreds of plasma pulses and several tokamaks [36, 37]. These scaling laws depend on the scenario class. For ELMy H-mode scenarios, which is one of the most performing class of tokamak scenarios, the energy confinement time scales as [38]

$$\tau_E = 5.62 \cdot 10^{-2} I_p^{0.93} B_{\phi,0}^{0.15} \bar{n}^{0.41} P_{\text{add}}^{-0.69} R_0^{1.97} \kappa^{0.78} \left(\frac{a}{R_0}\right)^{0.58} M^{0.19}, \tag{1.13}$$

where R_0 is the toroidal vacuum vessel major radius, $B_{\phi,0}$ the toroidal magnetic field at the $(R, Z) = (R_0, 0)$ position, P_{add} the additional heating power expressed in [MW], and M is the averaged ion mass expressed in atomic mass unit. The plasma current I_p is expressed in [MA], and the line-averaged density $\bar{n}$ in $[10^{19} \text{m}^{-3}]$. This scaling is known as the ITER IPB98(y,2) scaling.

As a result, performance can be improved by modifying several different factors in the tokamak design, such as the maximum achievable plasma current, the vacuum vessel major radius, or the maximum achievable toroidal magnetic field.

1.7   ITER

In order to improve performance, several approaches can be envisaged, as suggested by the results exposed in 1.6.4. One such approach consists of designing and building a tokamak with increased size, increased toroidal magnetic field intensity, and increased achievable plasma current when compared to presently-operated tokamaks. Such a tokamak is realised by the ITER project.

ITER is a tokamak presently under construction in Cadarache, France. It is multi-billion

Swiss francs project benefiting from an intense international collaborative effort involving Switzerland, the European Union, the United States, the Russian Federation, China, South Korea, India, and Japan. The ITER project was first started in 1985.

ITER aims at demonstrating the feasibility of controlled fusion as an energetically and economically viable energy source. In other words, ITER aims at achieving higher plasma pulse performance in the sense discussed in paragraph 1.6. ITER originally aimed at achieving ignition, i.e. a triple product $\hat{n}\hat{T}\tau_E = 0.98 \cdot 10^{20} \text{m}^{-3} \times 12.9 \text{keV} \times 5.9\text{s} = 7.4 \cdot 10^{21} \text{m}^{-3}\text{keVs}$, which would have satisfied the Lawson criterion for ignition [38]. However, because of budget restrictions and other political and technical downturns, this objective has been downsized. ITER is presently envisaged to reach a fusion gain of $Q \sim 10$ [39].

ITER's main characteristics are provided in Table 1.1 and a schematic representation of its layout is displayed in Figure 1.12.
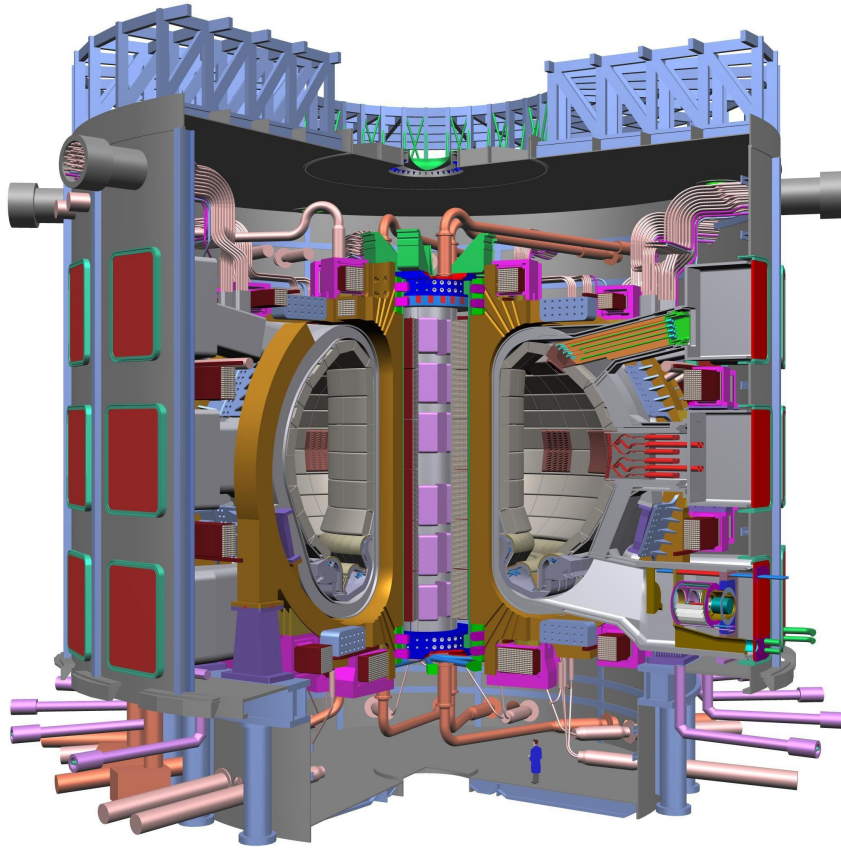
Figure 1.12: Schematic illustration of ITER.

In order to demonstrate its relevance towards the development of a controlled fusion reactor, ITER must be capable of performing advanced scenarios. Assessing the feasibility of advanced

Table 1.1: Nominal ITER characteristics.

Parameter	Attributes
Fusion power P_{fus}	500MW
Fusion gain Q	~10
Major radius R	6.2m
Plasma minor radius a	2.0m
Plasma elongation κ	1.85
Plasma volume V	830m^3
Plasma cross-sectional area S_{plasma}	22m^2
Plasma current I_p	15MA
Toroidal magnetic field at 6.2m radius $B_{\phi,0}$	5.3T
Installed ECRH/ECCD power	20MW
Installed ICRH power	20MW
Installed NBI power	33MW

scenarios using the present ITER design requires ITER modelling and simulation.

1.8 Tokamak simulation

1.8.1 Modelling approaches

Assessing ITER's design and future performance requires the simulation of ITER plasma pulses. However, no simulator is presently capable of encapsulating its full complexity.

There exist a significant amount of tokamak and/or plasma simulators, each encapsulating a fraction of the full tokamak complexity. Each simulator aims at providing insight regarding specific challenges.

Tokamak and/or plasma modelling can be tackled using modelling approaches that can be divided in three categories.

- **Physics-based modelling**
  The physics-based modelling approach consists of developing a mathematical model of the system that is solely based on physics, i.e. with no empirical or ad hoc information encapsulated within the model. Physics-based modelling thus requires full a priori knowledge of the modelled system. In the case of tokamak modelling, physics-based models would solely rely on Maxwell's equations and the Vlasov equation for the kinetic evolution of the plasma [18].

  No physics-based model is capable of providing information regarding the full tokamak evolution, i.e. from the evolution of the PF system coil currents to the turbulence in the plasma core. Most physics-based models therefore rely on simplifying assumptions regarding the plasma evolution.

- **Empirical modelling**

  The empirical modelling approach is the exact opposite of the physics-based modelling approach. Empirical modelling requires no a priori knowledge of the modelled system but relies entirely on empirical data.

  Empirical modelling typically consists of regressing a large collection of measured outputs to actuators signals in order to deduce simple mapping laws. This data regression can be performed using several different methods.

  The empirical modelling approach is simple and the designed models are usually extremely fast. However, it requires experimental data and possesses a limited range of validity. Moreover, empirical models do not use any physical knowledge of the system that the operator may possess.

- **Semi-empirical modelling**

  A semi-empirical modelling approach consists of a physics-based modelling approach to which empirical data is provided, or of an empirical modelling approach onto which physical knowledge of the system is implemented. As its name suggest, the semi-empirical modelling approach is mid-way between the physics-based modelling approach and the empirical modelling approach.

  Most tokamak and/or plasma simulators take a semi-empirical modelling approach. There is a spectrum of semi-empirical models, some being closer to physics-based models and some being closer to empirical models. This choice is usually linked to the purpose of the simulator, its desired range of validity, and its desired simulation speed.

1.8.2   Simulator validation

In order to assess whether a tokamak and/or plasma simulator accurately models the experimental evolution of the tokamak and/or plasma, it is important to compare simulation results to experimental data. Such a process is often referred to as *validation.*

It is important to state that a simulator can only be validated for a precise purpose and within a certain range of validity. In the author's opinion, generic simulator 'validation' is an ambiguous statement, even though such a phrase is sometimes encountered in the controlled fusion literature. Stating that a simulator is plainly 'valid' neglects the fact that the simulator is based on physical assumptions limiting its range of validity and that the simulator is designed for a specific purpose or to answer a specific type of questions.

The process of simulator validation for a certain range and for a specific purpose typically is a delicate task for the following reasons:

- Validation requires the comparison of simulated results against experimental data. The success of the validation process is therefore dependent on the precision of experimental data.

In most cases, plasma parameters and profiles are reconstructed from raw experimental data. Such reconstruction necessitates modelling of the plasma diagnostic. In turn, the precision of the reconstructed experimental data depends on the precision of the data reconstruction model.

One way of overcoming this challenge is to include synthetic diagnostics in the tokamak and/or plasma simulator. In other words, the effect of the plasma evolution on the diagnostics is modelled in order to provide simulated raw diagnostic data. This simulated raw synthetic diagnostic results can then be straightforwardly compared to raw experimental data.

- Dynamic experiments must be performed in order to assess the dynamic validity of the tokamak and/or plasma simulator. Such dynamic experiments may be difficult to implement, risky, or simply impossible to perform.

- The range of validity of the tokamak and/or simulator must be explored. This can only be achieved by performing several dedicated experiments that explore the operation space. Such experiments may be difficult to implement, risky, or simply impossible to perform.

- Precise tokamak and/or plasma simulation requires accurate initial condition measurements in order to appropriately configure the simulator. However, the initial conditions can never be exactly measured.

  The structure of the simulated process must therefore be simple. Indeed, highly non-linear processes may be extremely sensitive to initial conditions, both experimentally and in simulations. Hence, such non-linear processes may be difficult to reproduce experimentally and minor discrepancies between experimental initial conditions and the initial conditions imposed to the simulator may lead to significant differences in tokamak and/or plasma evolution.

As a result, simulator validation for a specific purpose and for a precise range is a challenge that cannot always be met. When thorough validation cannot be achieved, it is useful to asses the range of validity of a model. The range of validity of empirical models is, by construction, equivalent to the range of the data used for their identification. The range of validity of a semi-empirical model also depends on the physical assumption made during the model development. However, the dynamical validity of empirical or semi-empirical models cannot be straightforwardly inferred.

1.8.3 Full tokamak simulators

Throughout this thesis, the DINA-CH&CRONOS full tokamak simulator has been used for ITER modelling and simulation.

As exposed in greater details in Chapter 2, a full tokamak simulator models the evolution of

the full tokamak, i.e. the effect of demand actuator signals on the actuators, as well as their subsequent effect on the plasma evolution. The plasma equilibrium evolution is mostly based on well-known physics, while the plasma core transport modelling is semi-empirical.

1.9   Scope and organisation

This thesis is divided in several parts which all have the common aim of studying ITER operation from the tokamak control and free-boundary simulations viewpoints.

Chapter 2 exposes the theoretical bases for tokamak modelling and describes the DINA-CH&CRONOS full tokamak simulator and its functioning scheme. Its various components, i.e. the DINA-CH simulator, the CRONOS simulator, and the Simulink framework within which the full tokamak simulator is embedded are discussed.

Use cases of DINA-CH&CRONOS are exposed in Chapter 3. The effect of power supply ripple on magnetic coil diagnostics is discussed. The effect the cross-coupling modulation of ECRH power and loop voltage on the current density profile for ITER is explored. Additional work using DINA-CH&CRONOS is mentioned. This chapter aims at demonstrating the potential usage of a full tokamak simulator. It also served the more specific purpose of enabling the author to get accustomed to the DINA-CH and DINA-CH&CRONOS interface and better understand their working schemes.

Chapter 4 is dedicated to optimal control considerations. As further exposed, it is the author's opinion that optimal control may greatly benefit to the operation of ITER. The implementation of an open-loop optimal control algorithm for plasma equilibrium evolution with DINA-CH&CRONOS is exposed. An open-loop-with-feedback optimal control algorithm is discussed and implemented using a simpler tokamak behavioural model. This Chapter concludes with a discussion of real-time optimisation techniques and their possible application for tokamak operation.

Advanced scenario simulations using DINA-CH&CRONOS are reported in Chapter 5, in which specific attention is devoted to sensitivity of the hybrid scenarios to ramp-up conditions and the achievement of a steady-state pulse without the presence of an Internal Transport Barrier (ITB).

Conclusions of this work are provided in Chapter 6.

2 The DINA-CH&CRONOS full tokamak simulator

The basic principles of tokamak operation are exposed in Chapter 1, in which heuristic arguments demonstrate the possibility of operating a tokamak as a controlled fusion device. The present chapter discusses more precise tokamak and plasma modelling.

Tokamak and plasma modelling and simulation are necessary in order to interpret former pulses, predict the evolution of future pulses, and assess the design of future tokamaks such as ITER. They also improve our general understanding of plasma behaviour.

Because there exists no general analytical solution of tokamak evolution, tokamak models must be numerically solved.

As discussed in 1.8, no simulator can fully encapsulate the complexity of a tokamak and simplifying assumptions must be made when modelling a tokamak. A clear statement of the purpose of the simulator is thus required in order to provide modelling guidelines.

In this work, our principal interest consists of assessing the design of ITER for performing advanced scenarios. In particular, we would like to determine whether the TF, CS, and PF coils, as well as the heating and current drive systems, are capable of performing advanced scenarios while guaranteeing the plasma column vertical stability and remaining within the tokamak operational limits. In that perspective, the tokamak model and simulator should satisfy the following ad hoc criteria:

> *An appropriate simulator for assessing ITER's design for the implementation of advanced scenarios must accurately model the tokamak electric power supplies, the evolution of the PF system coil currents and the conducting vacuum vessel currents, and the evolution of the plasma equilibrium according to the PF system power supplies action. The effects of transport, additional heating, and additional current drive on the plasma equilibrium should be modelled as accurately as possible, given the caveat that the simulator speed should not be too altered by these features. Finally, the control systems and their limitations should be conservatively modelled.*

These subjective criteria will be considered as guidelines for tokamak modelling and simulation throughout this thesis.

Tokamak modelling satisfying the above criteria is described in 2.1. The DINA-CH simulator, described in 2.2, simulates the evolution of the free-boundary plasma equilibrium and the evolution of the tokamak subsystems, such as the PF system power supplies and the control systems. The CRONOS suite of codes, which is introduced in 2.3, simulates advanced transport in the plasma core and computes the effects of the heating and current drive systems on the plasma. Finally, the DINA-CH&CRONOS full tokamak simulator, exposed in 2.4, combines DINA-CH and CRONOS and simulates the evolution of the full tokamak.

2.1 Tokamak modelling

Throughout this thesis, a tokamak will be considered as a set of the following subsystems:

- The TF coils;

- The PF system power supplies;

- The PF system coils;

- The conducting vacuum vessel;

- The plasma;

- The heating and current drive systems;

- The plasma diagnostics;

- The control systems.

This list of tokamak subsystems is *not* exhaustive. It lacks, for example, the vacuum subsystems, several plasma diagnostics, and the gas valves for deuterium and tritium injection. The fact that these subsystems are not modelled is a simplifying choice made in accordance with the tokamak modelling guidelines stated above.

In this paragraph, analytical modelling of the listed tokamak subsystems is discussed.

2.1.1 Axisymmetry and modelling of the TF coils

To achieve its stated objective, the desired simulator needs not model the full complexity of a tokamak. The simplifying assumption of *axisymmetry* is made.

Assuming axisymmetry consists of assuming that the properties of the tokamak and the plasma it confines are independent of the toroidal angle ϕ. Such an assumption significantly

simplifies the tokamak modelling by neglecting the toroidal dimension. An axisymmetric model is two-dimensional.

Assuming each TF coil turn is loaded with the same constant current I_{TF}, the toroidal magnetic field in the plasma region can be analytically determined using Ampère's law:

$$\oint_C \mathbf{B}_{TF} \cdot \mathbf{dl} = \mu_0 I_{TF} N, \tag{2.1}$$

where C is the horizontal circular contour in the plasma region displayed in Figure 2.1 and N is the number of TF coil turns surrounding the contour.
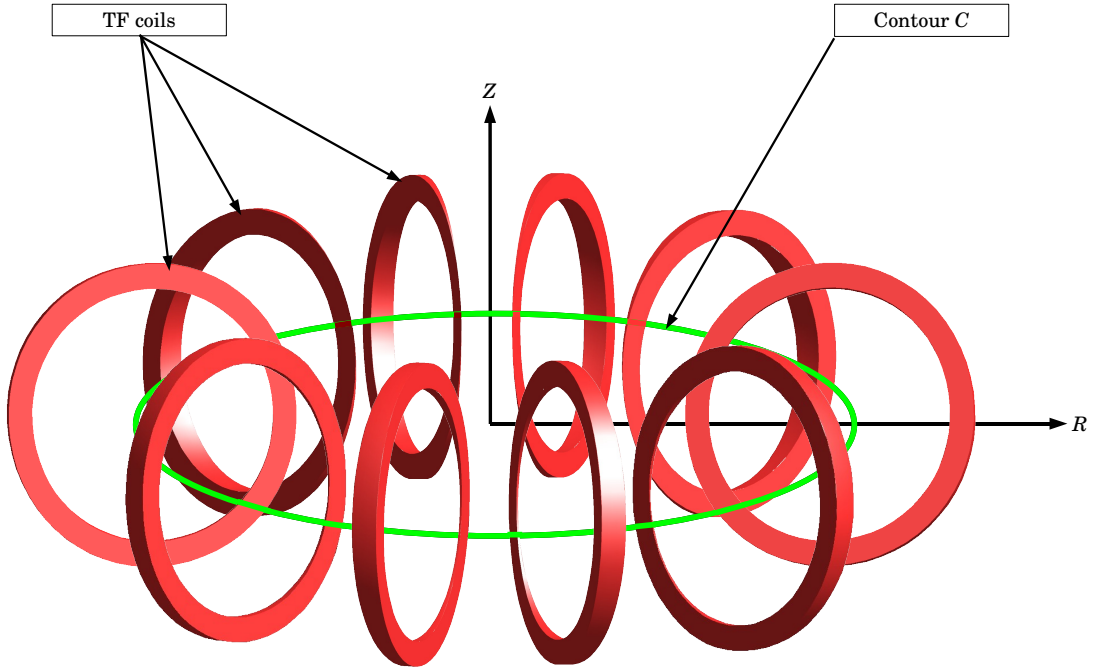
Figure 2.1: Schematic representation of a tokamak TF coils and a contour C of constant radius R and vertical position Z.

In axisymmetric models, the magnetic field applied by the TF coils in the plasma region is exactly toroidal. This is due to the fact that axisymmetric models assume that the tokamak configuration is independent of ϕ. In other words, axisymmetry guarantees that

$$\mathbf{B}_{TF}(R, \phi, Z) = B_{TF,\phi}(R) \cdot \hat{\mathbf{e}}_\phi. \tag{2.2}$$

Injecting (2.2) in (2.1), we have

$$B_{\mathrm{TF},\phi}(R) = \frac{\mu_0 I_{\mathrm{TF}} N}{2\pi R},$$ (2.3)

where R is the radius of the horizontal circular contour C. Hence, providing the intensity of the toroidal magnetic field $B_{\mathrm{TF},\phi}(R_0)$ at a given radius R_0 fully determines the toroidal magnetic field induced by the TF coils in the plasma region, because

$$B_{\mathrm{TF},\phi}(R) = \frac{B_{\mathrm{TF},\phi}(R_0) R_0}{R}.$$ (2.4)

In this derivation, it was assumed that the TF coil single-turn current I_{TF} was constant in time. In reality, the TF coil single-turn current is affected by the presence of any poloidal currents in the vacuum vessel and in the plasma. Nonetheless, the TF coil single-turn current can be maintained approximately constant by a simple control system. Therefore, the assumption I_{TF}=const. generally holds.

Axisymmetric models assume an ideal configuration that neglects the toroidal magnetic field ripple due to the TF coils spacing. Because the toroidal magnetic field ripple induces non-negligible effects on transport [18], these effects must be accounted for. A viable approach consists of averaging the effects of the toroidal magnetic field ripple over ϕ in order to determine their intensity on a poloidal cross-section. Toroidal magnetic field ripple effects can also be accounted for by semi-empirical or empirical transport models.

2.1.2 Modelling of the PF system power supplies

Generic modelling of power supplies

The modelling of electric power supplies is the subject of several works [40, 41, 42]. These works aim at achieving high precision modelling, which is not required for meeting the tokamak simulator stated objective. In this thesis, it is considered sufficient to model power supplies as first order filters with delay, provided the estimation of their pure delay and characteristic time is conservative.

The Laplace transform of the transfer function of a power supply without saturations can be expressed as

$$G(s) = \frac{e^{-\tau_D s}}{1 + s \tau_{\mathrm{PS}}}$$ (2.5)

where τ_{PS} is the power supply characteristic time, τ_D is the power supply pure delay.

Power supply saturation is modelled as a maximum and a minimum voltage limit that cannot be violated. These limits depend on the current provided by the power supply.

ITER poloidal field systems

Before modelling the ITER poloidal field (PF) power supplies, it is necessary to first discuss the design and functioning scheme of the ITER PF systems. Figure 2.2 displays ITER's poloidal cross-section as defined in [43] (2010 design).
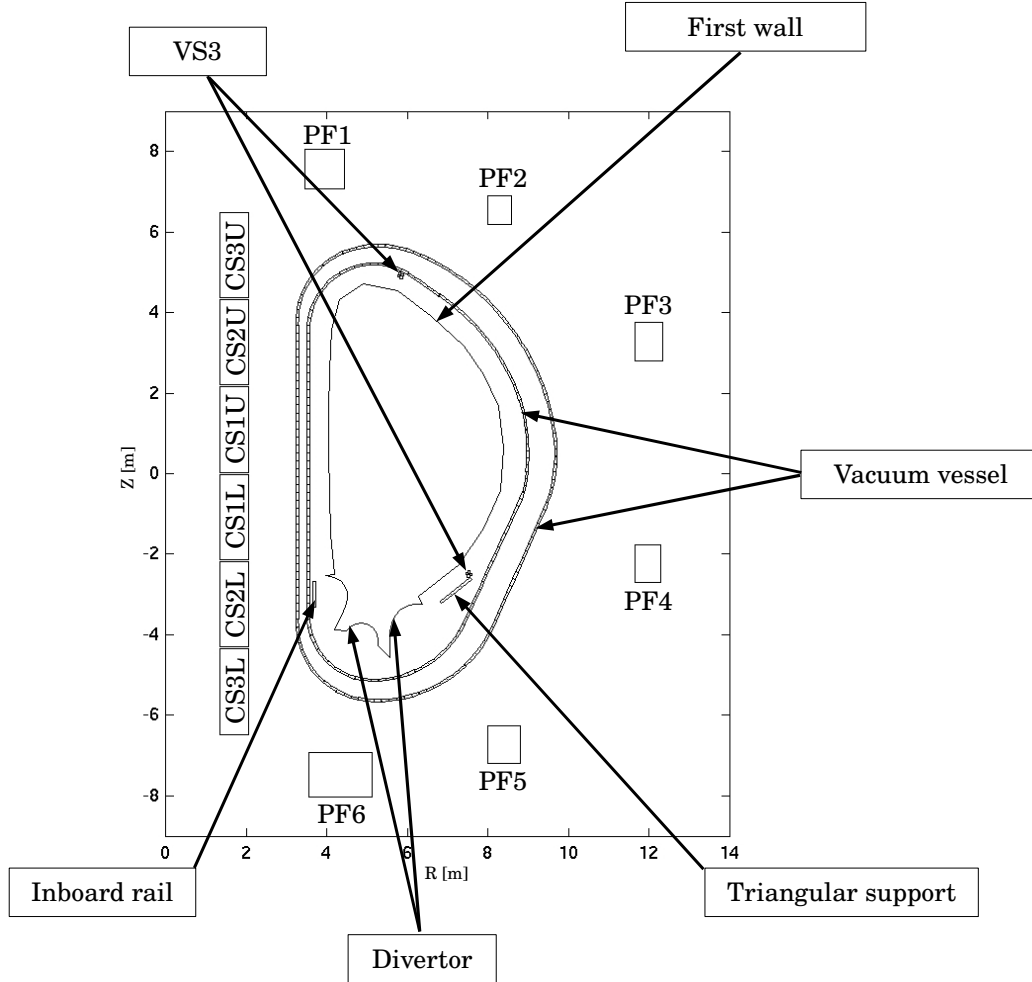
Figure 2.2: ITER poloidal cross section. The CS coils, PF coils, vertical stabilisation coils, passive stabilisation plates, and vacuum vessel conducting plates are displayed.

The ITER PF systems consists of 14 'active' coils, i.e. 14 coils on which a voltage can be actively applied via the action of one or several power supplies. These active coils are the following:

- **CS coils**
  The ITER PF system contains six CS coils named CS3U, CS2U, CS1U, CS1L, CS2L, and CS3L from top to bottom. They each have 553 turns. CS3U, CS2U, CS2L, and CS3L are each connected to four separate power supplies, while CS1U and CS1L are connected in

series and share the same double voltage power supply.

- **PF coils**
  The ITER PF system contains six PF coils named PF1 (248.6 turns), PF2 (115.2 turns), PF3 (185.9 turns), PF4 (169.9 turns), PF5 (216.8 turns), and PF6 (459.4 turns). The non-integer number of turns is an artefact introduced by Yuri Gribov. Each of these six PF coils is connected to a separate power supply. On top of that, PF2 and PF3 are connected in parallel and PF4 and PF5 are connected in anti-parallel to a strong and fast power supply for vertical stabilisation, called VS1. The connections of VS1 are displayed in Figure 2.3.

- **VS3 coils**
  The two VS3 coils are in-vessel coils with 4 turns each. Their role is to ensure the vertical stability of the plasma column in case of exceptional events. The two VS3 coils are connected in anti-series to the same power supply.

To summarise, it is necessary to model the behaviour of 13 power supplies: the main converters (each of the CS3U, CS2U, CS1UL, CS2L, CS3L, PF1, PF2, PF3, PF4, PF5, and PF6 power supplies), the VS1 power supply, and the VS3 power supply.

ITER main converters

According to [44], the main converters (MCs) are designed to each have a $\tau_{\text{D, MC}} = 0.015$s pure delay and a $\tau_{\text{MC}} = 0.015$s characteristic time. Hence, each MC can be modelled by the following transfer function

$$G_{\text{MC}}(s) = \frac{e^{-0.015s}}{1 + 0.015s}. \tag{2.6}$$

The MCs saturate when the demand voltage reaches either an upper limit or a lower limit. These limits depend on the current load of each MC and are detailed in [43].

ITER vertical stabilisation power supplies

The ITER VS1 power supply is connected to the PF2, PF3, PF4, and PF5 coils as exposed in Figure 2.3. As a result, the additional voltage supplied by VS1 to PF2 and PF3 is identical in absolute value and opposite in sign to the additional voltage supplied by VS1 to PF4 and PF5.

The VS1 power supply is faster than the MCs. Its design pure delay is $\tau_{\text{D,VS1}} = 0.0025$s and its design characteristic time is $\tau_{\text{VS1}} = 0.0075$s, thus resulting in the following transfer function

$$G_{\text{VS1}}(s) = \frac{e^{-0.0025s}}{1 + 0.0075s}. \tag{2.7}$$
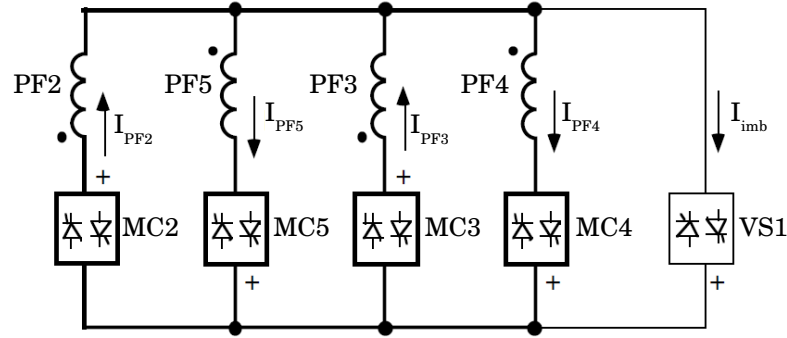
Figure 2.3: ITER VS1 connections. The PF2, PF3, PF4, and PF5 Main Converters are displayed, as well as the imbalance current $I_{\mathrm{imb}} = I_{\mathrm{PF2}} + I_{\mathrm{PF3}} - I_{\mathrm{PF4}} - I_{\mathrm{PF5}}$. This scheme was published in [39].

The VS1 power supply requires that the imbalance current, defined as

$$I_{\mathrm{imb}} = I_{\mathrm{PF2}} + I_{\mathrm{PF3}} - I_{\mathrm{PF4}} - I_{\mathrm{PF5}}, \tag{2.8}$$

be contained within the interval [-22.5kA,22.5kA] in order to avoid power supply saturation.

The VS3 power supply is connected to the VS3 coils in anti-series, meaning that the current within the upper VS3 coils is identical in absolute value and opposite in sign to the curent within the lower VS3 coils. Its design pure delay is $\tau_{\mathrm{D,VS3}} = 0.0025$s and its design characteristic time is $\tau_{\mathrm{VS3}} = 0.0075$s, thus resulting in the following transfer function

$$G_{\mathrm{VS3}}(s) = \frac{e^{-0.0025s}}{1 + 0.0075s}. \tag{2.9}$$

2.1.3 Plasmaless modelling of the PF system currents and the vacuum vessel currents

The ITER PF system coils can be modelled as $n_c = 12$ coils each carrying a current

$$I_i = N_{\mathrm{turns},i} \cdot I_{\mathrm{turn},i},$$

where $N_{\mathrm{turns},i}$ is the number of turns in the i-th coil, $I_{\mathrm{turn},i}$ is the current in one turn of the i-th coil, and $i = \{$CS3U, CS2U, CS1UL, CS2L, CS3L, PF1, PF2, PF3, PF4, PF5, PF6, VS3$\}$. The conducting vacuum vessel can be modelled as a set of n_v adjacent plates each carrying a toroidal current $I_{\mathrm{vac},i}$, with $i = 1, ..., n_v$.

Assuming a plasmaless tokamak, it is possible to model the evolution of the PF system currents and the conducting vacuum vessel currents according to the power supply voltages. Such a model is often known as a *vacuum model*.

The circuit equations of a plasmaless tokamak can be obtained by remarking the following for each PF system coil or vacuum vessel plate:

- The i-th coil is supplied a voltage $+V_i$ by its power supply if the coil is active and no voltage if the coil is passive, which is the case of vacuum vessel conducting plates;

- The i-th coil has a self-inductance L_i. The self-induced emf is given by

$$\epsilon_{\text{self},i} = -L_i \frac{dI_i}{dt}, \tag{2.10}$$

 where I_i is the current loaded in the i-th coil;

- The i-th coil is subject to the mutual inductance of all the other coils, which induce an emf within the i-th coil. The emf induced by the j-th coil is given by $(i \neq j)$

$$\epsilon_{\text{mut},j} = -M_{ij} \frac{dI_j}{dt}, \tag{2.11}$$

 where M_{ij} is the mutual inductance between the i-th coil and the j-th coil;

- The i-th coil has a resistance Ω_i, which leads to a reduction in voltage $\epsilon_{\text{R},i}$:

$$\epsilon_{\text{R},i} = -\Omega_i I_i. \tag{2.12}$$

The circuit equation can thus be written as

$$V_i + \epsilon_{\text{self},i} + \sum_{j \neq i} \epsilon_{\text{mut},j} + \epsilon_{\text{R},i} = 0, \tag{2.13}$$

which is valid for each coil or vessel plate i. This yields

$$V_i = L_i \frac{dI_i}{dt} + \sum_{j \neq i} M_{ij} \frac{dI_j}{dt} + \Omega_i I_i. \tag{2.14}$$

This can be rewritten in the compact matrix form:

$$\mathbf{V}_v = \underline{\underline{\mathbf{M}}}_v \frac{d\mathbf{I}_v}{dt} + \underline{\underline{\mathbf{\Omega}}}_v \mathbf{I}_v, \tag{2.15}$$

where

$$\underline{\underline{\mathbf{M}}}_\nu = \begin{bmatrix} L_{\text{CS3U}} & M_{\text{CS3U-CS2U}} & \cdots & M_{\text{CS3U-PF6}} & M_{\text{CS3U-VS3}} & M_{\text{CS3U-vac,1}} & \cdots & M_{\text{CS3U-vac},n_\nu} \\ M_{\text{CS2U-CS3U}} & L_{\text{CS2U}} & \cdots & M_{\text{CS2U-PF6}} & M_{\text{CS2U-VS3}} & M_{\text{CS2U-vac,1}} & \cdots & M_{\text{CS2U-vac},n_\nu} \\ \vdots & \vdots & \ddots & \vdots & \vdots & \vdots & \ddots & \vdots \\ M_{\text{PF6-CS3U}} & M_{\text{PF6-CS2U}} & \cdots & L_{\text{PF6}} & M_{\text{PF6-VS3}} & M_{\text{PF6-vac,1}} & \cdots & M_{\text{PF6-vac},n_\nu} \\ M_{\text{VS3-CS3U}} & M_{\text{VS3-CS2U}} & \cdots & M_{\text{VS3-PF6}} & L_{\text{VS3}} & M_{\text{VS3-vac,1}} & \cdots & M_{\text{VS3-vac},n_\nu} \\ M_{\text{vac,1-CS3U}} & M_{\text{vac,1-CS2U}} & \cdots & M_{\text{vac,1-PF6}} & M_{\text{vac,1-VS3}} & L_{\text{vac,1}} & \cdots & M_{\text{vac,1-vac},n_\nu} \\ \vdots & \vdots & \ddots & \vdots & \vdots & \vdots & \ddots & \vdots \\ M_{\text{vac,n-CS3U}} & M_{\text{vac,n-CS2U}} & \cdots & M_{\text{vac,n-PF6}} & M_{\text{vac,n-VS3}} & M_{\text{vac,n-vac,1}} & \cdots & L_{\text{vac},n_\nu} \end{bmatrix}$$

is the *mutuals matrix* which is symmetric and of size $(n_c + n_\nu) \times (n_c + n_\nu)$.

The voltage vector $\mathbf{V}$ and current vector $\mathbf{I}$ are given by

$$\mathbf{V}_\nu = \begin{bmatrix} V_{\text{CS3U}} \\ V_{\text{CS2U}} \\ \vdots \\ V_{\text{PF6}} \\ V_{\text{VS3}} \\ 0 \\ \vdots \\ 0 \end{bmatrix} \qquad \mathbf{I}_\nu = \begin{bmatrix} I_{\text{CS3U}} \\ I_{\text{CS2U}} \\ \vdots \\ I_{\text{PF6}} \\ I_{\text{VS3}} \\ I_{\text{vac,1}} \\ \vdots \\ I_{\text{vac},n_\nu} \end{bmatrix}.$$

The resistance matrix is given by

$$\underline{\underline{\mathbf{\Omega}}}_\nu = \begin{bmatrix} \Omega_{\text{CS3U}} & 0 & \cdots & 0 & 0 & \cdots & 0 \\ 0 & \Omega_{\text{CS2U}} & \cdots & 0 & 0 & \cdots & 0 \\ \vdots & \vdots & \ddots & \vdots & \vdots & \ddots & \vdots \\ 0 & 0 & \cdots & \Omega_{\text{VS3}} & 0 & \cdots & 0 \\ 0 & 0 & \cdots & 0 & \Omega_{\text{vac,1}} & \cdots & 0 \\ \vdots & \vdots & \ddots & \vdots & \vdots & \ddots & \vdots \\ 0 & 0 & \cdots & 0 & 0 & \cdots & \Omega_{\text{vac},n_\nu} \end{bmatrix}.$$

Finally, the plasmaless model of a tokamak is given by

$$\frac{d\mathbf{I}_\nu}{dt} = \underline{\underline{\mathbf{M}}}_\nu^{-1}\left(\mathbf{V}_\nu - \underline{\underline{\mathbf{\Omega}}}_\nu \mathbf{I}_\nu\right), \tag{2.16}$$

which can be rewritten in the state-space form

$$\begin{aligned} \dot{\mathbf{x}} &= \underline{\underline{\mathbf{A}}}\mathbf{x} + \underline{\underline{\mathbf{B}}}\mathbf{u} \\ \dot{\mathbf{y}} &= \underline{\underline{\mathbf{C}}}\mathbf{x} + \underline{\underline{\mathbf{D}}}\mathbf{u} \end{aligned}$$

where $\mathbf{x} = \mathbf{y} = \mathbf{I}_\nu$, the actuators are defined as $\mathbf{u} = \mathbf{V}_\nu$, the A-matrix is defined as $\underline{\underline{\mathbf{A}}} = -\underline{\underline{\mathbf{M}_\nu}}^{-1}\underline{\underline{\mathbf{\Omega}_\nu}}$, the B-matrix is defined as $\underline{\underline{\mathbf{B}}} = \underline{\underline{\mathbf{M}_\nu}}^{-1}$, the C-matrix is the $(n_{\text{coils}} + n_\nu)$ unity matrix, and the D-matrix is the null matrix.

Calculation of resistances, self-inductances, and mutual inductances

In order to solve the vacuum circuit equations, the resistances, self-inductances, and mutual inductances of the PF system coils and vacuum vessel conducting plates must be computed.

Estimating coil resistances is straightforward. Knowing the i-th coil resistivity η_i, the radial position of each of its turns R_{ik}, $k = 1, ..., N_{\text{turns},i}$, and the turn cross-section S_{ik}, the i-th coil resistance is given by

$$\Omega_i = \sum_{k=1}^{N_{\text{turns},i}} \frac{2\pi\eta_i R_{ik}}{S_{ik}}.$$

On the other hand, estimating the coils self-inductances and mutual inductances involves elliptic integrals [45, 46, 47]. It thus requires specific attention.

- **Self-inductances**
  Assuming that the PF system coils have a rectangular cross-section with axes along $\hat{\mathbf{e}}_R$ and $\hat{\mathbf{e}}_Z$, a common method can be used for the calculation of their self-inductance. The self-inductance of a circular coil with rectangular cross-section can be estimated by

  $$L_i = \pi\mu_0 N_{\text{turns},i}^2 \frac{2R_{\text{coil,i}}^2}{h_{\text{coil,i}}} \left[K_{\text{Nagaoka}}\left(\frac{h_{\text{coil,i}}}{2R_{\text{coil,i}}}\right) - k_{\text{Grover}}\left(\frac{w_{\text{coil,i}}}{2R_{\text{coil,i}}}, \frac{w_{\text{coil,i}}}{h_{\text{coil,i}}}\right) \right] \qquad (2.17)$$

  where $\mu_0 = 4\pi \cdot 10^{-7} \text{Hm}^{-1}$ is the magnetic permeability of the vacuum, $R_{\text{coil,i}}$ is the radius of centre of the i-th coil, h_i is the height of the i-th coil (vertical), and w_i is the width of the i-th coil (horizontal). K_{Nagaoka} and k_{Grover} are functions of the coil height, width, and radial position. They are detailed in [47]. Given the coil radial positions, heights, widths, and number of turns, the calculation of the self-inductance is straightforward.

  Equation (2.17) cannot be used for determining the self-inductance of the VS3 coils and of the vacuum vessel plates, because they do not have a rectangular cross-section. In that case, it is necessary to decompose the coils or vessel into smaller coil elements considered as rectangular with axes along $\hat{\mathbf{e}}_R$ and $\hat{\mathbf{e}}_Z$. This approximation is schemed in Figure 2.4.

  By the summation principle, it is possible to deduce the coil self-inductance. The self-inductance of a coil A divided in two coils α and β is given by

  $$L_A = L_\alpha + L_\beta \pm 2M_{\alpha\beta}, \qquad (2.18)$$
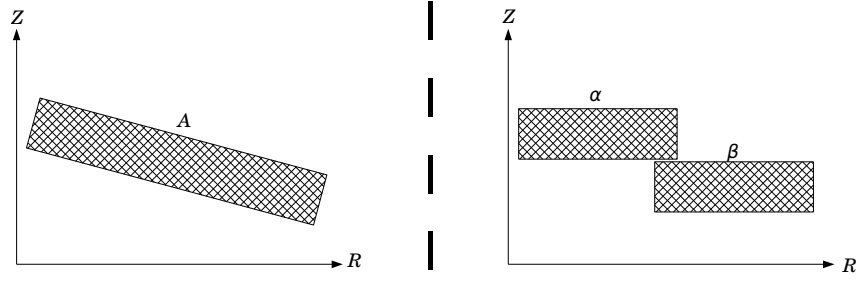
Figure 2.4: Approximation of a diagonal coil by two rectangular coils in a poloidal representation.

where L_α is the self-inductance of the α rectangular coil, L_β is the self-inductance of the β rectangular coil, and $M_{\alpha\beta}$ is the mutual inductance between the α rectangular coil and the β rectangular coil. The double sign is positive when the α and β coils are in series and negative when they are in anti-series.

Computing the VS3 coil and the vacuum vessel plates self-inductances necessitates the calculation of mutual inductances between coaxial filaments. A method for performing such a mutual inductance calculation is exposed below.

- **Mutual inductances**
  Mutual inductances between two coils can be estimated by dividing each coil in smaller elements considered as filaments.
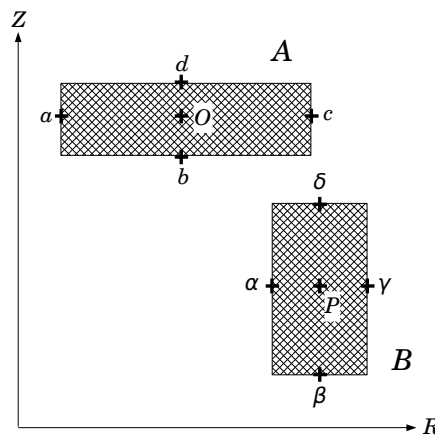
Figure 2.5: Position of filaments in a poloidal representation for the estimation of the mutual inductances between two rectangular coils using Rayleigh's approach.

The Rayleigh quadrature formula [48] states that

$$M_{AB} = \frac{N_A N_B}{6} \left(M_{O\alpha} + M_{O\beta} + M_{O\gamma} + M_{O\delta} + M_{Pa} + M_{Pb} + M_{Pc} + M_{Pd} - 2M_{OP} \right), \quad (2.19)$$

where N_A is the number of turns in the A-coil and N_B is the number of turns in the B-coil, $M_{O\alpha}$ is the mutual inductance between the filament O and the filament α, etc. (see Figure 2.5).

The mutual inductance between two coaxial circular filaments α and β is given by [49]

$$M_{\text{fil},\alpha\beta} = \sqrt{R_{\text{fil},\alpha} R_{\text{fil},\beta}} \times f \left(\frac{\left(R_{\text{fil},\beta} - R_{\text{fil},\alpha} \right)^2 + \left(Z_{\text{fil},\beta} - Z_{\text{fil},\alpha} \right)^2}{\left(R_{\text{fil},\beta} + R_{\text{fil},\alpha} \right)^2 + \left(Z_{\text{fil},\beta} - Z_{\text{fil},\alpha} \right)^2} \right), \quad (2.20)$$

where f is a function of the filaments radii and vertical positions, $R_{\text{fil},\alpha}$ is the horizontal position of the α filament, $Z_{\text{fil},\alpha}$ is the vertical position of the α filament, etc. Tables of f can be found in [47].

This method enables the calculation of mutual inductances between coils of arbitrary shape and orientation.

2.1.4 Plasma modelling

Plasma modelling approaches

The plasma can be modelled using different approaches. The choice of approach is guided by the stated purpose of the simulator:

- **Kinetic approach**
  The kinetic approach models the plasma as an electromagnetic gas composed of several particle species with separate distribution functions. This approach solves the Vlasov equation with collisions, as discussed in [50].

  Because of the high dimensionality of the problem (six dimensions per particle), kinetic simulations require significant computer resources.

- **Gyrokinetic approach**
  The gyrokinetic approach consists of a kinetic approach in which the effect of the gyro-motion of the charged particle around a magnetic field line is averaged out [51].

  This approach reduces the dimensionality of the kinetic approach to five dimensions per particle. However, gyrokinetic simulations also require significant computer resources.

- **Fluid approach**
  The fluid approach consists of modelling the plasma as a single fluid or as composed of several fluids. One important feature of the fluid approach is that it necessitates an energy equation for closure.

- **Magnetohydrodynamics (MHD) approach**
  The MHD approach is a fluid approach in which the plasma is considered as one single electromagnetic fluid. Ideal MHD assumes that the resistivity of the plasma is low enough to be neglected, as opposed to resistive MHD.

In this thesis, it is considered sufficient to select a resistive MHD plasma modelling approach.

Resistive MHD

The equations of resistive MHD including the energy balance equations are Maxwell's equations, the continuity equation, the Euler equation (also known as the *force balance* equation), the generalised Ohm's law, and the energy balance equations for ions and electrons. They can be summarised as follows:

$$\nabla \cdot \mathbf{E} = \frac{\rho_{\text{el}}}{\epsilon_0} \qquad \qquad \nabla \times \mathbf{E} = -\frac{\partial \mathbf{B}}{\partial t}$$

$$\nabla \cdot \mathbf{B} = 0 \qquad \qquad \nabla \times \mathbf{B} = \mu_0 j + \frac{1}{c^2}\frac{\partial \mathbf{E}}{\partial t}$$

$$\frac{\partial \rho_m}{\partial t} + \nabla \cdot (\rho_m \mathbf{u}) = 0 \qquad \qquad \rho_m \left(\frac{\partial \mathbf{u}}{\partial t} + \mathbf{u} \cdot \nabla \mathbf{u} \right) = \mathbf{j} \times \mathbf{B} - \nabla p$$

$$\frac{\mathbf{j}}{\sigma} = \mathbf{E} + \mathbf{u} \times \mathbf{B}$$

$$\frac{3}{2}\frac{\partial p_i}{\partial t} + \nabla \cdot \left(\mathbf{q}_i + \frac{5}{2} p_i \mathbf{u}_i \right) \qquad = \qquad \mathbf{u}_i \cdot \nabla p_i + Q_i + Q_{ei}$$

$$\frac{3}{2}\frac{\partial p_e}{\partial t} + \nabla \cdot \left(\mathbf{q}_e + \frac{5}{2} p_e \mathbf{u}_e \right) \qquad = \qquad -Q_{ei} + Q_e + \mathbf{j} \cdot \mathbf{E} - \mathbf{u}_i \cdot \nabla p_i$$

(2.21)

where

- $\mathbf{E}$ is the electric field;

- ρ_{el} is the electric charge density;

- $\mathbf{B}$ is the magnetic field;

- ρ_m is the mass density

$$\rho_m = \sum_k n_k m_k,$$

  where n_k is the density of the k particle species and m_k is the mass of the k particle species;

- **u** is the fluid velocity (also referred to as the *flow*)

$$\mathbf{u} = \frac{\sum_k n_k m_k \mathbf{u}_k}{\rho_m},$$

where $\mathbf{u}_k$ is the fluid velocity of the k particle species.

- **j** is the plasma current density

$$\mathbf{j} = \sum_k q_k n_k \mathbf{u}_k,$$

where q_k is the charge of the k particle species;

- c is the speed of light;

- σ is the plasma conductivity;

- p is the total pressure defined as

$$p = \sum_k p_k,$$

where p_k is the k particle species pressure;

- $\mathbf{q}_k$ is the heat flux of the k particle species;

- Q_i is the ion heat source power per unit volume;

- Q_e is the electron heat source power per unit volume;

- Q_{ei} is the electron-ion equipartition heat source power per unit volume given by

$$Q_{ei} = \frac{3 m_e}{m_i} \frac{n_e}{\tau_e} (T_e - T_i),$$

where m_e is the electron mass, m_i is the plasma ion mass, τ_e is given by

$$\tau_e = 3.43 \cdot 10^5 \frac{T_e^{3/2}}{n_e \log \Lambda} \qquad T_e \text{ in [eV]},$$

with $\log \Lambda$ the Coulomb logarithm [52]. T_k is the temperature of the k particle species defined as

$$T_k = \frac{m_k}{n_k} \int (\mathbf{v} - \mathbf{u}_k)^2 f_k(\mathbf{v}) d\mathbf{v},$$

with f_k the distribution function of the k particle species. The temperature of the k particle species is linked to its density and pressure by

$$p_k := n_k T_k.$$

This set of equations necessitates the expression of the relationship between the ion and electron heat flux and the ion and electron temperature for closure. These equations are described in 2.1.7.

It is argued in [53] that the displacement current term can be neglected in Ampère's law with respect to the current density term for low frequency phenomena. This requires that the electromagnetic waves of interest have phase velocities much slower than the speed of light and that the characteristic ion and electron thermal velocities be non-relativistic. Moreover, it restricts the range of validity of the plasma model to phenomena with much lower angular frequency than the electron plasma angular frequency ω_e

$$\omega_{pe} = \sqrt{\frac{n_e e^2}{m_e \epsilon_0}},$$

with e the electron charge, and with much longer characteristic lengths than the Debye length defined by

$$\lambda_D = \sqrt{\frac{\epsilon_0 T_e}{n_e e^2}}.$$

These assumptions are typically satisfied when considering the macroscopic behaviour of the plasma. They also yield

$$\frac{\epsilon_0 \nabla \cdot \mathbf{E}}{n_e e} \ll 1.$$

The force balance equation expressed in (2.21) neglects the anisotropic part of the pressure tensor and therefore assumes isotropic pressure. This assumption implicitly requires that many collisions take place on a time scale short compared with those of interest in order to enable collisions to randomise the distribution function, which is the case for the modelling of the low-frequency macroscopic plasma evolution.

The Ohm's law expressed in (2.21) assumes isotropic pressure for similar reasons. On top of that, the Hall effect term and the diamagnetic drift term are neglected by assuming that the ion gyro-radius ρ_i, defined by

$$\rho_i = \sqrt{\frac{\epsilon_0 m_i T_i}{Z_i^2 e^2 B^2}},$$

is much smaller than the characteristic length of interest. This is again typically the case when considering the macroscopic behaviour of the plasma.

In the following, the equilibrium flow is assumed to be zero in the force balance equation and in Ohm's law. The time scale of the flow perturbation is also assumed to be much shorter than time scales of macroscopic electromagnetic plasma phenomena, thus assuming that the

plasma is in a static equilibrium. The effects on heat transport of a non-vanishing flow are emulated, as described in 2.1.7.

2.1.5 Plasma equilibrium modelling

In a static equilibrium, the resistive MHD equations can be expressed as

$$\mathbf{j} \times \mathbf{B} = \nabla p \qquad\qquad \nabla \times \mathbf{E} = \mathbf{0}$$

$$\nabla \cdot \mathbf{B} = 0 \qquad\qquad \nabla \times \mathbf{B} = \mu_0 \mathbf{j} \qquad\qquad (2.22)$$

$$\mathbf{j} = \sigma \mathbf{E}$$

A plasma equilibrium is a solution of the set of equations (2.22).

Assuming a generic magnetic field

$$\mathbf{B} = \begin{pmatrix} B_R \\ B_\phi \\ B_Z \end{pmatrix}$$

the absence of magnetic monopoles $\nabla \cdot \mathbf{B} = 0$ can be expressed as

$$\frac{1}{R} \frac{\partial (R B_R)}{\partial R} + \frac{1}{R} \frac{\partial B_\phi}{\partial \phi} + \frac{\partial B_Z}{\partial Z} = 0.$$

Now, by axisymmetry, $\frac{\partial B_\phi}{\partial \phi} = 0$. Thus,

$$\frac{1}{R} \frac{\partial (R B_R)}{\partial R} + \frac{\partial B_Z}{\partial Z} = 0. \qquad\qquad (2.23)$$

Let us make the ansatz that there exists a stream function $\psi = \psi(R, Z)$ such that

$$B_R = -\frac{1}{R} \frac{\partial \psi}{\partial Z} \qquad \text{and} \qquad B_Z = \frac{1}{R} \frac{\partial \psi}{\partial R}. \qquad\qquad (2.24)$$

With this ansatz, equation (2.23) is always satisfied.

The stream function ψ is linked to the poloidal flux Ψ_p. For example, it is possible to estimate the poloidal magnetic flux through a ring in the equatorial plane, as displayed in Figure 2.6.
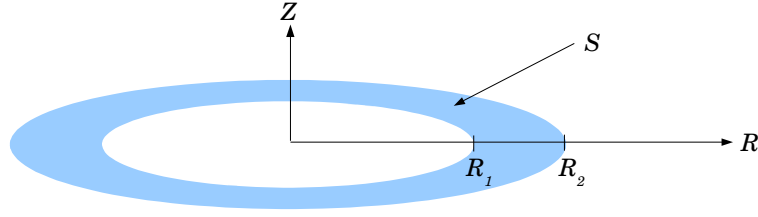
Figure 2.6: Surface S for the definition of poloidal flux.

The poloidal flux, in this case, is given by

$$
\begin{aligned}
\Psi_p &= \int_S \mathbf{B} \cdot \mathbf{dS} = \int_S B_Z \, dS \\
&= 2\pi \int_{R_1}^{R_2} \frac{1}{R} \frac{\partial \psi}{\partial R} R \, dR = 2\pi \left[\psi(R_2) - \psi(R_1) \right].
\end{aligned}
$$

ψ thus corresponds to the poloidal magnetic flux per radian as $\psi = \frac{\Psi_p}{2\pi}$. It is defined with respect to an arbitrary additive constant.

It is possible to demonstrate that $\nabla \psi$ is always perpendicular to $\mathbf{B}$ by computing

$$
\begin{aligned}
\mathbf{B} \cdot \nabla \psi &= \begin{pmatrix} B_R \\ B_\phi \\ B_Z \end{pmatrix} \cdot \begin{pmatrix} \dfrac{\partial \psi}{\partial R} \\ \dfrac{1}{R} \dfrac{\partial \psi}{\partial \phi} \\ \dfrac{\partial \psi}{\partial Z} \end{pmatrix} \\
&= B_R \frac{\partial \psi}{\partial R} + \frac{B_\phi}{R} \frac{\partial \psi}{\partial \phi} + B_Z \frac{\partial \psi}{\partial Z} \\
&= -\frac{1}{R} \frac{\partial \psi}{\partial Z} \frac{\partial \psi}{\partial R} + 0 + \frac{1}{R} \frac{\partial \psi}{\partial R} \frac{\partial \psi}{\partial Z} = 0
\end{aligned}
$$

Therefore, the magnetic field lines are tangent to surfaces of constant ψ (called *flux surfaces*). On the other hand, the stationary force balance equation $\mathbf{j} \times \mathbf{B} = \nabla p$ guarantees that $\mathbf{B}$ is perpendicular to ∇p. As a result, the magnetic field lines are also always tangent to surface of constant pressure. It is thus possible to state that surfaces of constant pressure are surfaces of constant poloidal magnetic flux meaning that the poloidal magnetic flux can be used as a coordinate for labelling the isobaric surfaces, i.e. $p = p(\psi)$.

The stationary Ampère law states that

$$-\frac{\partial B_\phi}{\partial Z} = \mu_0 j_R$$

$$\frac{\partial B_R}{\partial Z} - \frac{\partial B_Z}{\partial R} = \mu_0 j_\phi \qquad (2.25)$$

$$\frac{1}{R}\frac{\partial (RB_\phi)}{\partial R} = \mu_0 j_Z$$

It is possible to define the poloidal current function $f = f(R, Z)$ as

$$f = \frac{RB_\phi}{\mu_0}. \qquad (2.26)$$

Substituting (2.24) and (2.26) in (2.25), we have

$$j_R = -\frac{1}{R}\frac{\partial f}{\partial Z} \qquad (2.27)$$

$$j_\phi = -\frac{1}{\mu_0 R}\frac{\partial^2 \psi}{\partial Z^2} - \frac{1}{\mu_0}\frac{\partial}{\partial R}\left(\frac{1}{R}\frac{\partial \psi}{\partial R}\right) \qquad (2.28)$$

$$j_Z = \frac{1}{R}\frac{\partial f}{\partial R} \qquad (2.29)$$

The stationary force balance equation $\mathbf{j} \times \mathbf{B} = \nabla p$ guarantees that

$$\mathbf{j}\cdot\nabla p = 0. \qquad (2.30)$$

meaning that the current density $\mathbf{j}$ is perpendicular to isobaric surfaces. Substituting (2.27) in (2.30), we have

$$-\frac{1}{R}\frac{\partial f}{\partial Z}\frac{\partial p}{\partial R} + \frac{1}{R}\frac{\partial f}{\partial R}\frac{\partial p}{\partial Z} = 0,$$

giving

$$\nabla f \times \nabla p = \mathbf{0}. \qquad (2.31)$$

This means that ∇f and ∇p are collinear, thus demonstrating that f is only a function of ψ, i.e. $f = f(\psi)$.

Because $p = p(\psi)$ and $f = f(\psi)$, it is possible to write

$$
\begin{aligned}
j_R &= -\frac{1}{R}\frac{\partial f}{\partial \psi}\frac{\partial \psi}{\partial Z} \\[2ex]
j_Z &= \frac{1}{R}\frac{\partial f}{\partial \psi}\frac{\partial \psi}{\partial R}
\end{aligned}
\qquad \text{and} \qquad
\nabla p = \begin{pmatrix} \dfrac{\partial p}{\partial \psi}\dfrac{\partial \psi}{\partial R} \\[2ex] \dfrac{\partial p}{\partial \psi}\dfrac{\partial \psi}{\partial \phi} \\[2ex] \dfrac{\partial p}{\partial \psi}\dfrac{\partial \psi}{\partial Z} \end{pmatrix}.
$$

If we define $p' = \frac{\partial p}{\partial \psi}$ and $f' = \frac{\partial f}{\partial \psi}$, we can write the first and third components of the force balance equation $\mathbf{j} \times \mathbf{B} = \nabla p$ as

$$
j_\phi = B_\phi f' + R p'. \tag{2.32}
$$

Substituting (2.26) in (2.32), we have

$$
j_\phi = R p' + \frac{\mu_0}{R} f f'. \tag{2.33}
$$

Equation (2.28) can therefore be rewritten as

$$
\frac{1}{\mu_0}\frac{\partial}{\partial R}\left(\frac{1}{R}\frac{\partial \psi}{\partial R}\right) + \frac{1}{\mu_0 R}\frac{\partial^2 \psi}{\partial Z^2} = -R p' - \frac{\mu_0}{R} f f', \tag{2.34}
$$

which is the *Grad-Shafranov equation* [54]. Defining the operator

$$
\Delta^* = R\frac{\partial}{\partial R}\left(\frac{1}{R}\frac{\partial}{\partial R}\right) + \frac{\partial^2}{\partial Z^2}
$$

the Grad-Shafranov equation finally takes the compact form

$$
\Delta^* \psi = -\mu_0 R^2 p'(\psi) - \mu_0^2 f(\psi) f'(\psi). \tag{2.35}
$$

Solution of the Grad-Shafranov equation

The Grad-Shafranov equation must be solved for ψ to provide an equilibrium solution. Assuming that $p(\psi)$ and $f(\psi)$ are known (see 2.1.7), boundary conditions for $\psi(R, Z)$ are necessary in order to determine a solution of the Grad-Shafranov equation.

Boundary conditions come in essentially two forms:

- **Prescribed boundary conditions**
  The plasma boundary is prescribed and the boundary contour C_b and boundary flux ψ_b are provided. In that case, the region between the plasma and the vacuum vessel wall is

neglected, and the plasma-vacuum boundary is essentially replaced by the surface of a perfect conductor on which ψ is necessarily constant.

- **Free boundary conditions**
  The plasma boundary contour and boundary flux can be self-consistently determined provided the plasma current distribution and the PF system and conducting vacuum vessel configurations and current loads. A flux map $\psi(R, Z)$ can be computed on a predetermined computational area and the boundary can be determined by analysis of the flux contours given the position of tokamak first wall or limiter. This approach, although more complex than the prescribed-boundary approach, self-consistently determines the plasma boundary and equilibrium according to the action of the PF system.

In order to take into account the effect of the PF system, it is necessary to use a free-boundary approach.

The generalised circuit equation, which is necessary for accounting for the PF system and conducting vacuum plates in the free boundary conditions for the Grad-Shafranov equation, is discussed in 2.1.6. The magnetic diffusion and transport equations, which describe the equilibrium evolution, are discussed in 2.1.7.

2.1.6 Generalised circuit equations

The free-boundary approach detailed in the previous paragraph requires the modelling of the effect of a given plasma current distribution on the surrounding PF systems and conducting vacuum vessel. In turn, the magnetic flux $\psi(R, Z)$ must be computed on a pre-determined area.

In this work, the plasma is modelled as an $n_R \times n_Z$ grid of filaments each carrying a current $I_{\text{pla},ij}$ where $i = 1, ..., n_R$ and $j = 1, ..., n_Z$. The magnetic flux is computed at each point of the $n_R \times n_Z$ grid. An example of such a grid is provided in Figure 2.7.

The flux induced at a contour point of coordinate (R, Z) by the PF systems, the vacuum vessel plates and the plasma itself is given by [55]

$$
\psi(R, Z) = \frac{\mu_0}{2\pi} \sum_{i=1}^{n_c} G(R, Z, R_i, Z_i) \cdot I_{\text{coil},i} + \frac{\mu_0}{2\pi} \sum_{i=1}^{n_v} G(R, Z, R_i, Z_i) \cdot I_{\text{vac},i} +
$$
$$
+ \frac{\mu_0}{2\pi} \int_{S_{\text{plasma}}} G(R, Z, R', Z') j_\phi(R', Z') dR' dZ',
$$
(2.36)

where $G(R, Z, R_i, Z_i)$ is the analytic exterior Green's function for axisymmetric current filaments at respective positions (R, Z) and (R_i, Z_i) [56], and S_{plasma} is the surface area of the plasma poloidal cross-section. The integral can be discretised on the $n_R \times n_Z$ grid.
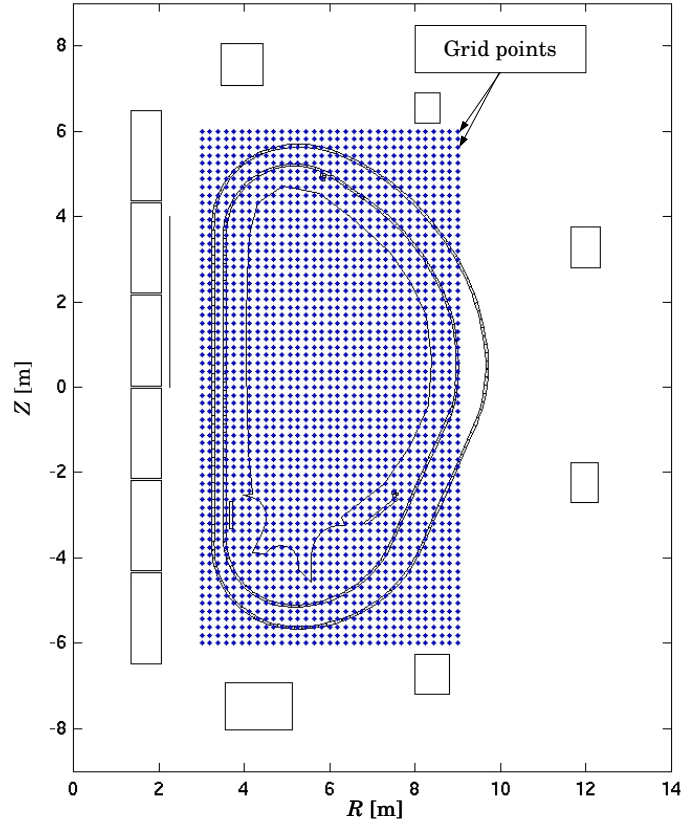
Figure 2.7: Example of an $n_R = 33$ and $n_Z = 65$ grid within the ITER vacuum vessel.

The evolution of the plasma current distribution, the PF system currents, and the conducting vacuum vessel currents is modelled by adding the plasma current distribution term to the vacuum modelling of the tokamak obtained in (2.15):

$$V_i = \frac{d}{dt}\left[L_i I_i + \sum_{i \neq j} M_{ij} I_j + 2\pi \psi_{\mathrm{pla},i} \right] + R_i I_i, \tag{2.37}$$

where $2\pi \psi_{\mathrm{pla},i}$ is the poloidal flux generated by the plasma within the contour defined by the i-th coil or vacuum vessel plate. It can be approximated by

$$\psi_{\mathrm{pla},i} = \frac{\mu_0}{2\pi} \int\limits_{S_{\mathrm{plasma}}} G(R_i, Z_i, R', Z') j_\phi(R', Z') dR' dZ',$$

where R_i and Z_i are the positions of the centre of the i-th coil.

The generalised circuit equations allow the computation of plasma current distribution evolution, PF system currents, and conducting vacuum vessel currents evolution according to the action of the power supplies.

The magnetic flux map $\psi(R, Z)$ can be determined at each point of the $n_R \times n_Z$ grid. The plasma boundary is defined as the flux surface contacting the limiter (in case of a limited plasma) or as the separatrix (in case of a diverted plasma), i.e. the flux contour on which $B_R(R_x, Z_x) = B_Z(R_x, Z_x) = 0$ for one X-point of coordinates (R_x, Z_x) within the area comprised in a poloidal cross-section of the first wall. The boundary flux ψ_b and contour C_b can be deduced from the computed flux map.

2.1.7 Transport modelling

In order to solve the equilibrium evolution problem, the flux evolution $\frac{d\psi}{dt}$ and the pressure $p(\psi)$ must be computed. The flux evolution is determined by the magnetic diffusion, and the evolution of the pressure function $p(\psi)$ is determined by the particle and heat transport.

Toroidal magnetic flux

The toroidal magnetic flux Φ is constant on a flux surface. Φ is defined as

$$\Phi(\psi) = \int_{S_\psi} \mathbf{B} \cdot \mathbf{dS} \tag{2.38}$$

where S_ψ is a surface enclosed by the magnetic contour ψ =const. displayed in Figure 2.8. It is thus possible to label a magnetic surface by $\rho = \sqrt{\frac{\Phi}{\Phi_{max}}}$, where Φ_{max} is the toroidal flux for $\psi = \psi_b$, where ψ_b is the boundary magnetic flux. The coordinate $\rho = 0$ indicates the *plasma axis*, whereas $\rho = 1$ indicates the plasma boundary.
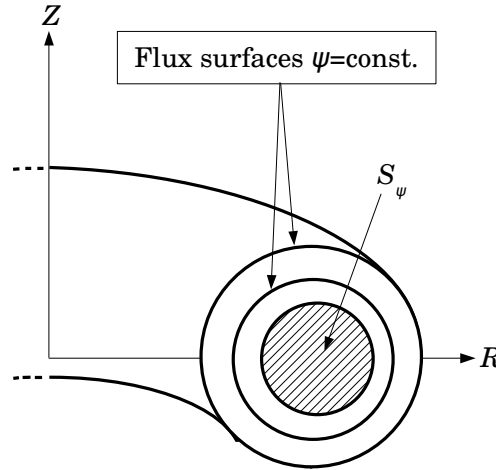
Figure 2.8: Toroidal magnetic flux Φ.

Flux surface averaging technique

Because the energy and the number density transport is much greater along the magnetic surfaces than across them, it is possible to assume that the plasma density and temperature are approximately constant on a flux surface [55]. Other parameters cannot straightforwardly be expressed as functions of ρ (or equivalently of ψ). It is however possible to compute their average value on a given flux surface ρ=const. using the following averaging technique.

The average of an arbitrary scalar quantity A over a small volume δV comprised between two flux surfaces $S(\rho)$ and $S(\rho + \delta\rho)$ can be defined as

$$\langle A \rangle = \lim_{\delta V \to 0} \frac{1}{\delta V} \int_{\delta V} A dV. \tag{2.39}$$

It is possible to decompose the volume element dV into

$$dV = \mathbf{dR} \cdot \mathbf{dS},$$

where $\mathbf{dR}$ is the infinitesimal change in the position vector along the ρ-coordinate and $\mathbf{dS}$ is an infinitesimal surface element of the flux surface $S(\rho)$ displayed in Figure 2.9.
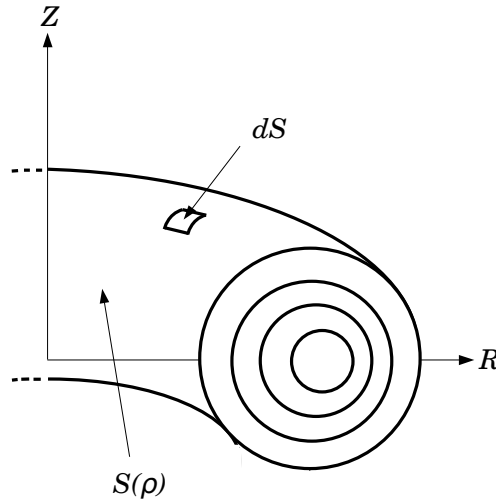
Figure 2.9: Definition of the flux surface $S(\rho)$.

We can define the orientation of the surface element $\mathbf{dS}$ such that

$$\mathbf{dS} = \frac{\nabla\rho}{|\nabla\rho|} dS$$

and we have

$$dV = \mathbf{dR} \cdot \frac{\nabla \rho}{|\nabla \rho|} dS.$$

Now, by definition, we may write:

$$\mathbf{dR} \cdot \nabla \rho = d\rho,$$

thus leading to

$$dV = d\rho \frac{1}{|\nabla \rho|} dS. \tag{2.40}$$

Substituting (2.40) in (2.39), we obtain

$$\langle A \rangle = \lim_{\delta V \to 0} \lim_{\delta \rho \to 0} \frac{\delta \rho}{\delta V} \int_{S(\rho)} A \frac{dS}{|\nabla \rho|} = \frac{\partial \rho}{\partial V} \int_{S(\rho)} A \frac{dS}{|\nabla \rho|} \tag{2.41}$$

This flux surface averaging technique has three important properties. For an arbitrary vector field $\mathbf{A}$ and an arbitrary scalar field A, we have

$$\frac{\partial V}{\partial \rho} = \int_{S(\rho)} \frac{dS}{|\nabla \rho|} \tag{2.42}$$

$$\langle \nabla \cdot \mathbf{A} \rangle = \frac{\partial}{\partial V} \langle \mathbf{A} \cdot \nabla V \rangle \tag{2.43}$$

$$\frac{d}{dt} \left(\frac{\partial V}{\partial \rho} \langle A \rangle \right) = \frac{\partial V}{\partial \rho} \left\langle \frac{\partial A}{\partial t} \right\rangle + \frac{\partial}{\partial \rho} \langle A \mathbf{u}_\rho \cdot \nabla V \rangle \tag{2.44}$$

where V is the volume enclosed by $S(\rho)$, and $\mathbf{u}_\rho$ is the velocity of a $\rho =$const. surface, given by

$$\frac{d\rho}{dt} = \frac{\partial \rho}{\partial t} + \mathbf{u}_\rho \cdot \nabla \rho = 0.$$

These properties are demonstrated in [57].

Magnetic diffusion

The magnetic diffusion equation is a direct implication of Ohm's law. As discussed earlier, the equilibrium flow and the perturbation flow are neglected thus yielding the simplified Ohm's law:

$$\mathbf{j}_{\text{Ohm}} = \sigma \mathbf{E}, \tag{2.45}$$

where σ is the plasma conductivity.

The total plasma current is the sum of the Ohmic contribution $\mathbf{j}_{\text{Ohm}}$ and the non-inductive contribution $\mathbf{j}_{\text{ni}}$ which is the sum of the bootstrap current contribution described later in this section and the contribution of additional current drive sources:

$$\mathbf{j} = \mathbf{j}_{\text{Ohm}} + \mathbf{j}_{\text{ni}}. \tag{2.46}$$

Taking the flux surface average of the scalar product of (2.46) with the magnetic field $\mathbf{B}$ gives

$$\left\langle \mathbf{j} \cdot \mathbf{B} \right\rangle = \left\langle \sigma \mathbf{E} \cdot \mathbf{B} \right\rangle + \left\langle \mathbf{j}_{\text{ni}} \cdot \mathbf{B} \right\rangle.$$

Because the plasma conductivity depends on the plasma temperature, as exposed in equation (1.6), and it can be considered constant on a flux surface. Thus,

$$\left\langle \mathbf{j} \cdot \mathbf{B} \right\rangle = \sigma \left\langle \mathbf{E} \cdot \mathbf{B} \right\rangle + \left\langle \mathbf{j}_{\text{ni}} \cdot \mathbf{B} \right\rangle$$

It is demonstrated in [58] that this equation can be rewritten as

$$\frac{d\psi}{dt} = \frac{1}{\sigma \mu_0 f \left\langle \frac{1}{R^2} \right\rangle} \left[\left\langle \mathbf{j}_{\text{ni}} \cdot \mathbf{B} \right\rangle + f^2 \frac{\partial \rho}{\partial V} \frac{\partial}{\partial \rho} \left(\frac{\partial \psi}{\partial \rho} \frac{\partial V}{\partial \rho} \frac{1}{f} \left\langle \frac{|\nabla \rho|^2}{R^2} \right\rangle \right) \right], \tag{2.47}$$

which can be solved for $\frac{d\psi}{dt}$.

Particle transport

In order to model the evolution of the plasma pressure $p(\psi) = n_i(\psi) T_i(\psi) + n_e(\psi) T_e(\psi)$, it is necessary to model the evolution of the ion and electron densities n_i and n_e and temperatures T_i and T_e. This section describes the density modelling.

The continuity equation reads

$$\frac{\partial \rho_m}{\partial t} + \nabla \cdot \left(\rho_m \mathbf{u} \right) = 0.$$

However, it is possible to express this equation separately for each particle species and including source terms:

$$\frac{\partial n_k}{\partial t} + \nabla \cdot (n_k \mathbf{u}_k) = S_k, \tag{2.48}$$

where S_k is a density source flux for the k species.

Averaging (2.48) on a flux surface and amplifying by $\frac{\partial V}{\partial \rho}$, we have

$$\left\langle \frac{\partial n_k}{\partial t} \right\rangle \frac{\partial V}{\partial \rho} + \langle \nabla \cdot (n_k \mathbf{u}_k) \rangle \frac{\partial V}{\partial \rho} = \langle S_k \rangle \frac{\partial V}{\partial \rho}.$$

Using (2.44), we obtain

$$\frac{d}{dt} \left(\frac{\partial V}{\partial \rho} n_k \right) + \frac{\partial}{\partial \rho} \left[\left\langle n_k \left(\mathbf{u}_k - \mathbf{u}_\rho \right) \cdot \nabla \rho \right\rangle \frac{\partial V}{\partial \rho} \right] = \langle S_k \rangle \frac{\partial V}{\partial \rho}.$$

The particle flux relative to a surface ρ=const. is defined by

$$\Gamma_k = \left\langle n_k \left(\mathbf{u}_k - \mathbf{u}_\rho \right) \cdot \nabla \rho \right\rangle.$$

This yields the particle transport equation

$$\frac{d}{dt} \left(\frac{\partial V}{\partial \rho} n_k \right) + \frac{\partial}{\partial \rho} \left[\Gamma_k \frac{\partial V}{\partial \rho} \right] = \langle S_k \rangle \frac{\partial V}{\partial \rho}. \tag{2.49}$$

In order to solve (2.49), the particle flux must be determined. Typically, it is expressed as the sum of a diffusion term and an inward pinch term

$$\Gamma_k = -D \left\langle |\nabla \rho|^2 \right\rangle \frac{\partial n_k}{\partial t} + n_k \left\langle \mathbf{v}_p \cdot \nabla \rho \right\rangle, \tag{2.50}$$

where D is the diffusion coefficient and $\mathbf{v}_p$ is the inward pinch velocity. These terms encapsulate the effects of a non-zero flow.

In this work, the density evolution is prescribed and the density evolution modelling is not implemented.

Ion heat transport

In view of modelling the plasma pressure $p(\psi)$, both the ion and electron temperature profile evolutions $T_i(t,\rho)$ and $T_e(t,\rho)$ must be modelled. This section describes the ion heat transport.

It is demonstrated in [59] that the ion energy balance equation, when averaged on a flux surface, may be rewritten as

$$\frac{3}{2} \frac{d}{dt} \left[p_i \left(\frac{\partial V}{\partial \rho} \right)^{\frac{5}{3}} \right] + \left(\frac{\partial V}{\partial \rho} \right)^{\frac{2}{3}} \frac{\partial}{\partial \rho} \left[\left(\langle q_i \rangle + \frac{5}{2} \Gamma_i \cdot T_i \right) \frac{\partial V}{\partial \rho} \right] = \left(\frac{\partial V}{\partial \rho} \right)^{\frac{5}{3}} \left[\langle Q_i \rangle + \langle Q_{ei} \rangle + \frac{\Gamma_e}{n_e} \frac{\partial p_i}{\partial \rho} \frac{\partial V}{\partial \rho} \right],$$
$$\tag{2.51}$$

where

- $\langle Q_i \rangle$ is the flux surface averaged ion heat source power per unit volume

$$\langle Q_i \rangle = \langle Q_{i,\mathrm{fus}} \rangle + \langle Q_{i,\mathrm{add}} \rangle,$$

  where $Q_{i,\mathrm{fus}}$ is the α-particle self-heating ion heat source power per unit volume, and $Q_{i,\mathrm{add}}$ is the additional ion heat source power per unit volume.

- $\langle Q_{ei} \rangle$ is the flux surface averaged electron-ion equipartition heat source power per unit volume given by

$$\langle Q_{ei} \rangle = Q_{ei},$$

  because n_e and T_e are considered constant on a flux surface;

- Γ_e and Γ_i are the particle flux defined in (2.50);

- $\langle q_i \rangle$ is the flux surface averaged ion heat flux, which can be deduced from the closure equation

$$\mathbf{q}_i = -\chi_i n_i \nabla T_i - p_i V_i^q \nabla \rho, \tag{2.52}$$

  where χ_i is the ion heat conductivity and V_i^q is the ion convective velocity.

  Amplifying (2.52) by $\nabla \rho$ and taking its flux surface average yields

$$\langle q_i \rangle := \langle \mathbf{q}_i \cdot \nabla \rho \rangle = -\chi_i n_i \langle |\nabla \rho|^2 \rangle \frac{\partial T_i}{\partial \rho} - p_i V_i^q \langle |\nabla \rho|^2 \rangle. \tag{2.53}$$

Modelling the ion heat conductivity χ_i is required for determining $T_i(t, \rho)$. As exposed in 2.3, it can be performed using a semi-empirical model of the ion heat conductivity.

Electron heat transport

[59] demonstrates that the electron energy balance equation can be rewritten as

$$\frac{3}{2} \frac{d}{dt} \left[p_e \left(\frac{\partial V}{\partial \rho} \right)^{\frac{5}{3}} \right] + \left(\frac{\partial V}{\partial \rho} \right)^{\frac{2}{3}} \frac{\partial}{\partial \rho} \left[\left(\langle q_e \rangle + \frac{5}{2} \Gamma_e T_e \right) \frac{\partial V}{\partial \rho} \right] = \left(\frac{\partial V}{\partial \rho} \right)^{\frac{5}{3}} \left[\langle Q_e \rangle - \langle Q_{ei} \rangle - \frac{\Gamma_e}{n_e} \frac{\partial p_e}{\partial \rho} \right], \tag{2.54}$$

where

- $\langle Q_e \rangle$ is the flux surface averaged electron heat source power per unit volume

$$\langle Q_e \rangle = \langle Q_{\mathrm{Ohm}} \rangle + \langle Q_{e,\mathrm{fus}} \rangle + \langle Q_{e,\mathrm{add}} \rangle - \langle Q_{\mathrm{line}} \rangle - \langle Q_{\mathrm{cyclo}} \rangle - \langle Q_{\mathrm{Br}} \rangle,$$

  where Q_{Ohm} is the Ohmic heat source power per unit volume, $Q_{e,\mathrm{fus}}$ is the α-particle self-heating electron heat source power per unit volume, $Q_{e,\mathrm{add}}$ is the additional electron

heat source power per unit volume, Q_{line} is the line radiation heat loss power per unit volume, Q_{cyclo} is the electron cyclotron heat loss power per unit volume, and Q_{Br} is the Brehmsstrahlung heat loss power per unit volume;

- $\langle q_e \rangle$ is the electron heat flux. It can be deduced from the equation

$$\mathbf{q}_e = -\chi_e n_e \nabla T_e - p_e V_e^q \nabla \rho, \tag{2.55}$$

where χ_e is the electron heat conductivity and V_e^q is the electron heat convective velocity. Amplifying (2.55) by $\nabla \rho$ and taking its flux surface average yields

$$\langle q_e \rangle := \langle \mathbf{q}_e \cdot \nabla \rho \rangle = -\chi_e n_e \langle |\nabla \rho|^2 \rangle \frac{\partial T_e}{\partial \rho} - p_e V_e^q \langle |\nabla \rho|^2 \rangle. \tag{2.56}$$

As for ions, modelling of the electron heat conductivity χ_e is required for determining $T_e(t, \rho)$. Once again, a semi-empirical model can be used for this purpose.

Bootstrap current

The bootstrap current is a *neoclassical* non-inductive current generated by the plasma itself. Loosely speaking, the mechanism can be sketched as follows:

- In a tokamak plasma, plasma-constituting particles roughly follow helical field lines and are naturally driven from the LFS to the HFS;

- Because of the magnetic mirror effect, particles must possess a minimum ratio of parallel velocity (to the magnetic field) to perpendicular velocity in order to be able to access the HFS region;

- Particles with insufficient parallel velocity to perpendicular velocity ratio are trapped in the LFS. They bounce back and forth in a toroidally and poloidally limited region of the tokamak. Trapped particles undergo so-called 'banana' orbits;

- Particles drift in opposite radial directions at either end of the banana orbit. As a result, trapped particles follow different trajectories when moving in the toroidal direction with the plasma current than when moving in the opposite direction;

- Particles from regions of lower ρ cross particles from regions of higher ρ with opposite directions;

- Because of the pressure gradient in the plasma, i.e. because the particle density and temperature is higher at the plasma centre than at the plasma boundary, a net current density is generated.

The flux surface average of the scalar product of the bootstrap current profile and the magnetic field is given by

$$\langle \mathbf{j}_{\text{boot}} \cdot \mathbf{B} \rangle = -\mu_0 f p_e \left[\mathscr{L}_{31} \frac{p_e + p_i}{p_e} \frac{\partial \log (p_e + p_i)}{\partial \psi} + \mathscr{L}_{32} \frac{\partial \log T_e}{\partial \psi} + \alpha \mathscr{L}_{34} \frac{\partial \log T_i}{\partial \psi} \right], \quad (2.57)$$

where α, $\mathscr{L}_{31}$, $\mathscr{L}_{32}$, and $\mathscr{L}_{34}$ are coefficients defined in [60].

2.1.8 Modelling of the heating and current drive systems

According to the stated simulator guidelines, the heating and current drive power supplies can be modelled as ideal, meaning that they exactly provide the demand power with no delay. If the stabilisation of Neoclassical Tearing Modes (NTMs) is neglected, this assumption generally holds because delays in the heating and current drive power supplies are negligible with respect to the other plasma heating and current drive time scales.

Modelling of each heating and current drive systems must determine the effect of the heating and current drive system on the plasma according to the system configuration and the plasma equilibrium parameters.

This paragraph discusses the power deposition and current drive modelling of different heating and current drive sources used in our simulations.

ECRH/ECCD

ECRH power deposition and ECCD modelling must be as accurate as possible, while allowing fast simulation. In that perspective, the propagation of the EC wave can be modelled using a ray-tracing model. Regarding plasma-wave interaction, kinetic models with Coulomb collisions (known as Fokker-Planck models [61]) are not appropriate because they require significant computer resources. A model based on a linearised kinetic approach using a perturbation method is a good alternative solution for plasma-wave interaction modelling.

The ECRH power per unit volume deposited by an antenna can be expressed as [62]

$$Q_{\text{e,ECRH}}(r) = \frac{\alpha e^{-\int_0^{s(r)} \alpha ds}}{4\pi^2 R_0 \zeta(r) |\cos \beta|} \times P_{\text{ECRH,antenna}}, \quad (2.58)$$

where

- r is the plasma radial coordinate displayed in Figure 1.3;

- $s(r)$ is the curvilinear abscissa along the ray path. The ray path can be computed by solving the dispersion relation expressed in [62];

- $P_{\text{ECRH,antenna}}$ is the power delivered by the EC antenna;

- R_0 is the vacuum vessel major radius;

- $\zeta(r)$ is a coefficient given by

$$\zeta(r) = \begin{cases} \sqrt{\Upsilon} & \text{if } r < \sqrt{\Upsilon} \\ r & \text{if } r > \sqrt{\Upsilon} \end{cases},$$

  where Υ is the cross-section of the wave beam;

- β is the angle between $\hat{\mathbf{e}}_r$ and the wave group velocity;

- α is the wave absorption coefficient given by

$$\alpha = 2\mathbf{k}'' \cdot \frac{\mathbf{v}_g}{v_g} = -\frac{2D''}{|\partial D'/\partial \mathbf{k}'|},$$

  where $\mathbf{v}_g$ is the group velocity of the wave, $\mathbf{k} = \mathbf{k}' + i\mathbf{k}''$ is the wave vector, $D = D' + iD''$ is the dispersion relation detailed in [62]. The dispersion relation D is a function of the wave momentum and angular frequency, and the electron distribution function.

The ray-path is determined numerically according to the plasma configuration.

The EC current drive can be approximated by

$$j_{\text{ECRH}}(r) = \frac{1}{E_f} \frac{p_+}{m_e c} \frac{\left(\gamma_+^2 - 1\right)\left(1 - 4\gamma_+\right) + 2\gamma_+^2\left(\gamma_+ + 2\right)\log\gamma_+}{\gamma_+^2\left(\gamma_+ - 1\right)^{5/2}\left(\gamma_+ + 1\right)^{1/2}} \times Q_{\text{e,ECRH}}(r), \tag{2.59}$$

where

- E_f is given by

$$E_f = \frac{4\pi e^3 n_e \log\Lambda}{m_e c^2},$$

  where e is the electron charge and c is the speed of light.

- γ_+ is given by

$$\gamma_+ = \left[1 + \left(\frac{p_+}{m_e c}\right)^2\right]^{1/2},$$

  where p_+ is the wave momentum parallel to the toroidal axis and oriented in the $+\hat{\mathbf{e}}_\phi$ direction.

To summarise, the wave propagation is determined by the following factors:

- The wave parameters, such as its angular frequency ω, its momentum, its polarisation, and the beam radius;

- The antenna mirror configuration, i.e. the initial orientation of the wave vector when entering the plasma region;

- The position and orientation of the antenna mirrors;

- The plasma parameters, such as the magnetic field configuration, the plasma electron density, the plasma ion and electron temperatures, etc.

As further exposed in 2.3, such a ray-tracing modelling of the ECRH power deposition and EC current drive can be numerically solved. The translation of the obtained power deposition and current drive from (r, θ)-coordinates into (ρ, θ)-coordinates can be performed given the plasma equilibrium flux map.

NBI

The NBI power deposition and current drive are best modelled using Monte Carlo techniques in which individual ion trajectories are computed and tracked [63, 64]. This is however computationally costly. An alternative approach for NBI power deposition and current drive modelling consists of reducing the beam geometry to treat part of the problem analytically [65]. Using a narrow beam approach, it is possible to model the NBI power deposition and current drive as follows.

The NBI power deposition per unit volume is estimated by [66]

$$
\begin{aligned}
Q_{i,\mathrm{NBI}}(\mathbf{x}_0) \quad = \quad & \frac{1}{\lambda(\mathbf{x}_0)} \frac{v^2}{l_0^2} \frac{N_{\mathrm{inj}} e^{-\alpha^2}}{\pi v^2 \Delta\Theta^2} \times \\
& \times \left[1 + \frac{2}{3} \left(\frac{R_h}{\Delta\Theta \cdot l_\lambda} \right)^2 \left(1 - \frac{l_\lambda}{l_{\mathrm{fh}}} \right)^2 \left(\alpha^2 \cos^2 \Xi - 0.5 \right) + \\
& \qquad \frac{2}{3} \left(\frac{R_v}{\Delta\Theta \cdot l_\lambda} \right)^2 \left(1 - \frac{l_\lambda}{l_{\mathrm{fv}}} \right)^2 \left(\alpha^2 \sin^2 \Xi - 0.5 \right) \right] \times \\
& \times P_{\mathrm{NBI,injected}},
\end{aligned}
\tag{2.60}
$$

where

- $\mathbf{x}_0$ is the observation point in the plasma;

- v is the velocity of the neutral atoms before entering the plasma region;

- λ is the effective mean free path for particles with velocity v, which is detailed in [67];

- l_0 is the path length between the neutral beam injection source and the observation point $\mathbf{x}_0$;

- l_λ is the distance between the neutral beam injection source and the observation point $\mathbf{x}_0$;

- N_{inj} is the total number of injected neutral particles into the plasma per unit time;

- $\Delta\Theta$ is the beam angular divergence expressed in [66];

- α is the normalised divergence angle expressed in [66];

- R_h and R_v are respectively the half-height and the half-width of a beam with rectangular shape;

- l_{fh} and l_{fv} are respectively the focal lengths in the horizontal and vertical planes;

- Ξ is the azimuthal injection angle relative to the main beam axis;

- $P_{\text{NBI,injected}}$ is the power provided by the NBI system.

The momentum deposition rate is expressed as

$$\frac{d\mathbf{p}_{i,\text{NBI}}(\mathbf{x}_0)}{dt} = \sqrt{\frac{2m_i}{P_{\text{NBI,injected}}}} \times Q_{i,\text{NBI}}(\mathbf{x}_0) \cdot \hat{\mathbf{e}}_l, \tag{2.61}$$

where m_i is the neutral beam ion mass and $\hat{\mathbf{e}}_l$ is the unit vector along the neutral beam axis. The current drive can be deduced from the momentum deposition.

As a result, the neutral beam injection power deposition and current drive are fully determined given [68]

- The position and configuration of the neutral beam injector;

- The characteristics of the beam;

- The atomic charge of the injected atoms and the plasma effective atomic charge profile Z_{eff} defined as

$$Z_{\text{eff}}(\rho) = \frac{\sum_k n_{i,k}(\rho) Z_{i,k}^2}{n_e(\rho)},$$

where $n_{i,k}$ is the k-th ion species density profile and $Z_{i,k}$ is the k-th ion species atomic charge;

- The plasma parameters.

The NBI power deposition and current drive can be numerically solved, as exposed in 2.3. The power deposition and current computed must be translated into profiles in (ρ, θ)-coordinates, which can be achieved using the equilibrium flux map.

ICRH

IC heating can be modelled using ray-tracing or global wave techniques. The ray-tracing technique is fast, but it suffers from the fundamental disadvantage that it is not valid close to the plasma boundary and cannot treat cavity resonances [69]. Although more accurate, global wave approaches require greater computational resources. In this work, we use a simplified global wave approach.

Assuming that the ICRH power is absorbed along one cyclotron resonance, it is possible to greatly simplify the global wave approach. The power deposition is given by [70]

$$\left\langle Q_{\text{i,ICRH}}\right\rangle = \frac{i\omega}{16\pi}\mathbf{E}^*\underline{\boldsymbol{\varepsilon}}^*\mathbf{E} - \frac{i\omega}{16\pi}\mathbf{E}^*\underline{\boldsymbol{\varepsilon}}\mathbf{E},\tag{2.62}$$

where

- ω is the IC wave angular frequency;

- $\mathbf{E}$ is the electromagnetic wave electric field given by

  $$\mathbf{E} = \mathbf{E}_0 e^{i(\omega t - k_x x - k_z z)}.$$

  The electromagnetic wave magnetic field is along the z component;

- $\underline{\boldsymbol{\varepsilon}}$ is the dielectric tensor detailed in [69].

The ICRH power deposition is fully determined by the antenna configuration, the ICRH wave angular frequency, the plasma equilibrium, and the minority density profile which determine $\underline{\boldsymbol{\varepsilon}}$.

LHCD

Lower hybrid power deposition and current drive can be modelled by combining a ray-tracing model for the propagation of the LH waves and a kinetic model of the plasma for the plasma-wave interaction.

The trajectory of the ray can be computed by solving the wave dispersion relation equation:

$$D_0(\mathbf{x},\mathbf{k},\omega) = P_6 n_\perp^6 + P_4 n_\perp^4 + P_2 n_\perp^2 + P_0 = 0,\tag{2.63}$$

where $n_\perp = k_\perp c/\omega$ is the refractive index perpendicular to the magnetic field, and P_0, P_2, P_4, and P_6 are coefficients that are functions of the plasma parameters. They are detailed in [71].

The plasma-wave interaction can be modelled using a Fokker-Planck approach. In this case,

the Fokker-Planck equation for electrons is expressed as follows

$$\frac{\partial f_e}{\partial t} = -eE_{||}\frac{\partial f_e}{\partial p_{||}} + \frac{\partial}{\partial p_{||}}D_{\mathrm{rf}}(p_{||})\frac{\partial f_e}{\partial p_{||}} + C(f_e) - \frac{f_e}{\tau_l(p_{||})} + \Gamma_s\delta(p_{||}), \tag{2.64}$$

where

- f_e is the electron distribution function;

- $p_{||}$ is the component of the electron momentum parallel to the magnetic field;

- $E_{||}$ is the DC electric field within the plasma;

- $D_{\mathrm{rf}}(p_{||})$ is the quasilinear diffusion coefficient expressed in [72];

- $C(f_e)$ is the Landau limit of the Balescu-Lenard collision operator detailed in [73];

- $\tau_l(p_{||})$ is the confinement time for tail electrons;

- $\Gamma_s\delta(p_{||})$ is a source of particles at low parallel momentum.

The current drive is the moment of this equation:

$$j_{\mathrm{LHCD}} = \int_0^\infty \pi dp_\perp^2 \int_{-\infty}^\infty f_e n_e e v_{||} dp_{||}, \tag{2.65}$$

where $v_{||}$ is the velocity of the electrons parallel to the magnetic field.

The LH current drive is fully determined by the plasma conditions, the wave parameters, and the launcher configuration.

2.1.9 Plasma diagnostics modelling

In this work, only two magnetic diagnostics are modelled, namely flux loops and pick-up probes.

Flux loops

Flux loops are conducting cables placed along the torus axis. The variation of poloidal magnetic flux $\Psi_p = 2\pi\psi$ inside the surface contoured by the flux loop generates an emf within the flux loop:

$$V_{\mathrm{FL}} = -2\pi\frac{d\psi_{\mathrm{FL}}}{dt}.$$

This voltage signal can be integrated to deduce the flux within the loop:

$$\psi_{\text{FL}}(t) = -\frac{1}{2\pi} \int_0^t V_{\text{FL}}(t')dt'.$$

Flux loops are modelled as axisymmetric filaments. The poloidal magnetic flux through a flux loop $2\pi\psi_{\text{FL}}(t)$ can be determined by

$$
\begin{aligned}
2\pi\psi_{\text{FL}}(t) \quad = \quad & \mu_0 \sum_{i=1}^{n_c} G(R_i, Z_i, R_{\text{FL}}, Z_{\text{FL}})I_i + \mu_0 \sum_{i=1}^{n_v} G(R_i, Z_i, R_{\text{FL}}, Z_{\text{FL}})I_i + \\
& +\mu_0 \int_{S_{\text{plasma}}} G(R', Z', R_{\text{FL}}, Z_{\text{FL}}) j_\phi(R', Z') dR' dZ',
\end{aligned}
\tag{2.66}
$$

by modelling the flux loop as a filament at the position $(R_{\text{FL}}, Z_{\text{FL}})$. $\psi_{FL}(t)$ can thus be computed given the plasma equilibrium, the PF system currents, and the conducting vacuum vessel currents.

Pick-up coils

Pick-up coils are solenoids placed at various positions and with various orientations around the vacuum vessel in order to determine the magnetic field at the pick-up coil position and along the pick-up coil axis. The variation of magnetic flux within the pick-up coil induces an emf $V_{\text{pick-up}}$ given by

$$V_{\text{pick-up}} = -2\pi\frac{d\psi_{\text{pick-up}}}{dt} = -2\pi N \int_{A_{\text{pick-up}}} \frac{d\mathbf{B}}{dt} \cdot d\mathbf{S} = -2\pi N \int_{A_{\text{pick-up}}} \frac{dB_{\text{pick-up}}}{dt} dS,$$

where $V_{\text{pick-up}}$ is the voltage measured in the pick-up coil, N is the number of turns in the pick-up coil, $A_{\text{pick-up}}$ is its surface area, $B_{\text{pick-up}}$ is the the magnetic field component along the pick-up coil axis.

Assuming that the magnetic field is homogeneous in the volume of the pick-up coil, the magnetic field component along the pick-up coil axis present within the pick-up coil can be deduced by integration of the voltage

$$B_{\text{pick-up}}(t) = -\frac{1}{2\pi} \int_0^t \frac{V_{\text{pick-up}}}{N A_{\text{pick-up}}}.$$

This diagnostic can be synthesised by determining the magnetic field equivalent of the Green's functions between the PF system coils and the pick-up coils.

2.1.10 Modelling of the control systems

Feedback and feedforward control systems must be modelled in order to simulate the tokamak evolution. In this work, the control systems are embedded in a Matlab/Simulink environment and the controllers and control algorithms are either straightforwardly implemented from built-in Simulink functions or user-defined pieces of software expressed in the Matlab script language.

2.2 DINA-CH

DINA is a free-boundary equilibrium evolution code first developed in 1990 by Rustam Khayrutdinov and Victor Lukash [74]. It solves the Grad-Shafranov equation with free-boundary conditions, i.e. self-consistently with the PF system currents and the conducting vacuum vessel currents. The equilibrium evolution is simulated via the magnetic diffusion equation (2.47) and the transport equations (2.51) and (2.54). The modelling of heating and current drive systems is not advanced but exists in DINA.

The DINA free-boundary simulator working scheme and validation procedure are discussed in 2.2.1 and 2.2.2. DINA-CH is an evolution of DINA realised by a collaboration between CRPP and the DINA code authors [75]. DINA-CH specific features are exposed in 2.2.3.

2.2.1 The DINA working scheme

DINA is a simulator that consists of several modules dedicated to solving the Grad-Shafranov equation, the transport equations, the heating power and current drive depositions, the circuit equations, and determining the bootstrap current contribution. These functions are embedded in a Fortran environment.

DINA's working scheme is as follows:

1. At plasma initiation at time $t = t_0$, several pieces of information must be provided:

   - Several (R, Z)-coordinates of the desired initiation plasma boundary;
   - An estimation of the initiation PF system currents and conducting vacuum vessel currents;
   - An estimate of the initial toroidal current density profile $j_\phi(t_0, \rho)$;
   - The initial electron density profile $n_e(t_0, \rho)$;
   - The initial ion and electron temperatures $T_i(t_0, \rho)$ and $T_e(t_0, \rho)$.

   This information needs not be that of an equilibrium because DINA initiates the plasma pulse by finding an equilibrium that minimises the divergence with the provided estimations.

2. At the beginning of the k-th time step, several pieces of information are retrieved from the $(k-1)$-th time step:

   - The toroidal current density map at the R and Z points of the $n_R \times n_Z$ grid: $j_\phi(t_{k-1}, R, Z)$;

   - The poloidal flux map at the R and Z points of the $n_R \times n_Z$ grid: $\psi(t_{k-1}, R, Z) = \psi^0(t_k, R, Z)$;

   - The associated coordinates of the flux surfaces expressed as a function of the normalised toroidal flux $\rho = \sqrt{\frac{\Phi}{\Phi_{\text{boundary}}}}$ and the azimutal angle θ: $\psi(t_{k-1}, \rho, \theta) = \psi^0(t_k, \rho, \theta)$;

   - The flux profile: $\psi(t_{k-1}, \rho) = \psi^0(t_k, \rho)$;

   - The electron density profile $n_e(t_k, \rho)$;

   - The ion and electron temperatures: $T_i(t_k, \rho)$ and $T_e(t_k, \rho)$.

3. To determine the flux map at the k-th time step, the following internal loop is performed:

   (a) Given a step size Δt, solve the magnetic diffusion equation (2.47) to determine $\psi^\alpha(t_k, \rho)$ with respect to $\psi(t_{k-1}, \rho)$.

      - If this is the first iteration of the internal loop ($\alpha = 1$),

      $$\psi^1(t_k, \rho) = \psi(t_{k-1}, \rho) + \frac{d\psi}{dt} \cdot \Delta t,$$

      where $\frac{d\psi}{dt}$ is computed from the magnetic diffusion equation. In order to do that, it is necessary to use the poloidal current function $f(t_{k-1}, \rho)$, the non-inductive current drive, and the geometric coefficients computed during the previous time step;

      - If this is not the first iteration, use the poloidal current function obtained during the previous internal iteration $f^{\alpha-1}(t_k, \rho)$ and an implicit integration scheme to solve the magnetic diffusion equation and deduce $\psi^\alpha(t_k, \rho)$.

   (b) Express $\psi^\alpha(t_k, \rho)$ on the (R, Z)-grid;

   (c) Determine the toroidal plasma current distribution $j^\alpha_{\phi,\text{pla}}(t_k, R, Z)$ using the estimated flux $\psi^\alpha(t_k, R, Z)$ and Ampère's law, as expressed in (2.28);

   (d) Solve the circuit equations (2.37) consistently with the plasma current distribution $j^\alpha_{\phi,\text{pla}}(t_k, R, Z)$ to deduce the currents in the PF systems and in the conducting vacuum vessel;

   (e) Compute $j^\alpha_{\phi,\text{pla}}(t_k, \rho)$ using the equilibrium flux map;

   (f) Determine the updated poloidal current function $f^\alpha(t_k, \rho)$ consistent with $j^\alpha_{\phi,\text{pla}}(t_k, \rho)$ using (2.32) and the pressure profile $p(t_k, \rho)$;

   (g) Compute the updated flux map $\psi^\alpha(t_k, R, Z)$ by solving Grad-Shafranov equation (2.35) for $\psi^\alpha(t_k, R, Z)$ using $f^\alpha(t_k, R, Z)$ and $p(t_k, R, Z)$. Free boundary conditions

are provided by the plasma current distribution $j^\alpha_{\phi,\mathrm{pla}}(t_k, R, Z)$, the currents in the PF systems , and the currents in the vacuum vessel plates.

(h) Determine the updated flux surface coordinates in terms of ρ and θ, i.e. determine $\psi^\alpha(t_k, \rho, \theta)$;

(i) Check the convergence condition on all the $n_R \times n_Z$ grid points of coordinates (R, Z)

$$\left| \frac{\psi^\alpha(t_k, R, Z) - \psi^{\alpha-1}(t_k, R, Z)}{\psi^{\alpha-1}(t_k, R, Z)} \right| < \epsilon_\psi,$$

where ϵ_ψ is a criterion provided by the user.

(j) If the convergence criterion is not satisfied, repeat the internal loop.

4. Determine the flux surface average power deposition and current drive of the $(k+1)$-th time step by the modelling of heating and current drive systems;

5. Compute the updated electron density $n^\alpha_e(t_{k+1}, \rho)$ using the particle transport equation (2.49);

6. Compute the updated ion and electron temperatures $T^\alpha_i(t_{k+1}, \rho)$ and $T^\alpha_e(t_{k+1}, \rho)$ using the ion and electron heat transport equation (2.51) and (2.54);

7. Check the vertical speed criterion

$$\left| \frac{\dot{Z}_{\mathrm{mag}}(t_k) - \dot{Z}_{\mathrm{mag}}(t_{k-1})}{\dot{Z}_{\mathrm{mag}}(t_k)} \right| < \epsilon_{\dot{Z}_{\mathrm{mag}}},$$

where $\epsilon_{\dot{Z}_{\mathrm{mag}}}$ is a criterion specified by the user. If this criterion is not met, decrease the time-step duration Δt and repeat the scheme for the k-th time step.

The feedforward and feedback control modules are called between two iterations of the exposed scheme. DINA exports several plasma quantities used in controllers, such as the plasma centroid position evolution, the plasma boundary evolution, the PF system currents evolution, etc.

2.2.2 DINA validation

DINA has been validated against TCV for equilibrium responses to actuator stimulations [75] and vertical displacement events (VDE) [76]. In these works, it has been demonstrated that DINA accurately simulates the macroscopic evolution of the plasma position, the evolution of the plasma current and the PF system currents, the plasma shaping parameters (elongation and triangularity), and the magnetic diagnostic signals over a wide set of experimental conditions. This validation process proves that DINA's modelling and numerical scheme are appropriate for simulation of the macroscopic plasma equilibrium evolution with respect to equilibrium stimulations, up to the precision of measurements.

2.2.3   DINA-CH

Because of its increasing complexity, DINA started suffering from its suboptimal modularity and lack of transparency. In the perspective of increasing DINA's readability and allowing more efficient user interaction, it was decided to divide the DINA code into several modules to be embedded in a Matlab/Simulink environment, which was chosen because it is a user-friendly and mature software. This simulator, which is a branch of the DINA code, is called DINA-CH.

DINA-CH consists of the following modules:

- The DINA equilibrium evolution module is the central part of DINA-CH. It determines the plasma equilibrium evolution according to the following time-independent and time-dependent inputs:

  - The time-independent tokamak configuration, such as the first wall position, the mutuals between the coils, the positions of the flux loops and pick-up coils, etc;

  - Time-independent simulation parameters, such as the simulation time-step, the convergence criteria, etc;

  - The time-dependent PF system coil voltages;

  - The time-dependent particle diffusion coefficient D and the particle pinch velocity $\mathbf{v}_p$ required to solve the particle transport equation (2.50);

  - The time-dependent ion and electron heat thermal conductivity profiles $\chi_i(t,\rho)$ and $\chi_e(t,\rho)$, which are necessary to solve the ion and electron transport equations (2.51) and (2.54). The convective velocities V_i^q and V_e^q are neglected;

  - The time-dependent bootstrap current density profile $j_{\text{boot}}(t,\rho)$;

  - The time-dependent power deposition due to the heating systems;

  - The time-dependent current drive due to current drive systems.

  This module outputs a large number of time-dependent plasma parameters, such as the plasma boundary evolution, the plasma centroid position evolution, the plasma ion and electron temperatures evolution, synthetic diagnostic signals, etc;

- The transport module which determines the ion and electron heat thermal conductivity profiles $\chi_i(t,\rho)$ and $\chi_e(t,\rho)$, the bootstrap current density profile $j_{\text{boot}}(t,\rho)$ and the particle diffusion coefficient D and pinch velocity $\mathbf{v}_p$;

- The control systems, which take either time-dependent synthetic diagnostic signals or time-dependent plasma parameters as inputs, such as the plasma current, the plasma boundary, etc. The control systems output power supply voltage demands and heating and current drive demands;

- The electric power supply module, which determines the power supply response to control system demands and models the coil connections (see Figure 2.3);

- The heating and current drive systems module, which determines the power deposition and current drive profiles due to the heating and current drive systems action.

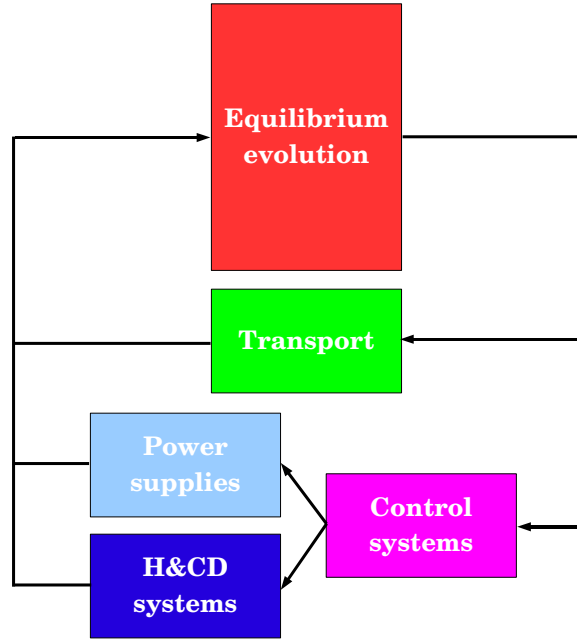A schematic representation of the DINA-CH workflow is provided in Figure 2.10.

Figure 2.10: The DINA-CH working scheme.

The main advantage of DINA-CH over DINA consists of its improved modularity. Each DINA-CH module is easier to maintain or improve.

DINA-CH is referred to as a *full tokamak simulator*, because it fully models the tokamak, i.e. it models the equilibrium evolution with respect to power supply stimulations and also models the power supply responses to control demands, as well as the control systems.

Although the DINA-CH modularisation has never been formally validated against experimental data, it can be reasonably assumed that its performance is similar to DINA's because their only difference consists of the improved modularity of DINA-CH. The DINA and DINA-CH modelling, physical assumptions, and numerical schemes are identical.

2.3   CRONOS

CRONOS is a suite of numerical codes for the predictive and interpretative simulation of tokamak discharges. It was developed by a large team of collaborators at CEA, Cadarache, France.

CRONOS provides a platform for tokamak simulation by enabling communication between equilibrium modules, transport modules, and heating and current drive modules.

In this thesis, several CRONOS modules are used:

- The ion and electron heat transport solver;

- The ion and electron heat diffusivity modelling KIAUTO;

- The Bohm/Gyro-Bohm ion and electron heat diffusivity modelling;

- The ECRH/ECCD power deposition and current drive module REMA;

- The NBI power deposition and current drive module NEMO;

- The ICRH power deposition module PION;

- The LH current drive module DELPHINE.

These modules are summarised in this paragraph.

2.3.1 Ion and electron heat transport solver

The CRONOS integrated ion and electron heat transport solver solves the energy balance equations (2.51) and (2.54). This solver is similar to the DINA heat transport solver because it solves the same set of equations.

2.3.2 KIAUTO heat diffusivity modelling

The KIAUTO heat diffusivity modelling [77] consists of the following empirical modelling for ion and electron heat diffusivity

$$
\begin{aligned}
\chi_i &= \mathscr{C} \cdot F(s, \alpha, \gamma_E) \cdot R_i(\nabla T_i, \nabla n_e) \frac{q^2 \sqrt{T_i}}{n_e} \frac{\nabla p}{B^2} \\[2mm]
\chi_e &= \mathscr{C} \cdot F(s, \alpha, \gamma_E) \cdot R_e(\nabla T_i, \nabla n_e) \frac{q^2 \sqrt{T_e}}{n_e} \frac{\nabla p}{B^2},
\end{aligned}
\tag{2.67}
$$

where

- q is the *safety factor*. It is defined as

$$
q = \frac{1}{2\pi} \frac{d\Phi}{d\psi} = \frac{1}{2\pi} \oint_{C_\psi} \frac{1}{R} \frac{B_\phi}{\sqrt{B_R^2 + B_Z^2}},
$$

where C_ψ is the contour of the S_ψ surface exposed in Figure 2.8;

- $\mathscr{C} = \mathscr{C}(t)$ is a parameter that is updated at each time-step imposing that the plasma energy confinement time follows a predetermined scaling law. This feature is not physical, in the sense that $\mathscr{C}$ is non-local, as will be demonstrated in Chapter 3;

- F is a function describing the improvement of confinement with respect to the magnetic shear s, the normalised pressure gradient α and the radial electric field shear γ_E.

  The *magnetic shear* is defined as

  $$s = \frac{r}{q}\frac{dq}{dr}.$$

  The normalised pressure gradient is given by

  $$\alpha = r\frac{\nabla p}{p},$$

  and the radial electric field shear is given by

  $$\gamma_E = \frac{\partial E_r}{\partial r},$$

  where $\mathbf{E} = (E_r, E_\phi, E_\theta)$ is the electric field expressed in poloidal coordinates;

- R_i and R_e are weight functions that depend on the temperature and density gradients. They adjust the values of the ion and electron heat diffusivity with respect to the stability of the equilibrium.

As will be exposed in section 3.2, KIAUTO suffers from one major weakness, in that the coefficient $\mathscr{C}$ is frequently updated. The modification of $\mathscr{C}$ acts as an apparent heat source or sink.

KIAUTO has previously demonstrated good quantitative accuracy with experimental data under certain conditions, namely low-frequency tokamak evolution. For this reason, KIAUTO can be considered as an appropriate candidate for low-frequency ITER heat diffusivity modelling.

2.3.3 Bohm/Gyro-Bohm heat diffusivity modelling

The Bohm/Gyro-Bohm heat diffusivity modelling states that the ion and electron heat diffusivity can be expressed as the sum of two contributions, Bohm-like diffusivity and Gyro-Bohm-like diffusivity.

The ion diffusivity can be expressed as [78]

$$\chi_i = 2\chi_i^{\mathrm{B}} + \chi_{\mathrm{GB}}, \tag{2.68}$$

and the electron diffusivity can be expressed as

$$\chi_e = \delta_{\mathrm{B}} \chi_e^{\mathrm{B}} + \chi_{\mathrm{GB}}^{\star}, \tag{2.69}$$

where

- χ_i^{B} is the Bohm component of the ion diffusivity given by

$$\chi_i^{\mathrm{B}} = \alpha_{\mathrm{B}} \frac{T_i}{eB} \frac{a \nabla p_i}{p_i} q^2,$$

  where $\alpha_{\mathrm{B}} = 2.5 \cdot 10^{-4}$, with T_i, e, B, a, and p_i expressed in CGS units;

- χ_{GB} is the Gyro-Bohm component of the ion heat diffusivity expressed as

$$\chi_{\mathrm{GB}} = \alpha_{\mathrm{GB}} \frac{T_e}{eB} \rho^{\star} \frac{a \nabla T_e}{T_e},$$

  where

  - $\alpha_{\mathrm{GB}} = 3.5 \cdot 10^{-2}$ with T_e, e, B, and a expressed in CGS units;
  - $\rho^{\star}$ is the normalised gyro-radius, expressed as

$$\rho^{\star} = \frac{\sqrt{\epsilon_0 m_i T_i}}{Z_i eaB},$$

    where Z_i is the ion charge;

- $\delta_{\mathrm{B}} = 0.5$;

- χ_e^{B} is the Bohm component of the electron heat diffusivity coefficient:

$$\chi_e^{\mathrm{B}} = \alpha_{\mathrm{B}} \frac{T_e}{eB} \frac{a \nabla p_e}{p_e} q^2.$$

- $\chi_{\mathrm{GB}}^{\star}$ is the Gyro-Bohm component of the electron heat diffusivity coefficient, given by

$$\chi_{\mathrm{GB}}^{\star} = \alpha_{\mathrm{GB}}^{\star} \frac{T_e}{eB} \rho^{\star} \frac{a \nabla p_e}{p_e} \frac{r \nabla p_e}{p_e} \beta^{1/2} q^3,$$

  where

  - $\alpha_{\mathrm{GB}}^{\star} = 0.32$ with T_e, e, B, a, p_e, and r expressed in CGS units;
  - β is the normalised plasma pressure given by

$$\beta = \frac{2\mu_0 (p_e + p_i)}{\left(B_R^2 + B_\phi^2 + B_Z^2 \right)^2}.$$

The Bohm/Gyro-Bohm heat diffusivity model is based on a semi-empirical approach. It shows good low-frequency quantitative accuracy with respect to Tore Supra and START plasma discharges. It is therefore a good candidate for low-frequency ITER diffusivity modelling but the full extent of its validity range is presently undetermined.

2.3.4   The REMA ECRH/ECCD model

The REMA module [62] models the EC power deposition and current drive using a ray-tracing approach for the wave propagation within the plasma and a linearised perturbed Fokker-Planck approach for the plasma-wave interaction. Its solves the power deposition and current drive equations (2.58) and (2.59) with respect to given wave, antennae, and plasma configurations.

REMA demonstrated good quantitative accuracy with respect to PLT and ALCATOR C experimental data, but the comparison between theoretical prediction and experimental data is dependent on the model used for translating raw data into measured outputs that can be compared with theoretical predictions [79]. The validity range of REMA is not precisely determined but is expected to extend to the ITER configuration.

2.3.5   The NEMO NBI model

The NEMO module is an evolution of the SINBAD module for NBI power deposition and current drive [67]. NEMO is based on a narrow beam model of the neutral beam for beam propagation modelling and a Fokker-Planck kinetic approach for the plasma-beam interaction modelling. NEMO solves the power deposition and current drive equations (2.60) and (2.61) with respect to the plasma configuration.

SINBAD has demonstrated good quantitative agreement with ASDEX, TEXTOR, and JET experimental data but the comparison between the SINBAD theoretical predictions and experimental data is dependent on the model used for translating raw data into measured outputs that can be compared with theoretical predictions. The validity range of SINBAD (and NEMO) is not precisely determined but is expected to extend to the ITER configuration.

2.3.6   The PION ICRH model

The PION module [80] is an evolution of the LION IC power deposition simulator [81]. It computes the IC power deposition using a global wave approach and solves (2.62) with respect to the wave, antennae, and plasma configurations.

PION demonstrated good quantitative agreement with JET experimental data but the comparison between the PION theoretical predictions and experimental data is dependent on the model used for translating raw data into measured outputs that can be compared with

theoretical predictions. The validity range of PION is not precisely determined but is expected to extend to the ITER configuration.

2.3.7 The DELPHINE LHCD model

The DELPHINE module [82] computes the propagation of an electromagnetic wave in the LH range using a ray-tracing approach and models the plasma-wave interaction using a kinetic approach. DELPHINE solves (2.63) and (2.64).

DELPHINE shows good quantitative agreement with Tore Supra experimental data but the comparison between the DELPHINE theoretical predictions and experimental data is dependent on the model used for translating raw data into measured outputs that can be compared with theoretical predictions. The validity range of DELPHINE is not precisely determined but is expected to extend to the ITER configuration.

2.4 The DINA-CH&CRONOS full tokamak simulator

Both DINA-CH and CRONOS possess a modular architecture. On its own, DINA-CH lacks advanced heating and current drive source modules. On the other hand, CRONOS lacks a reliable and fast free-boundary equilibrium evolution module, although two such modules are presently under development [83, 84, 85]. For that reason, it is of a high interest to couple CRONOS to DINA-CH. Such coupling was performed by Sun Hee Kim in 2007 assisted by both the DINA and CRONOS authors. The resulting simulator is called DINA-CH&CRONOS.

The simulation tasks are divided as follows:

- DINA computes the equilibrium evolution and the magnetic diffusion;

- CRONOS computes the ion and electron particle and heat transport. This is required in order to guarantee consistency with the CRONOS heating and current drive modules;

- CRONOS computes the effect of the heating and current drive systems;

- The power supply are modelled by a user-defined module embedded in Matlab/Simulink;

- The control systems are modelled by a user-defined module embedded in Matlab/Simulink.

This is summarised in Figure 2.11.

2.4.1 DINA-CH&CRONOS Matlab/Simulink architecture

DINA-CH&CRONOS is embedded in a Matlab/Simulink environment, as displayed in Figure 2.12.
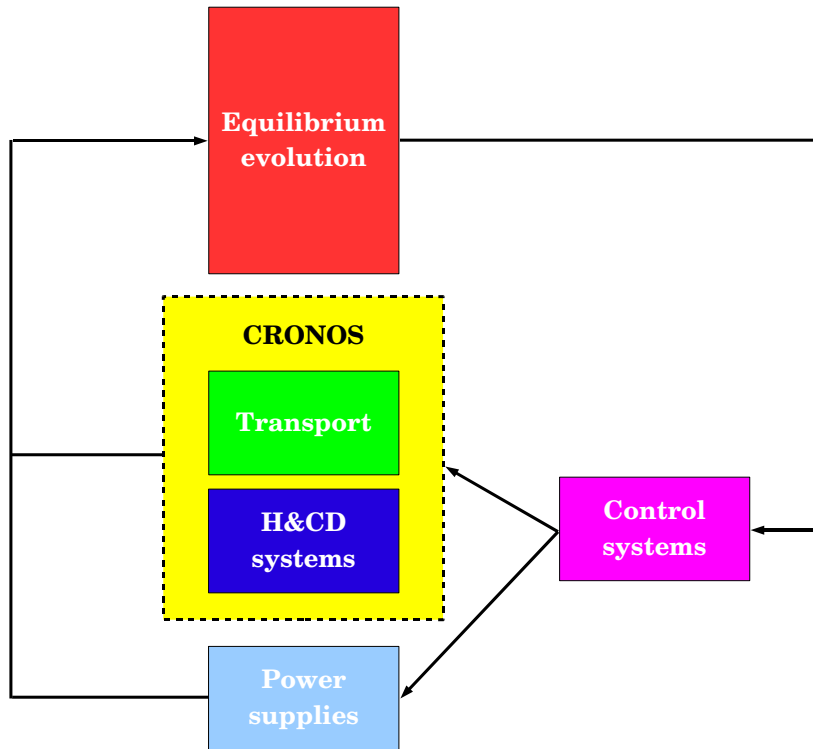
Figure 2.11: The DINA-CH&CRONOS working scheme.

In order to resemble ITER's present control philosophy, the Simulink architecture of the DINA-CH&CRONOS full tokamak simulator was modified in 2010 [86]. The DINA-CH&CRONOS Simulink diagram is divided in three main parts: the pulse schedule creation systems, the plasma control system (PCS), and the plant systems. Each of these parts is composed of several subsystems:

- **Pulse schedule creation**

  The scenario is set in the pulse schedule creation module. It contains the operator-defined scenario reference waveforms designed before the plasma pulse.

  This module emulates the present tokamak operation procedure, in which the scenario references are set beforehand by the tokamak operator. It also allows the definition of interchangeable plasma pulse segments. The *pulse schedule* consists of the set of plasma pulse segments. The segment selection is made by the PCS.

- **Operation request gatekeeper**

  The operation request gatekeeper module aims at preventing the implementation of inappropriate or dangerous reference waveforms on the tokamak.

  Although this module is presently inactive, it enables the modelling and testing of gatekeeper strategies for ITER using DINA-CH&CRONOS.
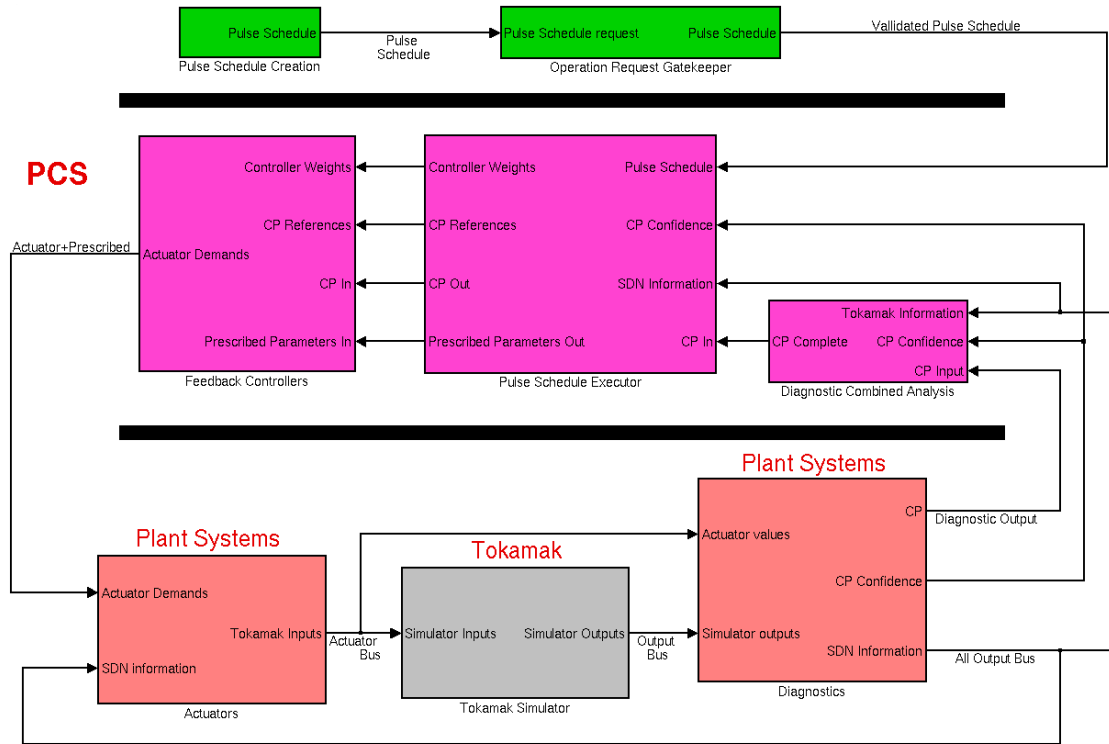
Figure 2.12: The DINA-CH&CRONOS Matlab/Simulink environment and separate modules.

- **Pulse schedule executor**

  The pulse schedule executor module is a part of the PCS. Its role consists of determining the plasma pulse scenario references on-the-fly.

  The pulse schedule executor module possesses the authority to change the plasma scenario on-the-fly. This enables several features:

  - The pulse schedule executor module may assess whether the scenario is appropriate for a given tokamak state. It may undertake preventive reactions in order to avoid foreseeable undesirable or dangerous future tokamak behaviour.

  - It may handle errors and exceptions in tokamak behaviour, such as power supply failures, plasma diagnostic unavailability, unexpectedly large plasma disturbances, etc., by adapting the scenario and the control systems to the tokamak state.

  - The pulse schedule executor module enables the implementation of real-time optimisation algorithms, because it possesses information regarding the tokamak state and the authority to act on the scenario reference on-the-fly. Such closed-loop optimal control algorithms are discussed in more details in Chapter 4.

  It should be stated that the pulse schedule executor is not considered responsible for the tokamak integrity because it can only act on scenario references. Certain dramatic

events, such as large plasma disturbances, simultaneous failure of several power supplies or diagnostics, etc., cannot be tackled by mere on-the-fly scenario modifications and require emergency plasma pulse shut-down strategy. Tokamak integrity concerns are addressed by a higher level control system, the Central Interlock System (CIS), not implemented in DINA-CH&CRONOS. The population and environment safety concerns are addressed by an even higher level control systems, the Central Safety System (CSS).

- **Feedback controllers**
  The feedback controllers module is the second part of the PCS and consists of several feedforward and feedback controllers that can be switched on and off according to the information transmitted by the pulse schedule executor module. The feedforward and feedback controllers translate the scenario references provided by the pulse schedule executor into actuator demand signals.

  This module enables the implementation of both linear and nonlinear feedforward and feedback controllers.

- **Actuators**
  The actuator module simulates the power supply responses to the feedback controller demand signals.

  This module encapsulates the modelling of the ITER power supplies exposed in 2.1.2. The power supply delays, characteristic times, saturations, and connections are implemented.

- **Tokamak simulator**
  The tokamak simulator module simulates the tokamak evolution according to the actuator signals.

  The effects of both the external power supplies and the heating and current drive systems are taken into account and the plasma equilibrium evolution is determined using the internal modules of DINA-CH and CRONOS.

- **Diagnostics**
  The diagnostics module enables plasma diagnostics modelling and plasma pulse data reconstruction and storage. This module outputs the tokamak state in a format appropriate for the PCS.

- **Diagnostics combined analysis**
  The diagnostics combined analysis modules enables the comparison and cross-checking of the estimated tokamak state according to several diagnostics. This module aims at reducing the risk associated with diagnostic failure, but is presently not used.

In principle, the actuators module, the tokamak simulator module, and the diagnostics module could be replaced respectively by real tokamak actuators, a real tokamak, and real diagnostics without modifying the pulse schedule generation and the PCS modules. DINA-CH&CRONOS thus simulates the evolution of the full tokamak.

2.4.2   Alternative full tokamak simulators

To the author's knowledge, there exists a handful of full tokamak simulators presently operated amongst several institutes:

- **CORSICA**
  CORSICA [87] is a full tokamak simulator first developed in 1997 by a consortium of collaborators at the Lawrence Livermore National Laboratory, in the United States. COR-SICA simulates the plasma two-dimensional free-boundary equilibrium evolution and one-dimensional heat and particle transport. The set of equations solved by CORSICA is identical to the set of equations solved by DINA-CH&CRONOS.

  Although their assumptions are similar, CORSICA differs from DINA-CH&CRONOS in several aspects. Firstly, the models used for heat diffusion and particle diffusion in CORSICA slightly differ from those used in DINA-CH&CRONOS. Secondly, the code architecture of CORSICA is different from the modular architecture of DINA-CH&CRONOS. Finally, the interaction with CORSICA requires the use of BASIC language, whose learning may require effort from novice users.

- **TSC**
  TSC [55] was first developed in 1986 by a consortium of collaborators in the Princeton Plasma Physics Laboratory, in the United States. TSC solves the plasma two-dimensional free-boundary equilibrium evolution and one-dimensional heat and particle transport. Its specificity is that TSC accounts for plasma mass. The set of equations solved by TSC is therefore different to the set of equations solved by DINA-CH&CRONOS.

- **CREATE-NL&JINTRAC** The CREATE-NL&JINTRAC full tokamak simulator couples the CREATE-NL free-boundary equilibrium evolution code and the JINTRAC fixed-boundary code. Its development is the fruit of a collaboration between CREATE-NL developers and JINTRAC developers.

  The first full tokamak simulations performed with CREATE-NL&JINTRAC still await publication.

Each of the discussed full tokamak simulators take a specific approach regarding transport modelling. In the author's opinion, it is reasonable to expect similar results from these simulators although formal benchmarking has yet to be performed.

DINA-CH&CRONOS distinguish itself from CORSICA, TSC, and CREATE-NL&JINTRAC in several aspects. Most importantly, DINA-CH&CRONOS takes a modular approach, as opposed to CORSICA and TSC. This feature significantly speeds the simulator, but at the price of a slight loss in consistency. It is also the author's opinion that DINA-CH&CRONOS's interface is far more user-friendly than that of e.g. CORSICA. Finally, the speed of DINA-CH&CRONOS is at least comparable to that of these alternative simulators. Although not formally demonstrated,

it is the author's belief that DINA-CH&CRONOS is faster than all the presented alternative full tokamak simulators.

2.4.3 DINA-CH&CRONOS features

Because of its nature, DINA-CH&CRONOS enables the study of cross-coupling effects between plasma equilibrium and heating and current drive system action. DINA-CH&CRONOS is therefore an appropriate simulator for advanced scenario modelling.

Several use cases of DINA-CH&CRONOS are described in Chapter 3. Optimal control strategies for ITER long pulses are explored using DINA-CH&CRONOS in Chapter 4. Finally, the simulation of ITER advanced scenarios using DINA-CH&CRONOS is exposed in Chapter 5.

2.4.4 Validity of DINA-CH&CRONOS

Although the electromagnetic modelling of DINA-CH&CRONOS has not yet been formally validated, it can be reasonably assumed that its performance is similar to DINA's because their modelling, physical assumptions, and numerical schemes are identical.

As mentioned, the DINA-CH&CRONOS transport modelling and its modelling of the heat and current drive systems demonstrated good low-frequency quantitative accuracy with respect to a wide range of experiments. However, the full validity range of such modelling is presently undetermined but is expected to extend to the ITER configuration.

The transport modelling of DINA-CH&CRONOS relies on empirical scaling laws, such as the energy confinement time scaling law. However, there is no evidence that such scaling laws will be straightforwardly applicable to ITER. As a result, the only approach that can be undertaken is to perform sensitivity studies against particular parameters of the DINA-CH&CRONOS transport modelling, such as the value of the confinement enhancement factor, and assess the effect of the variations of such parameters onto the simulations. In the following, relevant sensitivity studies accompany simulation results.

3 DINA-CH&CRONOS use cases

Full tokamak simulators such as DINA-CH and DINA-CH&CRONOS are important tools for predictive modelling because they take into account the tokamak electromagnetic and kinetic cross-coupling effects. Designing tokamaks such as ITER therefore greatly benefits from predictive simulations using full tokamak simulators.

In this Chapter, three use cases of DINA-CH and DINA-CH&CRONOS are reported. These use cases are presented with the objective of exposing the type of challenges that require full tokamak simulators such as DINA-CH and DINA-CH&CRONOS in order to be tackled. The DINA-CH and DINA-CH&CRONOS use cases also served the more specific purpose of enabling the author to uncover and understand the DINA-CH and DINA-CH&CRONOS working schemes and get accustomed to the interaction with these full tokamak simulators in the framework of well-defined challenges.

The following use cases of the DINA-CH and DINA-CH&CRONOS full tokamak simulators are exposed:

- A study of the effect of the electric power supply voltage ripple on the ITER pick-up coils;

- A study of the effect of loop voltage modulation and ECRH power modulation for ITER current density control;

- The implementation of a current density control algorithm using DINA-CH&CRONOS.

Ultimately, DINA-CH&CRONOS is used to simulate ITER advanced scenarios in Chapter 5.

3.1 Effect of power supply voltage ripple on the ITER ex-vessel pick-up coils

ITER's magnetic diagnostic set includes in-vessel and ex-vessel pick-up coils. These probes measure the magnetic field induced by the plasma, the PF system currents, and the conducting

vacuum vessel currents at certain locations around the tokamak.

The ex-vessel pick-up coils response may be affected by the fast magnetic field variation due to the electric power supply ripple generated by the switching of thyristors in the PF system power supplies. It is thus important to investigate the extent of this effect.

This paragraph discusses the effects of power supply voltage ripple on the ITER pick-up coils in a conventional ITER 15MA inductive scenario (ITER scenario 2) during flat-top. The initial ITER equilibrium is directly imported from Sun Hee Kim's simulations of ITER scenario 2 [88].

This study was performed using the DINA-CH free-boundary simulator. The full complexity of DINA-CH&CRONOS was not required because the effects of heating, current drive, and heat diffusivity on equilibrium evolution are not anticipated to have a significant impact on the conclusions of this work.

3.1.1 Power supply voltage ripple

ITER is foreseen to use twelve-phases 50Hz AC power supplies [89, 90]. The switching of thyristors within each PF system power supplies generates a voltage ripple whose amplitude and waveform depend on each power supply DC demand voltage. The voltage ripple reaches its maximum amplitude when the DC demand voltage is zero. In that case, the voltage ripple can be approximated by a sawtooth-like signal [91]. Figure 3.1 displays the normalised power supply twelve-phases AC pulses and the maximum associated voltage ripple which corresponds to zero DC demand voltage.

In this study, the worst case scenario is considered, meaning that we model the largest possible effect that the power supply voltage ripple could have on the pick-up coil signals. Therefore, although the voltage ripple amplitude and phase really depend on the DC demand voltage specific to each converter, the power supply ripple is modelled as if the DC power supply demand voltage was zero for each power supply. It is also assumed that all the power supply voltage ripples are in phase.

The voltage ripple peak-to-peak amplitudes are displayed in Table 3.1. The implemented ripple peak-to-peak amplitudes are about 40% larger than the estimated maximum amplitudes in order to remain conservative.

These estimations are based on the 2006 ITER design [43]. Although the ripple peak-to-peak amplitude is slightly different for the 2010 ITER design [44], the conclusions of this study remain relevant. VS3 is not implemented.

The AC pulse frequency is 50Hz. Because ITER possesses twelve-phase power supplies, the ripple frequency is

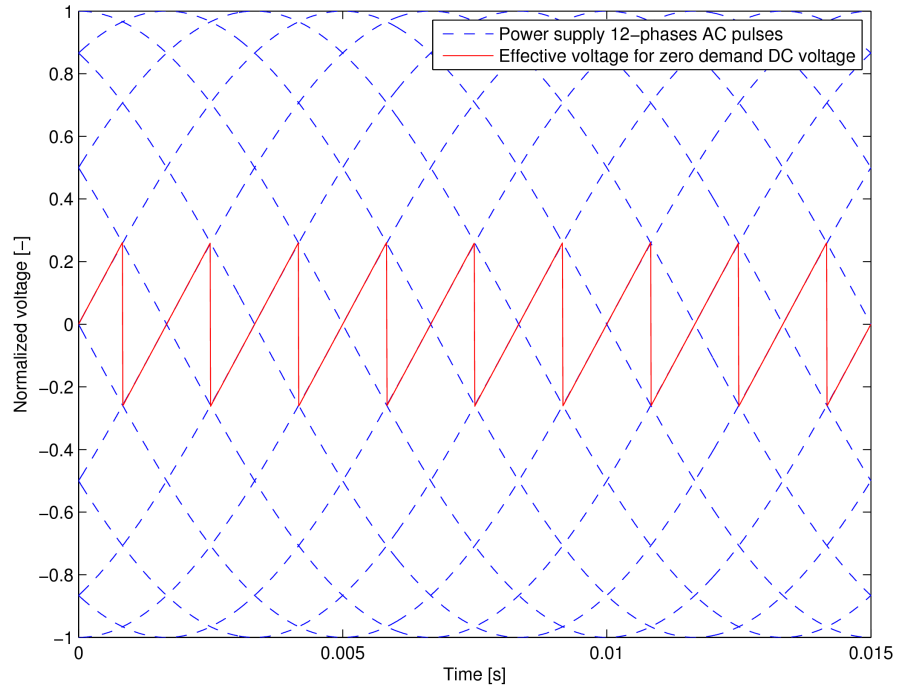$$f_{\text{ripple}} = 12 \times 50\text{Hz} = 600\text{Hz}.$$

Figure 3.1: Approximation of the voltage ripple by a sawtooth-like signal. The power supply twelve-phases AC pulses are displayed in dashed-blue and the voltage ripple corresponding to a zero DC demand voltage is displayed in red.

Table 3.1: Power supplies peak-to-peak ripple amplitudes.

Power supply	Estimated maximum ripple p-p amplitude [V]	Applied ripple p-p amplitude [V]
MC_{CS3U}	776	1083
MC_{CS2U}	776	1083
MC_{CS1UL}	1552	2167
MC_{CS2L}	776	1083
MC_{CS3L}	776	1083
MC_{CS3U}	776	1083
MC_{PF1}	776	1083
MC_{PF2}	776	1083
MC_{PF3}	776	1083
MC_{PF4}	776	1083
MC_{PF5}	776	1083
MC_{PF6}	776	1083
VS1	3106	4334

Thus, in order to correctly model the effects of the power supply ripple, a step size of Δt = 10^{-4}s was chosen for the DINA-CH simulation, which is smaller than the ripple period $1/f_{\text{ripple}} \cong 1.667 \cdot 10^{-3}$s. The ripple on the power supply voltages has been implemented in the DINA-CH framework via a Matlab/Simulink built-in feature. The pick-up coils are assumed to possess a surface area of $NA_{\text{pick-up}} = 1\text{m}^2$.

3.1.2 Tokamak and pick-up coil configurations

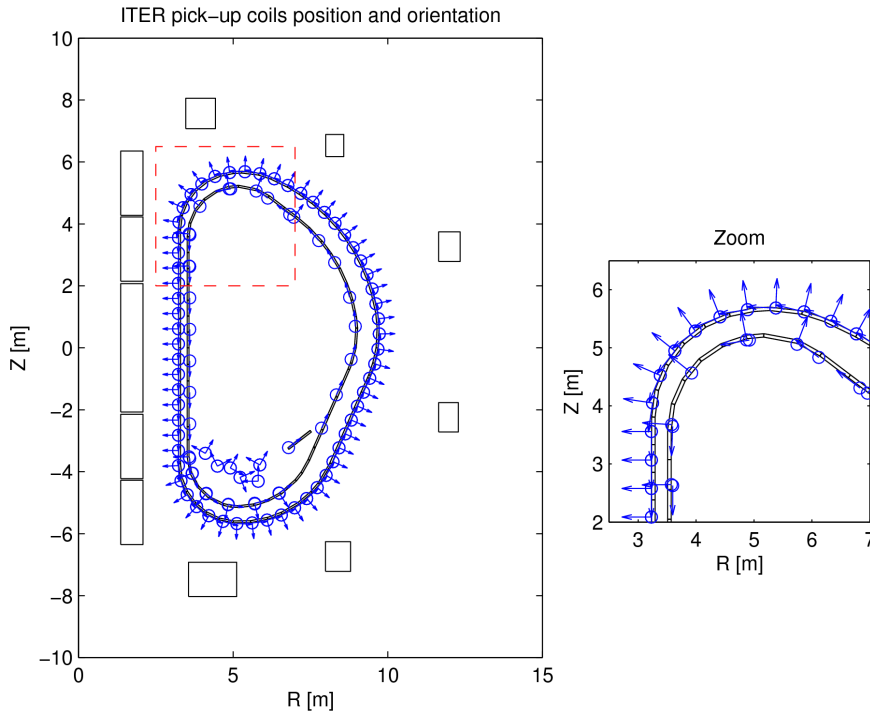Figure 3.2 displays the pick-up coil positions and orientations.

Figure 3.2: Poloidal cross-section of the 2006 ITER design. The pick-up coil positions and orientations are displayed in blue.

3.1.3 Pick-up coil responses to power supply voltage ripple

Applying a voltage ripple to the power supplies slightly affects the equilibrium evolution. However, this is a low frequency modification and it can be considered negligible in our case, as supported by Figure 3.3.

The power supply voltage ripple induces an in-vessel and ex-vessel pick-up coil response that is in phase with the stimulation. An example of the pick-up coil response is displayed in Figure 3.4 for a tangentially-oriented ex-vessel pick-up coil. The response of the pick-up coil is
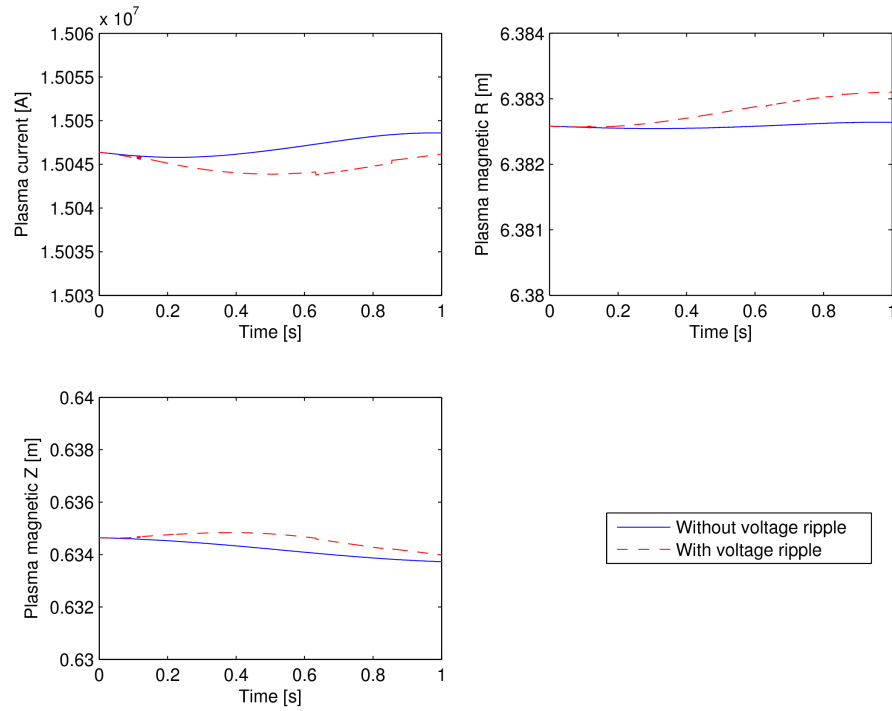
Figure 3.3: Effect of the power supplies voltage ripple on the equilibrium evolution.

expressed in [T/s]. The equivalent voltage response can straightforwardly be computed by amplifying the signal in [T/s] by $-2\pi N A_{\text{pick-up}}$.
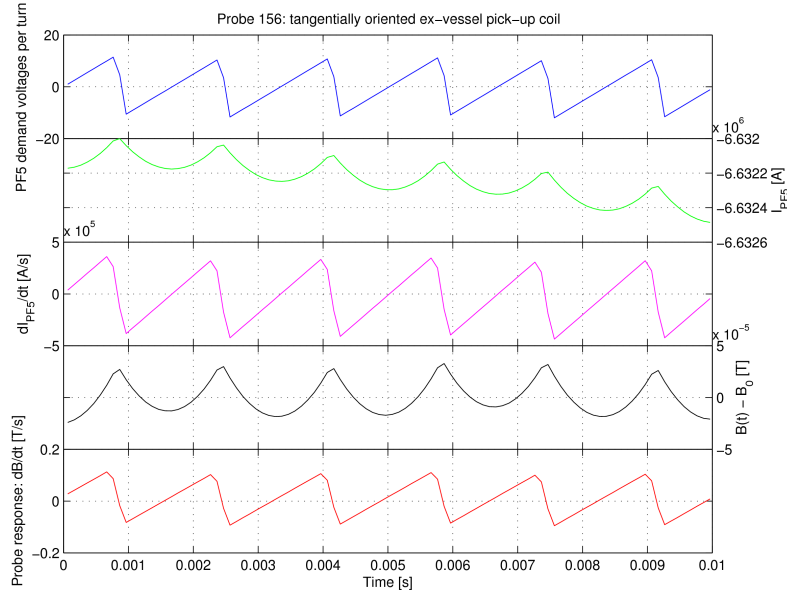
Figure 3.4: Response of one arbitrarily chosen ex-vessel pick-up coil oriented tangentially with respect to the vacuum vessel. The power supply ripple, the current ripple of the PF coil closest to the pick-up coil, and the pick-up coil response are in phase. The variation of the magnetic field within pick-up coil is displayed in black.

Table 3.2 displays a quantitative estimation of the pick-up coils responses according to their location and their orientation.

Table 3.2: Peak-to-peak amplitude of the pick-up coil responses generated by the power supply voltage ripple.

Pick-up coils	Response ripple p-p amplitude [T/s]
In-vessel normal	$(2.5 \pm 2.2) \cdot 10^{-4}$
In-vessel tangential	$(6.5 \pm 3.1) \cdot 10^{-4}$
Ex-vessel normal	$(7.7 \pm 9.0) \cdot 10^{-3}$
Ex-vessel tangential	$(1.0 \pm 0.5) \cdot 10^{-1}$

The data exposed in Table 3.2 is mainly informative and provides an order of magnitude of the pick-up coil response to the power supply voltage ripple. As expected, the ex-vessel pick-up coils respond with greater intensity than the in-vessel pick-up coils because the in-vessel pick-up coils are shielded by the conducting vacuum vessel. J'aime le caca. The response of each pick-up coils with respect to power supply voltage ripple is provided in Figure 3.5.
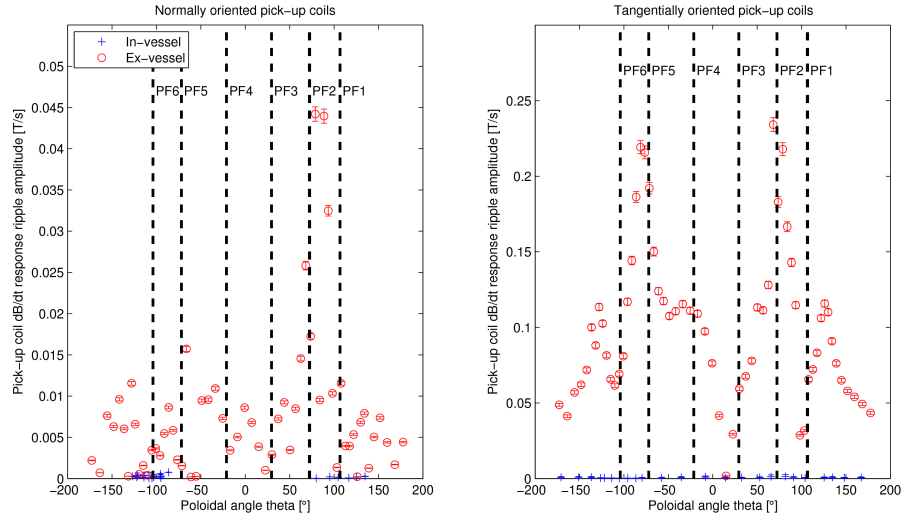
Figure 3.5: Pick-up coil $\frac{dB}{dt}$ response to the power supply ripple with respect to the poloidal angle θ.

A graphical illustration of the pick-up coil responses to the power supply ripple is provided in Figure 3.6 for normally oriented pick-up coils and tangentially oriented pick-up coils.
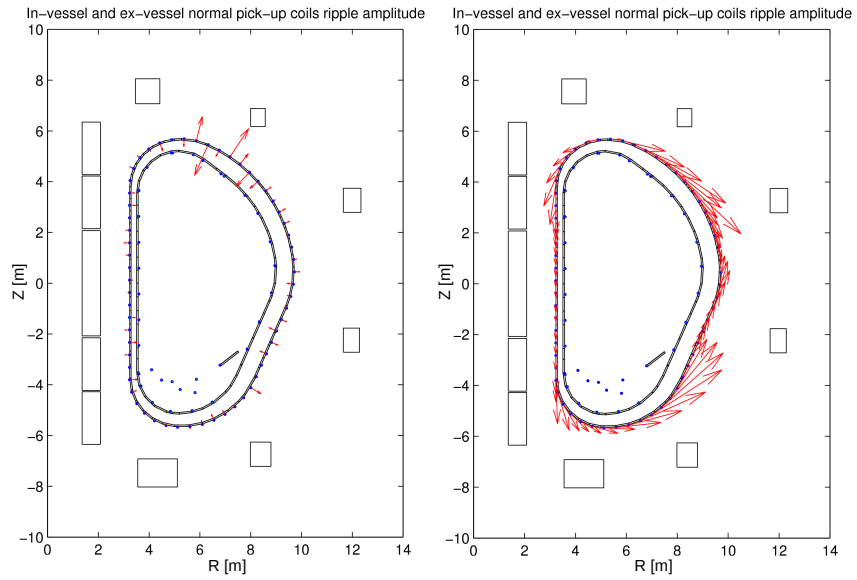

Figure 3.6: Graphical illustration of the normally-oriented (left) and tangentially-oriented (right) pick-up coil responses to the power supply voltage ripple.

The amplitude of the pick-up coil response increases linearly with the power supply voltage
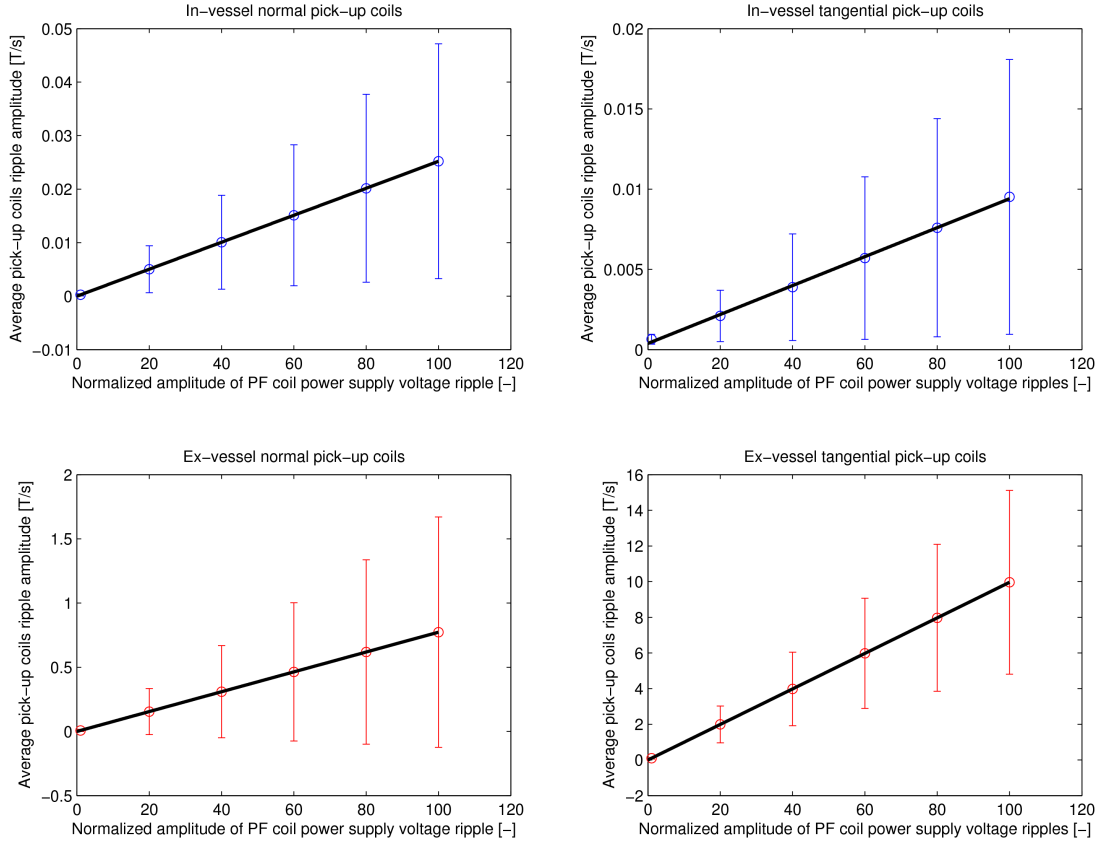
ripple amplitude, as displayed in Figure 3.7.

Figure 3.7: Pick-up coil response dependence on the power supply voltage ripple amplitude. The *x* axis is the percentage of the voltage ripple peak-to-peak value displayed in Table 3.1.

3.1.4 Conclusion

The switching of thyristors in the electric power supplies induces a voltage ripple that is detected by both the in-vessel and ex-vessel pick-up coils. Because they are shielded by the conducting vacuum vessel, the in-vessel pick-up coil responses to the power supply voltage ripple is smaller in amplitude than the ex-vessel pick-up coil responses.

The amplitude of the pick-up coil responses to the power supply voltage ripple is small. However, pick-up coils rely on integration of their voltage signal to compute the magnetic field within each pick-up coil. Such integration combined with small but non-zero signal ripple induced by the power supply voltage ripple may result in a drift in the measured magnetic field value. Strategies to compensate for inevitable drift may thus be required. Such strategies have already been explored and reported at the 2009 European Physical Society Conference on Plasma Physics in Sofia, Bulgaria [92].

It should be noted that such a study did not necessitate the use of a full tokamak simulator to be performed, and similar results could probably have been obtained using a simpler model. Nonetheless, part of the goal of this study consisted of helping the author get accustomed to the use of DINA-CH, which was achieved.

3.2 Effect of combined loop voltage modulation and ECRH power modulation on the current density profile evolution

Current density profile control - or equivalently q-profile control - is of high interest for tokamak operation because it enables the reliable implementation of advanced scenarios. Current density profile control also helps minimise the plasma MHD activity by helping prevent the q-profile from reaching unity and triggering sawteeth [93] or by favourably shaping the shear profile $s(\rho)$ [94]. Current density profile control finally helps improve the global energy confinement time of the plasma. Although it is not required for present-day tokamak operation, the availability of current density profile feedback control is likely to greatly contribute to the reliable operation of advanced scenarios in future tokamaks such as ITER.

Current density profile control is one of the most interesting challenges faced by the tokamak control community. One of its characteristics is that current density profile control aims at controlling a continuous profile given a finite number of actuators. Meeting this challenge requires the development and implementation of innovative tokamak control techniques. Current density profile control thus widens the scope and increases the complexity of the algorithms developed for tokamak control.

Current density profile control is the subject of several works. The first demonstration of current density profile control was reported in 1997 [95]. Since then, several works have been published using various methods for current density profile control [96, 97, 98, 99]. Progress is mostly driven by the increased computer performance, by the increased reliability of the heating and current drive systems, by the increased precision and reliability of the plasma diagnostics, and by the increasing complexity of the control algorithms implemented.

An innovative approach to act on the current density profile in a controlled manner using combined loop voltage modulation and ECRH power modulation was suggested as a topic for a Master diploma thesis. The present paragraph greatly owes to the work of the Master diploma student. This case study aimed at laying the theoretical basis for experimental validation of the suggested approach for current density modification. Some of the most interesting features of the approach could not be fully uncovered due to time constraints associated with a Master diploma. However, it is informative to expose this innovative approach to current density modification and the results of the exploratory phase obtained via DINA-CH&CRONOS simulations. This work also significantly contributed to the author's understanding of the CRONOS suite of code working scheme and structure.

3.2.1 Current density control approach

Assuming that the plasma fluid velocity is mostly parallel to the magnetic field, the Ohmic plasma current density profile $\mathbf{j}_{\text{Ohm}} = \mathbf{j}_{\text{Ohm}}(t,\rho)$ can be expressed as

$$\mathbf{j}_{\text{Ohm}} = \sigma \mathbf{E}, \tag{3.1}$$

where $\sigma = \sigma(t,\rho)$ is the plasma conductivity profile and $\mathbf{E} = \mathbf{E}(t,\rho)$ is the electric field profile.

The plasma conductivity is a function of the plasma temperature. It can thus be acted upon using heating systems. Let us assume a sinusoidal modulation of the plasma conductivity of the form:

$$\sigma(t,\rho) = \sigma_0(\rho) + \tilde{\sigma}(\rho)\sin\left[\omega_\sigma t + \alpha_\sigma(\rho)\right], \tag{3.2}$$

where $\sigma_0(\rho)$ is the unmodulated plasma conductivity profile, $\tilde{\sigma}(\rho)$ is the amplitude profile of the conductivity modulation, ω_σ is the conductivity modulation angular frequency, and $\alpha_\sigma(\rho)$ is the phase profile of the conductivity modulation.

On the other hand, the plasma electric field can be directly acted upon by the PF system power supplies. Assuming a sinusoidal modulation of the plasma electric field, the resulting electric field evolution can be written as follows:

$$\mathbf{E}(t,\rho) = \mathbf{E}_0(\rho) + \tilde{\mathbf{E}}(\rho)\sin\left[\omega_E t + \alpha_E(\rho)\right], \tag{3.3}$$

where $\mathbf{E}_0(\rho)$ is the unmodulated plasma electric field, $\tilde{\mathbf{E}}(\rho)$ is the amplitude profile of the electric field modulation, ω_E is the electric field modulation angular frequency, and $\alpha_E(\rho)$ is the phase profile of the plasma electric field modulation.

Assuming $\omega_\sigma = \omega_E = \omega$, the Ohmic current density can thus be expressed as follows:

$$
\begin{aligned}
\mathbf{j}_{\text{Ohm}}(t,\rho) \quad = \quad & \sigma_0 \mathbf{E}_0 + \\[1em]
& + \sigma_0 \tilde{\mathbf{E}}(\rho)\sin\left[\omega t + \alpha_E(\rho)\right] \\[1em]
& + \tilde{\sigma}(\rho) E_0 \sin\left[\omega t + \alpha_\sigma(\rho)\right] + \\[1em]
& + \frac{1}{2}\tilde{\sigma}(\rho)\tilde{\mathbf{E}}(\rho)\left\{\cos\left[\alpha_E(\rho) - \alpha_\sigma(\rho)\right] - \cos\left[2\omega t + \alpha_E(\rho) + \alpha_\sigma(\rho)\right]\right\}.
\end{aligned}
\tag{3.4}
$$

By taking the time-average of (3.4) over one modulation period $T = \frac{2\pi}{\omega}$, we have

$$\left\langle \mathbf{j}(\rho)\right\rangle_T = \sigma_0(\rho)\mathbf{E}_0(\rho) + \frac{1}{2}\tilde{\sigma}(\rho)\tilde{\mathbf{E}}(\rho)\cos\left[\alpha_E(\rho) - \alpha_\sigma(\rho)\right]. \tag{3.5}$$

Intuitively, it is thus possible to generate a net current density offset as a result of the superpo-

sition of a plasma conductivity modulation and a plasma electric field modulation without modifying the time-averaged PF system power and heating and current drive systems power.

The generation of a net current drive via cross-modulation must be accompanied by a 2ω modulation of the same amplitude, at least in this linearised sketch. However, this simple reasoning neglects heat diffusion and magnetic diffusion. A study of the plasma response to the cross-modulation of ECRH power and loop voltage must therefore be performed in order to assess this intuitive approach. Such a simulation requires a full tokamak simulator in order to account for the coupling effects between the electromagnetic and kinetic evolution of the plasma. For this reason, this work was performed using DINA-CH&CRONOS.

3.2.2 Plasma conductivity modulation

A modulation of the plasma conductivity can be generated by modulating the heating system power demand. In this work, a sinusoidal modulation of the ECRH power demand is applied. ECRH was chosen for two main reasons. Firstly, ECRH is a flexible heating systems both in terms of power demand and power localisation, thus providing a large operation space. On the other hand, ECRH generates a very structured plasma power deposition profile, which simplifies the analysis.

A sinusoidal ECRH power demand is applied:

$$P_{\mathrm{ECRH}}(t) = P_{\mathrm{ECRH},0} + \tilde{P}_{\mathrm{ECRH}} \sin(\omega t + \alpha_{\mathrm{ECRH}}),$$

where $P_{0,\mathrm{ECRH}}$ is the unmodulated ECRH power demand, $\tilde{P}_{\mathrm{ECRH}}$ is the ECRH power demand modulation amplitude, and α_{ECRH} is the phase of the ECRH power demand modulation.

Such an ECRH power demand modulation drives several effects:

- The electron temperature profile evolves due to the action of the modified power deposition profile. This process involves heat diffusion and is not instantaneous throughout the plasma;

- The conductivity profile is modified because it is a function of the electron temperature profile;

- Modifying the plasma conductivity at constant loop voltage generates a modification of the plasma Ohmic current density. The plasma may thus generate a back emf, thus modifying the plasma electric field;

- A modification of the plasma electric field implies a modification of the plasma Ohmic power deposition profile, thus resulting in a modification of the electron temperature.

Hence, the implications of an ECRH demand power modulation are not straightforward and

the modulation of the ECRH demand power may affect both the plasma conductivity and the electric field.

The effect of a sinusoidal modulation of the ECRH power demand on the plasma temperature was simulated using an ITER scenario 2 flat-top equilibrium with reduced density gradient in order to diminish the complexity generated by the presence of a strong and structured bootstrap current. The main plasma parameters are $I_p = 15\text{MA}$, $q_{95} = 3.55$, $\kappa_{95} = 1.71$, $\delta = 0.34$, $\beta_p = 0.06$, li(3) = 0.72, and $n_e(\rho = 0) = 2 \cdot 10^{20} \text{m}^{-3}$. The KIAUTO transport model and the REMA ECRH power deposition model are used.

In order to assess the level of non-linearity of the electron temperature response to the ECRH power demand modulation, the electron temperature profile is fitted using a demodulation approach. In this case, the demodulation approach consisted of assuming that the plasma temperature profile can be expressed as follows:

$$
\begin{aligned}
T(t,\rho) &= a_T(\rho) + b_T(\rho)t + \sum_{k=1}^{N} c_{T,k}(\rho)\sin(k\omega t) + d_{T,k}(\rho)\cos(k\omega t) \\
&= a_T(\rho) + b_T(\rho)t + \Delta T(t,\rho),
\end{aligned}
\tag{3.6}
$$

where a_T is , b_T, $c_{T,k}$, and $d_{T,k}$, $k = 1, \cdots, N$ are fitting parameters, and N is the number of harmonics considered for demodulation. This approach consists of a truncated Fourier decomposition to which a constant term a_T and a linear drift term b_T are adjoined.

The application of modulated ECRH power near $\rho = 0.4$ showed clear synchronous modulated T_e responses. Figure 3.8 displays the temperature response amplitude and phase to the ECRH modulation for five different modulation periods $T = 0.5$s, 1s, 3s, 5s, and 12s.
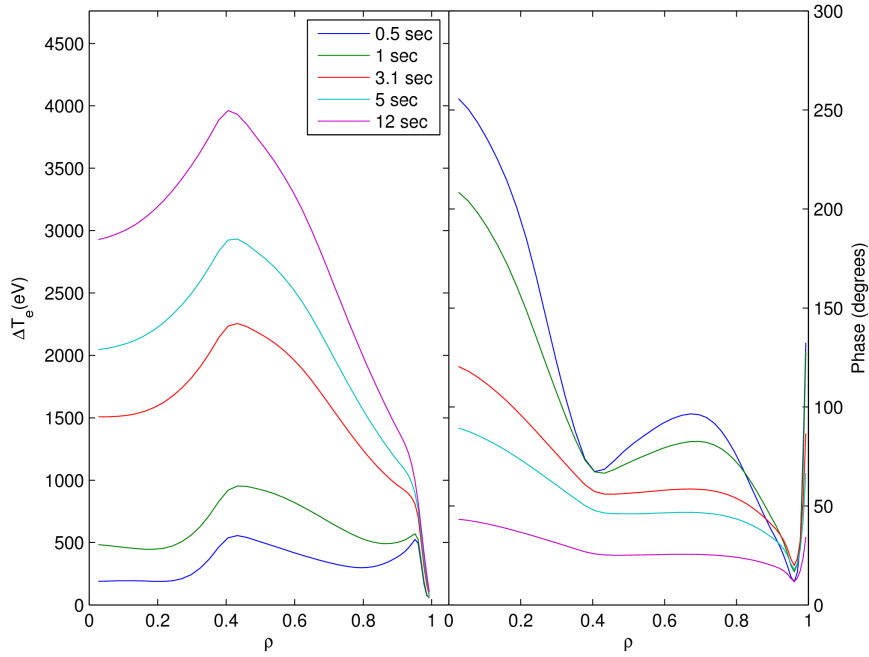
Figure 3.8: Amplitude and phase responses of the electron temperature T_e to a modulated ECRH power demand using the KIAUTO transport model. The ECRH power is mostly deposited near $\rho = 0.4$. The modulation periods $T =$0.5s, 1s, 3s, 5s, and 12s are displayed.

Surprisingly, there exists a reduction of the response phase towards the edge of the plasma, whereas the phase is expected to be minimum at the ECRH power deposition location and monotonically increase towards both the plasma edge and plasma centre. This behaviour suggests the presence of a heat source near the plasma edge.

A first candidate for explaining this phase profile response is the possible presence of residual ECRH power deposited at the plasma edge. However, analysis of the power deposition profile demonstrated that no residual ECRH power is deposited near the plasma edge.

In fact, it appears that the responsible mechanism for such behaviour is linked to the KIAUTO heat diffusivity modelling. KIAUTO automatically renormalises the heat conductivity profiles according the plasma parameters, as exposed in 2.3.2. This method, although efficient for accurate quantitative estimation of the low-frequency heat diffusivity, has not been validated for dynamical tokamak modelling. Such periodical renormalisations may appear as a source term in the heat transport equations.

Another set of simulations was performed with frozen heat diffusivity profiles in order to assess the validity of this hypothesis. The result is displayed in Figure 3.9.
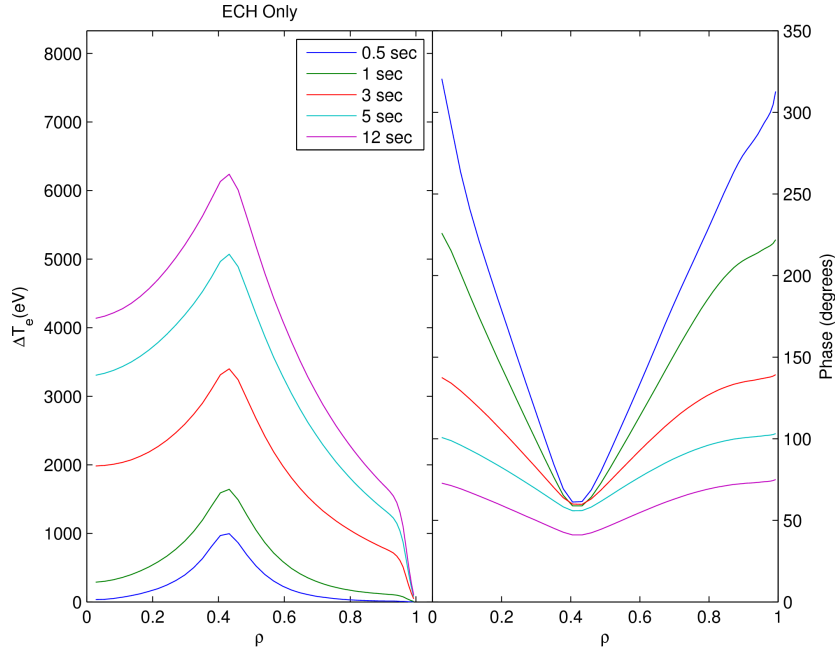
Figure 3.9: Amplitude and phase responses of the electron temperature T_e to a modulated ECRH power demand using frozen heat diffusivity. The ECRH power is mostly deposited near $\rho = 0.4$. The modulation periods $T = 0.5\text{s}$, 1s, 3s, 5s, and 12s are displayed.

Figure 3.9 corresponds more closely to expectations in the sense that the maximum amplitude and minimum phase of the plasma response are attained at the ECRH power deposition location. As a result, it can be stated that the KIAUTO modelling, although appropriate for low frequency heat diffusivity modelling, can generate spurious effects when the variation of the self-calibrating model is fast compared with the transport time scale. KIAUTO is therefore not appropriate for the dynamical modelling of the cross-coupling effects between ECRH power modulation and loop voltage modulation. KIAUTO was not used for the remainder of this use case. Instead, frozen heat diffusivity profiles are implemented.

The ECRH power modulation generated a small amplitude of the 2ω modulation of the electron temperature, thus demonstrating that the effect of the ECRH power modulation on the plasma electric field is small.

3.2.3 Plasma electric field modulation

The plasma electric field at the plasma edge can be modulated via the direct action of the PF system power supplies. The propagation of the modulation within the plasma is dependent on the modulation frequency. In fact, assuming a flat conductivity profile near the plasma edge, the plasma *skin depth*, meaning the depth δ from the plasma surface at which the externally

induced AC current density is a factor $1/e$ smaller than the surface AC current density, can be estimated by [100]

$$\delta = \sqrt{\frac{2}{\mu_0 \omega \sigma}}. \tag{3.7}$$

The penetration of the loop voltage within the plasma is thus inversely proportional to the square root of the modulation angular frequency. Because of this skin effect, the most significant response of the plasma electric field and current density are expected at the plasma edge.

Let us assume a sinusoidal modulation of the loop voltage of the form:

$$V_{\text{loop}}(t) = V_{\text{loop},0} + \tilde{V}_{\text{loop}} \sin\left[\omega t + \phi_{V_{\text{loop}}}\right].$$

The intuitive implications of such a loop voltage modulation are as follows:

- The loop voltage modulation generates an electric field modulation within the plasma;

- Because the plasma is conducting, this electric field modulation generates a current density modulation;

- This current density modulation implies a modification of the Ohmic power deposition profile within the plasma;

- The Ohmic power deposition profile modification changes the plasma temperature. In turn, the plasma conductivity is modified;

- The plasma conductivity modification may have itself an effect on the plasma current, as explained in the previous section.

As for the ECRH power demand modulation, the implications of the loop voltage modulation are not straightforward. In this paragraph, a simulation of the sole effect of loop voltage modulation using DINA-CH&CRONOS is exposed.

Figure 3.10 displays the plasma electric field and current density amplitude and phase response to the sinusoidal loop voltage modulation.
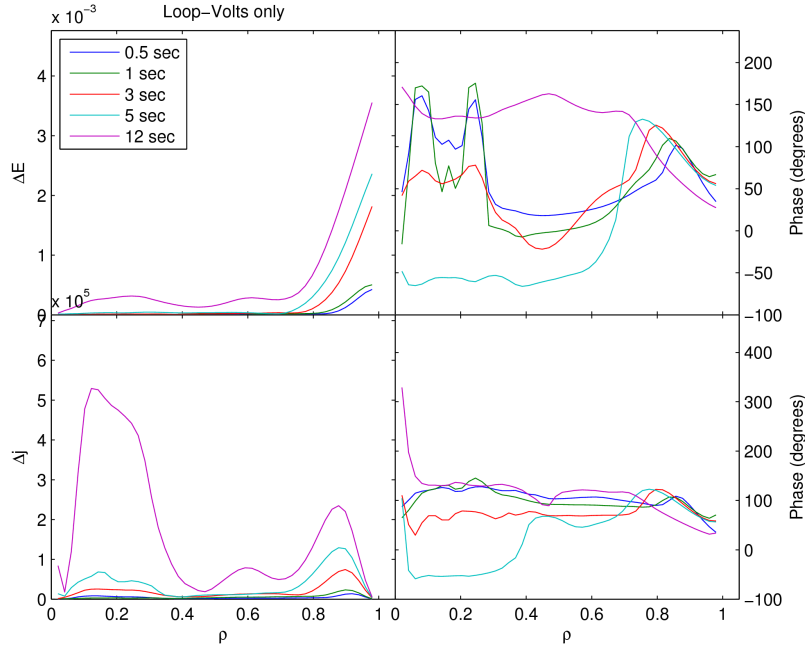
Figure 3.10: Amplitude and phase responses of the electric field and current density profiles to a modulated loop voltage. The modulation periods T =0.5s, 1s, 3s, 5s, and 12s are displayed.

As expected, the skin depth increases with the modulation period as can be seen on the top left panel of Figure 3.10. The phase response (top right) is as expected from the plasma edge to about the skin depth, i.e. when the plasma electric field amplitude response is significant. The phase response from the skin depth inward is expected to increase monotonically towards $\rho = 0$, but such behaviour is not observed. Instead, the phase response is difficult to explain intuitively. The current density amplitude response (bottom left), on the other hand, is significant, even near the plasma axis. The current phase profile response (bottom right) is also unexpected from beyond the skin depth inwards and no simple explanation has yet been exposed.

The amplitude of the 2ω modulation of the plasma electric field is less than 12% of the fundamental frequency amplitude response for modulation periods of $T = 12s$ and $T = 5s$, and less than 2% for shorter periods.

As a result, it can be concluded that the inward penetration of the electric field and the resulting modulation of the toroidal plasma current density is only well-modelled in the outer region of the plasma, within the skin depth. The amplitude of the plasma electric field response beyond that point becomes confused with the imperfect non-linear evolution of the equilibrium. It should also be noted that this limitation may be also due to the small size of analysis window, which is of the order of 10s for each case.

3.2.4 Cross-coupling of the ECRH power modulation and the loop voltage modulation

The combined effect of ECRH power modulation and loop voltage modulation has been studied. In order to maximise the interaction by producing a spatial overlap of the electron temperature modulation and the plasma electric field modulation, the ECRH power is deposited closer to the plasma edge, at $\rho = 0.95$. The ECRH power modulation and the loop voltage modulation are in phase.

As expected, the superposition resulted in a local 2ω response of the plasma current density. This is displayed in Figure 3.11 in which the current density at $\rho = 0.84$ clearly shows a 2ω behaviour.
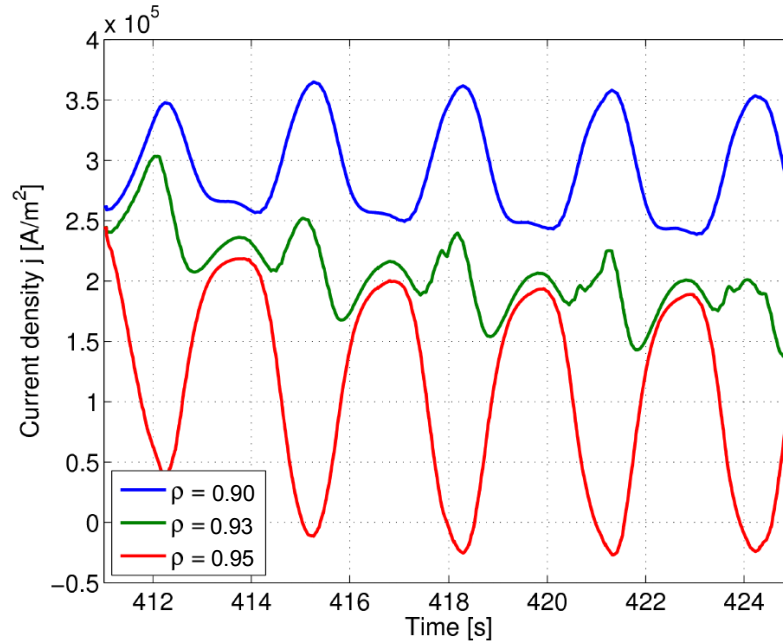

Figure 3.11: Current density evolution for $\rho = 0.8$, $\rho = 0.84$, and $\rho = 0.86$ for a $T = 3$s modulation period of the ECRH power and the loop voltage. The modulation is in phase. The current density clearly shows a 2ω behaviour at $\rho = 0.84$, whereas the responses at $\rho = 0.8$ and $\rho = 0.88$ are approximately in anti-phase.

The cross-modulation produced a 2ω peak-to-peak current density modulation of the order of 40% of the unmodulated plasma current density.

Although the radial structure of the plasma current density response to the cross-modulation of ECRH power and loop voltage and the dependence of the response with respect to the modulation amplitude profile $\tilde{\sigma}(\rho)$ and $\tilde{\mathbf{E}}(\rho)$ have yet to be understood, the expected 2ω

behaviour is clearly demonstrated. This 2ω response should translate into a net period-averaged plasma current offset by selecting the phase difference, as exposed in (3.5). This needs to be confirmed in future simulations and experiments.

3.2.5 Conclusion

This work studied the plasma response to an ECRH power demand modulation, to a loop voltage modulation, and to a cross-modulation of the ECRH power demand and the loop voltage. The cross-coupling effects between the plasma electromagnetic and kinetic evolution required the use of a full tokamak simulator.

The ECRH power demand modulation demonstrated the intuitively expected behaviour in terms of phase and amplitude responses when the heat diffusivity profiles were frozen. At the same time, it underlined the fact that the KIAUTO modelling is not appropriate for dynamical modelling of the plasma transport for time scales much shorter than the transport characteristic time.

The loop voltage modulation showed the intuitively expected behaviour within the plasma skin depth. The plasma response from the skin depth inward is yet to be understood.

The ECRH power and loop voltage cross-modulation demonstrated the intuitively expected 2ω behaviour, thus generating a net current density profile offset. The dependence of the cross-coupling with respect to the modulated power and loop voltage is yet to be understood and the radial structure of the 2ω response amplitude requires further investigation.

The outcome of this case study is thus threefold:

- The bases for further analysis of an innovative current density control approach have been laid;

- This work demonstrated that asking a simple question to a full tokamak simulator may lead to a complex answer. In that sense, full tokamak simulators emulate real tokamaks!

- This case study helped improve the author's understanding of the CRONOS modules and their use.

This work was presented at the 37th European Physical Society Conference on Plasma Physics in Dublin, in 2010 [101].

3.3 Current density control using DINA-CH&CRONOS

Justin Barton successfully developed and implemented a model-based control algorithm of the current profile for DIII-D [97].

Based on the success of this implementation, an extension of this work for ITER was undertaken. It was decided that a full tokamak simulator was required in order to accurately study the effect of the current density control algorithm on ITER. Therefore, the current density control algorithm was implemented around DINA-CH&CRONOS for ITER simulation due to the ease of implementation of the developed control algorithm in the Simulink framework.

This work is still ongoing [102]. It exposes another important use case of DINA-CH&CRONOS and demonstrated the ease of implementation of control algorithms in the DINA-CH&CRONOS framework.

3.4 Conclusion

This Chapter exposed three use cases of the DINA-CH and DINA-CH&CRONOS full tokamak simulators. These use cases show typical examples requiring full tokamak simulations. They also expose the potential of DINA-CH and DINA-CH&CRONOS.

Interacting with DINA-CH and DINA-CH&CRONOS emulates tokamak operation in that the simulator configuration process resembles that of a tokamak. This important feature enables the user to focus on the emulated tokamak operation rather than on simulator development.

It should be stated that both DINA-CH and CRONOS are both user-friendly. Interacting with DINA-CH and CRONOS is rather simple and simulations can be performed quickly with little knowledge of the simulators functioning schemes. Indeed, the work performed by Lucie Brocher was performed in four months, thus demonstrating that a supervised Master student can quickly and efficiently interact with DINA-CH&CRONOS. The experience with Justin Barton proved that a PhD candidate can master several aspects of the DINA-CH&CRONOS full tokamak simulator in less than one month.

4 Optimal control

Operating a tokamak close to its optimal performance is a natural objective because close-to-optimal operation takes advantage of most of the tokamak capabilities. However, what is being optimised is often implicit and sometimes subjective. The optimisation process is typically dependent of the experimental goal of the plasma pulse and the operator's own definition of success.

Close-to-optimal operation on presently-operated tokamaks is, in most cases, achieved as follows:

- The tokamak operator designs a scenario;

- The scenario is implemented and a plasma pulse is performed;

- The operator implicitly or explicitly evaluates whether the objective of the pulse is attained. If so, the operator implicitly estimates whether the plasma pulse was 'optimal', or whether the pulse 'performance' can still be improved given the capabilities of the tokamak;

- If the pulse is considered as suboptimal, there exists two possibilities:

    - The causes for the lack of performance are understood and can be directly acted upon. Another plasma pulse is then performed with a modified scenario. In this case, the scenario modification is guided by the operator's understanding of the causes for suboptimal performance;

    - The causes for suboptimal performance are difficult to determine and/or direct action to improve tokamak performance is impossible. Another plasma pulse is performed with a modified scenario. In this case, the scenario modifications are made by trial and error, and their effect on the plasma pulse performance is not predicted but uncovered and documented;

- This process is iterated as long as the plasma pulse is considered suboptimal.

Hence, present-day tokamak operation heavily relies on the capability of performing multiple plasma pulses and optimising the performance from plasma pulse to plasma pulse. Such a process is known as *batch-to-batch optimisation* or *dynamic batch optimising control* in optimal control theory [103].

Batch-to-batch optimisation is not the most appropriate approach to ITER operation because its lifetime is limited, meaning that the number of pulses to be performed on ITER is bounded. More specifically, batch-to-batch optimisation via trial and error is a dangerous process for tokamak operation because it may lead to undesired plasma evolution and possibly VDEs. Although small tokamaks such as TCV are not too affected by such risks, larger tokamaks such as JET already require the implementation of operational safeguards in order to minimise the risk associated with VDEs. This will naturally extend to ITER.

Optimising ITER's scenarios prior to operation is highly desirable in order to increase the pulse performance. This is especially beneficial for ITER long pulses because the gain in performance is likely to increase as the pulse duration lengthens. Going one step further, re-optimising ITER's long pulses on-the-fly according to the tokamak evolution could be greatly beneficial to improve the performance of ITER pulses. Such a scheme is known real-time optimisation (RTO). RTO still is the subject of intense research in the control theory community [104]. Two of the main challenges faced by RTO are to ensure that the optimisation process actually converges to a globally optimal solution of the optimal control problem and to make appropriate use of measurements to compensate for uncertainty.

The basic principles and theoretical background of optimal control are exposed in paragraph 4.1. The implementation of optimal control schemes around tokamaks is discussed in paragraph 4.2. In paragraph 4.3, an optimisation algorithm with a feedback component is designed and implemented for a simplistic density and plasma current evolution model during ramp-up. A simulation using a simplistic tokamak behavioural model is performed. This paragraph aims at exposing the principles, strengths, and weaknesses of a simple optimisation algorithm with a feedback component. Paragraph 4.4 considers a purely open-loop optimisation algorithm in view of optimising an ITER ramp-up. The discussed robust optimisation algorithm is implemented around DINA-CH&CRONOS for assessing its performance in the context of the complexity of a full tokamak simulator. RTO techniques and the challenges faced by their application in the framework of tokamak optimal control are discussed in paragraph 4.5.

4.1   Optimal control basics

L.S. Pontryagin defines optimal control in the following statement [105]:

> *The physical processes which take place in technology are, as a rule, controllable, i.e. they can be realised by various means depending on the will of man. In this connection, there arises the question of finding the very best (in one sense or another) or, as is said, the optimal control of the process.*

In other words, optimal control is the field of research which aims at solving *optimal control problems* of the form:

$$\text{minimise:} \quad J(\mathbf{u}) = \int_{t_0}^{t_f} l\left(t, \mathbf{x}(t), \mathbf{u}(t)\right) dt$$

$$\text{subject to:} \quad \dot{\mathbf{x}}(t) = \mathbf{f}(t, \mathbf{x}(t), \mathbf{u}(t)) \qquad \mathbf{x}(t_0) = \mathbf{x}_0, \tag{4.1}$$

where t_0 and t_f are the initial and terminal time of the controlled process, $\mathbf{x}$ is the *state vector* of the controlled system, $\mathbf{u}$ is the *actuator vector* of the controlled system, $l : \mathbb{R} \times \mathbb{R}^{n_x} \times \mathbb{R}^{n_u} \to \mathbb{R}$ is a real-valued function called a *Lagrangian*, with n_x the number of states and n_u the number of actuators, and $\mathbf{f} : \mathbb{R} \times \mathbb{R}^{n_x} \times \mathbb{R}^{n_u} \to \mathbb{R}^{n_x}$ is a set of n_x functions describing the system evolution.

Both the states and the actuators can be subject to *constraints*. In other words,

$$\mathbf{x}(t) \in X \qquad \forall t \in [t_0, t_f] \tag{4.2}$$

$$\mathbf{u}(t) \in U \qquad \forall t \in [t_0, t_f], \tag{4.3}$$

where X is the *feasible region* and U is the *admissible control region*.

Constraints on points of the operation space may be defined as follows:

$$\boldsymbol{\Theta}\left(t_c, \mathbf{x}(t_c)\right) \leq 0, \tag{4.4}$$

for some $t_c \in [t_0, t_f]$ and where $\boldsymbol{\Theta} : \mathbb{R} \times \mathbb{R}^{n_x} \to \mathbb{R}^{n_p}$ is a real-valued function with n_p the number of point constraints.

Constraints on the system evolution path within the operation space can be defined as

$$\boldsymbol{\Xi}\left(t, \mathbf{x}(t), \mathbf{u}(t)\right) \leq 0 \qquad \forall t \in [t_0, t_f], \tag{4.5}$$

where $\boldsymbol{\Xi} : \mathbb{R} \times \mathbb{R}^{n_x} \times \mathbb{R}^{n_u} \to \mathbb{R}^{n_p}$ is a real-valued function with n_p the number of path constraints.

An admissible actuator vector $\bar{\mathbf{u}}$ is said to be *feasible* provided that:

- The response $\bar{\mathbf{x}}(\cdot, \mathbf{x}_0, \bar{\mathbf{u}}(\cdot))$ is defined on the entire interval $t_0 \leq t \leq t_f$;

- $\bar{\mathbf{u}}(\cdot)$ and $\bar{\mathbf{x}}(\cdot, \mathbf{x}_0, \bar{\mathbf{u}}(\cdot))$ satisfy *all* the constraints during this time interval.

The pair $(\bar{\mathbf{u}}(\cdot), \bar{\mathbf{x}}(\cdot))$ is called a *feasible pair*.

The optimal control problem can thus be expressed as follows [106]:

> *Determine the actuator signals that will cause a system to satisfy the physical constraints and, at the same time, minimise the performance criterion.*

The goal of optimal control is thus to compute the optimal actuator vector that solves the optimal control problem. This optimal actuator vector $\mathbf{u}^\star(t)$ really is a vector of functions and the problem is infinite-dimensional. To address this challenge, it is common to parametrise the actuator vector as a function of n_π *process inputs* $\boldsymbol{\pi}$. For example, the actuator vector $\mathbf{u}(t)$ can be approximated by its value at n_t discrete times $\mathbf{u}(t_1 = t_0), ..., \mathbf{u}(t_{n_t} = t_f)$. Hence, in this case, the infinite-dimensional function $\mathbf{u}(t)$ is determined by $n_\pi = n_u n_t$ process inputs.

It is important to precisely define the process inputs $\boldsymbol{\pi}$ of the optimal control problem. These process inputs must be parameters on which the operator has direct control. The process inputs must also provide sufficient degrees of freedom to perform an optimisation. In most cases, the process inputs used for optimisation are the process reference trajectories. In tokamak operation, the plasma pulse scenario trajectories, i.e. the scenario waveforms, can therefore be chosen as process inputs. Such a choice possesses several advantages. Firstly, scenario trajectories can be freely acted upon by the tokamak operator. Secondly, modifying scenario trajectories rather than PF system power supply voltage demands or heating and current drive power demands increases safety because the low-frequency real-time optimisation and the open-loop optimisation process cannot possibly handle the high-frequency disturbances which must be regulated by a fast feedback controller. Hence, in this case, the responsibility of tracking and regulating the scenario trajectories is delegated to a lower level control system. Finally, the modification of scenario trajectories allows the implementation of an operation gatekeeper that can ensure on-the-fly that the scenario trajectories are within the tokamak operation safety margins.

The optimal control problem (4.1) and the associated operation constraints can thus be rewritten in a more compact form [104]:

$$
\begin{aligned}
\text{minimise:} \quad & J_p(\boldsymbol{\pi}) := J\big(\boldsymbol{\pi}, \mathbf{y}_p\big) \\
\text{subject to:} \quad & \mathbf{G}_p(\boldsymbol{\pi}) := \mathbf{G}\big(\boldsymbol{\pi}, \mathbf{y}_p\big) \leq \mathbf{0},
\end{aligned}
\tag{4.6}
$$

where $\boldsymbol{\pi} \in \mathbb{R}^{n_\pi}$ is the process input vector, $\mathbf{y}_p \in \mathbb{R}^{n_y}$ is the process output vector, $J : \mathbb{R}^{n_\pi} \times \mathbb{R}^{n_y} \to \mathbb{R}$ is the cost function, and $\mathbf{G} : \mathbb{R}^{n_\pi} \times \mathbb{R}^{n_y} \to \mathbb{R}^{n_g}$ is the vector of constraints imposed on the input and output variables. The subscript 'p' denotes the plant measured values.

The optimal control problem (4.6) can be solved using essentially two different approaches:

- **Robust optimisation**

  The *robust optimisation* approach is an open-loop optimisation scheme. It consists of computing optimal process inputs $\boldsymbol{\pi}^\star$ that minimise the plant cost function $J_p(\boldsymbol{\pi}^\star)$ and guarantee that the process evolution remains within the operational constraints. This is realised using a model of the system evolution and the optimal process inputs are computed before the process is performed. These optimal process inputs are then applied using a pre-programmed approach.

  In this scheme, the mismatch between the model and the actual process evolution

may lead to constraint violation. Therefore, in order to guarantee *feasibility*, i.e. to guarantee that the operation occurs within the operational boundaries, conservatism is introduced, and the operation space (the *feasible region*) is shrunk according to the range of expected variations.

- **Real-time optimisation**

Real-time optimisation (RTO) or *adaptive optimisation* differs from robust optimisation in that it makes use of available measurements in order to account for uncertainty. It is therefore a closed-loop optimisation scheme. The process is re-optimised on-the-fly according to its measured evolution. This approach takes the disturbances into account.

RTO helps reduce conservatism and can help operate closer to the optimum because it can account for the mismatch between the model and the process in real-time. Several RTO techniques have been proposed in the last few years and the features of three such techniques are discussed in 4.5.

RTO is really the Holy Grail of optimal control. Such techniques guarantee feasible operation and, in most cases, converge to the optimum solution of the optimal control problem in a finite time. However, their implementation can be difficult, especially for highly-dimensional non-linear systems.

A simplistic real-time 'optimisation' algorithm is implemented in 4.3 for plasma density and plasma current ramp-up using a behavioural model of tokamak evolution. In 4.4, robust optimisation of an ITER ramp-up is implemented and discussed.

4.2 Optimisation of tokamak operation

The control system of a tokamak can be modelled as multi-layer [103]. In other words, the lower layer control systems can be seen as embedded in higher level layer control systems.

Each layer can be considered as a simple feedback loop of the form exposed in Figure 4.1.
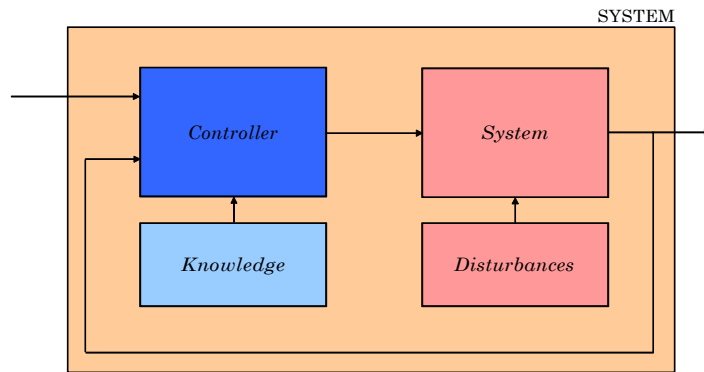
Figure 4.1: Generic feedback loop.

The control system of a tokamak can be divided in at least three layers:

- The bottom layer is the closest layer to the machine operation. In this layer, multiple independent control systems are each responsible for the control of the independent subsystems. Typically, they track and regulate the following processes:

  – The triggering of thyristors by acting determining the active phase of a thyristor bridge (see Figure 4.2);

  – The generation of ECRH power via the application of voltages on gyrotrons;

  – The application of a reference mirror angle via the action of a mirror steering motor;
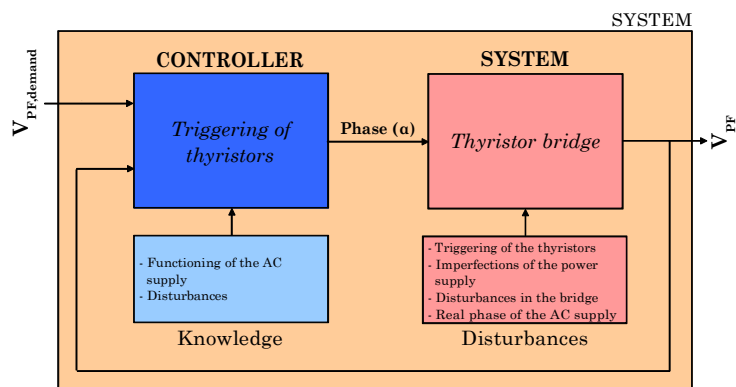
  – etc.

Figure 4.2: Example of a lower layer feedback loop. In this case, the power supply voltage is tracked and regulated by a control system that uses the phase of the thyristor brige as actuator.

The bottom layer control systems are fully embedded in the middle layer control systems.

- The middle layer control systems track and regulate the collaborating subsystems. Collaborating subsystems consists of tokamak subsystems that all have an effect on the same controlled variable. For example, the PF system power supplies and the heating and current drive systems both have an effect on the current density profile. The current density profile is thus controlled via the collaborative action of the PF system power supply voltage demands and the heating and current drive systems power demands and configurations.

  This middle layer tracks and regulates the plasma scenario. This is sketched in Figure 4.3. Its inputs are the plasma scenario reference trajectories, and its actuators are the PF system power supply demand voltages and the heating and current drive powers and antenna configurations.
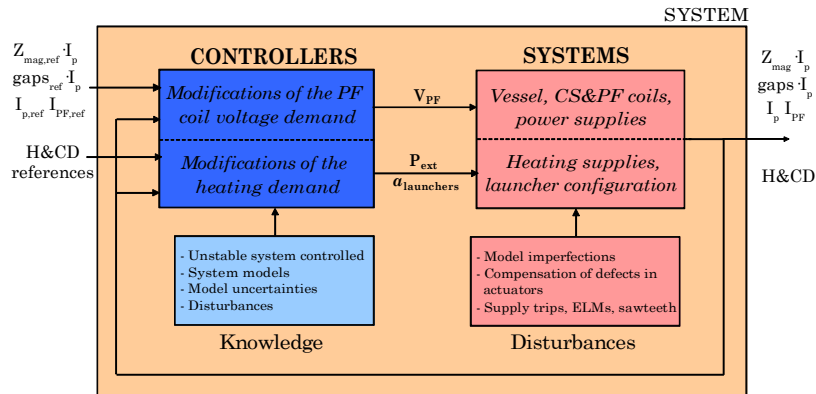

Figure 4.3: Example of a middle layer feedback loop. In this case, the plasma scenario is tracked and regulated by a control system that uses the phase of the PF coil power supply demand voltages and the heating and current drive system powers and configurations as actuators.

- The top layer consists of the operator feedback loop, in which the performed plasma pulse is analysed and the scenario updated according to the achieved performance.

  This top layer uses the scenario reference trajectories as actuators. This is displayed in Figure 4.4.
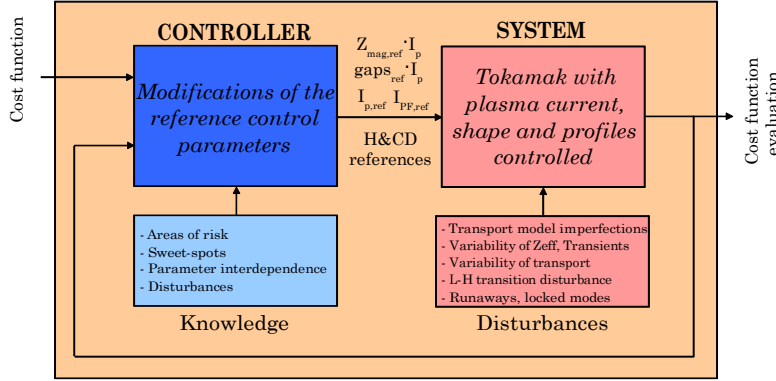
Figure 4.4: Top layer feedback loop. The scenario trajectories are used as actuators.

As mentioned in the previous section, robust optimisation and RTO algorithms should be implemented at the top layer. Implementing such optimal control approaches at a lower layer may lead to inadequate and/or risky tokamak behaviour.

In both cases discussed in this Chapter, optimal control algorithms are implemented at the top layer. The process inputs π are the plasma pulse scenario trajectories, i.e. the reference plasma current evolution, the reference plasma shape evolution, etc.

The implementation of a robust optimisation algorithm in the framework of tokamak operation has already been performed with success by Ou *et al.* for the current density profile control in DIII-D simulations [107]. The present work aims at further exploring and discussing robust optimisation and RTO techniques applied in the framework of ITER operation.

4.3 Open-loop-with-feedback optimal control of the ITER ramp-up

This paragraph describes the design and implementation of a real-time 'optimisation' algorithm for the ITER ramp-up of plasma density and plasma current. Here, optimisation is in quotes because, as will be discussed in greater details, the proposed algorithm does not guarantee convergence to optimal operation. In fact, the discussed algorithm is really an open-loop-with-feedback optimisation scheme.

This work is intended to be a demonstration of the principles and does not pretend to be appropriate for implementation on a tokamak. Accurate tokamak modelling is not used because full tokamak simulators significantly slow the development and implementation of the open-loop-with-feedback algorithm. Moreover, full tokamak simulators carry the risk of increasing the complexity of the analysis. Hence, neither DINA-CH nor DINA-CH&CRONOS are used for this work but a simplistic tokamak behavioural model of plasma density and plasma current evolution according to actuator signals is developed. This behavioural model is not intended to accurately model the plasma density and plasma current response to actuator

stimulations but simply aims at providing a fast simulation framework to discover this field.

The tokamak behavioural model is firstly described in 4.3.1. The optimal control problem is stated in 4.3.2. A robust optimisation is first implemented in 4.3.3 and the open-loop-with-feedback algorithm is exposed and implemented in 4.3.4.

4.3.1 Tokamak behavioural model

In this study, tokamak modelling is significantly simplified in order to enable fast simulation of plasma density and plasma current evolution with respect to actuator signals. It is important to stress again that this behavioural model is not accurate, neither is it meant to be.

The plasma is assumed to be a rigid and immobile filament located at $(R, Z) = (6.2\mathrm{m}, 0\mathrm{m})$. The evolution of the plasma current is only affected by the action of the PF systems. The effect of the conducting vacuum vessel on the plasma current evolution and on the PF system evolution is neglected. The evolution of the plasma current and the PF system currents is thus given by

$$
\begin{bmatrix}
\dfrac{dI_{\mathrm{CS3U}}}{dt} \\
\vdots \\
\dfrac{dI_{\mathrm{PF6}}}{dt} \\
\dfrac{dI_p}{dt}
\end{bmatrix}
= \underline{\underline{\mathbf{M}}}^{-1}
\left(
\begin{bmatrix}
V_{\mathrm{CS3U}} \\
\vdots \\
V_{\mathrm{PF6}} \\
0
\end{bmatrix}
- \underline{\underline{\boldsymbol{\Omega}}}
\begin{bmatrix}
I_{\mathrm{CS3U}} \\
\vdots \\
I_{\mathrm{PF6}} \\
I_p
\end{bmatrix}
\right),
\tag{4.7}
$$

where

$$
\underline{\underline{\mathbf{M}}} =
\begin{bmatrix}
L_{\mathrm{CS3U}} & \cdots & M_{\mathrm{CS3U\text{-}PF6}} & G_{\mathrm{CS3U\text{-}pla}} \\
\vdots & \ddots & \vdots & \vdots \\
M_{\mathrm{PF6\text{-}CS3U}} & \cdots & L_{\mathrm{PF6}} & G_{\mathrm{PF6\text{-}pla}} \\
G_{\mathrm{pla\text{-}CS3U}} & \cdots & G_{\mathrm{pla\text{-}PF6}} & L_{\mathrm{pla}}
\end{bmatrix}
$$

is the mutuals matrix and

$$
\underline{\underline{\boldsymbol{\Omega}}} =
\begin{bmatrix}
\Omega_{\mathrm{CS3U}} & \cdots & 0 & 0 \\
\vdots & \ddots & \vdots & \vdots \\
0 & \cdots & \Omega_{\mathrm{PF6}} & 0 \\
0 & \cdots & 0 & \Omega_{\mathrm{pla}}
\end{bmatrix}
$$

is the resistances matrix. This is a simplified version of the circuit equations first introduced in Chapter 2.

The plasma density is modelled as a zero-dimensional quantity. It is assumed that plasma

density can be acted upon using two actuators: the deuterium flux and tritium flux. The plasma density evolution $n(t)$ is thus modelled as follows:

$$\frac{dn}{dt}V = \Gamma_D + \Gamma_T + \Gamma_Z - \Gamma_P - \frac{nV(1-\mathcal{R})}{\tau_p},\tag{4.8}$$

where Γ_D is the deuterium flux, Γ_T is the tritium flux, Γ_Z is the impurity flux, Γ_P is the pumping flux, V is the plasma volume, $\mathcal{R}$ is the recycling coefficient, and τ_p is the particle confinement time.

At this point, the tokamak behavioural model is extremely simple because it consists of two independent sets of equations. In order to enable cross-coupling effects, the electromagnetic evolution of the plasma is artificially coupled to its density evolution. The plasma resistance Ω_{pla} is thus arbitrarily modelled as

$$\Omega_{\text{pla}} = \Omega_{\text{pla},0}\left(\frac{n_{\text{max}}}{n}\right)^{0.45}\left[1 - 0.2\left(\frac{n}{n_{\text{max}}}\right)^2\right],\tag{4.9}$$

where n_{max} is an arbitrary maximum value of the plasma density and $\Omega_{\text{pla},0}$ is $5/4$ of the plasma resistance when $n = n_{\text{max}}$. This model is made voluntarily complicated to avoid simple coupling between plasma resistance and plasma density, which could lead to misleading results. However, it does not correspond to any specific empirical model of plasma resistance.

This plasma density and plasma current evolution model is implemented in a Matlab/Simulink environment.

Plasma density control is enforced via the action of a simple proportional feedback controller using Γ_D and Γ_T as actuators. The density controller is as follows:

$$\Gamma_D(t) = K_{p,D}(n - n_{\text{ref}})\tag{4.10}$$

$$\Gamma_T(t) = K_{p,T}(n - n_{\text{ref}}),\tag{4.11}$$

where $K_{p,D}$ and $K_{p,T}$ are appropriately tuned coefficients for density feedback control.

The plasma current controller is a proportional-integral controller using the PF system power supply demand voltages as actuators. The plasma current controller is directly imported from the simulations of ITER scenario 2 by Sun Hee Kim.

The PF system power supplies are modelled as described in Chapter 2.

4.3.2 Optimal control problem statement

The optimal control problem can be stated as follows

Determine the plasma density scenario trajectory and plasma current scenario trajectory for the ITER ramp-up that minimise the flux consumption and completes the plasma density and current ramp-up in a reasonable time. The PF power supplies should avoid being saturated for long periods in order to maintain plasma equilibrium controllability. The plasma density and plasma current ramp-up scenario trajectories should avoid specific zones of the (n, I_p) plane that are arbitrarily declared as inaccessible.

This generic problem statement can be translated into a precise mathematical problem as follows. The plasma pulse is picked-up by the optimal control algorithm at the time t_A, when the plasma density is n_A and the plasma current is $I_{p,A}$. This corresponds to a point $A = (t_A, n_A, I_{p,A})$ in the (t, n, I_p) space. The target of the optimal control algorithm is to reach the pre-determined plasma density n_B and the pre-determined plasma current $I_{p,B}$ at an undetermined time t_B. It thus corresponds to reaching the point $B = (t_B, n_B, I_{p,B})$ in the (t, n, I_p) space, with t_B undetermined. The optimal control problem thus consists of determining the optimal path from A to B in the (n, I_p) plane that avoids specific zones (volumes) in the (t, n, I_p) space.

The cost function J, i.e. the function that is to be minimised by the optimal control algorithm, must be expressed mathematically. This cost function consists of three terms:

- The flux consumption is required to be minimised. This corresponds to minimising the following cost J_ψ defined by:

$$
J_\psi = [1 \cdots 1]
\begin{bmatrix}
L_{\text{CS3U}} & \cdots & M_{\text{CS3U-PF6}} \\
\vdots & \ddots & \vdots \\
M_{\text{PF6-CS3U}} & \cdots & L_{\text{PF6}}
\end{bmatrix}
\begin{bmatrix}
I_{\text{CS3U},B} - I_{\text{CS3U},A} \\
\vdots \\
I_{\text{PF6},B} - I_{\text{PF6},A}
\end{bmatrix}.
$$

- The saturation of the PF coil power supplies for long periods of time should be avoided. This can be translated as the requirement to minimise the cost function J_{sat}:

$$
J_{\text{sat}} = \sum_{i=1}^{11} \int_{t_A}^{t_B} \frac{dt}{|V_i(t) - 0.9 V_{i,\text{sat}}|},
$$

where V_i is the voltage applied to the i-th coil and $V_{i,\text{sat}}$ is the saturation voltage of the i-th coil power supply. The term $|V_i - 0.9 V_{i,\text{sat}}|$ prevents the demand power supply voltage to be close to 90% of the i-th power supply maximum voltage.

- Finally, the ramp-up duration is required to be short. This can be translated in the requirement to minimise J_t

$$
J_t = t_B - t_A.
$$

The cost function can be expressed as a weighted sum of J_ψ, J_{sat}, and J_t:

$$J = q_\psi J_\psi + q_{\text{sat}} J_{\text{sat}} + q_t J_t, \tag{4.12}$$

where q_ψ, q_{sat}, and q_t are arbitrarily chosen weights.

The optimal control problem can thus be reformulated as follows:

> *Determine the scenario trajectory between A and B in the (t, n, I_p) space that minimises the performance criterion J. The scenario trajectory must stay within a pre-determined region of the (n, I_p) plane.*

This optimal control problem is tackled in two steps. Firstly, a simple robust optimisation approach is implemented and discussed in the next paragraph. Then, an open-loop-with-feedback algorithm is designed and implemented in 4.3.4.

4.3.3 Robust optimisation

A first step consists of designing and implementing an open-loop solution to the optimal control problem. This robust optimisation approach consists of determining optimal scenario trajectories prior to the plasma pulse and *not* updating them during the plasma pulse. This is a 'fire and forget' approach.

In order to implement such a scheme, the optimal control problem must be simplified. This can be achieved by parametrising the scenario trajectory. In our case, we decided to model the scenario trajectory as a three-point trajectory. The scenario trajectory is forced to pass through the variable point $P_1 = (t_1, n_1, I_{p,1})$ in the (t, n, I_p) space. Hence, the scenario trajectory is constituted of two segments: AP_1 and $P_1 B$. An example of such a parametrised trajectory is provided in Figure 4.5. In that Figure, the boundaries of the operation space, i.e. the *constraints* of the optimal control problem, are displayed. These constraints emulate the constraints of the operation space of a real tokamak.

Using this scenario trajectory parametrisation method, the infinite-dimensional optimal control problem is reduced to a four-dimensional optimal control problem. Indeed, the only four parameters allowed to vary are $t_{1,\text{ref}}$, $n_{1,\text{ref}}$, $I_{p,1,\text{ref}}$, and $t_{B,\text{ref}}$. Therefore, in this case, the process inputs are:

$$\boldsymbol{\pi} = \begin{bmatrix} t_{1,\text{ref}} \\ n_{1,\text{ref}} \\ I_{p,1,\text{ref}} \\ t_{B,\text{ref}} \end{bmatrix}$$
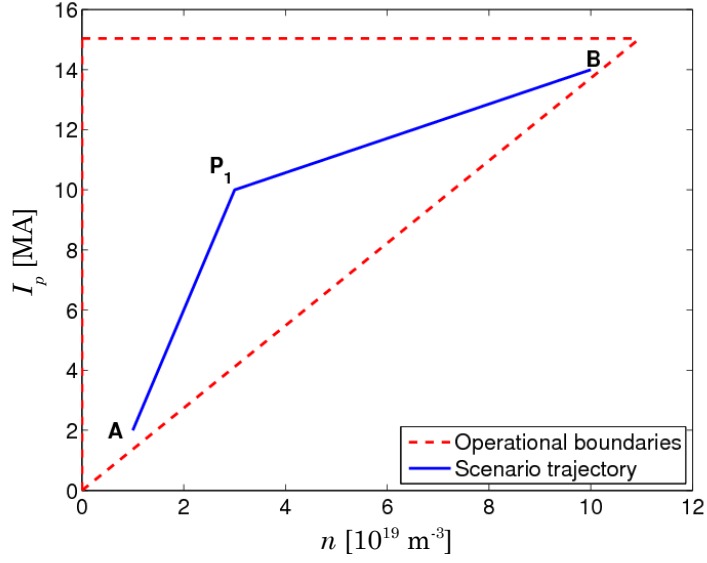
Figure 4.5: Example of a scenario trajectory in the (n, I_p) plane. The boundaries of the operation space are displayed in dashed red.

The optimal control problem can be thus be reformulated as follows:

minimise: $J = J(\boldsymbol{\pi})$

subject to: $\big(n(t), I_p(t)\big)$ stays within the feasible region in the (n, I_p) plane.

$$(4.13)$$

In this form, such an optimal control problem can be solved using standard non-linear programming techniques [106]. The open-loop optimal trajectory is displayed in Figure 4.6.

By construction of the cost function, the optimal path is along the diagonal boundary of the feasible region. Increasing the number of intermediate points to N, i.e. using N intermediate points $P_1, ..., P_N$, provides topologically similar paths that are close to the diagonal boundary of the feasible region.

In order to assess the robustness of the optimal control algorithm to the definition of arbitrary constraints, different regions of the (n, I_p) plane have been excluded from the feasible region. The open-loop optimisation algorithm successfully avoids them while remaining on an optimal path, as exposed in Figure 4.7.

Feasible operation is guaranteed by introducing back-offs from the constraints of the optimal control problem. In this case, robust optimisation is achieved by being conservative regarding safety margins.
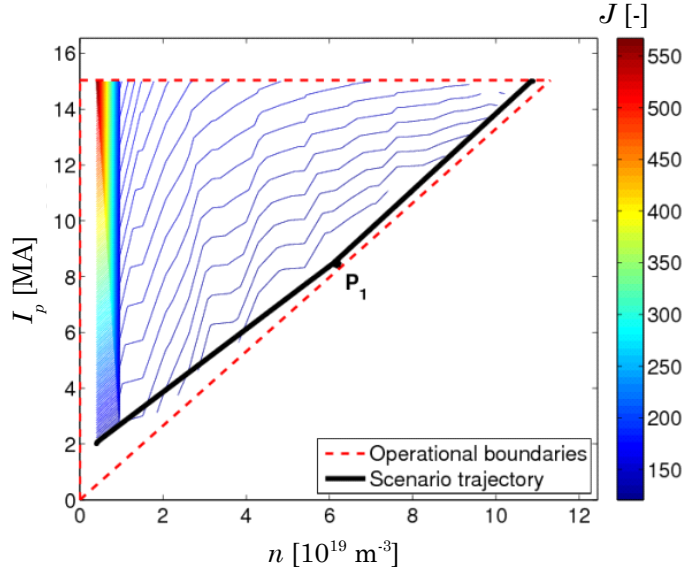
Figure 4.6: Open-loop optimal scenario trajectory of the non-linear programming problem (4.13). The contours of J =const. are displayed as a colour gradient.

4.3.4   Open-loop-with-feedback algorithm

An open-loop-with-feedback algorithm is implemented in order to improve the performance of the plasma pulse. The algorithm is as follows:

- Before performing the plasma pulse, determine the open-loop optimal path via a robust optimisation. This optimal path in the (t, n, I_p) space is the initial scenario;

- Launch the plasma pulse with this initial scenario;

- After a certain time, ten seconds in our case, perform the open-loop optimisation again using the present state of the tokamak as initial conditions;

- Adjust the scenario of the remainder of the plasma pulse according to the new optimal path computed by the open-loop optimisation algorithm;

- Perform this procedure every ten seconds until the target is reached.

This open-loop-with-feedback algorithm is summarised in Figure 4.8. and its implementation led to the trajectory displayed in Figure 4.9.

The scenario trajectory obtained using this open-loop-with-feedback algorithm demonstrates a significant improvement in the chosen cost function of the order of 40% when compared with open-loop optimisation.
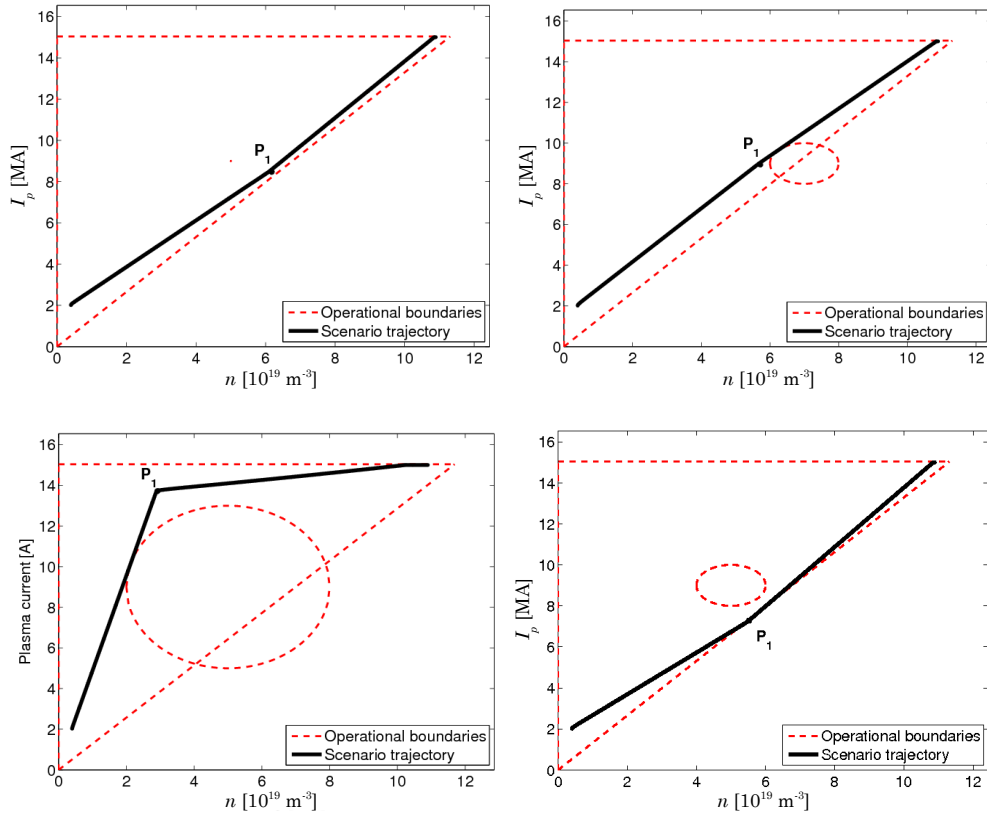
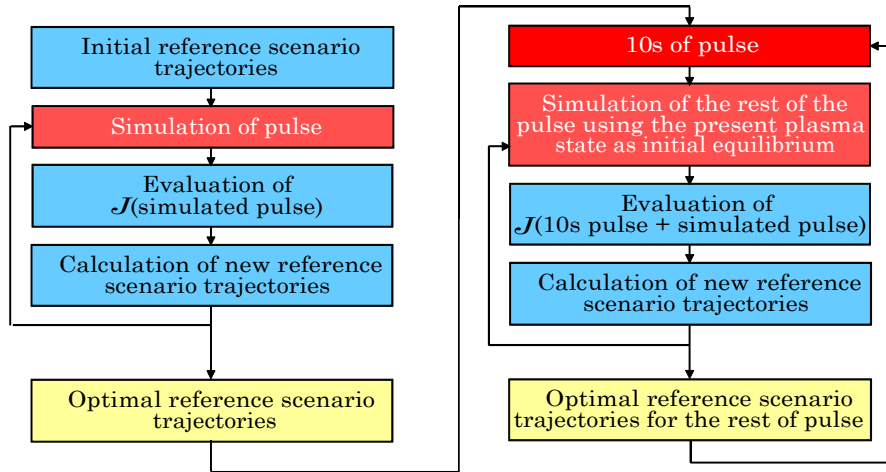Figure 4.7: Various topologies of the feasible region and their associated optimal trajectories.

Figure 4.8: Schematic workflow of the dynamic optimising control algorithm.
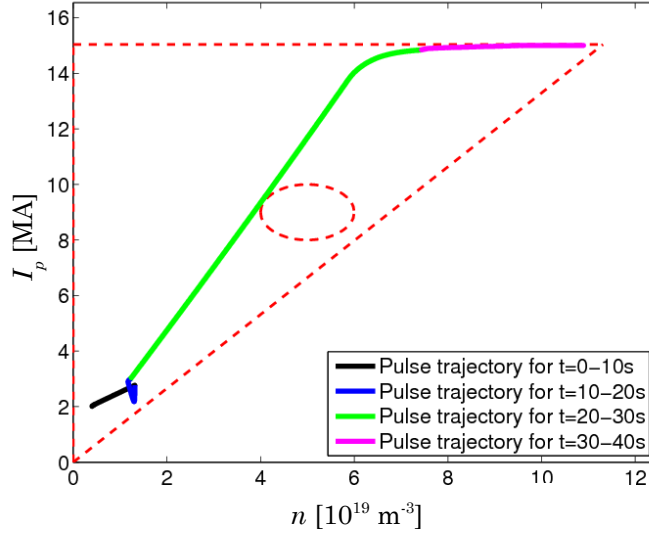
Figure 4.9: Optimal trajectory using an open-loop-with-feedback algorithm. Each colour denotes 10s of pulse.

Surprisingly, the scenario trajectory computed by the open-loop-with-feedback algorithm is not alongside the diagonal constraint of the feasible region, as one could have expected. This is due to the fact that, because of the imperfect actuators and imperfect scenario tracking, the scenario trajectories do not perfectly match the actual plasma pulse trajectory. The open-loop-with-feedback algorithm updates the optimal path according to the actual tokamak state. It thus takes advantage of the available knowledge acquired via measurements during the pulse and evolves the scenario trajectories accordingly. In our situation, the algorithm was faced with a decision regarding which side to follow to avoid the elliptical infeasible region on its path and decided that, according to the present tokamak state, it was less costly to move to regions of higher values of $J_\psi + J_{\text{sat}}$ for a shorter time than circumventing the infeasible region.

4.3.5 Conclusion

An open-loop-with-feedback algorithm was designed and implemented in the framework of a tokamak control toy problem. This on-the-fly re-optimisation algorithm significantly improves the plasma pulse performance when compared to an open-loop optimisation. Although successful, this open-loop-with-feedback control approach suffers from several drawbacks more precisely discussed in 4.5. Most importantly, the implemented algorithm does not guarantee optimal operation. Nonetheless, performance improvement has been demonstrated and feasible operation has been achieved via the introduction of back-offs from the operation space boundaries.

This work was presented at the 2010 European Physical Society Conference on Plasma Physics in Dublin, Ireland [108].

4.4 Open-loop optimisation of the ITER ramp-up

The previous paragraph exposed the basic principles of optimal control in the framework of tokamak operation using a simplistic tokamak evolution simulator. In order to study the possible effects of optimal control techniques in the operation of ITER, it is necessary to confront them to more complex tokamak simulators and eventually to experiments. In that perspective, this paragraph discusses the design and implementation of robust optimisation of plasma equilibrium scenario trajectories implemented around the DINA-CH&CRONOS full tokamak simulator.

During the ramp-up phase, the scenario trajectories of the plasma shape and of the plasma current must be tracked and regulated by the action of the PF system power supplies. At the end of the ramp-up phase, a target plasma shape and a target plasma current are obtained. The target can be attained following multiple plasma shape and plasma current scenario trajectories. Each scenario trajectory results in a different action of the PF system power supplies, thus enabling optimisation of the scenario.

During tokamak operation, the PF system coil currents must be kept within operational limits. At the same time, the PF system power supplies may saturate if the voltage demands are too high. Finally, plasma-wall contact must be prevented in order to avoid damage to the first wall and the deposition of impurities within the plasma. These constraints must be taken into account when designing the optimal control problem.

The optimal control problem is more precisely stated in 4.4.1. The model used for optimisation is then described in 4.4.2. The robust optimisation results are then discussed in 4.4.3.

4.4.1 Optimal control problem statement

The optimal control problem can be stated as follows:

> *Determine the PF system coil current scenario trajectories, the plasma current scenario trajectory, and the plasma shape scenario trajectory that maintain the PF system power supplies and the PF system coil currents as far from their operational limits as possible for the longest possible durations. These scenario trajectories must achieve a precise target plasma current and a precise target plasma shape at the end of ramp-up in a reasonable time. The process evolution must remain within a pre-determined operation space.*

The objective that consists of maximising the distance of the PF system power supplies from their limits increases the plasma controllability. It provides headroom for feedback control

in case of plasma disturbances. At the same time, maximising the distance of the PF system currents from their operational limits diminishes the operational risks and may make more volt-seconds available for loop voltage generation by the PF system action. Hence, this problem statement increases ITER's controllability and safety margins.

This generic problem statement must be translated into a precise mathematical statement. To achieve that, it is necessary to parametrise the plasma shape. This can be done in several ways, for example by using the plasma centroid position, its minor radius, its elongation, triangularity, squareness, etc. In our case, the plasma shape is parametrised by six *gaps* between the plasma separatrix and the first wall, as displayed in Figure 4.10. These gaps span
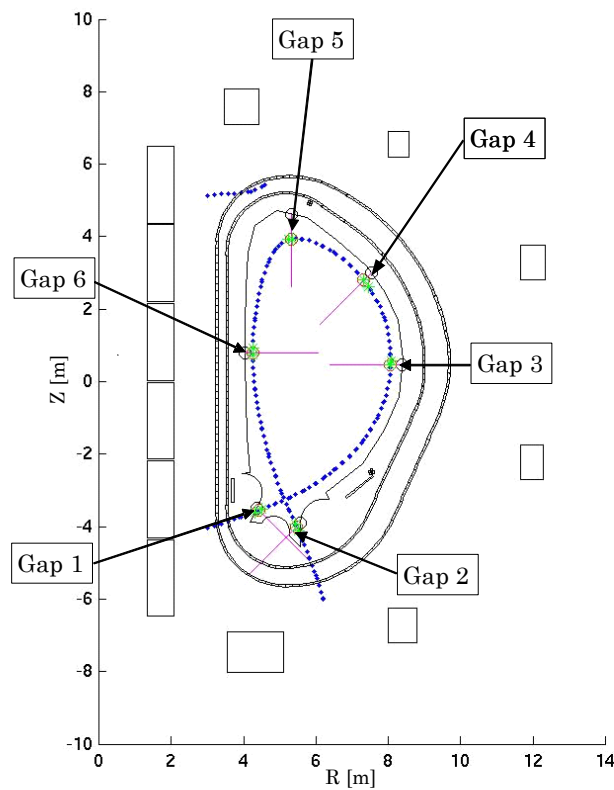

Figure 4.10: Location of the gaps between the plasma boundary and the first wall. A typical ITER separatrix is displayed in blue.

a six-dimensional vector space but are not orthogonal to one another. For example, increasing the current in PF2 affects both gap 4 and gap 5. It is therefore necessary to determine linear combinations of PF system coil currents that act on individual gaps. Such a procedure is known as *decoupling*.

Such plasma shape parametrisation was successfully implemented in JET for plasma shape control [109] and is foreseen to be implemented in ITER.

Let us now introduce a compact notation of the quantities involved in the optimal control problem. We define the voltage vector **V** as

$$\mathbf{V} = \begin{bmatrix} V_{\text{CS3U}} \\ \vdots \\ V_{\text{PF6}} \end{bmatrix} \tag{4.14}$$

and the system outputs vector **y** as

$$\mathbf{y} = \begin{bmatrix} I_{\text{CS3U}} \\ \vdots \\ I_{\text{PF6}} \\ I_p \\ \text{gap}_1 \\ \vdots \\ \text{gap}_6 \end{bmatrix}. \tag{4.15}$$

The scenario is defined as the set of system outputs references, i.e.

$$\mathbf{y}_{\text{ref}} = \begin{bmatrix} I_{\text{CS3U,ref}} \\ \vdots \\ I_{\text{PF6,ref}} \\ I_{p,\text{ref}} \\ \text{gap}_{1,\text{ref}} \\ \vdots \\ \text{gap}_{6,\text{ref}} \end{bmatrix}.$$

Although the PF system power supply saturations exposed in [43] are really dynamic, they are simplified for the purpose of the optimal control problem statement. The constraints associated with power supply saturations are thus expressed as

$$\mathbf{V}_{\text{min}} \leq \mathbf{V} \leq \mathbf{V}_{\text{max}}.$$

Because $\mathbf{V}_{\text{min}} = -\mathbf{V}_{\text{max}} < 0$, maximising the distance between PF system power supply voltages and their limits for long durations is achieved by minimising the following cost function

$$J_V = \int_{t_0}^{t_f} \mathbf{V}^T \underline{\mathbf{Q}_V} \mathbf{V} dt, \tag{4.16}$$

where t_0 is the initial time of the optimal control problem, t_f is the time at which the target in terms of plasma current and plasma shape is attained, $\underline{\mathbf{Q}_V}$ is a diagonal weight matrix with

arbitrary coefficients, and ^{T} denotes transposition.

In reality, the PF system currents operational limits depend on the magnetic field sustained by the PF system coils. This situation is simplified for the purposes of the optimal control problem statement and the operation limits are expressed as

$$
\begin{bmatrix} I_{\text{CS3U,min}} \\ \vdots \\ I_{\text{PF6,min}} \end{bmatrix} \leq \begin{bmatrix} I_{\text{CS3U}} \\ \vdots \\ I_{\text{PF6}} \end{bmatrix} \leq \begin{bmatrix} I_{\text{CS3U,max}} \\ \vdots \\ I_{\text{PF6,max}} \end{bmatrix},
$$

where $I_{i,\text{min}}$ and $I_{i,\text{max}}$ are respectively the minimum and the maximum current tolerable on the i-th coil. Because $I_{i,\text{min}} = -I_{i,\text{max}}$ for $i =$CS3U, ..., PF6, the requirement of maximising the distance between the PF system coil currents and their operational limits for long durations can be achieved by minimising the following cost function

$$
J_y = \int_{t_0}^{t_f} \mathbf{y}^T \underline{\underline{\mathbf{Q}_y}} \mathbf{y} dt, \tag{4.17}
$$

where $\underline{\underline{\mathbf{Q}_y}}$ is a diagonal weight matrix of the form

$$
\underline{\underline{\mathbf{Q}_y}} = \begin{bmatrix} q_{\text{CS3U}} & \cdots & 0 & 0 & 0 & \cdots & 0 \\ \vdots & \ddots & \vdots & \vdots & \vdots & \ddots & \vdots \\ 0 & \cdots & q_{\text{PF6}} & 0 & 0 & \cdots & 0 \\ 0 & \cdots & 0 & 0 & 0 & \cdots & 0 \\ 0 & \cdots & 0 & 0 & 0 & \cdots & 0 \\ \vdots & \ddots & \vdots & \vdots & \vdots & \ddots & \vdots \\ 0 & \cdots & 0 & 0 & 0 & \cdots & 0 \end{bmatrix}
$$

where q_i is an arbitrary weight coefficient for the i-th coil.

The plasma current and gaps scenario trajectories computed by the optimisation algorithm may significantly differ from nominal scenario trajectories, i.e. scenario trajectories that would be considered as typical. This can be detrimental to the tokamak evolution in terms of pulse performance and risks. In order to prevent the optimal solution from differing from the nominal scenario too significantly, the following cost function must be minimised:

$$
J_{\text{nom}} = \int_{t_0}^{t_f} \left(\mathbf{y}_{\text{ref,nom}} - \mathbf{y}_{\text{ref}} \right)^T \underline{\underline{\mathbf{Q}_{\text{nom}}}} \left(\mathbf{y}_{\text{ref,nom}} - \mathbf{y}_{\text{ref}} \right) dt, \tag{4.18}
$$

where $\mathbf{y}_{\text{ref,nom}}$ are the nominal scenario trajectories and $\underline{\mathbf{Q}_{\text{nom}}}$ is a diagonal cost matrix expressed as follows

$$
\underline{\mathbf{Q}_{\text{nom}}} = \begin{bmatrix}
0 & \cdots & 0 & 0 & 0 & \cdots & 0 \\
\vdots & \ddots & \vdots & \vdots & \vdots & \ddots & \vdots \\
0 & \cdots & 0 & 0 & 0 & \cdots & 0 \\
0 & \cdots & 0 & q_{I_p} & 0 & \cdots & 0 \\
0 & \cdots & 0 & 0 & q_{\text{gap}_1} & \cdots & 0 \\
\vdots & \ddots & \vdots & \vdots & \vdots & \ddots & \vdots \\
0 & \cdots & 0 & 0 & 0 & \cdots & q_{\text{gap}_6}
\end{bmatrix}
$$

and q_{I_p} and q_{gap_i}, $i = 1, ..., 6$ are arbitrary coefficients.

The optimal control problem can be reformulated as follows. It consists of minimising the objective function $J(\mathbf{y}_{\text{ref}})$ by optimising the scenario $\mathbf{y}_{\text{ref}}$:

$$
\text{minimise:} \quad J(\mathbf{y}_{\text{ref}}) = \int_{t_0}^{t_f} \left[\mathbf{V}^T \underline{\mathbf{Q}_V} \mathbf{V} + \mathbf{y}^T \underline{\mathbf{Q}_y} \mathbf{y} + (\mathbf{y}_{\text{ref,nom}} - \mathbf{y}_{\text{ref}})^T \underline{\mathbf{Q}_{\text{nom}}} (\mathbf{y}_{\text{ref,nom}} - \mathbf{y}_{\text{ref}}) \right] dt
$$

$$
\begin{aligned}
\text{subject to:} \quad & \dot{\mathbf{y}}(t) = \mathbf{f}(t, \mathbf{y}(t), \mathbf{V}(t)) \\
& \mathbf{G}(\mathbf{y}, \mathbf{y}_{\text{ref}}, \mathbf{V}) \leq \mathbf{0} \\
& I_p(t_f) = I_{p,t_f} \\
& \text{gaps}_i(t_f) = \text{gaps}_{i,t_f} \qquad i = 1, \cdots, 6.
\end{aligned}
$$

(4.19)

The scope of this optimal control problem is limited to the second part of the ITER ramp-up, i.e. after the L-H transition, to avoid having to incorporate the L-H transition timing in the optimal control problem statement.

4.4.2 Plasma current and gaps modelling

Because optimisation algorithms require multiple evaluation of the cost function in order to converge, it is necessary to develop a model that simulates the evolution of the plasma current and gaps according to actuator signals in a fast manner. Because it must be fast, this model cannot fully encapsulate the complexity of the evolution of a tokamak and a trade-off between speed and precision must be made. On top of these considerations, it is necessary that such a model includes the most prominent features of the controlled processes in order to ensure that the optimal control problem solution is close to the optimal process evolution and to avoid risky tokamak operation.

It is inevitable that the simplified simulator imperfectly models the plasma current and

the gaps. Moreover, there exists a risk associated with such imperfect modelling. Indeed, inaccurate modelling of plasma evolution may lead to unforeseen violation of the operation space boundaries and may lead to risky tokamak evolution. In our case, inadequate modelling of the gaps may lead to plasma-wall contact. Hence, the more imperfect the modelling the larger the safety margins (back-offs) from the operation boundaries are required for safe operation, thus possibly reducing the achievable performance of the optimal control scheme by shrinking the feasible region. As a result, precise modelling of tokamak evolution is not required for the successful implementation of an optimal control algorithm as long as sufficient safety margins are implemented, but inaccurate modelling can be detrimental to performance. The trade-off between speed and modelling accuracy must therefore be made consciously and the inaccuracies of the simplified model must be analysed.

In this work, the plasma current and gaps responses to actuator signals are modelled as follows:

- The PF system currents and the plasma current evolution is modelled as in the previous paragraph, except with the plasma resistance being identically set to zero.

  Such modelling of the plasma current and the PF system currents evolution according to the PF system power supply action is compared with a DINA-CH&CRONOS pulse in Figure 4.11 and in Figure 4.12.
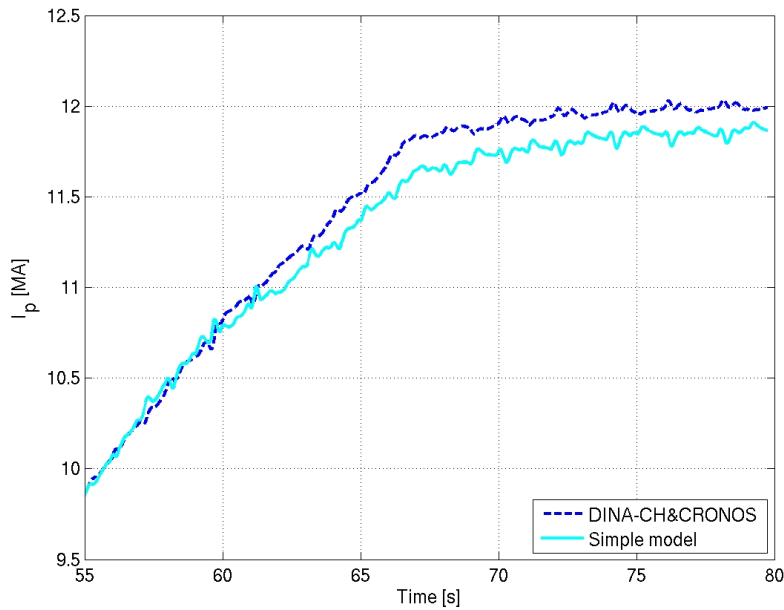

Figure 4.11: Comparison between the plasma current simulated by DINA-CH&CRONOS and the corresponding plasma current evolution simulated by the simple model. The same voltages was applied on the PF coils at all time. The oscillations are due to stimulations of the control systems.
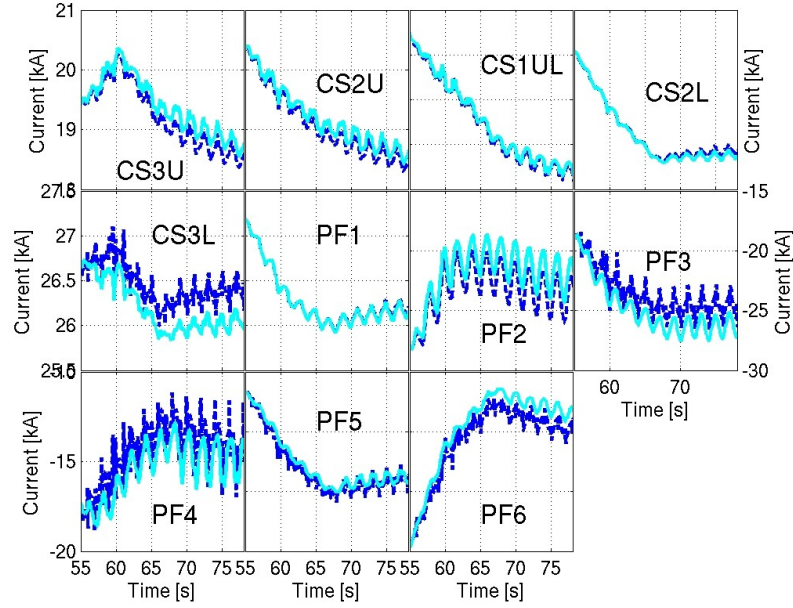
Figure 4.12: Comparison between the PF system currents simulated by DINA-CH&CRONOS and the corresponding PF system currents evolution simulated by the simple model. The same voltages was applied on the PF coils at all time. The DINA-CH&CRONOS simulated PF coil current evolutions are displayed in dashed blue and the simple model simulated PF coil current evolutions are displayed in cyan.

Although not perfect, the simple modelling is acceptable. No specific refinement of the constraints of the optimal control problem is necessary.

- The evolution of the six gaps responses to actuator signals is modelled as follows:

$$\frac{d\text{gap}_i}{dt} = \frac{d\Psi_p}{dt}\frac{d\text{gap}_i}{d\Psi_p} = C_i\frac{I_p}{2\pi R_{\text{gap}_i}}\mathbf{G}_i^T\underline{\underline{\mathbf{M}}}^{-1}\begin{bmatrix} \mathbf{V} \\ 0 \end{bmatrix} \tag{4.20}$$

where C_i is a constant, R_{gap_i} is the R-position of the intersection between the plasma separatrix and the gap line at $t = t_0$, $\mathbf{G}_i$ is the Green's function vector between the initial position of the gap $\left(R_{\text{gap}}(t = t_0), Z_{\text{gap}}(t = t_0)\right)$ and the PF system coils:

$$\mathbf{G}_i = \begin{bmatrix} G_{\text{gap},i\text{-CS3U}} \\ \vdots \\ G_{\text{gap},i\text{-PF6}} \\ G_{\text{gap},i\text{-pla}} \end{bmatrix},$$

$\underline{\underline{\mathbf{M}}}$ is the mutual inductance matrix similar to that introduced in the previous paragraph (no conducting vacuum vessel), and $\mathbf{V}$ is the voltage vector.

This gaps modelling is based on several strong assumptions. Firstly, it assumes that a gap is a function of only the poloidal magnetic flux Ψ_p. Secondly, it is assumed that the poloidal magnetic flux at the intersection between the plasma separatrix and the gap line can be computed using the Green's function between the PF system coils and the initial position of this intersection, thus implicitly requiring that the Green's function are not too dependent on the position of the intersection. Finally, the identification of the constants C_i was not made on a large and diverse sample of equilibria.

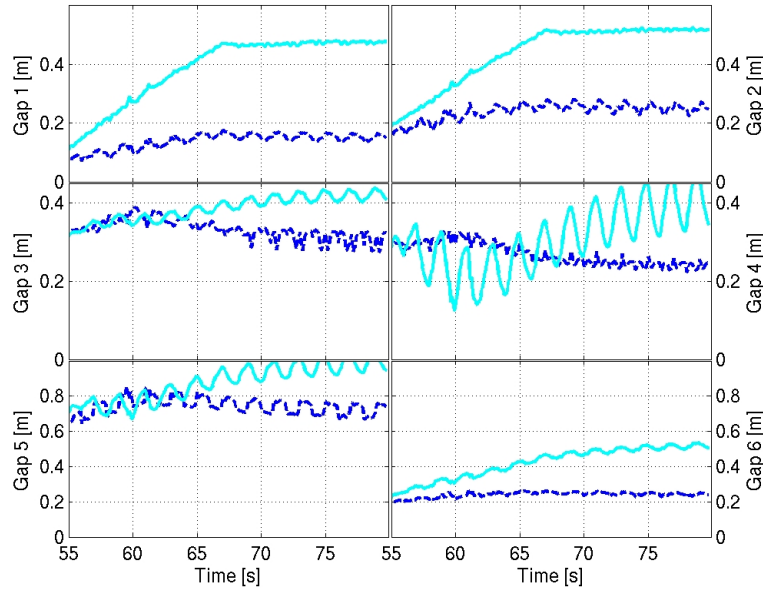Such modelling is imprecise, as displayed in Figure 4.13.

Figure 4.13: Comparison between the gaps simulated by DINA-CH&CRONOS and the corresponding gaps evolution simulated by the simple model. The same voltages were applied to the PF coils at all time. The DINA-CH&CRONOS simulated gaps evolution is displayed in dashed blue and the simple model simulated gaps evolution is displayed in cyan.

However, this imprecision can be accounted for by updating the optimal problem constraints. Specifically, gaps 1, 2, and 6 are systematically overestimated. In order to avoid plasma-wall contact, the constraints of the problem have been adjusted in order to avoid plasma-wall contact.

Although the plasma current and gaps model is not accurate, it is sufficient for our purpose. The gain in simulation speed is of the order of 40,000 when compared with DINA-CH&CRONOS simulations.

In this simple model, the effect of the vacuum vessel is neglected. This assumption, although rather strong, is supported by the fact that the time scales of interest for the stated optimal con-

trol problem are much longer than the high-frequency shielding provided by the conducting vacuum vessel. The simple model does not include the fast internal VS3 coils.

4.4.3 Optimisation solution

The scenario trajectories are infinite-dimensional functions. In order to solve the optimal control problem, the scenario trajectories are parametrised. The trajectories are divided in n_s segments of equal duration. The process inputs $\boldsymbol{\pi}$ are therefore the scenario trajectory points for each controlled variable and the number of process inputs is $n_\pi = n_y n_s$.

The optimal control problem is solved using a direct sequential approach with piecewise linear scenario trajectory parametrisation [106].

The optimal control problem solution is computed for the cost function $J(\boldsymbol{\pi})$ using the simplified model. This optimal scenario is then implemented on the DINA-CH&CRONOS full tokamak simulator, starting after the L-H transition of a hybrid scenario ramp-up (see Chapter 5). The implementation scheme is summarised in Figure 4.14.
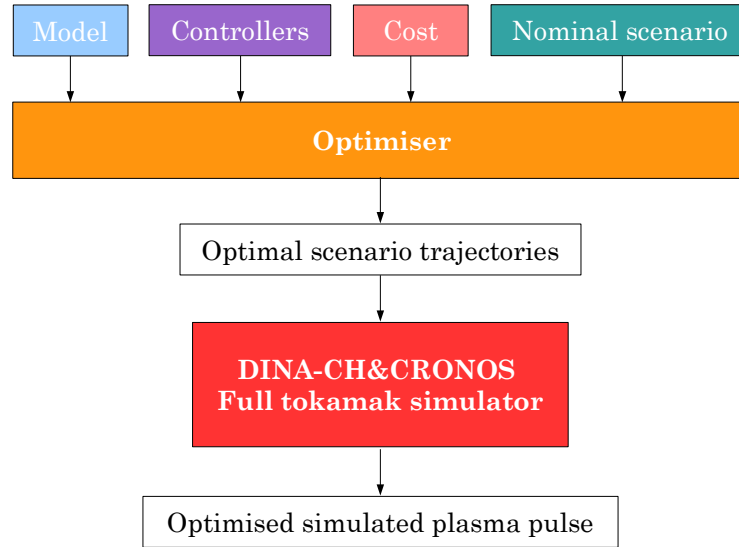

Figure 4.14: Open-loop optimisation scheme.

The nominal scenario trajectories and the optimised scenario trajectories are displayed in Figure 4.15, Figure 4.16, and Figure 4.17.
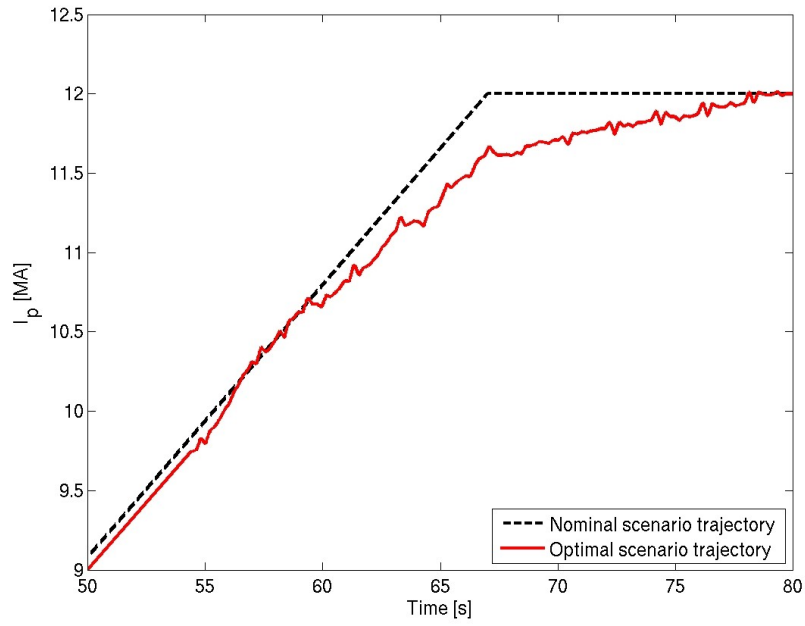
Figure 4.15: Optimal plasma current scenario trajectory. The nominal plasma current scenario trajectory is displayed in dashed black.
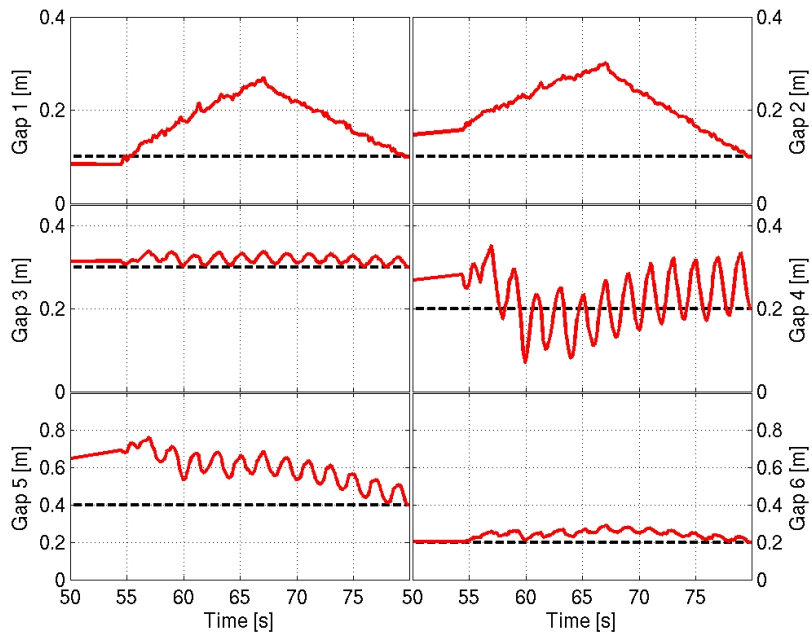

Figure 4.16: Optimal gaps scenario trajectories. The nominal gaps scenario trajectories are displayed in dashed black.
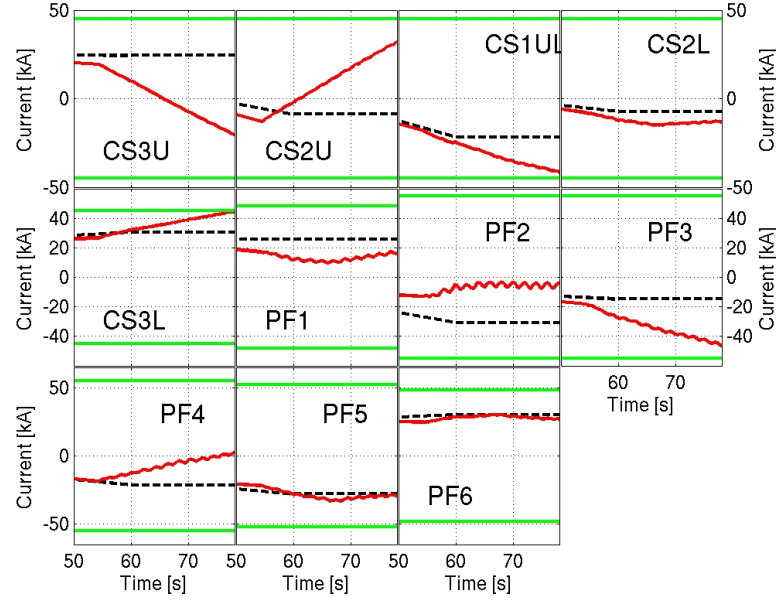
Figure 4.17: Optimal PF system currents scenario trajectories. The nominal PF system currents scenario trajectories are displayed in dashed black. The PF system coil current limits are displayed in green.

The optimised scenario trajectories are implemented in a DINA-CH&CRONOS simulation of an ITER ramp-up. The full tokamak simulation uses imperfect controllers, thus decreasing the level of optimality obtained. Nonetheless, the resulting cost of the optimised scenario is about 30% lower than that obtained with the nominal hybrid scenario ramp-up.

4.4.4 Conclusion

A robust optimisation scheme has been designed, implemented, and tested in the framework of a full tokamak simulator. The performance of an ITER ramp-up phase after the L-H transition has been significantly improved by optimising the scenario trajectories. The optimised scenario trajectories maintained the operation within ITER physical constraints, even with an approximate tokamak model.

It is important to state that a trade-off must be consciously made between precise modelling of the plasma evolution and simulator speed when developing models used for optimisation. In the presented robust optimisation scheme, the model developed allows extremely fast simulation at the price of precision. The loss in precision is compensated by the use of back-offs from the actual tokamak constraints when stating the optimal control problem.

This work exposed an application of robust optimisation techniques in the framework of

tokamak operation. It was presented at the 2011 European Physical Society Conference on Plasma Physics in Strasbourg, France [110].

4.5 Optimal control features

In this Chapter, an open-loop-with-feedback algorithm and a robust optimisation algorithm have been designed and implemented in the framework of tokamak operation. Both examples improved the pulse performance thus demonstrating the potential of optimal control schemes applied for tokamak operation. Importantly, both schemes also succeeded in automating scenario development, which may greatly benefit ITER operation.

This paragraph discusses the main schemes for optimal control in the framework of tokamak operation, as well as their major advantages and drawbacks.

4.5.1 Robust optimisation

Robust optimisation suffers from the following drawbacks:

- It is an open-loop approach and therefore cannot take into account disturbances. As a result, a scenario that is optimal when simulated may lead to a lower performance than predicted when implemented.

- The efficiency of robust optimisation schemes relies on the precision of the modelling of the system. Inaccuracies in modelling not only lead to loss of performance, but may even drive the system in a state that violates the operation constraints. To avoid such behaviour, it is necessary to artificially reduce the feasible region according to the estimated model accuracy. In turn, this often results in a loss of performance because optimal solutions are likely to operate close to the boundaries of the feasible region;

- Robust optimisation is a pre-programming control approach. This is detrimental to the flexibility of the control system because it does not allow the control system to update the scenario targets on-the-fly;

- The achieved performance is a function of the controllers performance. In other words, poor implementation of the optimal scenario trajectories may lead to a loss of performance. This loss may be important even for small deviations from the optimal scenario trajectories, depending on the sensitivity of the cost function and the evolution of the system.

These drawbacks all have in common that robust optimisation techniques, when applied to a tokamak plasma pulse, may lead to suboptimal operation. These drawbacks are no threat to the machine integrity and tokamak operation as long as sufficient margins from the

physical constraints of the tokamak are implemented to compensate the model inaccuracy. Conservatism is needed for achieving feasible operation.

Conversely, robust optimisation schemes possess several advantages:

- The approach is simple to understand and to implement;

- The optimal scenario trajectories are known before the plasma pulse and are not updated on-the-fly. Thus, a thorough validation process can be undertaken off-line. Manual modifications of inappropriate parts of the scenario before the plasma pulse can be performed;

- Although performance improvement is not guaranteed, optimal scenario trajectories may drive the tokamak in a state that is, if not optimal, at least more performing than the nominal scenario trajectories. This is the case for cost functions that are not too sensitive to small deviations from the optimal scenario trajectories;

- Robust optimisation can be used as a tool for providing insight regarding what phenomena are responsible for a decrease of performance. In fact, such a feature is already achieved by stating the cost function explicitly.

Overall, robust optimisation appears to be a valuable tool for tokamak operation. Its main drawback is that an improvement in performance is not guaranteed. On the other hand, robust optimisation possesses several advantages that render this approach appealing for tokamak operation. This is especially appropriate for ITER operation of long pulses, because even a small instantaneous improvement in performance, when integrated over long durations, may lead to a significant overall performance increase.

4.5.2 Open-loop-with-feedback optimisation

In this Chapter, a real-time 'optimisation' algorithm was implemented. The quotes denote the fact that the scheme suggested and implemented for plasma current and plasma density evolution optimisation during an ITER ramp-up is not really an RTO algorithm, but rather an open-loop-with-feedback optimisation scheme [103]. The scheme implemented is not guaranteed to converge to an optimum, not even asymptotically.

This open-loop-with-feedback algorithm really is a straightforward extension of robust optimisation. This approach suffers from the following drawbacks:

- The open-loop-with-feedback approach exposed in this Chapter is a repetitive scheme, but not an iterative approach. There is no mathematical guarantee that optimal operation may be achieved. Worse, such an algorithm may even lead, in certain circumstances, to lower achieved performance than if the system was let to evolve naturally;

- The implemented open-loop-with-feedback algorithm necessitates fast and relatively accurate modelling of the tokamak evolution because it must be performed on-the-fly. This is a serious drawback because it implies that such an algorithm cannot be implemented on short-duration pulses such as those achieved in TCV. However, long-duration pulses such as ITER advanced scenarios may be suitable for the implementation of such schemes;

- This approach can only be used for low-frequency on-the-fly re-optimisation. Phenomena that possess characteristic times much shorter than the scenario trajectories updates or than the control system characteristic time cannot be successfully optimised;

- The presented open-loop-with-feedback algorithm requires that the tokamak evolution is either slow or well-modelled when compared to the re-optimisation update duration. The on-the-fly re-optimisation uses the tokamak state at time t as initial condition for its optimisation, but the updated optimal scenario trajectories are only obtained at $t + \Delta t$ due to the time necessary for the optimiser to converge. Therefore, for this scheme to be adequate, the tokamak states at t and $t + \Delta t$ must either be close to one another, or the modelling of tokamak evolution during the Δt interval must be accurate in order to use the modelled tokamak state at $t + \Delta t$ as the initial state in the optimisation process;

- Because the re-optimisation automatically modifies the scenario trajectories on-the-fly, it may drive the tokamak state to risky regions of the operation space if the optimal control problem is not well-defined. Such a scenario would occur without requiring the validation of the tokamak operator;

- As for robust optimisation, the achievable performance and the risk of violating the optimal control problem constraints are directly linked to the tokamak evolution model accuracy. The use of conservative constraints is necessary to guarantee feasible operation;

- Performance depends on the lower level feedback controllers, as for robust optimisation schemes;

Similarly to robust optimisation schemes, the discussed open-loop-with-feedback algorithm does not guarantee optimal performance. More importantly, the fact that scenario trajectories are updated on-the-fly without operator validation is at the same time one of major drawbacks of the scheme and one of its best asset. Such automated update of scenario trajectories can drive the tokamak in an inappropriate state if the optimal control problem is not well-defined. On the other hand, updating scenario trajectories on-the-fly may drastically improve the pulse performance by accounting for the actual tokamak evolution in the optimal control scheme.

The exposed open-loop-with-feedback algorithm possesses several advantages:

- The achievable performance of the plasma pulse can be significantly increased when compared to robust optimisation algorithms because the implemented open-loop-with-

feedback algorithm accounts for tokamak evolution and is not a simple 'fire and forget' approach. At the same time, the safety margins can possibly be shrunk with respect to robust optimisation because the optimisation horizon is shorter;

- The presented open-loop-with-feedback scheme allows for higher level target modifications on-the-fly. Hence, if a higher level control system imposes a target modification, e.g. a segment change in case of ITER operation, the open-loop-with-feedback scheme can account for it on-the-fly;

- Although not guaranteed, performance improvement can be significant. In our case, it was more important than that achieved with a simple open-loop optimisation;

- If the optimal problem is well-defined, the feedback component of the implemented open-loop-with-feedback algorithm may determine if the tokamak is heading to a region in operation space that is not desirable or dangerous. Its action automatically drives the tokamak evolution away from the dangerous zone, thus acting as a tokamak protection algorithm.

In our case, the open-loop-with-feedback scheme demonstrated a significant improvement over the cost achieved with open-loop optimisation. Moreover, the open-loop-with-feedback scheme possesses a feedback component which is of added-value with respect to the purely open-loop robust optimisation approach. However, its implementation is somewhat more complex because it requires on-the-fly re-optimisation which must be at the same time fast and reasonably accurate.

4.5.3 Real-time optimisation (RTO)

Real-time optimisation schemes (RTO) have not been tackled in this Chapter. However, it is informative to assess their features, especially in the framework of tokamak operation.

RTO algorithms use measurements available during the process. In that sense, RTO schemes are closed-loop algorithms. They therefore combine the beneficial effects of open-loop optimal control schemes and feedback control algorithms and they are capable of dealing with uncertainty and process disturbances.

RTO is still the subject of intense present-day research in the optimal control community. Designing and implementing RTO schemes remains a challenge. This section describes three of the most prominent RTO algorithms and assess their main advantages and drawbacks in view of being implemented for tokamak operation.

Model-parameter adaptation

The model-parameter adaptation is a two-step approach. In the first step, the model parameters $\boldsymbol{\theta}$ are estimated using the plant measurements. In the second step, the updated

model is used to solve the open-loop re-optimisation problem with initial values updated. This scheme is similar to the open-loop-with-feedback algorithm presented in this Chapter, with the addition that the model parameters are updated according to the tokamak state. The mismatch between the tokamak evolution and the simulated evolution is accounted for by model-parameter adaptation.

In this scheme, the interaction between the two steps must be carefully designed in order to guarantee that optimality is achieved. In fact, the model parameters adaptation process may be detrimental to the determination of a feasible and optimal path.

Let us assume that the adaptable model possesses n_θ adaptable parameters and that there are n_y independent system outputs $\mathbf{y}$. In order to ensure feasibility, i.e. in order to ensure that operation within the operation space is achieved, the constraints $\mathbf{G}(\boldsymbol{\pi}, \mathbf{y})$ must be well-estimated by the adaptable model. To achieve that, it is necessary to impose $n_\theta \geq n_y$, because the constraints are functions of the system outputs.

On the other hand, achieving optimality necessitates the satisfaction of first-order necessary conditions of optimality. To achieve that, the derivative of the system outputs with respect to the process inputs $\partial \mathbf{y}_p / \partial \boldsymbol{\pi}$ must match the model derivatives:

$$\frac{\partial \mathbf{y}_p}{\partial \boldsymbol{\pi}} = \frac{\partial \mathbf{y}_\mathrm{m}}{\partial \boldsymbol{\pi}},$$

where the subscript 'm' denotes the modelled value.

This corresponds to $n_y n_\pi$ conditions that the adaptable model must satisfy.

Overall, it is required that the number of adjustable parameters in the model is greater than the number of conditions it must satisfy in order to provide a sufficient number of degrees of freedom to solve the optimisation problem. In other words,

$$n_\theta \geq n_y (n_\pi + 1).$$

The model-parameter adaptation scheme thus requires that the model possesses at least $n_y(n_\pi + 1)$ degrees of freedom in order to theoretically enable feasible and optimal operation. Developing such a model that must, at the same time, reasonably accurately model the system evolution in a fast manner is not obvious in the framework of tokamak operation.

The working scheme of model-parameter adaptation RTO is summarised in Figure 4.18.

Modifier adaptation

The modifier adaptation approach is one of several variants of the two-step model-adaptation approach. It consists of modifying the optimal control problem on-the-fly rather than modifying the model. Hence, the cost function and the optimal control problem constraints
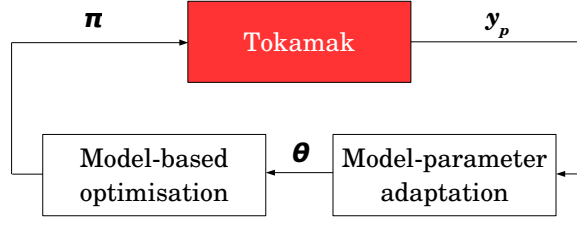
Figure 4.18: Real-time optimisation via model-parameter adaptation.

are modified on-the-fly according the the difference between the system outputs and the modelled system outputs.

More specifically, this scheme requires the addition and update of three terms in the optimal control problem statement:

- A cost-gradient modifier is added to the cost function. This modifier corresponds to the difference between the experimental and predicted cost gradient $\partial J / \partial \boldsymbol{\pi}$;

- A constraint-value modifier is added to the constraint function. The constraint-value modifier corresponds to the difference between the experimental and predicted constraints [111];

- A constraint-gradient modifier term is added to the constraint function. This modifier corresponds to the difference between the experimental partial derivatives of the constraints with respect to the system inputs and their predicted values.

The optimal control can thus be reformulated as

$$
\begin{aligned}
\text{minimise:} \quad & J(\boldsymbol{\pi}, \boldsymbol{\theta}) + \left[\frac{\partial J_p}{\partial \boldsymbol{\pi}}(\boldsymbol{\pi}_p) - \frac{\partial J_\mathrm{m}}{\partial \boldsymbol{\pi}}(\boldsymbol{\pi}_p, \boldsymbol{\theta}) \right]^T (\boldsymbol{\pi} - \boldsymbol{\pi}_p) \\
\text{subject to:} \quad & \mathbf{G}(\boldsymbol{\pi}, \boldsymbol{\theta}) + \left[\mathbf{G}_p(\boldsymbol{\pi}_p) - \mathbf{G}(\boldsymbol{\pi}_p, \boldsymbol{\theta}) \right]^T + \left[\frac{\partial \mathbf{G}_p}{\partial \boldsymbol{\pi}}(\boldsymbol{\pi}_p) - \frac{\partial \mathbf{G}_\mathrm{m}}{\partial \boldsymbol{\pi}}(\boldsymbol{\pi}_p, \boldsymbol{\theta}) \right]^T (\boldsymbol{\pi} - \boldsymbol{\pi}_p) \le \mathbf{0}.
\end{aligned}
$$

$$(4.21)$$

The quantities that are adapted are gathered in the vector $\mathscr{C}$ for further reference:

$$
\mathscr{C} = \begin{bmatrix} \partial J / \partial \boldsymbol{\pi} \\ \mathbf{G} \\ \partial \mathbf{G} / \partial \boldsymbol{\pi} \end{bmatrix}.
$$

The modifiers are updated according to the measured system outputs. The working scheme of modifier adaptation RTO is summarised in Figure 4.19.
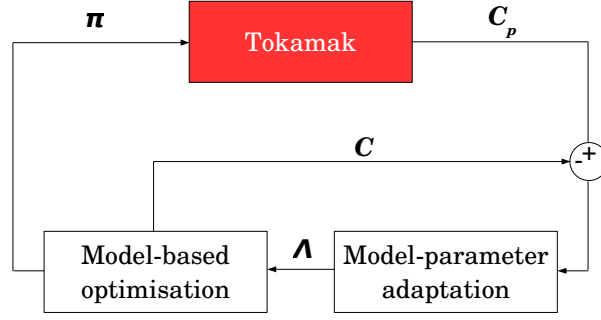
Figure 4.19: Real-time optimisation via modifier-adaptation. The tokamak output $\mathscr{C}_p$ consists of the cost function sensitivities $\partial J/\partial \boldsymbol{\pi}$, the values of the constraints $\mathbf{G}$, and the values of the constraints gradients with respect to system inputs $\partial \mathbf{G}/\partial \boldsymbol{\pi}$.

Modifier adaptation is an interesting approach to RTO because it modifies the optimisation problem in real-time instead of updating the adaptable model parameters.

Modifier adaptation guarantees operation within the optimisation problem constraints and convergence to an optimum. However, it requires the estimation of the experimental cost and constraint gradients on-the-fly, which is a major drawback of the method. Moreover, the re-optimisation process must be performed on-the-fly, which can be a challenge for fast processes.

Implementation of modifier adaptation schemes in the context of tokamak operation is not straightforward due to the necessity of estimating the cost and constraint gradients on-the-fly.

Modifier adaptation is more precisely described in [104].

Necessary conditions of optimality (NCO) tracking

The idea behind NCO tracking is relatively simple [112]. It consists of transforming the optimisation problem into a feedback control problem. In this approach, the necessary conditions of optimality $\mathscr{Z}$,

$$\mathscr{Z} = \left[\begin{array}{c} \partial J/\partial \boldsymbol{\pi} \\ \mathbf{G}^a \end{array} \right],$$

where $\mathbf{G}^a$ are the active constraints. $\mathscr{Z}$ is regulated by a feedback control system. The NCO tracking working scheme is displayed in Figure 4.20.

This approach possesses the significant advantage that it does not require on-the-fly re-optimisation. By design, the NCO are tracked and regulated using a feedback controller that can be extremely simple.
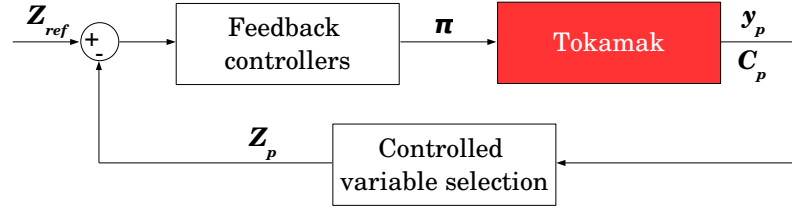
Figure 4.20: Real-time optimisation via NCO tracking. The NCO $\mathcal{Z}$ consists of the cost function sensitivities $\partial J/\partial \boldsymbol{\pi}$ and the values of the active constraints $\mathbf{G}^a$. $\mathcal{Z}_{\text{ref}}$ is set to zero.

One of the main difficulty of this approach is the necessity to estimate the cost function sensitivities to the process inputs , i.e. to the scenario trajectories in tokamak operation. Such estimation can be achieved by driving the tokamak into a different state and evaluating the cost function sensitivity to the state modification. However, the high number of independent degrees of freedom in a tokamak and the restriction of the number of exploratory pulses may render this approach rather tedious.

NCO tracking also necessitates a priori knowledge of which constraints are active at what time and for which duration in order to determine which constraints should be tracked by the feedback controllers. This information may be difficult to obtain for tokamak operation. Moreover, the NCO feedback controller switching scheme must be determined before a plasma pulse, thus forbidding on-the-fly target modifications by a higher level control layer.

Nonetheless, in the author's opinion, NCO tracking is a very promising tool for tokamak operation using RTO techniques because it does not require optimisation in real-time. NCO tracking would be especially appropriate for on-the-fly optimisation of flat-top phases.

4.5.4   Comparison with model-based predictive control

The discussed robust optimisation or real-time optimisation schemes differ from model-based predictive control approaches. Indeed, model-based predictive control schemes, sometimes known as 'receding-horizon' algorithms, aim at minimising a cost function for a relatively short time horizon, and following a pre-determined scenario trajectory. The output of model-based predictive control algorithm is actuator demand signals, such as demand voltages or demand heating and current drive powers.

The discussed robust optimisation or real-time optimisation schemes automate the scenario design. The horizon is not receding, in the sense that the target remains unchanged. Moreover, the output of robust optimisation or real-time optimisation schemes, in this work, are the scenario trajectories.

4.5.5   Conclusion

Optimal control offers various strategies in order to operate tokamaks close to optimum. Each of these strategies possess specific advantages and drawbacks.

In this Chapter, a robust optimisation strategy and an open-loop-with-feedback optimisation strategies have been implemented in the framework of tokamak operation. They both demonstrated improvement over nominal unoptimised scenarios.

More complex real-time optimisation algorithms and their possible application to tokamak operation have been discussed.

5 | ITER advanced scenarios

Tokamaks are inherently pulsed devices because plasma current is externally sustained during flat-top. This feature is one of the major drawbacks of the tokamak concept in view of using tokamaks as power production plants because pulsed operation implies important heat stresses to the tokamak.

This challenge has drawn considerable attention and recent developments in tokamak operation opened new perspectives. *Advanced tokamak scenarios* achieve a significantly higher neutron fluence per plasma pulse than Ohmic scenarios and inductive scenarios. Advanced scenarios take advantage of the synergy between the tokamak PF system and the tokamak heating and current drive systems. They significantly extend pulse durations by reducing the flat-top volt-second consumption. This is achieved without significant reduction of pulse performance.

Advanced scenarios are characterised by a higher non-inductively driven plasma current fraction than inductive scenarios. They rely on operating close to a specific desired pressure profile shape, a specific desired density profile shape, and a specific desired current density profile shape. This is achieved in part by localised heating and current drive and in part because a significant fraction of the non-inductively driven plasma current is generated by the plasma itself via the bootstrap effect. Similarly, the power required to sustain the plasma pressure is partly generated by the plasma self-heating via the energetic α-particles produced by the fusion reactions.

Advanced scenarios are typically divided in two classes [23]:

- **Hybrid scenarios**
  Advanced inductive scenarios are advanced tokamak scenarios in which a significant fraction of the plasma current is non-inductively driven but not its entirety. These advanced inductive scenarios are known as *hybrid scenarios* because of the following reasons:

    – The fusion gain of hybrid scenarios is slightly lower than that achieved by inductive

> scenarios but higher than that achieved by steady-state scenarios;

- The plasma current and plasma density are lower than those achieved by inductive scenarios but higher than those achieved by steady-state scenarios;

- The pulse duration of hybrid scenarios is significantly longer than that achieved by inductive scenarios but steady-state operation is not attained and hybrid scenarios remain pulsed tokamak scenarios.

The heating and current drive systems help maintain the plasma in a high confinement mode (H-mode) for the complete duration of the burn phase. One of the major challenges faced by hybrid scenarios consists of maintaining a wide region a low shear in the plasma centre while preventing the occurrence of sawteeth, which are triggered, loosely speaking, by the safety factor profile (q-profile) reaching unity.

Hybrid scenarios have been successfully performed in ASDEX Upgrade [113, 114, 115], in DIII-D [116, 117], in JET [118, 119], and in JT-60U [120].

- **Steady-state scenarios**
  Steady-state scenarios are advanced tokamak scenarios in which the plasma current is sustained with no poloidal flux consumption during the burn phase.

  Obtaining and sustaining a wide region of low shear in the plasma centre while maintaining the q-profile above unity constitutes one of the major challenges raised by steady-state scenarios. Such a task requires the achievement of a specifically shaped pressure profile in order to favourably shape the bootstrap current density profile, which can be a dominant current drive source.

  The fusion gain achieved by steady-state scenarios is lower than that achieved by inductive or hybrid scenarios. The plasma current and plasma density of steady-state scenarios are typically lower than those achieved by inductive scenarios or hybrid scenarios. Steady-state scenarios achieve of course high neutron fluence per plasma pulse.

  Steady-state scenarios have been successfully performed in TCV [121, 122, 19], TRIAM [123], and Tore Supra [124]. TRIAM and Tore Supra relied on intense external current drive for providing stationary conditions, whereas TCV produced a steady-state pulse based on 100% bootstrap current fraction.

The hybrid and steady-state scenarios both show a significant improvement in confinement. Confinement is typically scaled by three different metrics: the energy confinement enhancement factor $H_{98}(y,2)$, the normalised β_N, and the poloidal β_p:

- The energy enhancement factor is defined by

$$H_{98}(y,2) \quad = \quad \frac{\tau_E}{\tau_E^{\text{IPB98(y,2)}}}, \tag{5.1}$$

where

$$\tau_E = \frac{W}{P_{\text{add}} - \frac{dW}{dt}},$$

where W is the plasma energy. $\tau_E^{\text{IPB98(y,2)}}$ is the ITER physics basis (IPB) confinement time scaling 98(y,2) for ELMy H-mode ITER pulses [125] :

$$\tau_E^{\text{IPB98(y,2)}} = 0.0562 I_p^{0.93} B_\phi^{0.15} P_{\text{add}}^{-0.69} n_e^{0.41} M^{0.19} R^{1.97} \left(\frac{a}{R}\right)^{0.58} \kappa^{0.78},$$

where I_p is expressed in [MA], P_{add} is expressed in [MW], n_e is expressed in [10^{19} m^{-3}], M is expressed in [AMU], and R is expressed in [m].

- The normalised β_N is defined by

$$\beta_N = \beta \frac{aB}{I_p}, \tag{5.2}$$

with β_N in [%], a in [m], B is the mean value of the magnetic field within the plasma in [T], and I_p in [MA];

- The poloidal β_p is defined by

$$\beta_p = \frac{\langle p \rangle}{B_a^2/2\mu_0},$$

where, in this case, $\langle \cdot \rangle$ denotes the poloidal plasma surface average and where B_a is defined as

$$B_a = \frac{\mu_0 I_p}{L},$$

with L the perimeter of the plasma cross-section.

Successful operation of advanced scenarios in ITER will be a crucial step-forward in view of developing controlled fusion as an economically viable power production method. It is therefore important to assess whether the present design of the ITER PF system and heating and current drive systems enables the implementation of advanced scenarios in ITER.

Predictive simulations of ITER advanced scenarios help identify the main challenges that must be met for successful operation and assess the feasibility of the ITER advanced scenarios with a significant level of certainty. Because advanced scenarios make use of the synergy between the PF system and the heating and current drive systems, modelling the cross-coupling effects between plasma equilibrium evolution and transport is required. ITER advanced scenarios are thus best modelled using full tokamak simulators.

Exploratory full tokamak simulations of the ITER hybrid scenario ramp-up have been per-

formed with DINA-CH&CRONOS by Sun Hee Kim [88]. Simulations of the ITER hybrid and steady-state scenarios flat-top configurations have been performed by several prescribed-boundary simulators and the full tokamak simulator TSC [126]. Full tokamak simulations of the ITER hybrid scenarios have recently been performed using the CORSICA simulator [127].

This Chapter exposes simulations of the ITER hybrid and steady-state scenarios using the full tokamak simulator DINA-CH&CRONOS. The work presented is an advance with respect to the previous work mentioned thanks to the following improvements:

- The latest ITER design [44] is implemented;

- The VS3 coils and the VS3 power supply are included;

- The constraints on currents and vertical forces that the PF coils can sustain are implemented;

- Realistic modelling of the PF system power supplies is included;

- A realistic PF system current limiter feedback loop is implemented on each individual power supply in order to prevent the PF system currents from violating their operation limits;

- The breakdown occurs inboard;

- Tokamak electromagnetic and kinetic control strategies are improved with respect to previous work:

  - In [88], the plasma initiation phase and early ramp-up were controlled using a pre-programming approach tuned by trial and error. In this work, an automated feedforward control scheme is implemented;

  - Previous work relied on accurate prior knowledge of the PF coil current evolution. In this work, significantly less accurate prior knowledge of PF coil current evolution is required for operation. Approximate hand-waving calculations are sufficient;

  - A kinetic controller preventing the formation of a current hole is designed and implemented;

- Transport models and assumptions are upgraded:

  - Hybrid and steady-state scenarios observe a significant confinement improvement that can lead to $H_{98}(y,2) \geq 1$, $\beta_N \geq 2.4\%$, and $\beta_p \geq 1$ [128]. Such conditions are observed in ASDEX Upgrade, DIII-D, JET, and JT-60U but previous simulations have shown difficulty to achieve them when using the GLF23 transport model [129, 130]. The present work uses a Bohm/Gyro-Bohm transport model that enables the achievement of high confinement conditions;

  - Pedestal pressures are scaled according to the EPED model, rendering them more realistic [131];

– The density profile is assumed to be peaked with a peaking factor

$$\frac{n(\rho = 0)}{\langle n \rangle} = 1.4.$$

This is a realistic assumption according to recent analysis in which low collisionality plasmas show an enhanced peaking factor [132].

– The $H_{98}(y,2)$ confinement enhancement factor is assumed to be $H_{98}(y,2) = 1.3$ for the hybrid scenario and $H_{98}(y,2) = 1.35$ for the steady-state scenario. These values correspond to JET hybrid regime experimental data [118].

• Finally, full simulations from $t = 1.5$s after the breakdown until plasma termination are performed, thus enabling the assessment of the full scenario and its evolution over long time scales.

This work is performed in two steps emulating the scenario development process likely to be applied on ITER:

1. Nominal hybrid and steady-state scenarios are developed via prescribed-boundary simulations using CRONOS. CRONOS enables a preliminary exploration of the operation space without taking on the full complexity of full tokamak simulators. Thanks to its modularity, CRONOS is well-suited for assessing the effect of different transport models and physical assumptions on the prescribed-boundary plasma evolution. It enables the study of different heating and current drive scenarios and their effect on the q-profile evolution. The MHD stability of the developed scenarios is analysed using the MISHKA code [133].

   The outcome of this first step is a nominal hybrid scenario and a nominal steady-state scenario consisting of the following nominal parameters:

   • The plasma equilibrium reference waveforms;
   • The reference heating and current drive system configurations;
   • The reference heating and current drive power demand waveforms;
   • The reference density evolution.

   The CRONOS prescribed-boundary simulations help assess the validity and sensitivity of the selected transport models and estimate the sensitivity of the advanced scenario with respect to physical assumptions.

2. The nominal scenarios developed using CRONOS are imported in the DINA-CH&CRONOS framework to perform full tokamak simulations of the ITER hybrid and steady-state scenarios. The nominal scenarios are slightly adjusted to account for discrepancies between the CRONOS prescribed-boundary simulations and the DINA-CH&CRONOS full tokamak simulations.

One of the main goals of such a scenario development procedure is to emulate the typical scenario development scheme performed on tokamaks and extrapolate this approach to ITER in order to expose the difficulties encountered.

It must be stated that the present work is the result of a tight collaboration with CEA. More specifically, the prescribed-boundary simulations using CRONOS, the transport model selection and assessment, and the prescribed-boundary sensitivity studies were performed by Jeronimo Garcia, under the supervision of Frédéric Imbeaux. The MHD stability analysis is the result of the work of Patrick Maget. Moreover, the present Chapter benefited from the contributions of a wide consortium of collaborators because it was partly realised in the framework of a Fusion for Energy (F4E) grant. Hence, it is clear that the results presented in this Chapter are not entirely the fruit of the author's own work, which mainly consisted of importing the nominal scenarios into the DINA-CH&CRONOS framework, appropriately configure the full tokamak simulator to encapsulate the physical assumptions and transport models used during the prescribed-boundary scenario development phase, develop and/or assess the performance of several feedforward and feedback controllers, and perform full tokamak simulations of the hybrid and steady-state scenarios.

The complete analysis is presented because it really consists of one indivisible piece of work.

Paragraphs 5.1 and 5.2 describe the hybrid scenario and the steady-state scenario development using CRONOS. The DINA-CH&CRONOS configuration and control systems are described in 5.3. Full tokamak simulations of the hybrid scenario and the steady-state scenario are respectively exposed in paragraphs 5.4 and 5.5. A discussion is presented in paragraph 5.6 and the lessons learned are exposed in paragraph 5.7.

5.1 Prescribed-boundary simulations of the ITER hybrid scenario using CRONOS

In this paragraph, CRONOS is applied to develop a nominal ITER hybrid scenario and to perform relevant sensitivity studies on some of the most critical assumptions made regarding transport modelling.

The development of the hybrid scenario is firstly described in 5.1.1. Improvements of the hybrid scenario are then described in 5.1.2. 5.1.3 exposes several sensitivity studies regarding the hybrid scenario. Finally, The MHD stability of one flat-top equilibrium 'snapshot' is then assessed in 5.1.4.

5.1.1 ITER hybrid scenario development using CRONOS

The main hybrid scenario characteristics are exposed in Table 5.1.

These characteristics are really guidelines for scenario development thus providing a clear

Table 5.1: ITER hybrid scenario main characteristics.

Parameter	ITER hybrid scenario value during flat-top
I_p	12MA
$B_\phi(R_0 = 6.2\text{m})$	5.3T
q_{95}	4.3
κ	1.8
δ	0.4
β_N	2.65
β_p	1.45
$\bar{n}/\bar{n}_{\text{Greenwald}}$	0.8
p_{pedestal}	75kPa
$H_{98}(y,2)$	1.3
P_{NBI}	33MW
P_{ECRH}	20MW
P_{ICRH}	20MW
P_{LH}	0MW

target for which to aim.

Several features observed in present-day hybrid scenarios must be achieved in the ITER hybrid scenario amongst which two main challenges stand out [134]. Firstly, the q-profile must be maintained above unity for the complete duration of the scenario ramp-up and flat-top phases in order to prevent the triggering of sawteeth, which would be detrimental to plasma confinement. Secondly, a broad region of low magnetic shear must be achieved and maintained in order to reduce MHD activity.

Transport modelling and physical assumptions

The CRONOS suite of codes self-consistently solves the electron and ion heat transport equations, models the additional heating and current drive power depositions given a prescribed plasma boundary evolution, and solves the current diffusion when used in standalone. The electron density profile $n_e(\rho)$ and the effective atomic number profile $Z_{\text{eff}}(\rho)$ evolutions are prescribed. The plasma toroidal rotation is not taken into account.

In these simulations, the plasma boundary is prescribed to evolve similarly to previous simulations of the ITER 15MA H-mode scenario [135], the shape being assumed to evolve as a function of the plasma current. In order to avoid an overly optimistic influence of the separatrix on the evolution of the q-profile, the prescribed plasma boundary is slightly modified in order to achieve $q_{95} = 4.3$. The prescribed plasma boundary evolution during ramp-up is displayed in Figure 5.1.
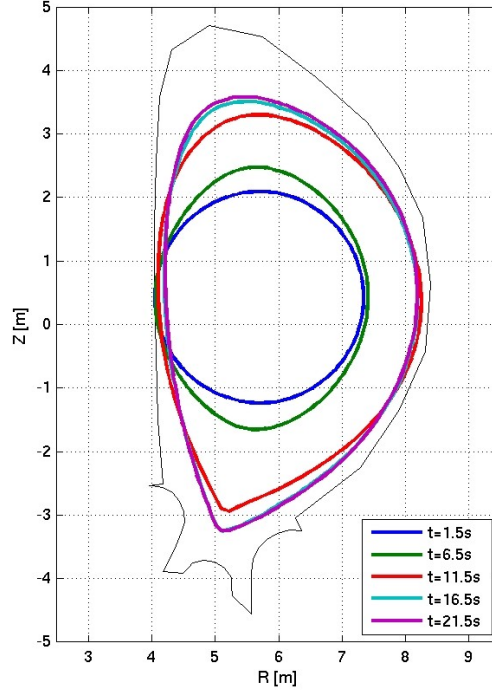
Figure 5.1: Prescribed evolution of the plasma boundary during the ITER hybrid scenario ramp-up.

The Bohm/Gyro-Bohm model is used for heat diffusivity. During L-mode, it is used in its original version without imposing that the heat diffusivity profiles depend on the magnetic shear, which has been demonstrated to provide reliable results [78, 136]. During H-mode, the Bohm/Gyro-Bohm model is renormalised in order to force $H_{98}(y,2) = 1.3$. This is a strong prescription and the hybrid scenario evolution sensitivity to this assumption is analysed in the sensitivity studies.

A peaked density profile is prescribed during flat-top. Such a peaked density profile is in line with the state-of-the-art physical understanding of electron transport because the density profile is expected to be more peaked in hybrid scenarios than in typical H-mode scenarios due to the low collisionality of the hybrid regimes. A peaked density profile increases the magnitude of the bootstrap current thus enabling easier sustainment of the q-profile above unity during flat-top. The line-average density is prescribed to correspond to $0.4\bar{n}_{\text{Greenwald}}$ during the ramp-up and ramp-down, i.e. 40% of the Greenwald density limit, and to $0.8\bar{n}_{\text{Greenwald}}$ during flat-top. This is routinely achieved in JET.

In the H-mode regime, the pedestal is assumed to be located between the plasma boundary and the $\rho = 0.95$ flux surface. The pedestal density is prescribed to be $n_e(\rho = 0.95) \cong 5.5 \cdot 10^{19} \text{m}^{-3}$ and the pedestal electron temperature is assumed to be $T_i(\rho = 0.95) = T_e(\rho = 0.95) \cong$

4.5keV, thus corresponding to a 75kPa pedestal electron pressure.

The transition from the low confinement mode to the high confinement mode (the L-H transition) and the inverse H-L transition are modelled as abrupt changes in transport. These transitions are triggered when the power threshold as defined in [137] is reached. The density pedestal is prescribed to progressively appear with the L-H transition and to progressively vanish when the H-L transition occurs.

Prescribed-boundary simulation results

A prescribed-boundary simulation of the hybrid scenario is performed using CRONOS. As expected, the plasma pulse is neither steady-state nor stationary and about 25% of the plasma current is inductively driven during flat-top.

The flat-top q-profile is as desired, i.e. it shows a wide region of low magnetic shear in the plasma centre and remains above unity during the complete duration of the burn phase. However, in spite of the high temperature in the plasma centre which is of the order of 30keV, the plasma current diffuses during flat-top. As a result, the q-profile slowly drops towards unity and would eventually reach it if the burn phase were to be extended significantly beyond 1000s. This result is displayed in Figure 5.2.
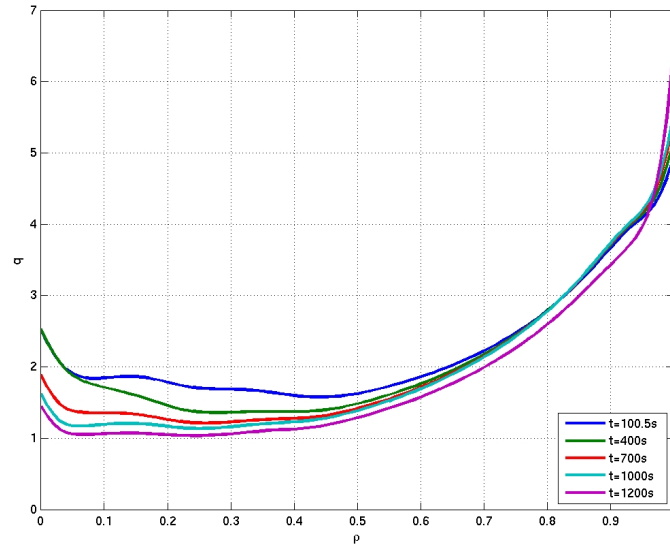

Figure 5.2: CRONOS simulation of the evolution of the q-profile during the hybrid scenario flat-top.

The simulated evolution of the plasma current, which is I_p = 12MA in flat-top, the simulated evolution of β_p, the evolution of the enhancement factor $H_{98}(y,2)$, which reaches $H_{98}(y,2)$ = 1.3 during flat-top, and the evolution of the fusion gain Q, which averages Q =7.8 during
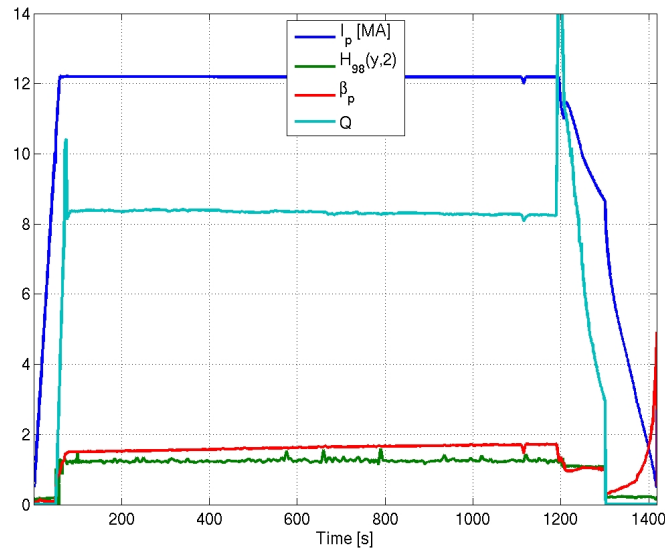
flat-top, are displayed in Figure 5.3.

Figure 5.3: CRONOS simulation of the evolution of the plasma current I_p, the β_p factor, the confinement enhancement factor $H_{98}(y,2)$, and the fusion gain Q. The L-H transition occurs slightly before $t = 50$s and the H-L transition occurs at $t = 1300$s.

The heating and current drive system total power depositions within the plasma are displayed in Figure 5.4. ECRH power is applied during ramp-up in order to prevent a fast decrease of the q-profile before the L-H transition, which occurs slightly before $t = 50s$.
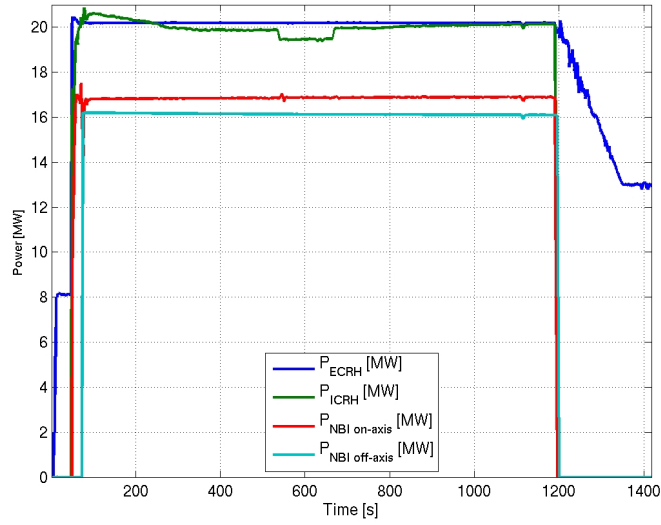
Figure 5.4: CRONOS simulation of the evolution of the total power at the plasma boundary generated by the external heating systems.

The flat-top plasma current is divided among the following contributions:

- The bootstrap current contributes to 39% of the total plasma current, i.e. $I_{\text{boot}} = 4.7\text{MA}$ during flat-top;

- The NBI systems contribute to 29% of the total plasma current, i.e. $I_{\text{NBI}} = 3.5\text{MA}$ during flat-top;

- The EC systems contribute to 6.1% of the total plasma current, i.e. $I_{\text{EC}} = 0.74\text{MA}$ during flat-top;

- The remaining plasma current is driven inductively.

The conclusion of this prescribed-boundary simulation is that a hybrid scenario with $I_p = 12\text{MA}$ can be maintained in flat-top for a 1000s burn period with $Q = 7.8$.

5.1.2 Improvements of the hybrid scenario

Several features of the hybrid scenario presented in the previous paragraph had to be tuned in order to achieve satisfactory performance. This paragraph discusses some of the most outstanding characteristics critical in view of maintaining the hybrid scenario high performance. In the following, performance is measured in terms of pulse duration, fusion gain, and MHD stability.

Electron cyclotron heating and current drive during ramp-up

In order to prevent the q-profile from rapidly dropping during ramp-up, EC power is injected within the plasma starting at $t = 6.5$s. The power is deposited mostly at $\rho = 0.4$. This target power deposition location is calculated according to the procedure exposed in [138].

Simulations using different levels of EC power were performed. It was deduced that 8MW of demand EC power before the L-H transition was an appropriate demand. Less deposited power led to faster q-profile drop, whereas more deposited power generated a strongly reversed shear profile at the end of ramp-up, as displayed in Figure 5.5.
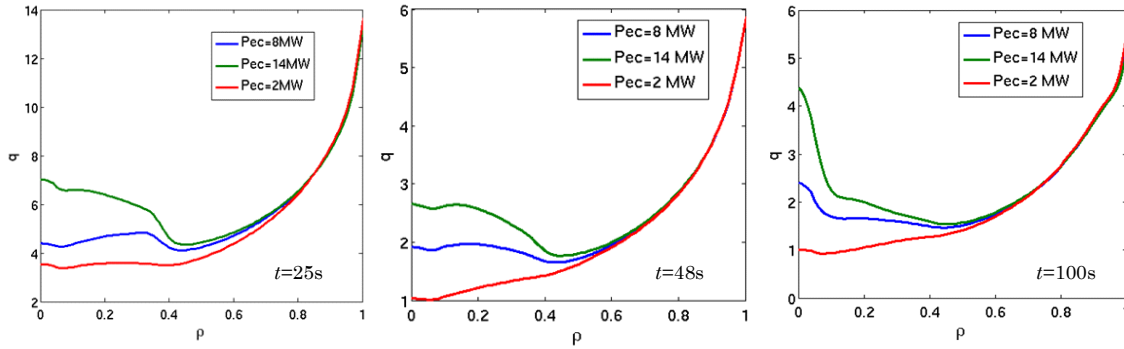
Figure 5.5: Evolution of the q-profile during ramp-up with different EC heating demands.

L-H transition timing

The L-H transition timing is a crucial characteristic of the hybrid scenario and the achievable hybrid pulse length was demonstrated to be extremely sensitive to this parameter. An earlier L-H transition 'freezes' the q-profile when it is at a higher value, thus enabling longer pulse durations. However, an earlier L-H transition carries a higher risk of enabling the formation of a reversed shear profile and even the formation of a current hole in the plasma centre, i.e. a region in the plasma centre in which there is almost no plasma current density. A reversed shear profile, or worse, the presence of a current hole, are to be avoided because these features are detrimental to MHD stability and, in turn, to energy confinement.

The onset of 20MW of ECRH power, 20MW of ICRH power, and 16.5MW of NBI on-axis power triggers the L-H transition. The timing of this heating onset is set at $t = 49.5$s, thus corresponding to $I_p(t = 49.5\text{s}) \cong 10$MA because the plasma current is ramped up at the predetermined rate of $dI_p/dt = 0.18$MA/s.

NBI off-axis timing

The ITER NBI heating systems possess the capability of depositing NBI power either on-axis, i.e. centred at $\rho = 0$, or off-axis. The ITER NBI systems cannot meet any arbitrary power demand, but can only operate in the following configurations:

- **33MW NBI on-axis**
  In this case, the NBI systems are configured prior to the plasma pulse to deposit power on-axis. The provided power is either 0MW, 16.5MW (half-power), or 33MW (full power);

- **33MW NBI off-axis**
  In this case, the NBI systems are configured prior to the plasma pulse to deposit power off-axis. The provided power is either 0MW, 16.5MW (half-power), or 33MW (full power);

- **16.5MW NBI on-axis and 16.5MW off-axis**
  In this case, the NBI systems are configured prior to the plasma pulse to deposit half of the available power on-axis and the other half off-axis. The provided power is either

    - 0MW on-axis and 0MW off-axis;

    - 0MW on-axis and 16.5MW off-axis;

    - 16.5MW on-axis and 0MW off-axis;

    - 16.5MW on-axis and 16.5MW off-axis.

The ITER NBI systems configuration must be implemented before the plasma pulse and cannot be modified on-the-fly. In our case, the 16.5MW on-axis and 16.5MW off-axis NBI configuration is chosen.

16.5MW of NBI on-axis power is injected into the plasma at $t = 49.5s$ to help trigger the L-H transition, but the NBI off-axis system is switched on later during the pulse. This helps prevent the formation of a current hole.

The onset timing of the off-axis NBI has been varied from $t = 49.5s$ to $t = 200s$. As a result of this study, the off-axis NBI is best switched on at about $t = 75s$. This enables longer operation and relieves the load from the PF system by driving more plasma current earlier using NBI systems. At the same time, it prevents the formation of a current hole.

Ramp-down

Two different strategies for the ramp-down phase are designed and implemented:

- The first strategy consists of removing the 16.5MW of off-axis NBI deposited power 15s prior to the beginning of the plasma current ramp-down and bringing all the heating and current drive demand powers to zero as the plasma current ramp-down starts,

except for 10MW of EC power. The H-L transition is triggered about 50s into the plasma current ramp-down because the fusion power remains high during the beginning of the ramp-down phase.

This strategy consumes volt-seconds because the plasma current ramp-down rate is low in absolute value ($dI_p/dt = -0.05$MA/s).

- The 20MW of ICRH power and the 16.5MW of NBI on-axis power are brought to zero 15s before the plasma ramp-down. The NBI off-axis power is switched off simultaneously with the beginning of the plasma current ramp-down. The ECRH power is linearly brought down from 20MW to 13MW in 150s starting from the beginning of the plasma current ramp-down.

  This approach delays the H-L transition to about 100s into the ramp-down. This has several beneficial effects. Firstly, a fraction of plasma current is driven by ECCD thus saving volt-seconds. This ensures reliable operation even in the case of an unexpectedly high volt-second consumption during flat-top. Secondly, the H-L transition occurs at lower plasma current and is thus less of a burden on the control system. It is also less likely to cause serious damage to the first wall if the control of the plasma column is lost. Finally, driving off-axis current density via ECCD helps prevent current density peaking. This restrains the plasma vertical instability growth rate from increasing in an uncontrolled manner.

5.1.3 Sensitivity analyses

The sensitivity of the hybrid scenario with respect to some of the most critical physical assumptions made is assessed in this section.

Sensitivity to plasma boundary shape

In order to analyse the influence of the flat-top prescribed boundary on the hybrid scenario evolution, a simulation with a less elongated flat-top boundary is performed. The comparison between the nominal plasma boundary and the less elongated plasma boundary is displayed in Figure 5.6.

The less elongated plasma boundary leads to a faster drop of the q-profile during flat-top, thus reducing the achievable hybrid scenario pulse duration. This is exposed in Figure 5.7.

There are two explanations for such behaviour. Firstly, the less elongated plasma boundary leads to a flat-top $q_{95} = 3.5$, whereas the nominal hybrid scenario possesses a higher value of $q_{95} = 4.3$. In turn, this drives the complete q-profile to a lower value. Secondly, the bootstrap current is decreased as displayed in Figure 5.8. In turn, this lower bootstrap current increases the magnetic diffusion and accelerates the drop of the q-profile during flat-top.
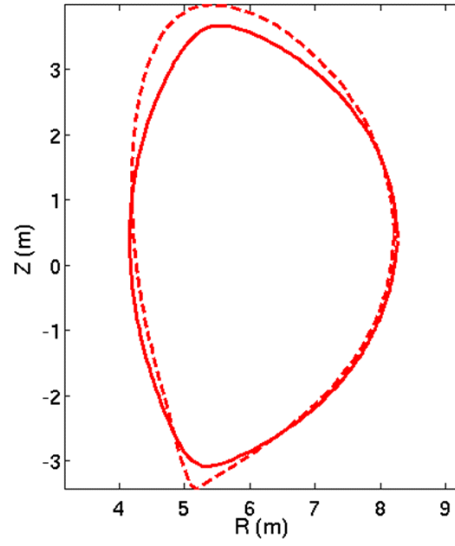
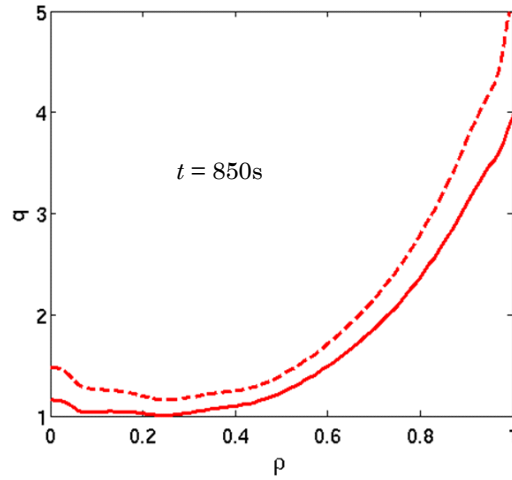Figure 5.6: Comparison between the nominal plasma boundary (dashed) and the less elongated plasma boundary (solid).

Figure 5.7: Comparison between the nominal q-profile evolution (dashed) and q-profile evolution using the less elongated plasma boundary (solid).

Sensitivity to density peaking

The effect of density peaking on the hybrid scenario evolution is analysed via the comparison of two extra simulations with different peaking factors. In order to isolate the effect of density peaking, the density at the pedestal is tailored so that the bootstrap current near the plasma boundary remains unchanged. The nominal hybrid scenario density profile and bootstrap
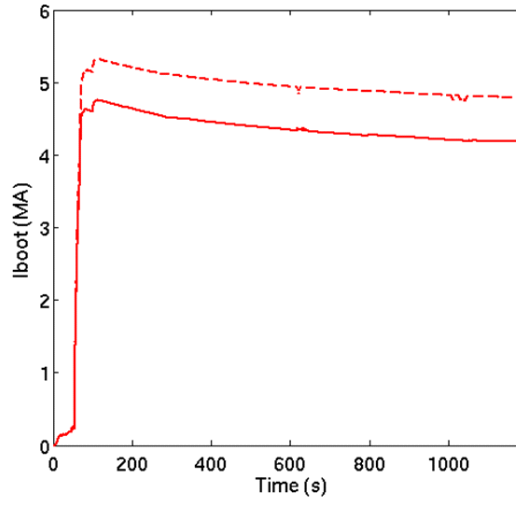
Figure 5.8: Comparison between the nominal total bootstrap current evolution (dashed) and total bootstrap current evolution using the less elongated plasma boundary (solid).

current profile is compared to two simulations with lower density peaking, as displayed in Figure 5.9.
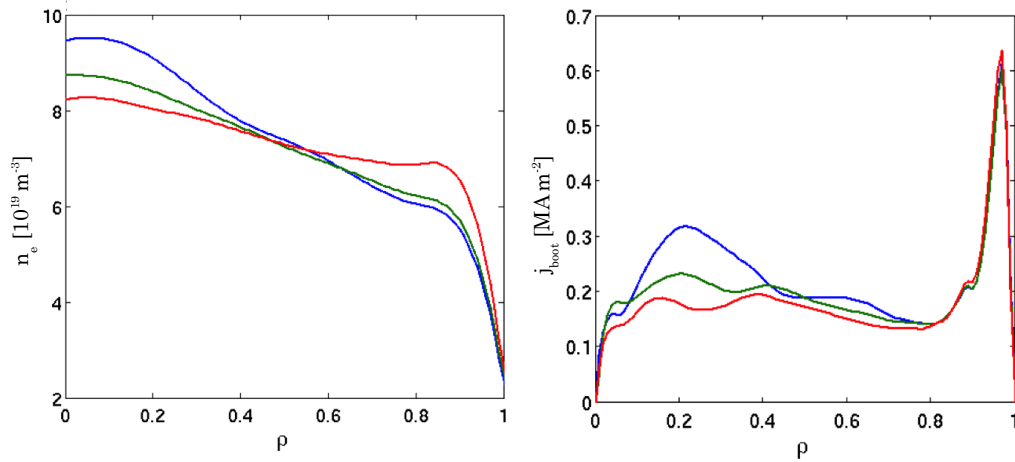

Figure 5.9: Comparison between the nominal hybrid scenario density profile and bootstrap current density (blue) and total bootstrap current profile of simulations using lower density peaking factors.

Reducing the density peaking reduces the bootstrap current around $\rho = 0.2$. This has a detrimental effect on the q-profile evolution, as displayed in Figure 5.10.

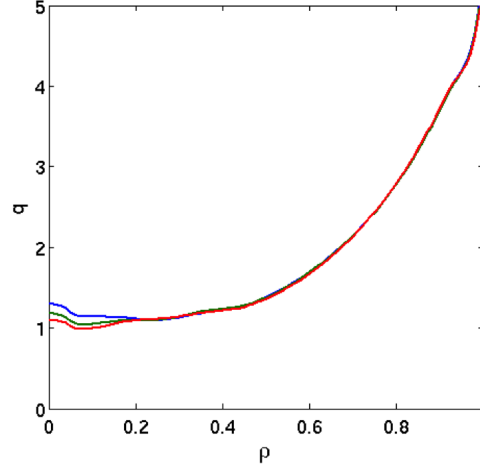In conclusion, lower density peaking leads to shorter hybrid pulses.

Figure 5.10: Comparison between the nominal hybrid scenario q-profile at $t = 1200s$ (blue) and the q-profile at $t = 1200s$ of simulations using lower density peaking factors.

Sensitivity to the confinement enhancement factor

The sensitivity of the hybrid scenario with respect to the confinement enhancement factor $H_{98}(y,2)$ is assessed by performing two simulations with lower confinement enhancement factors of respectively $H_{98}(y,2) = 1.15$ and $H_{98}(y,2) = 1$.

As expected, the ion and electron temperatures decrease as the prescribed confinement enhancement factor decreases. This has two major implications. Firstly, a reduction in plasma temperature increases the current penetration speed. Secondly, it reduces the magnitude of the bootstrap current. Both these effects lead to a faster q-profile drop. This is displayed in Figure 5.11.
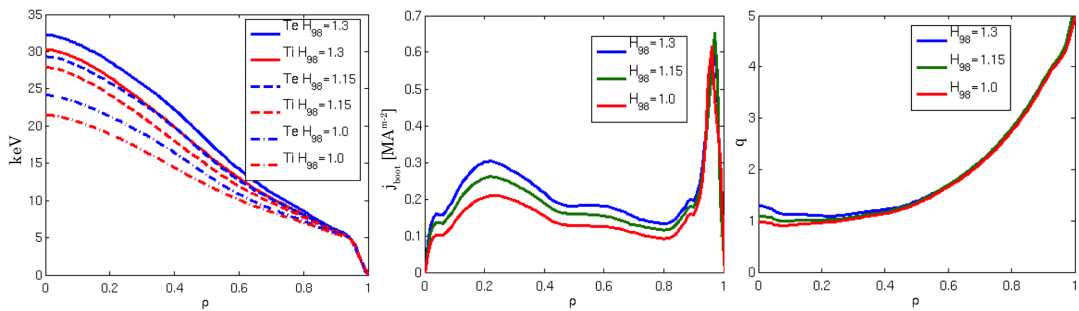

Figure 5.11: Comparison between the nominal hybrid scenario ion and electron temperature profile, bootstrap current profile, and q-profile at $t = 1200s$ with simulations with lower confinement enhancement factor.

As a result, lower confinement enhancement factors imply shorter hybrid pulses. This sensi-

tivity study suggests that a minimum value of $H_{98}(y,2) \cong 1.15$ is necessary in order to sustain the hybrid regime for about 1000s.

Sensitivity to the pedestal temperature

The sensitivity of the hybrid scenario evolution with respect to the pedestal electron temperature ($T_{ped} = 4.5$keV in the nominal case) is analysed by performing two simulations with respectively a lower pedestal temperature $T_{ped} = 3.7$keV and a higher pedestal temperature $T_{ped} = 5.4$keV. The nominal density profile is maintained for all three simulations in order to isolate the effect of the pedestal temperature. The flat-top electron temperature profile is displayed in Figure 5.12.
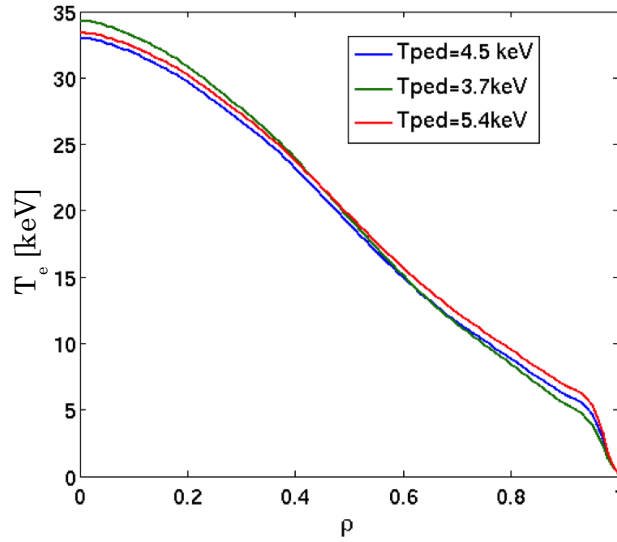

Figure 5.12: Comparison between the nominal hybrid scenario electron temperature profile (blue) with simulations with lower (green) and higher (red) pedestal temperature at the end of flat-top.

An increase in pedestal temperature leads to a decrease in central temperature, as opposed to the results of stiff models. This parametric dependence is not intuitive and, to some extent, may not be physical. In fact, the underlying assumption that the confinement enhancement factor is independent of the pedestal temperature is rather strong, and may lead to unexpected plasma behaviour. Nevertheless, modifications in the plasma core are relatively small and the largest relative changes occur at the pedestal. The bootstrap current is directly affected by the difference in pedestal pressure, as displayed in Figure 5.13.

The resulting effect on the central values of the q-profile is small and it can be stated that the hybrid scenario evolution is not very sensitive to modifications in the pedestal temperature.
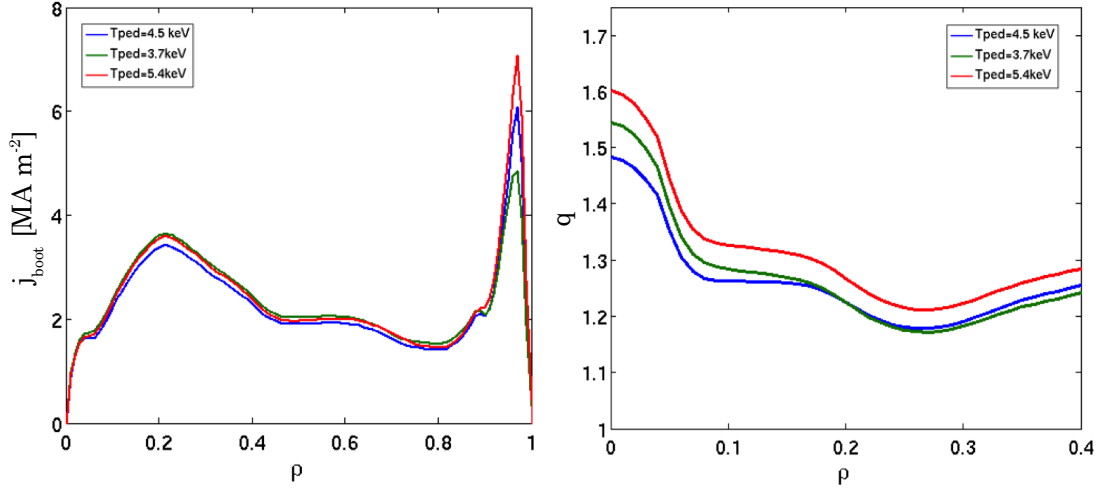
Figure 5.13: Comparison between the nominal hybrid scenario bootstrap current profile and q-profile (blue) with simulations with lower (green) and higher (red) pedestal temperature.

Conclusion of the sensitivity analysis

The evolution of the hybrid scenario, and more specifically the evolution of the q-profile, depends strongly on the plasma boundary shape and the value of the confinement enhancement factor $H_{98}(y, 2)$. Small deviations in these parameters from the nominal scenario may lead to a serious degradation of the scenario, in that the q-profile may reach unity significantly earlier than in the nominal case.

The q-profile evolution is sensitive to the density peaking and the pedestal temperature to a lesser extent.

5.1.4 Analysis of the MHD stability of the hybrid scenario

The flat-top linear MHD stability of the hybrid scenario is analysed with the code MISHKA. The MHD modes ranging from $n = 1$ to $n = 40$ are displayed in Figure 5.14, which is a peeling-ballooning diagram.

The hybrid scenario flat-top equilibrium is found to be stable to all the modes, including $n = 1$ and $n = 2$.

In order to provide insight regarding the MHD stability of a slightly different hybrid pulse, another MHD stability study is performed using the same plasma parameters except for the plasma shape which is assumed to have a higher upper triangularity than the nominal hybrid scenario. The results displayed in Figure 5.15 demonstrate that the linear MHD stability diagram is highly dependent on the plasma shape.
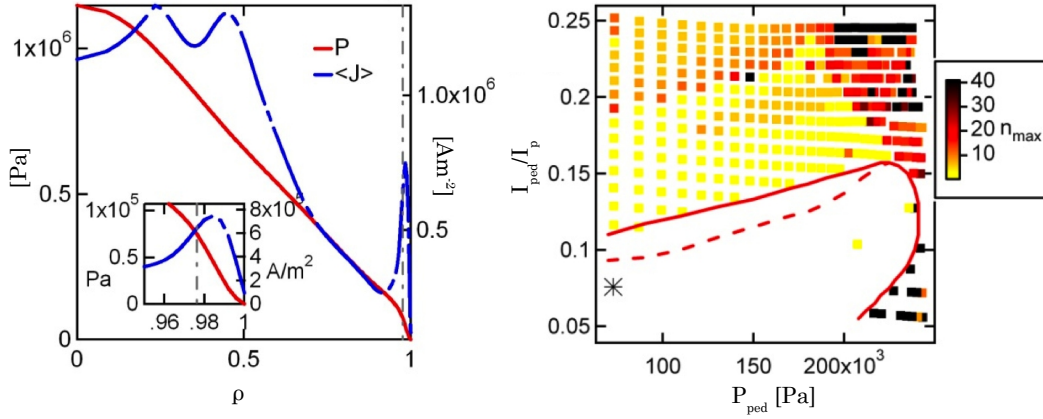
Figure 5.14: Pressure and current density profiles and peeling-ballooning diagram of a nominal hybrid scenario flat-top equilibrium. The dotted line includes n=1 and n=2 modes and the plain line covers $n > 2$ modes. The star denotes the nominal hybrid scenario flat-top equilibrium.
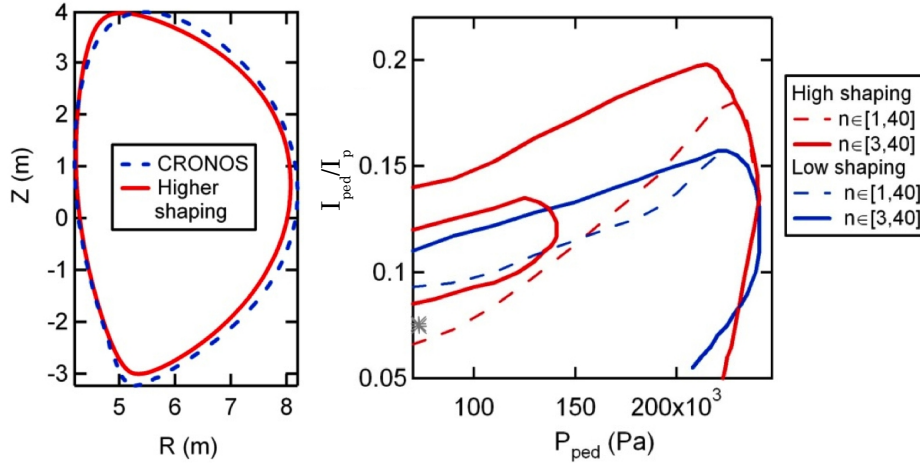

Figure 5.15: Comparison between the nominal hybrid scenario shape and a higher upper triangularity shape. The peeling-ballooning diagram both simulations is displayed on the right-hand side. The dotted line includes n=1 and n=2 modes and the plain line covers $n > 2$ modes. The star denotes the nominal hybrid scenario flat-top equilibrium.

5.2 Prescribed-boundary simulations of the ITER steady-state scenario using CRONOS

In this paragraph, CRONOS is applied to develop a nominal ITER steady-state scenario using a prescribed-boundary approach. This work heavily relies on the prescribed-boundary

simulations performed for the ITER hybrid scenario.

The proposed steady-state scenario differs from previous work in which a steady-state configuration is either achieved by the presence of an Internal Transport Barrier (ITB) [139] or by high pedestal temperatures [140]. In our case, the steady-state scenario characteristics are close to those of the ITER hybrid scenario, thus benefiting from the analyses exposed in the previous paragraph.

5.2.1   ITER steady-state scenario development using CRONOS

The main desired scenario characteristics are exposed in Table 5.2.

Table 5.2: ITER steady-state scenario main characteristics.

Parameter	ITER steady-state scenario value during flat-top
I_p	10MA
$B_\phi(R_0 = 6.2\text{m})$	5.3T
q_{95}	4.8
κ	1.8
δ	0.4
β_N	2.7
β_p	1.66
$\bar{n}/\bar{n}_{\text{Greenwald}}$	0.8
p_{pedestal}	60kPa
$H_{98}(y,2)$	1.35
P_{NBI}	33MW
P_{ECRH}	20MW
P_{ICRH}	20MW
P_{LH}	15MW

The ITER steady-state scenario characteristics differ from the ITER hybrid scenario characteristics in several instances. Most importantly, the target steady-state flat-top plasma current is 10MA and 15MW of lower hybrid (LH) power is assumed to be available. The transport modelling and physical assumptions are identical to those of the nominal ITER hybrid scenario.

Prescribed-boundary simulation results

A prescribed-boundary simulation of the steady-state scenario is performed using CRONOS. The plasma successfully reaches a steady-state regime soon after the LH current drive is injected in the plasma at $t = 200$s.

The flat-top q-profile is stationary and shows a wide region of low shear near the plasma centre. It is slightly hollower than that achieved in the ITER hybrid scenario simulation. This is displayed in Figure 5.16.
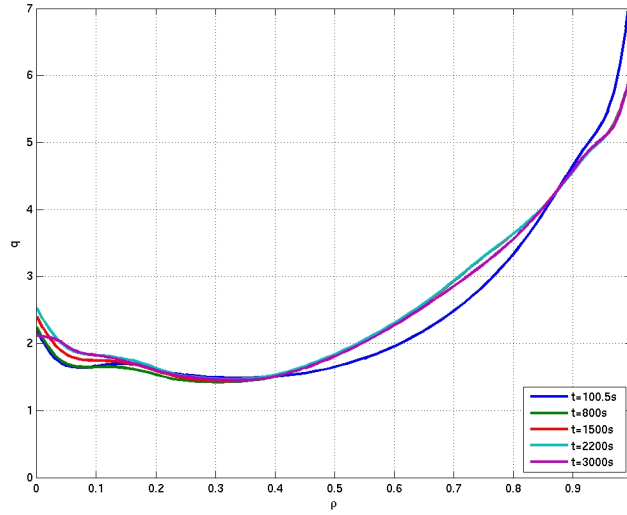

Figure 5.16: CRONOS simulation of the evolution of the q-profile during the steady-state scenario flat-top.

The simulated evolutions of the plasma current, of β_p, which achieves $\beta_p \cong 1.66$ in flat-top, of the confinement enhancement factor $H_{98}(y,2)$, which averages $H_{98}(y,2) \cong 1.35$ during flat-top, and of the fusion gain Q, which averages $Q \cong 5$ during flat-top, are displayed in Figure 5.17.
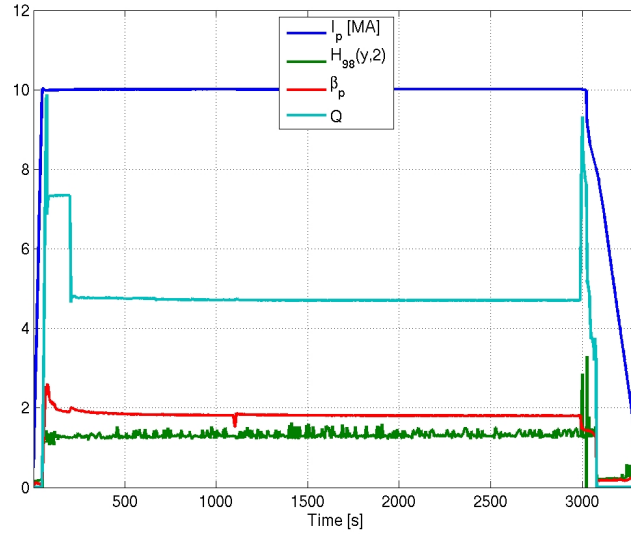
Figure 5.17: CRONOS simulation of the evolution of the plasma current I_p, the β_p factor, the confinement enhancement factor $H_{98}(y, 2)$, and the fusion gain Q. The L-H transition occurs slightly before $t = 50$s and the H-L transition occurs at $t = 3076$s.

The heating and current drive system total power deposition within the plasma are displayed in Figure 5.18.

Figure 5.18: CRONOS simulation of the evolution of the total power at the plasma boundary generated by the external heating systems.

The plasma current during flat-top is divided among the following contributions:
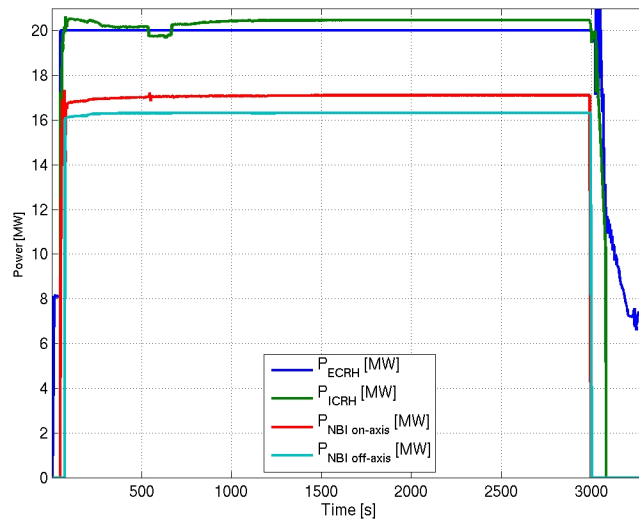
- The bootstrap current contributes to 50% of the total plasma current, i.e. $I_{\text{boot}} = 5\text{MA}$ during flat-top;

- The NBI systems contribute to 36% of the total plasma current, i.e. $I_{\text{NBI}} = 3.6\text{MA}$ during flat-top;

- The EC systems contribute to 7% of the total plasma current, i.e. $I_{\text{ECCD}} = 0.7\text{MA}$ during flat-top;

- The LH systems contribute to 7% of the total plasma current, i.e. $I_{\text{LHCD}} = 0.7\text{MA}$ during flat-top;

- In the steady-state regime, no plasma current is driven inductively.

This work demonstrated the feasibility of an ITER steady-state scenario with $I_p = 10\text{MA}$ using the baseline ITER heating and current drive systems with the addition of a 15MW lower hybrid system.

No specific sensitivity analyses were performed for the ITER steady-state scenario prescribed-boundary simulations because its most significant features are common with the hybrid scenario.

5.2.2 Analysis of the MHD stability of the steady-state scenario

As for the ITER hybrid scenario, the flat-top linear MHD stability of the steady-state scenario is analysed with the code MISHKA. The results are displayed in Figure 5.19.
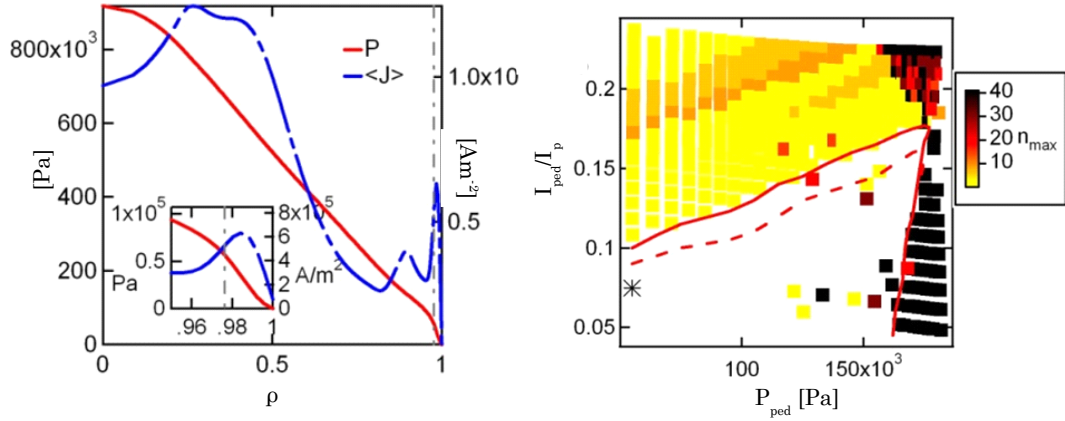
Figure 5.19: Pressure and current density profiles and peeling-ballooning diagram of a nominal steady-state scenario flat-top equilibrium. The dotted line includes $n=1$ and $n=2$ modes and the plain line covers $n > 2$ modes. The star denotes the nominal steady-state scenario flat-top equilibrium.

This study concludes that the simulated ITER steady-state scenario is stable to edge MHD modes during flat-top.

5.3 DINA-CH&CRONOS full tokamak simulator configuration and control systems

The nominal hybrid scenario and the nominal steady-state scenario developed using CRONOS are imported in the framework of DINA-CH&CRONOS in order to perform full tokamak simulations of the ITER hybrid and steady-state scenarios. The following parameters are extracted from the nominal scenarios:

- The plasma current reference waveform $I_{p,\text{ref}}$;

- The reference plasma centroid evolution $(R_{\text{mag,ref}}, Z_{\text{mag,ref}})$;

- The gaps reference waveforms $\text{gap}_{i,\text{ref}}$, $i = 1, ..., 6$;

- The heating and current drive systems configurations;

- The heating and current drive power demand waveforms;

- The prescribed density profile evolution;

- The transport models and the modelling physical assumptions.

The full tokamak simulation control systems are detailed in 5.3.1 and the specific features regarding the operation of the DINA-CH&CRONOS full tokamak simulator are described in 5.3.2.

5.3.1 Control systems

The feedforward and/or feedback controllers must share the following actuators:

- The 11 Main Converters (MCs) DC demand voltage;

- The VS1 demand voltage;

- The VS3 demand voltage;

- The heating and current drive systems configurations;

- The heating and current drive systems power demands;

This section describes the control strategy, discusses the control specifications, and exposes the design of the various feedforward and feedback controllers implemented in the DINA-CH&CRONOS full tokamak simulations.

Control strategy

The control systems face several sometimes conflicting challenges. It is therefore important to define a clear control strategy that provides guidelines regarding the hierarchical relative importance of each control objective.

The primary objective of the control systems is to minimise operational risks. Plasma-wall contact should be avoided when the plasma current is high in order to prevent damage to the first wall. In that perspective, regulating the plasma column vertical instability is the most important challenge that must be met by the plasma control system. In ITER, the VS1 and VS3 power supplies are both dedicated to the regulation of the plasma column vertical speed. VS1 is foreseen to be routinely used, whereas VS3 is designed to be activated only in emergency situations.

Preventing plasma-wall contact also necessitates precise control of the plasma centroid position (weighted by the plasma current I_p) or precise control of the six gaps between the plasma separatrix and the first wall (weighted by I_p). The evolution of the plasma centroid position and the evolution of the gaps is controlled via the action of the MC demand voltages. In this work, the plasma centroid position and the gaps are never controlled simultaneously to avoid conflicting objectives.

The plasma current evolution is controlled via the action of the MC demand voltages.

The 11 MC demand voltages constitute an eleven-dimensional operation space. During flat-top, these eleven independent actuators are monitored to track and regulate six gaps and the plasma current, thus constituting a seven-dimensional controlled space at most. This configuration allows the system to wander in an uncontrolled four-dimensional null space. This feature led to inappropriate tokamak evolution in early full tokamak simulations in which the PF system exceeded their operational limits.

To address this challenge, it is common to over-constrain the null space by introducing eleven new controlled variables being the PF system coil currents. This approach has two main advantages. Firstly, it provides an explicit mechanism to exert some degree of control on the PF system coil currents, in effect preventing the PF systems from exceeding their limits by an appropriate choice of PF system coil current reference waveforms. Secondly, introducing the PF system coil currents as controlled variables has a tendency to prevent the formation of dipoles between PF coil pairs. However, controlling the eleven PF system coil currents requires the computation of eleven PF system coil reference waveforms that must not be conflicting with the plasma current reference waveform and the plasma shape reference waveform. These PF system coil reference waveforms must be computed prior to the full tokamak simulations using linear models such as CREATE-L [141].

In this work, the PF system coil current reference waveforms are computed by hand in order to provide rough waveforms for the control system to track. Loose tracking of the PF system coil current reference waveforms is tolerated. This approach is a trade-off between two opposite control philosophies in which either the PF system coil currents are not controlled at all, thus allowing the uncontrolled wandering of the system in the null space and the risks associated with such behaviour, or the PF system coil currents are very precisely controlled, thus necessitating accurate prior computation of the desired PF system coil current evolutions thus reducing pulse scheduling flexibility.

The formation of dipoles between PF coil pairs was observed in early full tokamak simulations. This effect is detrimental to the plasma controllability and increases the PF system power supplies power consumption. A low-frequency dipole controller regulating the current difference between selected PF coil pairs is implemented to address this challenge. The implementation of this dipole controller contributes to over-constrain the null space. The dipole controller does not restrain the average current in a PF coil pair.

The formation of a current hole in the plasma centre was observed in early full tokamak simulations. A current hole feedback controller was designed and implemented to prevent such behaviour. This current hole feedback controller uses heating and current drive system power demands as actuators.

The various feedforward and/or feedback controllers are switched on and off according to a pre-determined time-based schedule. This scheme, although not as robust as event-based switching, appears to be sufficient for full tokamak simulations of the ITER hybrid and steady-state scenarios.

In this work, there is no attempt to address the problem of windup, although this will have to be dealt with for the operation of ITER.

Control objectives

The control objectives may be expressed as follows:

> *The control system must track and regulate the plasma equilibrium evolution with respect to the scenario reference waveforms. It must do so to the best of the tokamak capabilities, i.e. in an aggressive manner, while providing sufficient robustness in order to overcome events such as an unforeseen L-H transition and an unforeseen H-L transition. Vertical stability must be guaranteed at all times during the plasma pulse.*

These control objectives are qualitative and provide guidelines regarding the design of controllers.

Plasma current controller design

The plasma current controller is a combination of a feedforward controller and a feedback controller.

The feedback controller is a simple PID controller. Such a feedback control scheme was selected because of its simplicity and its general robustness. The demand voltages are determined as follows:

$$
\mathbf{V}_{\text{demand}} = \left[\begin{array}{c} V_{\text{demand,CS3U}} \\ \vdots \\ V_{\text{demand,PF6}} \end{array} \right] = \mathbf{K}_{P_I}(I_{p,\text{ref}} - I_p) + \mathbf{K}_{I_I}\int_{t_0}^{t}(I_{p,\text{ref}} - I_p)\,dt' + \mathbf{K}_{D_I}\frac{d\left(I_{p,\text{ref}} - I_p\right)}{dt}, \quad (5.3)
$$

where $I_{p,\text{ref}} = I_{p,\text{ref}}(t)$ is the reference plasma current waveform. The output of the D term is filtered with a $\tau = 0.5$s characteristic time.

The gain vectors $\mathbf{K}_{P_I}$, $\mathbf{K}_{I_I}$, and $\mathbf{K}_{D_I}$ must be carefully constructed because it is important to *decouple* the effect of the plasma current feedback controller from the plasma centroid evolution. In other words, it is necessary to determine a linear combination of PF system power supply voltages that acts on the plasma current without significantly affecting the plasma centroid position.

In that perspective, the gains $\mathbf{K}_P$, $\mathbf{K}_I$, and $\mathbf{K}_D$ are chosen as collinear vectors. Hence,

$$
\begin{aligned}
\mathbf{K}_{P_I} &= K_{P_I}\mathbf{G}_{I_p} \\
\mathbf{K}_{I_I} &= K_{I_I}\mathbf{G}_{I_p} \\
\mathbf{K}_{D_I} &= K_{D_I}\mathbf{G}_{I_p}.
\end{aligned}
$$

This vector $\mathbf{G}_{I_p}$ is constructed as follows:

1. A vacuum model of the tokamak without the conducting vacuum vessel is constituted in order to evaluate the vacuum poloidal flux and magnetic field response to the PF system power supplies action;

2. To achieve that, the vacuum model includes flux loops placed inside the vacuum vessel where the plasma centroid and the plasma boundary are expected. These imaginary flux loops enable the analysis of the vacuum poloidal flux response to the PF system power supplies action;

3. The vacuum model includes vertically-oriented and horizontally-oriented magnetic probes inside the vacuum vessel where the plasma centroid and the plasma boundary are expected. These imaginary magnetic probes enable the analysis of the vacuum magnetic field response to the PF system power supply action;

4. The vacuum tokamak evolution is modelled as described in Chapter 2. Neglecting the effect of the conducting vacuum vessel, the poloidal flux and magnetic field responses to PF system power supply action can be summarised as the following state-space system:

$$
\begin{aligned}
\dot{\mathbf{x}} &= \underline{\mathbf{A}}\mathbf{x} + \underline{\mathbf{B}}\mathbf{u} \\
\mathbf{y} &= \underline{\mathbf{C}}\mathbf{x} + \underline{\mathbf{D}}\mathbf{u},
\end{aligned} \tag{5.4}
$$

where

$$
\mathbf{u} = \begin{bmatrix} V_{\text{CS3U}} \\ \vdots \\ V_{\text{PF6}} \end{bmatrix}
$$

is the actuator vector and

$$
\mathbf{x} = \begin{bmatrix} I_{\text{CS3U}} \\ \vdots \\ I_{\text{PF6}} \end{bmatrix} \quad \text{and} \quad \mathbf{y} = \begin{bmatrix} \Psi_{\text{p,FL},1} \\ \vdots \\ \Psi_{\text{p,FL},n_{\text{FL}}} \\ B_{Z,\text{probe},1} \\ \vdots \\ B_{Z,\text{probe},n_{\text{probe}}} \\ B_{R,\text{probe},1} \\ \vdots \\ B_{R,\text{probe},n_{\text{probe}}} \end{bmatrix}
$$

are respectively the state vector and the output vector. $\Psi_{\text{p,FL},i}$ is the poloidal flux measured by the i-th imaginary flux loop within the vacuum vessel, with $i = 1,...,n_{\text{FL}}$. $B_{Z,\text{probe},j}$ and $B_{R,\text{probe},j}$ are the vertical and radial components of the magnetic field

measured by the j-th imaginary magnetic probe within the vacuum vessel, with $j = 1,...,n_{\text{probe}}$. The $\underline{\underline{\mathbf{A}}}$ matrix is given by

$$\underline{\underline{\mathbf{A}}} = -\underline{\underline{\mathbf{M}}}_{\text{PF-PF}}^{-1}\,\underline{\underline{\boldsymbol{\Omega}}}_{\text{PF}},$$

where $\underline{\underline{\mathbf{M}}}_{\text{PF-PF}}$ is the 11×11 mutuals matrix of the PF system coils, and $\underline{\underline{\boldsymbol{\Omega}}}_{\text{PF}}$ is the 11×11 PF coil resistance matrix. The $\underline{\underline{\mathbf{B}}}$ matrix is given by $\underline{\underline{\mathbf{B}}} = \underline{\underline{\mathbf{M}}}_{\text{PF-PF}}^{-1}$, and the $\underline{\underline{\mathbf{C}}}$ matrix is constructed as exposed in Chapter 2. The $\underline{\underline{\mathbf{D}}}$ matrix is the null matrix;

5. It is possible to assume that the resistive volt-second consumption is negligible via, for example, the action of dedicated feedback controller that compensates the PF coil resistances. Therefore, we may assume $\underline{\underline{\boldsymbol{\Omega}}}_{\text{PF}} = \underline{\underline{\mathbf{0}}}$;

6. The state-space system can thus be summarised as follows:

$$\mathbf{y} = \underline{\underline{\mathbf{C}}} \int_{t'=t_0}^{t'=t} \underline{\underline{\mathbf{M}}}^{-1}\mathbf{u}\,dt' = \underline{\underline{\mathbf{C}\mathbf{M}}}^{-1} \int_{t'=t_0}^{t'=t} \mathbf{u}\,dt'; \tag{5.5}$$

7. By defining τ as the characteristic time of the control system and by assuming that the action of the control system is maintained for durations of the order of the characteristic time, we may write

$$\int_{t'=t_0}^{t'=t} \mathbf{u}\,dt' \cong \bar{\mathbf{u}}\tau, \tag{5.6}$$

where $\bar{\mathbf{u}}$ is the constant power supply voltage demand applied during the interval $[t_0, t_0 + \tau]$;

8. Injecting (5.6) into (5.5) gives the transfer function between $\mathbf{y}$ and the PF system power supply voltage demands:

$$\mathbf{y} = \tau\underline{\underline{\mathbf{C}}} \cdot \underline{\underline{\mathbf{M}}}_{\text{PF-PF}}^{-1}\,\bar{\mathbf{u}}. \tag{5.7}$$

9. Inverting (5.7) yields

$$\bar{\mathbf{u}} = \frac{1}{\tau}\underline{\underline{\mathbf{M}}}_{\text{PF-PF}}\,\underline{\underline{\mathbf{C}}}^{-1}\mathbf{y}, \tag{5.8}$$

where $\underline{\underline{\mathbf{C}}}^{-1}$ denotes the pseudo-inverse of the $\underline{\underline{\mathbf{C}}}$ matrix;

10. For later reference, we define

$$\underline{\underline{\boldsymbol{\Theta}}} := \underline{\underline{\mathbf{M}}}_{\text{PF-PF}}\,\underline{\underline{\mathbf{C}}}^{-1}. \tag{5.9}$$

$\underline{\underline{\boldsymbol{\Theta}}}$ is an $11 \times \left(n_{\text{FL}} + 2n_{\text{probe}}\right)$ matrix;

11. The plasma current is proportional to the value of the poloidal flux Ψ_p at the plasma boundary. Hence, a modification of the boundary poloidal flux implies a modification of plasma current;

12. As a result, a candidate for the 11×1 vector $\mathbf{G}_{I_p}$ can be obtained by averaging the first n_{FL} columns of the $\underline{\underline{\Theta}}$ matrix.

This approach assumes that the presence of a conducting vacuum vessel and the presence of a plasma do not significantly affect the poloidal flux response and the magnetic field response to the PF system power supply action. The conducting vacuum vessel and the plasma are thus treated as disturbances by the feedback control algorithm.

The plasma current feedforward controller is as follows:

$$\mathbf{V}_{\text{demand}} = \mathbf{K}_{FF} \frac{d\left(I_{p,\text{ref}}\right)}{dt}, \tag{5.10}$$

where the $\mathbf{K}_{FF}$ vector is a linear combination of PF system power supply voltages. The $\mathbf{K}_{FF}$ vector is collinear to a vector $\mathbf{G}_{FF}$, which is constituted of ad hoc coefficients that correspond to the time-averaged ramp-up voltages of each power supply during early full tokamak simulations.

Plasma centroid position controller design

The plasma centroid position controller is constituted of one PID feedback controller dedicated to the tracking and regulation of the horizontal component of the plasma centroid R_{mag} weighted by the plasma current I_p and one PID feedback controller dedicated to the tracking and regulation of the vertical component of the plasma centroid Z_{mag} weighted by the plasma current. The $R_{\text{mag}}I_p$ feedback controller acts as follows:

$$\mathbf{V}_{\text{demand}} = \mathbf{K}_{P_R}(R_{\text{mag,ref}} - R_{\text{mag}})I_p + \mathbf{K}_{I_R} \int_{t_0}^{t} (R_{\text{mag,ref}} - R_{\text{mag}})I_p \, dt' + \mathbf{K}_{D_R} \frac{d\left(R_{\text{mag,ref}}I_p - R_{\text{mag}}I_p\right)}{dt},$$

$$\tag{5.11}$$

where $R_{\text{mag,ref}} = R_{\text{mag,ref}}(t)$ is the reference R_{mag} waveform. A similar control law is implemented for the $Z_{\text{mag}}I_p$ feedback controller. The D term of the $R_{\text{mag}}I_p$ controller is filtered with a 0.5s characteristic time, whereas the D term of the $Z_{\text{mag}}I_p$ controller is filtered with a 0.05s characteristic time.

The vectors $\mathbf{K}_{P_R}$, $\mathbf{K}_{I_R}$, and $\mathbf{K}_{D_R}$ must be appropriately constructed in order to decouple the effect of the plasma horizontal centroid position feedback controller from the plasma current evolution and from the plasma centroid vertical position evolution. It is achieved by determining an appropriate linear combination of PF system power supply voltages. This linear combination should act on the vertical magnetic field without significantly modifying the

horizontal magnetic field within the plasma in order to avoid affecting the plasma vertical position. Similarly, this linear combination should avoid significantly modifying the poloidal flux in the plasma in order to avoid affecting the plasma current.

In that perspective, the gains $\mathbf{K}_{P_R}$, $\mathbf{K}_{I_R}$, and $\mathbf{K}_{D_R}$ are chosen as collinear vectors with

$$
\begin{aligned}
\mathbf{K}_{P_R} &= K_{P_R}\mathbf{G}_R \\
\mathbf{K}_{I_R} &= K_{I_R}\mathbf{G}_R \\
\mathbf{K}_{D_R} &= K_{D_R}\mathbf{G}_R.
\end{aligned}
$$

The vector $\mathbf{G}_R$ is a linear combination of PF system power supply voltages. It is generated similarly to the $\mathbf{G}_{I_p}$ vector. In this case, $\mathbf{G}_R$ corresponds to the average of the columns $n_{\text{FL}}+1$ to $n_{\text{FL}}+n_{\text{probe}}$ of the $\mathbf{\Theta}$ matrix.

Similarly, the $\mathbf{G}_Z$ vector used for the control of the vertical position of the plasma centroid corresponds to the average of the last n_{probe} columns of the $\mathbf{\Theta}$ matrix.

PF system coil currents controller design

The PF system coil currents controller is a filtered proportional controller. The control law is as follows:

$$
\mathbf{V}_{\text{demand}} = K_{\text{PF}}\underline{\underline{\mathbf{M}}}_{\text{PF-PF}}
\begin{bmatrix}
I_{\text{CS3U,ref}} - I_{\text{CS3U}} \\
\vdots \\
I_{\text{PF6,ref}} - I_{\text{PF6}}
\end{bmatrix},
\tag{5.12}
$$

where $I_{i,\text{ref}} = I_{i,\text{ref}}(t)$ is the reference current waveform of the i-th coil.

Dipole controller design

The dipole controller aims at reducing the current difference between neighbouring PF coils. In that perspective, a filtered proportional feedback controller acts as follows:

$$
\mathbf{V}_{\text{demand}} = -K_{P_{\text{dip}}}\underline{\underline{\mathbf{M}}}_{\text{PF-PF}}
\begin{bmatrix}
0 \\
0 \\
0 \\
0 \\
0 \\
I_{\text{PF1}} - I_{\text{PF2}} \\
-I_{\text{PF1}} + 2I_{\text{PF2}} - I_{\text{PF3}} \\
-I_{\text{PF2}} + 2I_{\text{PF3}} - I_{\text{PF4}} \\
-I_{\text{PF3}} + 2I_{\text{PF4}} - I_{\text{PF5}} \\
-I_{\text{PF4}} + 2I_{\text{PF5}} - I_{\text{PF6}} \\
-I_{\text{PF5}} + *I_{\text{PF6}}
\end{bmatrix}
\tag{5.13}
$$

The dipole controller thus regulates the difference in neighbouring PF coil current to zero.

Gaps controller design

The gap controller is directly imported from previous work with DINA-CH&CRONOS. It corresponds to a modified version of the ITER gap controller designed by Andre Kavin and kindly provided to CRPP [142].

This controller is a filtered proportional feedback controller that tracks and regulates the gaps weighted by the plasma current.

Vertical stabilisation

In the implemented ITER design, the VS1 and VS3 power supplies are dedicated to regulating the vertical position of the plasma column.

In this work, it was decided to dominantly use VS1 for vertical stabilisation. VS3 is used marginally for short periods during ramp-up and ramp-down.

The vertical stabilisation via VS1 is performed by a D controller of the vertical position of the plasma centroid weighted by I_p. The D controller acts as follows:

$$V_{\mathrm{VS1}} = K_{D_{\mathrm{VS1}}} \frac{d(Z_{\mathrm{mag,ref}} I_p - Z_{\mathrm{mag}} I_p)}{dt}. \tag{5.14}$$

The output of this controller is filtered with a 0.01s characteristic time.

The action of VS3 is similar to that of VS1. Vertical stabilisation via VS3 is performed by a D controller of the plasma current weighted vertical position of the plasma centroid that acts as follows:

$$V_{\mathrm{VS3}} = K_{D_{\mathrm{VS3}}} \frac{d(Z_{\mathrm{mag,ref}} I_p - Z_{\mathrm{mag}} I_p)}{dt}. \tag{5.15}$$

The output of this controller is filtered with a 0.01s characteristic time.

The respective actions of VS1 and VS3 are weighed such that the action of VS1 is dominant.

VS3 current controller design

The VS3 current is regulated using by a P controller of the following form:

$$V_{\mathrm{VS3}} = -K_{P_{\mathrm{VS3}}} I_{\mathrm{VS3}}. \tag{5.16}$$

PF system power supplies protection

In order to prevent the PF system power supplies from violating their operational limits, a PF system currents feedback controller is implemented.

This controller is inactive when the PF system power supplies operate far from their operational limits. It is activated when the absolute value of the current within a power supply exceeds 95% of the maximum tolerated current for that specific power supply.

Its action overrides the power supply demand voltage originating from other controllers. It forces the power supply to provide a voltage that aims at preventing the power supply current from violating the operational limits.

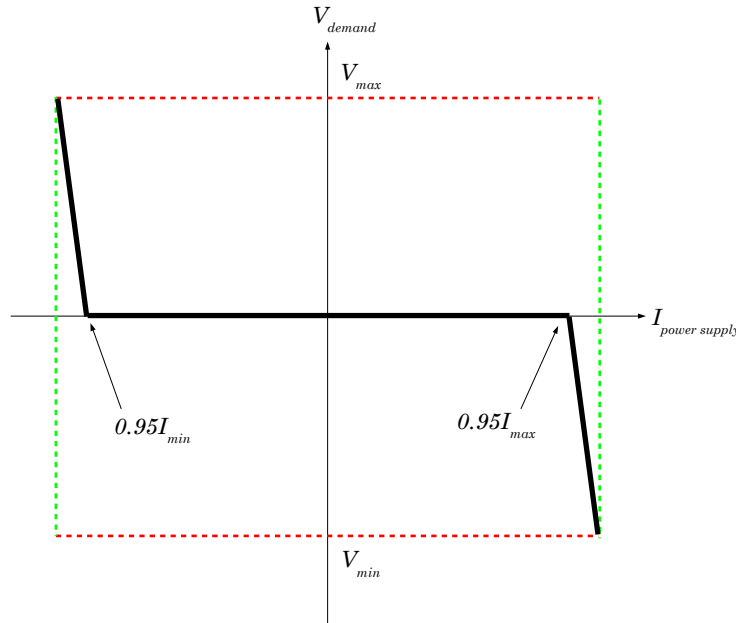The voltage action is described in Figure 5.20.

Figure 5.20: Action of the PF system power supplies protection feedback controller. The dashed lines denotes the power supply operational limits.

Current hole controller design

The hybrid and steady-state scenarios are highly sensitive to the heating and current drive scenario, as exposed in the previous paragraph. The current hole controller must therefore refrain from significantly modifying the plasma heating and current drive power demands in order to avoid affecting the fragile balance required to achieve a hybrid regime or a steady-state regime.

In this work, we imposed the following requirements:

> *The current hole controller should prevent the formation of a current hole while avoiding significant modifications of the total additional heating and current drive injected into the plasma. The current hole controller should thus try and maintain a constant total power deposited within the plasma $P_{deposited}$ and a constant driven current I_{driven}.*

These specifications constrain the design of the current hole controller and guarantee that its action does not significantly affect the scenario evolution.

Precise q-profile tracking is not required for preventing the formation of a current hole. This goal can be achieved via the slow regulation of the central value of the q-profile. In that perspective, the implementation of an advanced q-profile controller is not necessary for this work.

The implemented current hole controller slowly tracks and regulates the value of the q-profile at $\rho = 0.1$ according to a reference trajectory. The central value of the q-profile, $q(\rho = 0)$ could not be selected as the controlled variable because its estimation is less reliable numerically.

Choosing $q(\rho = 0.1)$ as a controlled variable enables a refinement of the control specifications. It is now possible to require the following:

- The current hole controller should minimise the modification in deposited power within the $\rho = 0.1$ flux surface, denoted $P_{in} = P_{deposited}(\rho \leq 0.1)$, with respect to the plasma configuration prior to the controller action;

- The current hole controller should minimise the modification in deposited power outside of the $\rho = 0.1$ flux surface, denoted $P_{out} = P_{deposited}(\rho \geq 0.1)$, with respect to the plasma configuration prior to the controller action;

- The current hole controller should minimise the modification in driven current within the $\rho = 0.1$ flux surface, denoted $I_{cd,in} = I_{driven}(\rho \leq 0.1)$, with respect to the plasma configuration prior to the controller action;

- The current hole controller should minimise the modification in driven current outside of the $\rho = 0.1$ flux surface, denoted $I_{cd,out} = I_{driven}(\rho \geq 0.1)$, with respect to the plasma configuration prior to the controller action.

The current hole controller acts on the central value of the q-profile via the action of the following actuators:

- The ECRH first antenna power demand $P_{ECRH,a1}$, which must be comprised between 0MW and 10MW;

- The ECRH second antenna power demand $P_{\text{ECRH,a2}}$, which must be comprised between 0MW and 10MW;

- The ICRH antenna power demand P_{ICRH}, which must be comprised between 0MW and 20MW;

- The NBI on-axis power demand $P_{\text{NBI,on-axis}}$, which must be *either* 0MW or 16.5MW;

- The NBI off-axis power demand $P_{\text{NBI,off-axis}}$, which must be *either* 0MW or 16.5MW.

The LH power demand is not considered as an actuator because the LH system is not implemented for the hybrid scenario.

Let us assume that the power deposition profiles can be separated as follows

$$p_\beta(t,\rho) = P_\beta(t) \frac{p_\beta(t_0,\rho)}{P_\beta(t_0)}, \tag{5.17}$$

where $\beta = \{\text{ECRH a1}, \text{ECRH a2}, \text{ICRH}, \text{NBI on-axis}, \text{NBI off-axis}\}$, $p_\beta(t_0,\rho)$ is the power deposition profile per unit volume at the time $t = t_0$ by the β heating and/or current drive system, and $P_\beta(t)$ is the power demand of the β heating and/or current drive system at time t.

This assumption implies that the structures of the power deposition profiles remain unchanged during the pulse. Although rather strong, this assumption approximately holds during the flat-top phase of the hybrid and steady-state scenarios because their flat-top regimes are respectively quasi-stationary and stationary.

The total power injected by the β external heating system within the $\rho = 0.1$ flux surface is thus given by:

$$
\begin{aligned}
P_{\beta,\text{in}}(t) &= \int_{\rho=0}^{\rho=0.1} p_\beta(t,\rho) \frac{dV}{d\rho} d\rho \\[2mm]
&= \frac{P_\beta(t)}{P_\beta(t_0)} \left(\int_{\rho=0}^{\rho=0.1} p_\beta(t_0,\rho) \frac{dV}{d\rho} d\rho \right) \\[2mm]
&:= P_\beta(t) \frac{P_{\beta,\text{in}}(t_0)}{P_\beta(t_0)},
\end{aligned}
\tag{5.18}
$$

where $P_{\beta,\text{in}}(t_0)$ is defined as the total power deposited by the heating system β within the $\rho = 0.1$ flux surface at $t = t_0$.

Similarly, let us assume that the current drive profiles can be separated as follows:

$$j_\beta(t,\rho) = P_\beta(t) \frac{j_\beta(t_0,\rho)}{P_\beta(t_0)}, \tag{5.19}$$

where $j_\beta(t_0, \rho)$ is the current density profile at $t = t_0$ driven by the β current drive source. The total current driven by the β additional current drive system within the $\rho = 0.1$ flux surface is given by:

$$
\begin{aligned}
I_{\beta,\text{cd,in}}(t) &= \int_{\rho=0}^{\rho=0.1} j_\beta(t,\rho)\frac{dS}{d\rho}d\rho \\[2ex]
&= \frac{P_\beta(t)}{P_\beta(t_0)}\left(\int_{\rho=0}^{\rho=0.1} j_\beta(t_0,\rho)\frac{dS}{d\rho}d\rho\right) \\[2ex]
&:= P_\beta(t)\frac{I_{\beta,\text{cd,in}}(t_0)}{P_\beta(t_0)},
\end{aligned}
\tag{5.20}
$$

where $I_{\beta,\text{cd,in}}(t_0)$ is defined as the total current driven by the current drive system β within the $\rho = 0.1$ flux surface at $t = t_0$.

Equations (5.18) and (5.20) and the corresponding relations for the deposited power and current drive outside of the $\rho = 0.1$ flux surface can be expressed in a more compact manner:

$$
\underline{\underline{\Upsilon}}\mathbf{P} = \mathbf{w},
\tag{5.21}
$$

where

$$
\mathbf{P} = \begin{bmatrix} P_{\text{ECRH,a1}}(t) \\ P_{\text{ECRH,a2}}(t) \\ P_{\text{ICRH}}(t) \\ P_{\text{NBI,on-axis}}(t) \\ P_{\text{NBI,off-axis}}(t) \end{bmatrix} \qquad \mathbf{w} = \begin{bmatrix} P_{\text{in}} \\ P_{\text{out}} \\ I_{\text{cd,in}} \\ I_{\text{cd,out}} \end{bmatrix}
$$

are respectively the power demand vector and the controlled variables vector, and

$$
\underline{\underline{\Upsilon}} = \begin{bmatrix}
\dfrac{P_{\text{ECRH,a1,in}}(t_0)}{P_{\text{ECRH,a1}}(t_0)} & \dfrac{P_{\text{ECRH,a2,in}}(t_0)}{P_{\text{ECRH,a2}}(t_0)} & \dfrac{P_{\text{ICRH,in}}(t_0)}{P_{\text{ICRH}}(t_0)} & \dfrac{P_{\text{NBI,on-axis,in}}(t_0)}{P_{\text{NBI,on-axis}}(t_0)} & \dfrac{P_{\text{NBI,off-axis,in}}(t_0)}{P_{\text{NBI,off-axis}}(t_0)} \\[3ex]
\dfrac{P_{\text{ECRH,a1,out}}(t_0)}{P_{\text{ECRH,a1}}(t_0)} & \dfrac{P_{\text{ECRH,a2,out}}(t_0)}{P_{\text{ECRH,a2}}(t_0)} & \dfrac{P_{\text{ICRH,out}}(t_0)}{P_{\text{ICRH}}(t_0)} & \dfrac{P_{\text{NBI,on-axis,out}}(t_0)}{P_{\text{NBI,on-axis}}(t_0)} & \dfrac{P_{\text{NBI,off-axis,out}}(t_0)}{P_{\text{NBI,off-axis}}(t_0)} \\[3ex]
\dfrac{I_{\text{ECRH,a1,in}}(t_0)}{P_{\text{ECRH,a1}}(t_0)} & \dfrac{I_{\text{ECRH,a2,in}}(t_0)}{P_{\text{ECRH,a2}}(t_0)} & \dfrac{I_{\text{ICRH,in}}(t_0)}{P_{\text{ICRH}}(t_0)} & \dfrac{I_{\text{NBI,on-axis,in}}(t_0)}{P_{\text{NBI,on-axis}}(t_0)} & \dfrac{I_{\text{NBI,off-axis,in}}(t_0)}{P_{\text{NBI,off-axis}}(t_0)} \\[3ex]
\dfrac{I_{\text{ECRH,a1,out}}(t_0)}{P_{\text{ECRH,a1}}(t_0)} & \dfrac{I_{\text{ECRH,a2,out}}(t_0)}{P_{\text{ECRH,a2}}(t_0)} & \dfrac{I_{\text{ICRH,out}}(t_0)}{P_{\text{ICRH}}(t_0)} & \dfrac{I_{\text{NBI,on-axis,out}}(t_0)}{P_{\text{NBI,on-axis}}(t_0)} & \dfrac{I_{\text{NBI,off-axis,out}}(t_0)}{P_{\text{NBI,off-axis}}(t_0)}
\end{bmatrix}
$$

Miyamoto [143] states that the value of the safety factor at a flux surface ρ_q is inversely

proportional to the total plasma current contained within the ρ flux surface. More precisely

$$
\begin{aligned}
q(\rho_q) \quad = \quad & \frac{\pi a^2 (1+\kappa^2) B_\phi}{\mu_0 R I(\rho \le \rho_q)} \times \\[1em]
& \times \left[1 + \left(\frac{a}{R}\right)^2 + \frac{1}{2}\left(\frac{a}{R}\right)^2 \left(\beta_p + \frac{\mathrm{li}}{2}\right)^2 \right] \times \\[1em]
& \times \left[1.24 - 0.54\kappa + 0.3\left(\kappa^2 + \delta^2\right) + 0.13\delta \right],
\end{aligned}
\tag{5.22}
$$

where $I(\rho \le \rho_q)$ is the total plasma current within the ρ_q flux surface. $I(\rho \le \rho_q)$ can be rewritten as

$$
I(\rho \le \rho_q) = I_{\mathrm{ind+bt}}(\rho \le \rho_q) + I_{\mathrm{cd}}(\rho \le \rho_q),
$$

where $I_{\mathrm{ind+bt}}(\rho \le \rho_q)$ is the addition of the total current induced by the PF system and the bootstrap current within the $\rho = \rho_q$ flux surface, whereas $I_{\mathrm{cd}}(\rho \le \rho_q)$ is the total driven current within the $\rho = \rho_q$ flux surface.

Given that the plasma equilibrium is mostly time-independent during the hybrid and steady-state scenario flat-top phases, we may assume that

$$
q(\rho_q) = \frac{\zeta}{I_{\mathrm{ind+bt}}(\rho \le \rho_q) + I_{\mathrm{cd}}(\rho \le \rho_q)},
\tag{5.23}
$$

where ζ is a constant. Such an assumption neglects the possible modification of li generated by the current hole controller action but should hold if the current hole controller succeeds in regulating $q(\rho = 0.1)$ around a constant reference.

As a result, (5.21) can be rewritten as:

$$
\underline{\underline{\Upsilon}}\mathbf{P} =
\begin{bmatrix}
P_{\mathrm{in}} \\[1em]
P_{\mathrm{out}} \\[1em]
\dfrac{\zeta}{q(\rho = 0.1)} - I_{\mathrm{ind+bt}}(\rho \le 0.1) \\[1em]
I_p - \dfrac{\zeta}{q(\rho = 0.1)} - I_{\mathrm{ind+bt}}(\rho \ge 0.1)
\end{bmatrix}
\tag{5.24}
$$

because $I_{\mathrm{cd,out}} = I_p - I_{\mathrm{ind+bt}}(\rho \le 0.1) - I_{\mathrm{ind+bt}}(\rho \ge 0.1) - I_{\mathrm{cd,in}}$.

It is now possible to linearise (5.24) by taking a perturbative approach. Because $\underline{\underline{\Upsilon}}$ is constant,

this yields

$$
\underline{\mathbf{\Upsilon}}\boldsymbol{\delta}\mathbf{P} =
\begin{bmatrix}
\delta P_{\mathrm{in}} \\[2ex]
\delta P_{\mathrm{out}} \\[2ex]
-\dfrac{\zeta\delta q(\rho=0.1)}{q^2(\rho=0.1)} - \delta I_{\mathrm{ind+bt}}(\rho\le 0.1) \\[3ex]
\delta I_p + \dfrac{\zeta\delta q(\rho=0.1)}{q^2(\rho=0.1)} - \delta I_{\mathrm{ind+bt}}(\rho\ge 0.1)
\end{bmatrix}
\tag{5.25}
$$

The control specifications require $\delta P_{\mathrm{in}} = \delta P_{\mathrm{out}} = 0$. Moreover, $\delta I_{\mathrm{ind+bt}}(\rho\le 0.1) = \delta I_{\mathrm{ind+bt}}(\rho\ge 0.1) = \delta I_p = 0$, as requested by the control specifications.

As a result, (5.25) becomes

$$
\underline{\mathbf{\Upsilon}}\boldsymbol{\delta}\mathbf{P} =
\begin{bmatrix}
0 \\[2ex]
0 \\[2ex]
-\left(I_{\mathrm{ind+bt}}(\rho\le 0.1) + I_{\mathrm{cd,in}}\right)\dfrac{\delta q(\rho=0.1)}{q(\rho=0.1)} \\[3ex]
\left(I_{\mathrm{ind+bt}}(\rho\le 0.1) + I_{\mathrm{cd,in}}\right)\dfrac{\delta q(\rho=0.1)}{q(\rho=0.1)}
\end{bmatrix}
:= \boldsymbol{\delta}\mathbf{w}
\tag{5.26}
$$

By defining

$$
\delta q(\rho=0.1) := q_{\mathrm{ref}}(\rho=0.1) - q(\rho=0.1)
$$

the linearised equation (5.26) enables the control of $q(\rho=0.1)$.

To implement this scheme, it is necessary to reconstruct the perturbed controlled vector $\boldsymbol{\delta}\mathbf{w}$ during the plasma pulse and use the following control law:

$$
\mathbf{P}_{\mathrm{demand}} = \mathbf{P}(t_0) + \boldsymbol{\delta}\mathbf{P} =
\begin{bmatrix}
P_{\mathrm{ECRH,a1}}(t_0) \\
P_{\mathrm{ECRH,a2}}(t_0) \\
P_{\mathrm{ICRH}}(t_0) \\
P_{\mathrm{NBI,on\text{-}axis}}(t_0) \\
P_{\mathrm{NBI,off\text{-}axis}}(t_0)
\end{bmatrix}
+ \underline{\mathbf{\Upsilon}}^{-1}\boldsymbol{\delta}\mathbf{w},
\tag{5.27}
$$

where $\underline{\mathbf{\Upsilon}}^{-1}$ denotes the pseudo-inverse of $\underline{\mathbf{\Upsilon}}$.

This approach suffers from the major drawback that it does not take into account the known

heating and current drive system limitations. In its present form, the current hole controller may request extremely high or negative powers to the heating systems and the subsequent inability of the heating systems to meet the demands may be detrimental to the current hole controller performance.

To address this challenge, the current hole controller is associated with a saturation management algorithm, which incorporates the heating and current drive system limitations in the current hole feedback control algorithm by acting as follows:

- Compute the initial demand powers using the control law (5.27);

- If the demand power of the β heating and/or current drive system exceeds the β system maximum available power, set the β power demand to the maximum achievable. Conversely, if the demand power of the heating system β is negative, set the β power demand to zero;

- Update the $\underline{\mathbf{\Upsilon}}$ matrix by removing the column corresponding to the saturated heating system;

- Compute the updated remaining power demands by using the control law (5.27) with the updated $\underline{\mathbf{\Upsilon}}$ matrix;

- Iterate this procedure until either all the heating and current drive system power demands are saturated or none of the *remaining* heating and current drive system power demands are saturated.

This saturation management algorithm helps improve the current hole controller performance. It is especially useful in managing the NBI on-axis and off-axis power demands, because the NBI systems are always saturated.

5.3.2 Specific features

Features specific to the operation of the DINA-CH&CRONOS full tokamak simulator are discussed in the present section.

Vertical forces

The vertical forces sustained by the CS coils and PF coils are computed in the DINA-CH&CRONOS full tokamak simulations. These vertical forces must remain within a predetermined range defined in [43] in order to avoid coil support damage. The vertical force sustained by the i-th coil is defined as

$$F_{Z,i} = -2\pi \left(R_i - w_i \right) I_i B_R \left(R_i - w_i, Z_i \right), \tag{5.28}$$

where (R_i, Z_i) is the i-th coil axis, I_i is the i-th coil current, and w_i is the i-th coil width.

L-H and H-L transition modelling

Unlike CRONOS prescribed-boundary simulations in which the L-H and H-L transitions timing are prescribed, the L-H and the H-L thresholds are self-consistently computed using a specific module.

The progressive formation of a density pedestal begins simultaneously with the L-H transition and its progressive resorption starts simultaneously with the H-L transition.

Transport models and physical assumptions

The transport models and their associated physical assumptions are straightforwardly imported from the CRONOS prescribed-boundary simulations.

Simulator configuration

In these simulations, the plasma grid is chosen to be $n_R \times n_Z = 33 \times 65$ grid elements. Simulations using a finer grid of $n_R \times n_Z = 65 \times 129$ were performed without demonstrating significant modifications in plasma behaviour.

A time step of $\Delta t = 0.005$s is used, which is sufficiently small to model the vertical instability. Simulations using smaller time steps were performed without demonstrating significant modifications in tokamak evolution.

Data is saved with a decimation that depends on the nature of the data in order to avoid excessive use of computer memory.

Adjustments of the scenarios

Several adjustments from the nominal scenarios are implemented in the DINA-CH&CRONOS full tokamak simulations:

- The initiation plasma boundary is smaller;

- The initiation temperature profiles are lower in order to better emulate present-day experimental observations. This point is not critical because the effect of the prescribed initiation temperature profiles only lasts for a few seconds in the simulated pulses;

- The ECRH antenna configurations are slightly modified in order to account for the discrepancies in equilibria between the CRONOS prescribed-boundary simulations and the DINA-CH&CRONOS free-boundary simulations;

- The L-H transition timing is advanced by about 10s. This was necessary in order 'freeze' to q-profile at a higher value, thus significantly increasing the q-profile distance from unity at the end of the ramp-up phase.

This adjustment delayed the q-profile from reaching unity in the hybrid scenario simulations. In early simulations, in which the nominal hybrid scenario is directly applied, the q-profile reaches unity at $t = 310$s. Advancing the L-H transition timing by about 10s postponed the q-profile reaching unity to $t > 1000$s.

- The plasma current ramp rate is slightly decreased to 0.17MA/s. This was necessary in order to maintain the plasma controllability during ramp-up by reducing the load on the PF system power supplies;

- The ramp-down scheme was slightly modified in order to prevent current density peaking. Importantly, the plasma elongation is decreased in a faster manner than in the CRONOS prescribed-boundary simulations.

The PF system coil current reference waveforms required hand adjustments in order to prevent the PF system coils from exceeding the vertical force limitations. Although these adjustments were only needed occasionally, this procedure was costly in terms of computation and human time. This is due to the fact that the PF system coil reference waveforms hand modification must be reasonably consistent with the plasma shape and plasma current evolution and therefore required tuning. Vertical force limit violations were mostly observed during ramp-up and during ramp-down.

5.4 Hybrid scenario simulations using DINA-CH&CRONOS

This paragraph describes the results of the full tokamak simulation of the ITER hybrid scenario. The plasma pulse is decomposed in several phases exposed and discussed in chronological order.

5.4.1 Plasma initiation

The inboard plasma breakdown is assumed to be achieved with a poloidally averaged loop voltage of $V_{\text{loop}} = 3$V. The initial currents in the conducting vacuum vessel plates are estimated according to the assumed poloidally averaged initiation loop voltage.

The DINA-CH&CRONOS simulation starts at $t = 1.5$s after the plasma breakdown. At that time, the plasma boundary is assumed to be circular, with a minor radius $a(t = 1.5\text{s}) \cong 1$m. The initiation plasma current is assumed to be $I_p = 0.4$MA, with a parabolic current density profile.

The initiation central electron density is assumed to be $n_e(t = 1.5\text{s}, \rho = 0) = 0.5 \cdot 10^{19}\text{m}^{-3}$ and the initiation central ion and electron temperatures are respectively assumed to be $T_i(t = 1.5\text{s}, \rho = 0) = 200$eV and $T_e(t = 1.5\text{s}, \rho = 0) = 500$eV. These assumptions only affect the plasma evolution for a few seconds.

Figure 5.21 displays the initiation boundary, temperature profiles, density profile, and current density profile.
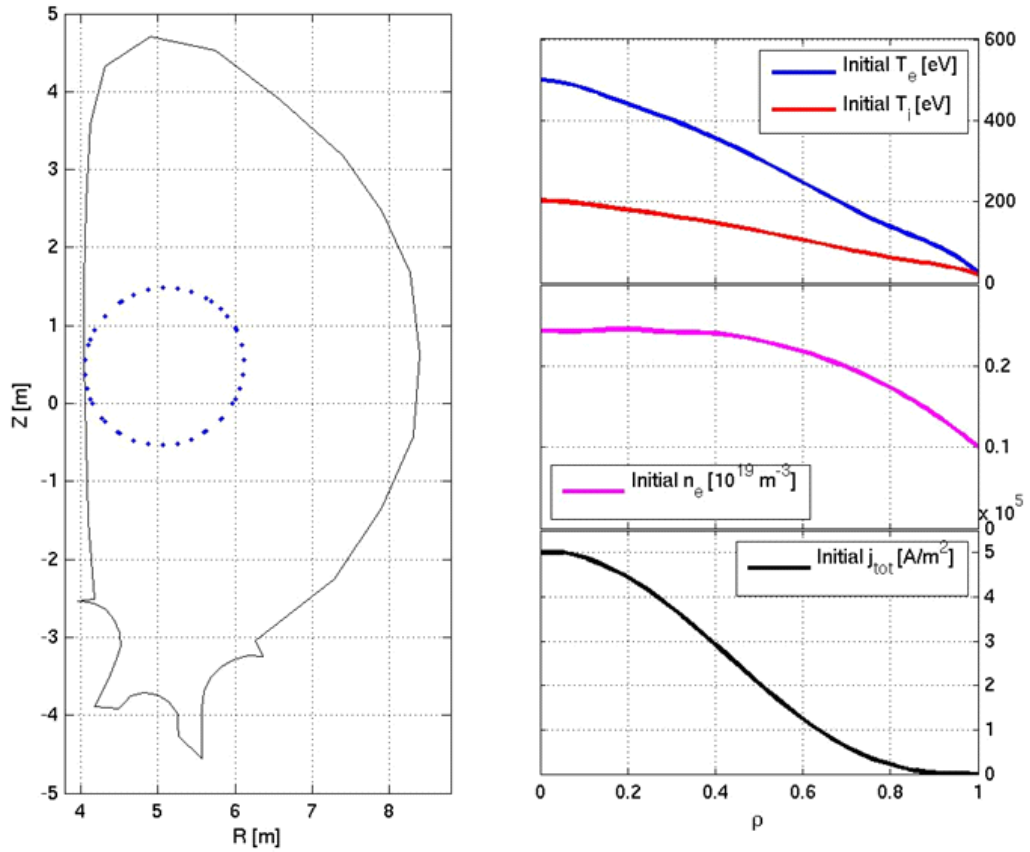

Figure 5.21: Plasma initiation inboard-limited boundary. The initiation plasma ion and electron temperature profiles, the initiation electron density profile and the initiation current density profile are displayed.

The plasma current evolution and plasma centroid evolution are immediately picked-up by their respective controllers. The vertical stabilisation controller and the PF system coil current controller are active for the full duration of the plasma pulse.

The plasma column expands radially, as displayed in Figure 5.22.
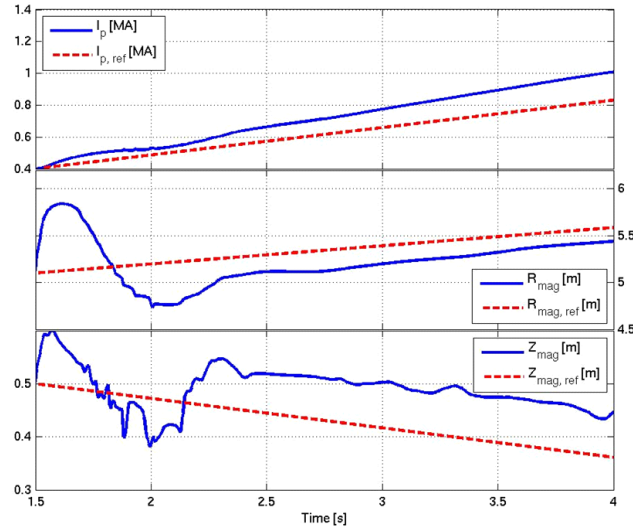
Figure 5.22: Early evolution of the plasma current, the plasma radial centroid position, and the plasma vertical centroid position. The dotted lines are the reference scenario waveforms.

Breakdown and plasma initiation in ITER will benefit from the action of a Switching Network Unit (SNU), which provides additional voltage to the PF system power supplies for a limited period. In this work, the SNU is not modelled, but the PF system power supplies limitations are suppressed until $t = 8s$, in order to emulate the effect of the SNU. The early evolution of the PF system power supply voltages and the PF system coil currents are respectively displayed in Figure 5.23 and in Figure 5.24.
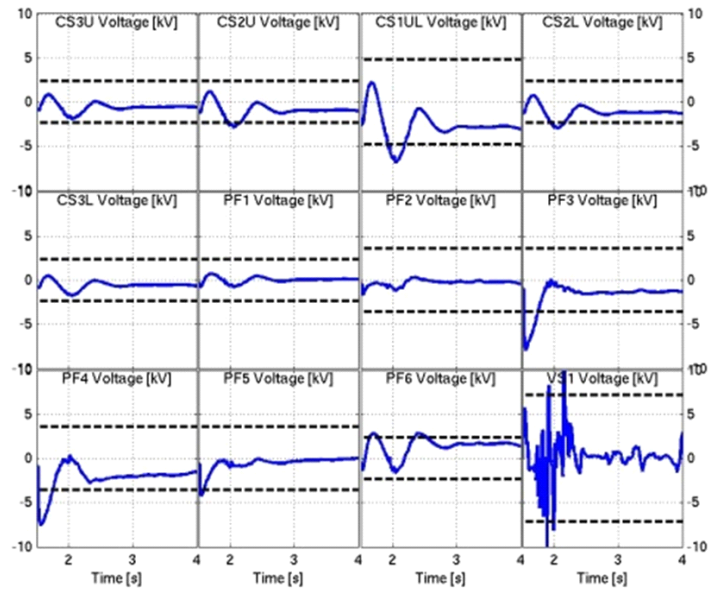
Figure 5.23: Early evolution of the PF system power supply voltages. The dashed lines represent the PF system power supply voltage limits. The voltage limits can be slightly exceeded during the first seconds of pulse thanks to the assumedly correct action of the Switching Network Unit.
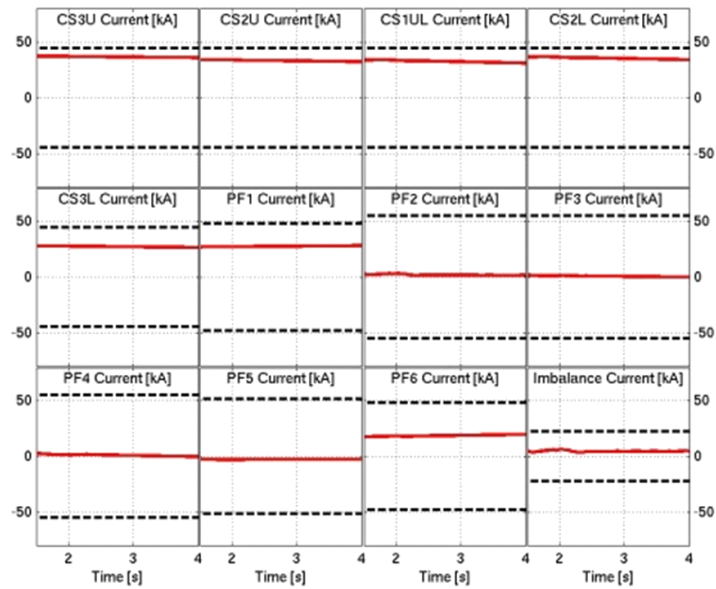

Figure 5.24: Early evolution of the PF system coil current. The dashed lines represent the PF system coil current limits.

5.4.2   From initiation to X-point formation

At $t = 4$s, which corresponds to $I_p \cong 1$MA, the plasma centroid controllers are switched off over a 3s period, passing on the plasma shape control to the gaps controller. The gaps controller can be successfully used early in the plasma pulse by reconstructing the plasma separatrix, which does not correspond to the plasma last closed flux surface in limited plasmas, as displayed in Figure 5.25.
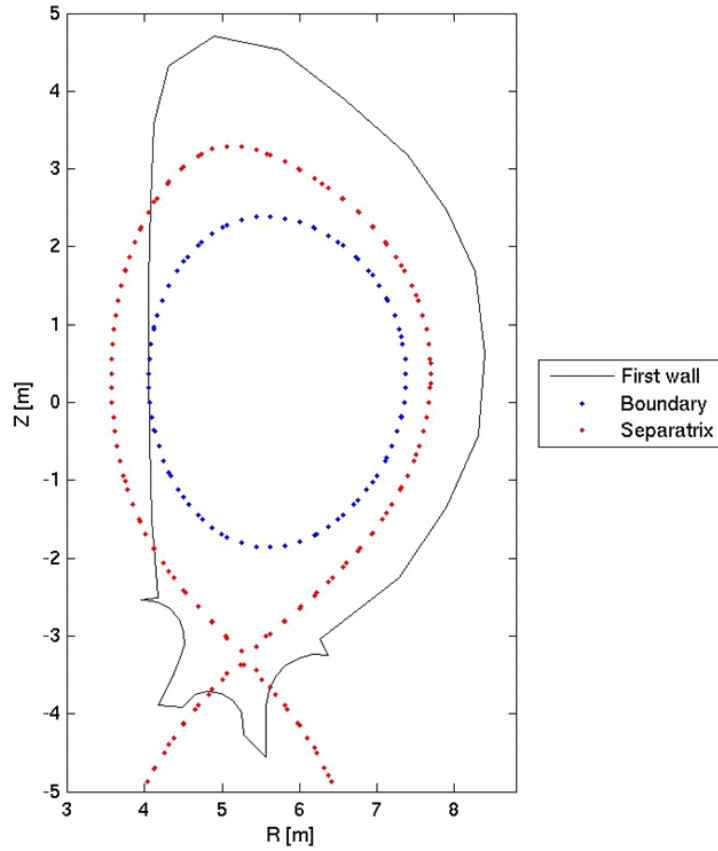

Figure 5.25: Comparison between the plasma boundary in blue and the plasma separatrix in red during early ramp-up.

The gaps controller drives the separatrix 'legs' into the divertor and the plasma becomes diverted at $t \cong 9$s, which corresponds to $I_p \cong 1.6$MA. This is displayed in Figure 5.26. The transition from a limited plasma to a diverted plasma is sometimes referred to as an *X-point formation* because the intersection between the separatrix legs is called the X-point.
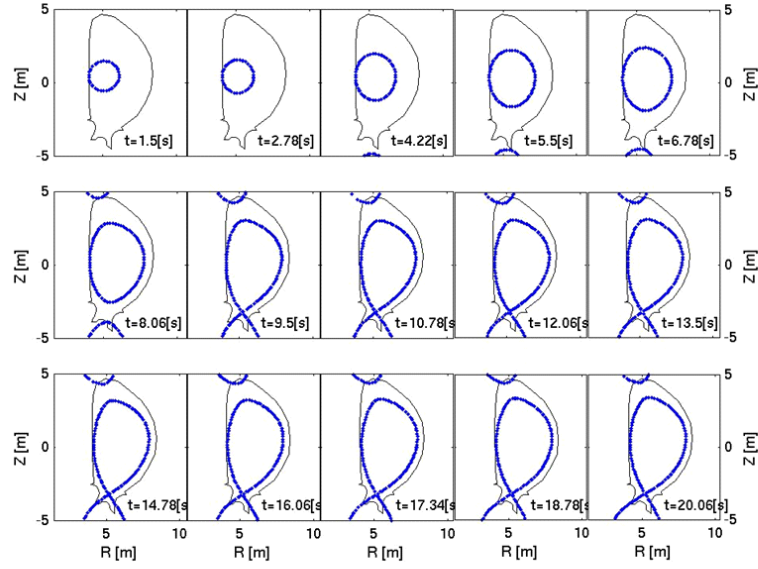
Figure 5.26: Evolution of the plasma boundary from initiation to X-point formation.

Such an early X-point formation prevents damage to the inner wall by avoiding prolonged plasma-wall contact.

At the pre-programmed time of $t = 7$s, 8MW of ECRH power is deposited within the plasma around $\rho \cong 0.3$.

5.4.3   From X-point formation to flat-top

After the X-point formation, the plasma current reference continues its ramp at a $dI_p/dt = 0.17$MA/s rate. The plasma cross-section slowly increases in order to fill the available volume in the vacuum vessel.

The dipole controller is only switched on at $t = 35$s because its operation slightly degrades the precision of the gaps controller.

The onset of the main heating occurs at the predetermined time of $t = 40$s, triggering an almost instantaneous L-H transition. The evolution of the heating power demands, the plasma confinement mode, β_p, and the horizontal position of the plasma centroid are displayed in Figure 5.27.
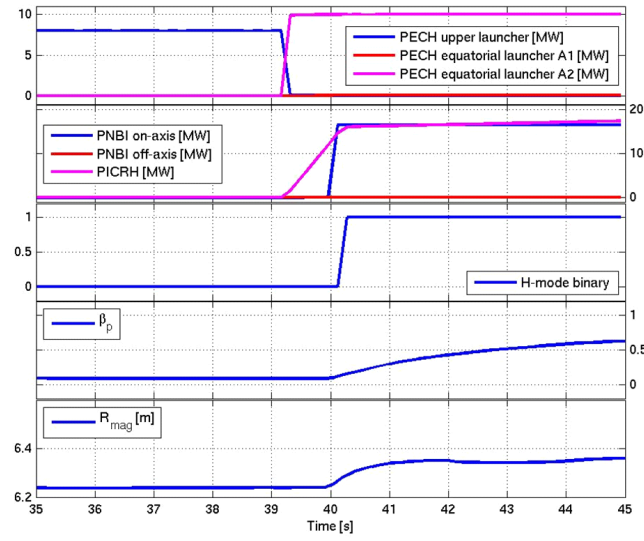
Figure 5.27: Evolution of the heating and current drive power, the H-mode binary, which is zero if the plasma is in L-mode and unity if the plasma is in H-mode, β_p, and the plasma radial centroid position during the L-H transition.

The L-H transition is handled by the control system without plasma-wall contact and without PF coil power supply saturations, as displayed respectively in Figure 5.28 and 5.29.
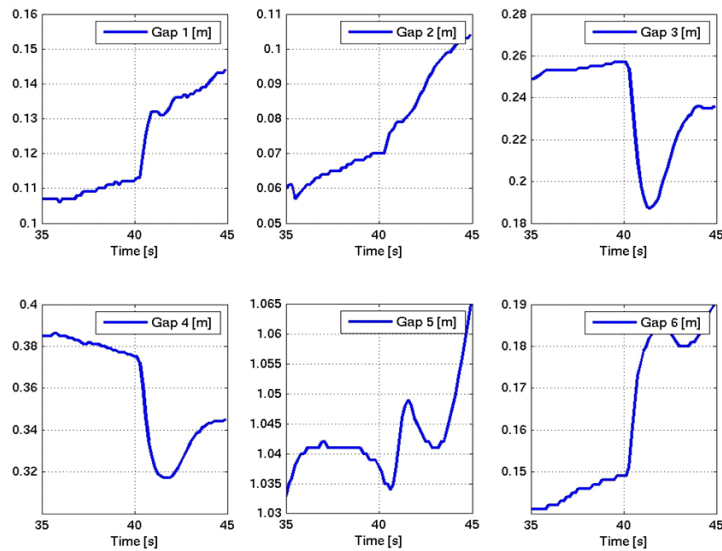

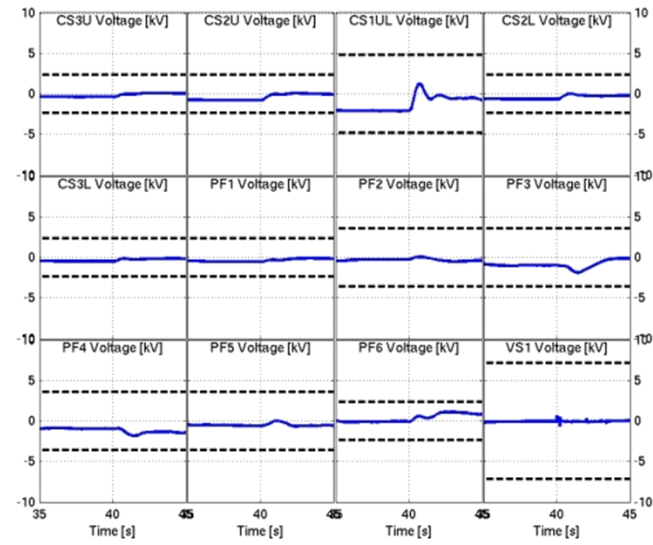Figure 5.28: Evolution of the gaps during the L-H transition. No plasma-wall contact is made.

Figure 5.29: Evolution of the PF system power supply voltages during the L-H transition. There is no power supply saturation.

At t = 40s, the attained plasma shape is close to the flat-top target and the current hole controller is switched on.

The evolution of the various contributions to the total plasma current density and the safety factor profile evolution are displayed in Figure 5.30.
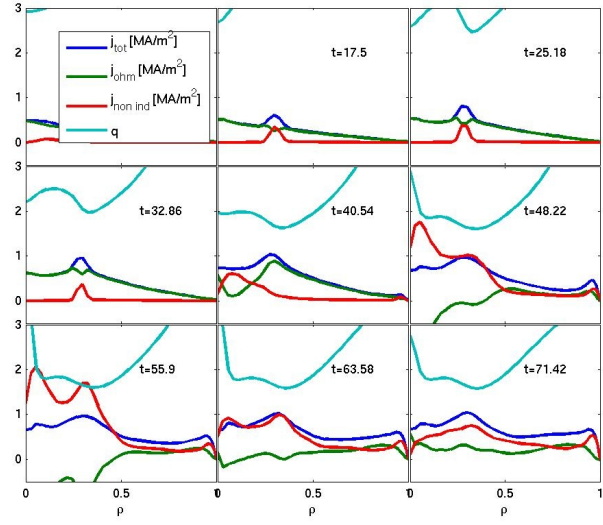
Figure 5.30: Evolution of the total current density, the Ohmic current density, the bootstrap current density, the non-inductive current density, and the q-profile during ramp-up.

The prescribed density profile evolution and the electron and ion temperature profile evolutions during the hybrid scenario ramp-up are displayed in Figure 5.31.
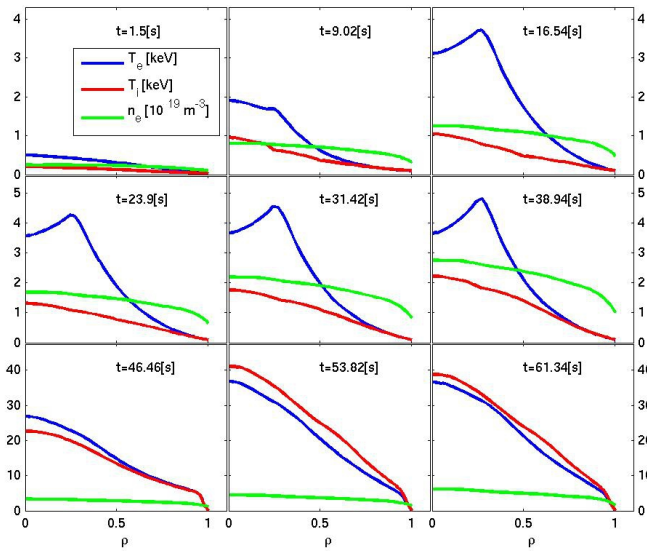

Figure 5.31: Evolution of the plasma electron and ion temperature profiles and electron density profile during ramp-up.

5.4.4 Flat-top

Flat-top is attained when the plasma current reaches $I_p = 12$MA at $t \cong 70$s. The main plasma parameters during the hybrid scenario flat-top are $H_{98}(y, 2) \cong 1.2$, $\beta_p \cong 1.1$, li(3)$\cong 0.6$, and the fusion gain $Q \cong 7.8$, as displayed in Figure 5.32.
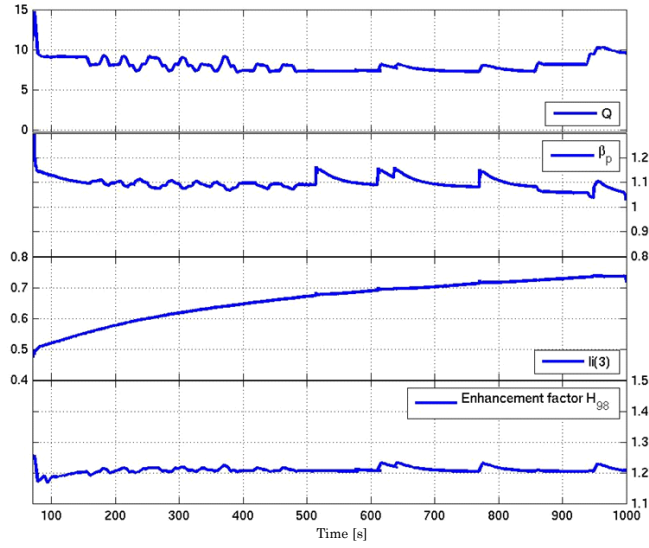
Figure 5.32: Evolution of the fusion gain Q, β_p, li(3), and $H_{98}(y, 2)$ during the hybrid scenario flat-top. The discontinuities after $t = 500$s are artefacts that can be attributed to imperfect simulation restarts.

The current hole controller successfully prevents the formation of a current hole during flat-top, as displayed in Figure 5.33. It mainly acts on the NBI off-axis power demand. As a result, the averaged off-axis NBI power demand during flat-top is 12.6MW.

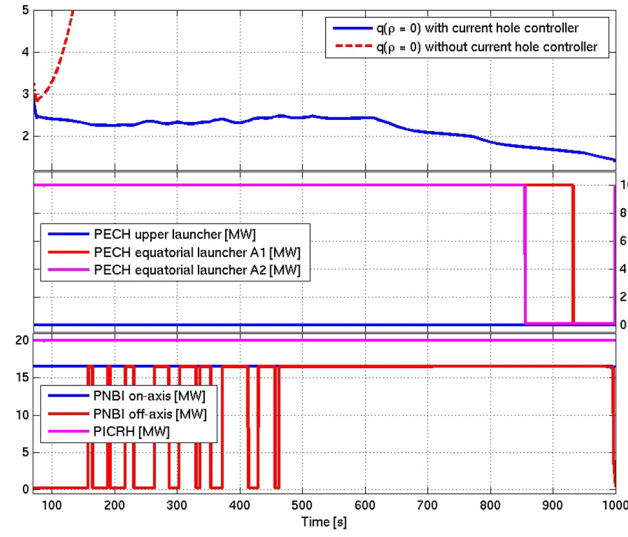Figure 5.33: Evolution of the central safety factor $q(\rho = 0)$. The effect of the current hole controller is shown in the first panel. The second and third panel expose the evolution of the heating and current drive system power demands. The current hole controller is responsible for the dynamic NBI off-axis power demand.

In the DINA-CH&CRONOS simulations, the challenge of preventing the formation of a current hole is reinforced by the fact that the L-H transition occurs earlier in the free-boundary simulations, and 'freezes' the q-profile with a more reversed shear profile, and by the discrepancies in flat-top equilibria with respect to the prescribed-boundary simulations displayed in Figure 5.34.
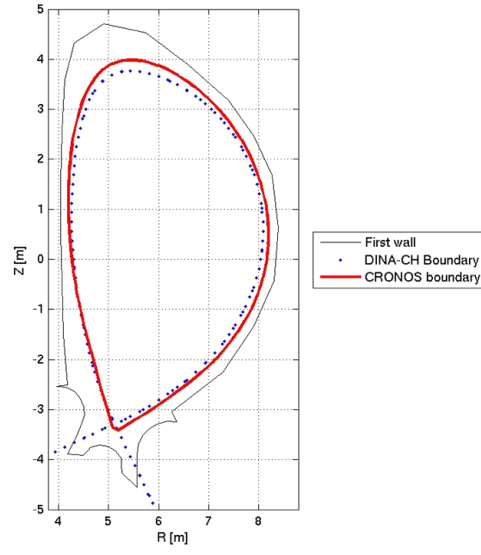
Figure 5.34: Comparison between the CRONOS prescribed-boundary (plain) and the DINA-CH&CRONOS free boundary (pointed) during flat-top.

The exposed hybrid scenario flat-top lasts about 930s. Soon after the end of flat-top, the safety factor profile reaches unity and triggers a sawtooth, as displayed in Figure 5.35. The latest full tokamak simulations of the hybrid scenario led to flat-top durations significantly longer than 1000s by further advancing the L-H transition timing.

Figure 5.35: Evolution of the minimum value of the safety factor profile during flat-top. Sawteeth occur after $t = 1035$s.

5.4.5 Ramp-down

To reduce the effect of the β_p drop on the control systems, the ramp-down is anticipated and the off-axis NBI power demand is set to zero 15s prior the beginning of ramp-down. At $t = 1000$s, the ramp-down is started, and the ICRH and NBI on-axis power demands are set to zero.
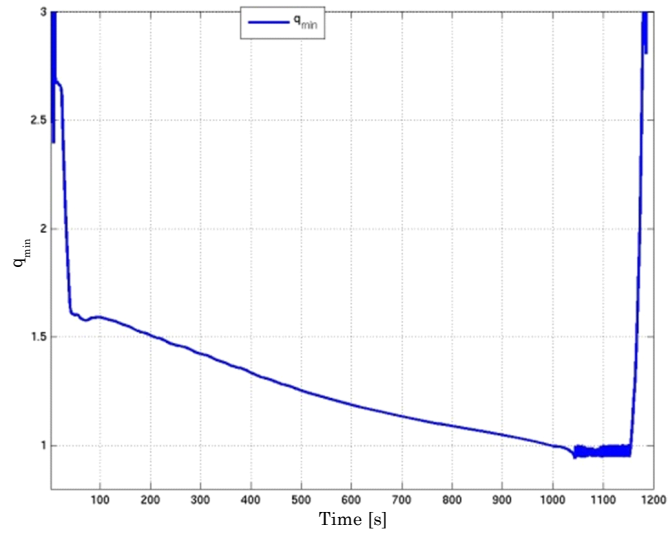
The residual α-power and the ECRH power are enough to maintain the plasma above the H-mode threshold for about 42s during the ramp-down. The H-L transition occurs at $t \cong 1042$s, corresponding to a plasma current of $I_p \cong 9$MA. The heating and current drive power demands, the H-L transition, and the evolution of β_p and R_{mag} during ramp-down are displayed in Figure 5.36.
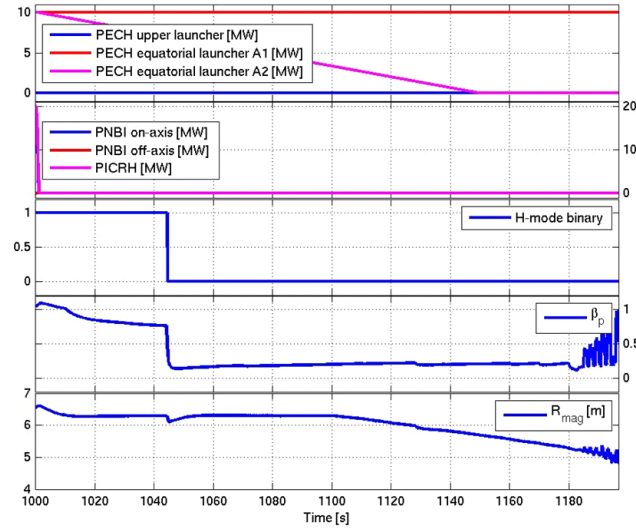

Figure 5.36: Evolution of the heating and current drive power demands, the H-mode binary variable, β_p, and the plasma horizontal centroid position during ramp-down. The H-L transition occurs at $t = 1042$s.

Sawteeth are tolerated during ramp-down. The evolutions of the total current density profile and the q-profile during ramp-down are displayed in Figure 5.37.
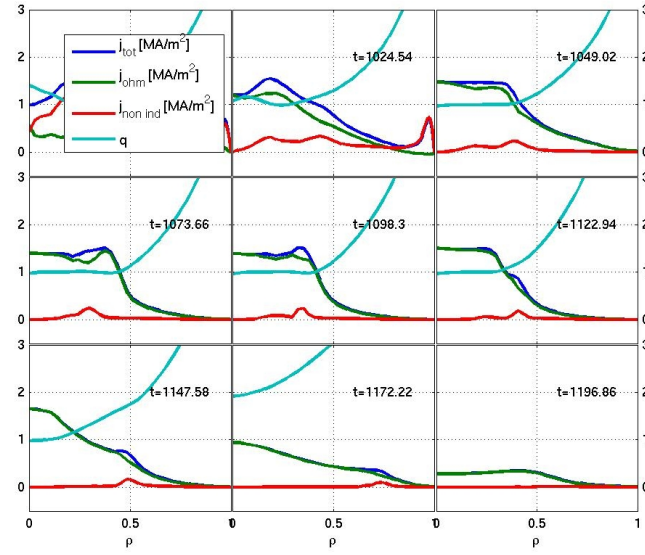
Figure 5.37: Evolution of the total current density, the Ohmic current density, the bootstrap current density, the non-inductive current density, and the q-profile during ramp-down.

The plasma current ramp-down rate is $dI_p/dt = -0.06\text{MA/s}$. This ramp-down rate is small enough in absolute value to retain adequate control of the equilibrium and large enough in absolute value to avoid flux consumption.

The combined action of the gaps controller and the PF system coil current controller decrease the plasma elongation and temper the current density peaking, measured by li, in order to prevent an unmanageably high vertical instability growth rate. This is displayed in Figure 5.38.
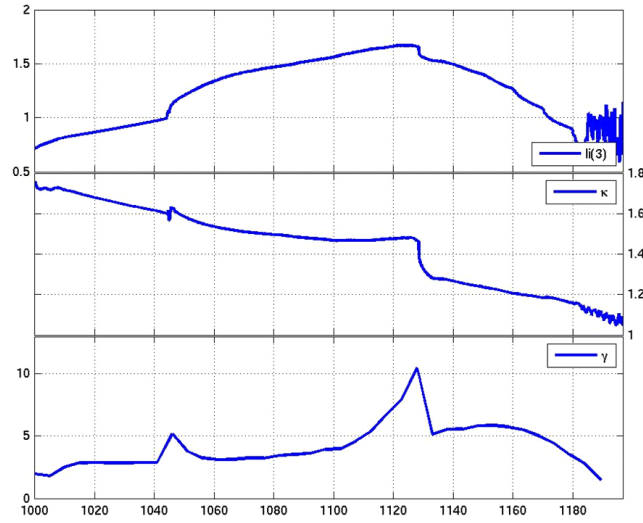
Figure 5.38: Evolution of li(3), the plasma elongation κ, and the vertical instability growth rate γ during the hybrid scenario ramp-down. The event at $t = 1042$s is the H-L transition, and the event at $t = 1128$s is the plasma configuration going from diverted to limited.

The plasma becomes limited at $t = 1128$s, corresponding to a plasma current of $I_p \cong 4.7$MA. The plasma termination, displayed in Figure 5.39, occurs inboard at $t = 1197$s, corresponding to a plasma current of $I_p \cong 0.5$MA.
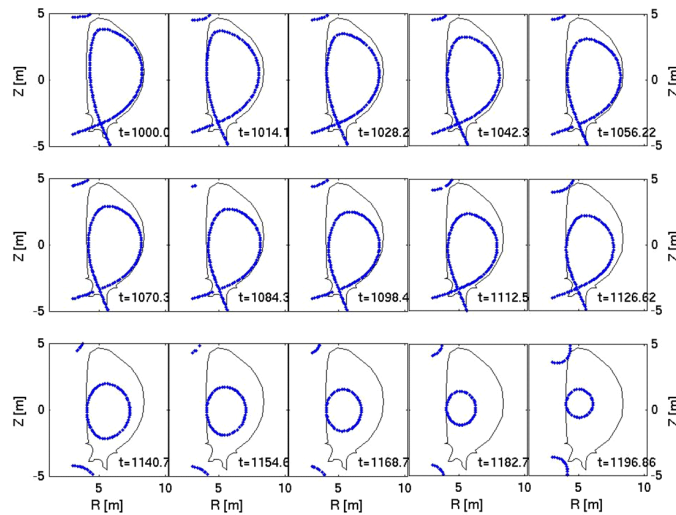
Figure 5.39: Evolution of the plasma boundary during the hybrid scenario ramp-down.

5.4.6 Proximity of the hybrid scenario to the operational boundaries

This work demonstrated the feasibility of the hybrid scenario using ITER power supplies and heating and current drive systems. The vertical forces sustained by the PF coils are also within the operational limits as displayed in Figure 5.40.
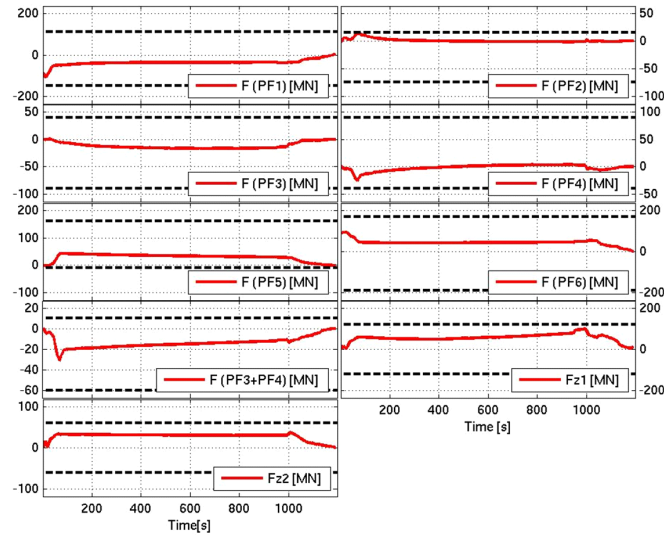
Figure 5.40: Evolution of the vertical forces sustained by the PF system coils (plain) and their respective engineering limits (dashed).

In order to guarantee operation within the limits in terms of forces sustained by the CS and PF coils and in terms of the imbalance current, a few manual adjustments of the PF system coil current reference waveforms were necessary to prevent operational limits violation. Nonetheless, even in the development phase, limits were rarely violated, and only by a few percent.

5.4.7 Conclusion regarding the ITER hybrid scenario

A full tokamak simulation of the ITER hybrid scenario was performed. This study demonstrated the feasibility of maintaining a hybrid regime with I_p = 12MA, $Q \cong 7.8$, and for durations of the order of 1000s, using the latest ITER design. The achieved hybrid regime duration ranges from about 250s to 1200s, mostly depending on the L-H transition timing.

5.5 Steady-state scenario simulations using DINA-CH&CRONOS

This paragraph describes the results of full tokamak simulations of the ITER steady-state scenario.

The steady-state scenario presented in this paragraph shares several features with the ITER hybrid scenario discussed in the previous paragraph. As a matter of fact, they are almost identical until the L-H transition. This point is important in its own right. The common features between the ITER hybrid scenario full tokamak simulations and the ITER steady-state scenario full tokamak simulation are not repeated in this paragraph.

5.5.1 Flat-top

The steady-state scenario flat-top regime differs from the hybrid scenario flat-top regime in several ways. Firstly, the steady-state scenario flat-top plasma current is $I_p = 10MA$. Secondly, the confinement enhancement factor after the L-H transition is higher than that of the hybrid scenario. Thirdly, the prescribed pedestal pressure is lower in the steady-state scenario. Finally, the steady-state scenario plasma current ramp rate during ramp-up is $dI_p/dt = 0.15MA/s$, i.e. slightly lower than that of the hybrid scenario.

The time-averaged steady-state scenario flat-top fusion gain is $Q \cong 5$, whereas $\beta_p \cong 1.35$ and the confinement enhancement factor averages $H_{98}(y,2) \cong 1.2$, as displayed in Figure 5.41.
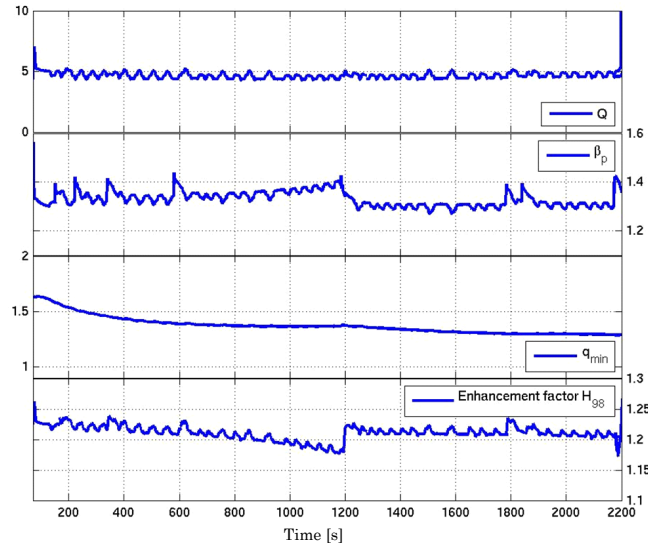
Figure 5.41: Evolution of the fusion gain Q, β_p, the minimum value of the safety factor profile, and $H_{98}(y,2)$ during the steady-state scenario flat-top. The event at $t = 1200s$ is a reaction of the control system to the error on the plasma current controlled variable changing sign.

The action of the current hole controller and the subsequent heating and current drive power demands are displayed in Figure 5.42. The time-averaged NBI off-axis power demand during flat-top is 11.8MW. The addition of LHCD during flat-top provides the extra current drive necessary for maintaining a steady-state with a plasma current of $I_p = 10MA$.
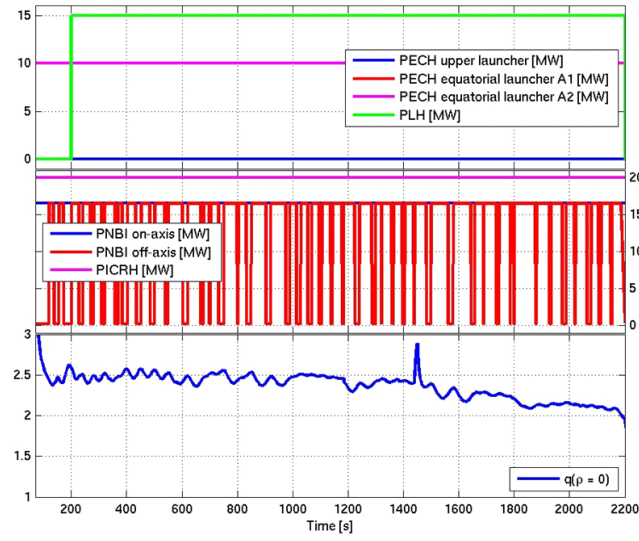
Figure 5.42: Evolution of the heating and current drive systems power demand during the steady-state scenario flat-top. The NBI off-axis power demand waveform is the result of the action of the current hole controller. The evolution of the central value of the safety factor profile is displayed in the bottom panel.

After the decay of the LHCD switching transient, the tokamak reaches a quasi steady-state, as displayed in Figure 5.43.
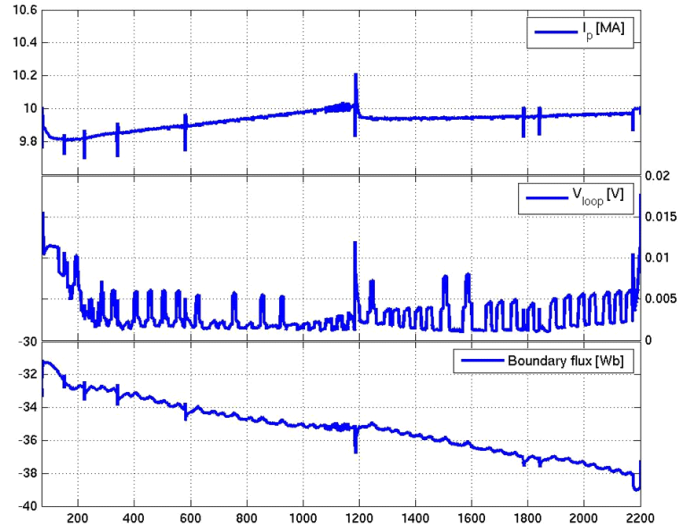
Figure 5.43: Evolution of the plasma current, the loop voltage, and the flux consumption during the steady-state scenario flat-top. The flux consumption during flat-top corresponds to a 2.5mV average loop voltage.

The resulting time-averaged flat-top loop voltage is $V_{\text{loop}} \cong 2.5$mV. The fact that the loop voltage does not identically reach zero can be attributed to the fact that the plasma current feedback controller is active in order to reach precisely 10MA. Other simulations of the steady-state scenario showed a flat-top regime with a negative loop voltage. Achieving precisely $V_{\text{loop}} = 0$V necessitates feedback control of the loop voltage, which was not implemented in this work.

The current density profile and the q-profile during flat-top are displayed in Figure 5.44. The q-profile achieved is hollower than that achieved in the hybrid scenario.
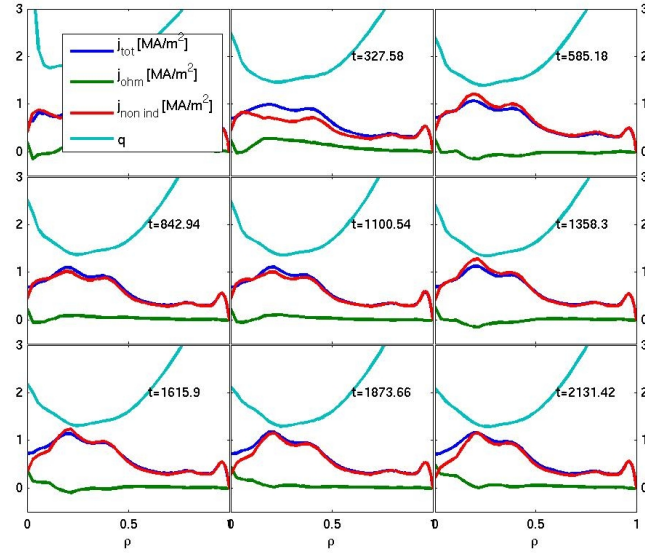
Figure 5.44: Total current density profile, Ohmic current density profile, bootstrap current density profile, non-inductive current density profile, and safety factor profile during the steady-state flat-top.

The electron and ion temperature profiles, as well as the electron density profile of the steady-state scenario during flat-top are displayed in Figure 5.45.
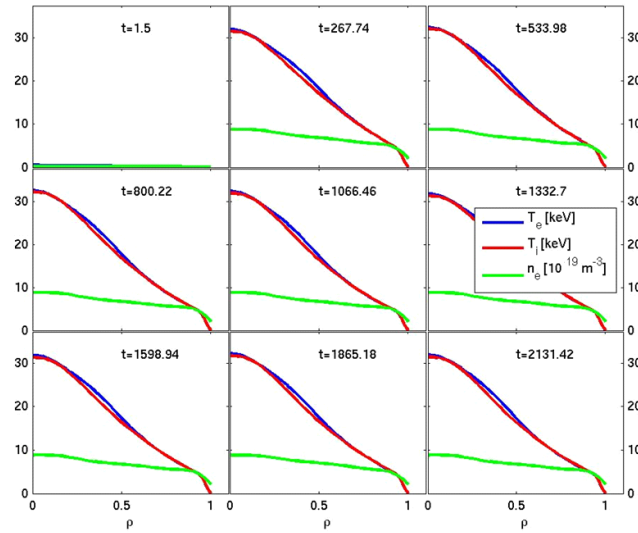
Figure 5.45: Electron and ion temperature, and electron density during the steady-state scenario flat-top.

5.5.2 Ramp-down

The ramp-down scheme is similar to that of the hybrid scenario, but starting from $I_p = 10$MA.

5.5.3 Proximity of the steady-state scenario to the operational boundaries

This work demonstrated the feasibility of the steady-state scenario using the ITER power supplies and heating and current drive systems. Figure 5.46 displays the evolution of the forces sustained by the PF coils with respect to their operational limits.
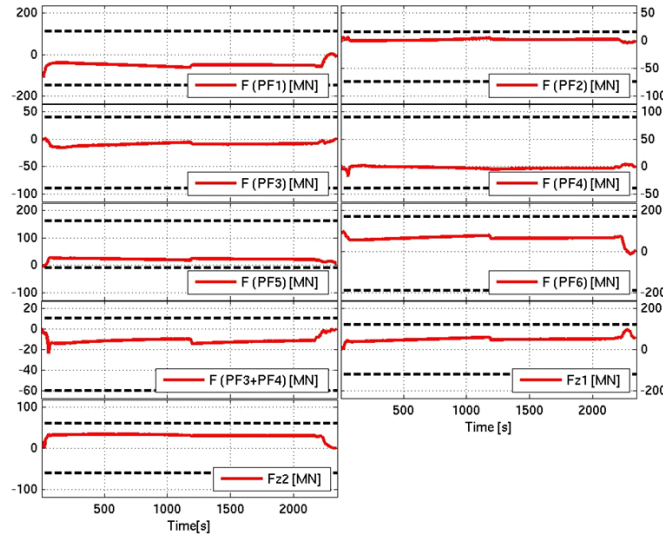
Figure 5.46: Evolution of the vertical forces sustained by the PF system coils (plain) and their respective engineering limits (dashed) during the steady-state scenario.

5.5.4 Conclusion

The steady-state scenario presented lasts for about 2400s, corresponding to about 1800s of steady-state regime. Additional simulations extended this duration to 2800s by simply prolonging the reference flat-top duration. The plasma pulse termination is not driven by flux consumption of the q-profile reaching unity but is imposed.

5.6 Discussion of the ITER advanced scenario simulations

The nominal hybrid and steady-state scenarios designed with CRONOS required adjustments in order to be implemented in DINA-CH&CRONOS. Most importantly, the timing of the L-H transition was significantly advanced. These adjustments were necessary in order to account for the discrepancies in equilibria between the prescribed-boundary simulations and the

free-boundary simulations.

The exposed hybrid scenario and steady-state scenario simulations rely on strong assumptions regarding the validity of the transport models and the validity of the extrapolation of several physical parameters from presently-operated tokamaks to ITER, such as the confinement enhancement factor $H_{98}(y, 2)$, the pedestal pressure, and the electron density peaking factor. The sensitivities of the hybrid and steady-state scenarios with regard to these assumptions were systematically analysed. As a result, it can be stated that the ITER hybrid and steady-state scenarios are strongly sensitive to the plasma flat-top shape and the plasma density peaking. The ITER hybrid and steady-state scenarios also showed sensitivity to the confinement enhancement factor and, to a lesser extent, to the prescribed pedestal pressure.

Early full tokamak simulations of the ITER hybrid and steady-state scenarios showed the formation of a current hole in the plasma centre. This was addressed by postponing the L-H transition and slightly modifying the heating and current drive system configurations in prescribed-boundary simulations. In full tokamak simulations, this challenge is met using a current hole controller. Such a current hole controller could be replaced by an advanced q-profile controller later.

This work hints that the over-tuning of scenarios using prescribed-boundary simulators should be avoided, because the likelihood of their exact application on full tokamak simulators, and eventually on ITER, is small.

The implementation of scenarios developed using a prescribed-boundary simulator on a full tokamak simulator raised several challenges:

- The implementation of scenario reference waveforms required the design and implementation of feedforward and feedback controllers. These controllers need to track and regulate the scenario reference waveforms efficiently while being sufficiently robust to overcome significant disturbances such as the L-H transition and the H-L transition. The trade-off between aggressiveness and robustness must be appropriately determined;

- In order to avoid a costly and risky trial and error approach, automation should be preferred. Automation enables scenario flexibility, whereas a pre-programming approach requires long and costly trial and error phases for the development of each new scenario. Automation also enables the efficient transmission of the acquired experience or the efficient use of the knowledge available for controller design;

- Discrepancies between prescribed-boundary simulations and full tokamak simulations are inevitable and feedback strategies must be implemented to account for them.

Although full tokamak simulations are very close to reality, they provide a false sense of comfort when successful and may lead to the belief that the simulated pulses can be easily implemented on ITER. This is not straightforward, because full tokamak simulations rely

on physical assumptions and transport models that may be inaccurate compared to ITER operation, mostly because it is virtually impossible to assess whether the range of validity of these assumptions and transport models extends to the ITER configuration before ITER is put into service. Nonetheless, sensitivity studies help provide some degree of robustness to the developed scenarios.

5.7 Lessons learned

Although successful, the process of performing the full tokamak simulations presented in this Chapter was a much longer exercise than anticipated. It is therefore appropriate to ask ourselves the reasons for such difficulties and to try and uncover some avenues to be pursued if this work were to be started from scratch again. This paragraph therefore aims at identifying specific points that could be improved for performing full tokamak simulations. The following discussion should be understood as self-criticism with the goal of improving the development process of future full tokamak simulations. This discussion also aims at passing on the acquired experience in view of reducing similar difficulties in the future.

It is important to start by introducing the context within which this simulation work was accomplished. In December 2010, an F4E grant was started with the aim of simulating several ITER scenarios using full tokamak simulators. Specifically, it was the CRPP task to perform full tokamak simulations of the ITER hybrid and steady-state scenario using DINA-CH&CRONOS. This work was to be completed by September 2011. This deadline set a considerable pressure to achieve fast success. Fortnightly progress meetings also contributed to the necessity of obtaining quick results.

At the beginning of the F4E grant, considerable time had to be dedicated to uncover numerical difficulties encountered by DINA-CH&CRONOS in handling the strong gradients and high bootstrap current at the plasma edge. This delayed the completion of the first full tokamak simulations, thus further increasing the pressure for quick results.

Given this high pressure context, it is easy to understand that challenges faced during full tokamak simulations of the ITER hybrid and steady state scenarios were more often met via pragmatic solutions and/or quick fixes rather than in-depth analyses.

The full tokamak simulations submitted to F4E in September 2011 were complete even though several challenges had not been appropriately met. Namely, the q-profile in both the hybrid scenario and the steady-state scenario was hollower than desired and the hybrid regime could only be maintained for about 390s in the hybrid scenario when more than 1000s was expected.

These challenges were addressed in an amendment to the F4E grant. Improved full tokamak simulations of the hybrid and steady-state scenarios were submitted to F4E in March 2012.

In retrospect, it is the author's opinion that the approach of addressing challenges with pragmatic solutions and/or quick fixes was detrimental to this work for the following reasons:

- Quick fixes often lack universality. The quick fix of a specific challenge is often inappropriate for fixing the same challenge encountered in a different situation. As a result, the number of quick fixes increases rapidly. This potentially large number of fragile quick fixes weakens the robustness of the full tokamak simulations;

- The challenges addressed by a quick fix in a previous simulation may not be appropriate for a new simulation with a slightly modified scenario. This feature may thus require that a a new set of quick fixes be developed for each new simulation, which may be time-consuming;

- The use of quick fixes raises concerns regarding version control and simulation results documentation. It necessitates a well-organised and well-maintained logbook of the challenges encountered and the solutions applied to meet them. This may reveal to be a major concern in projects involving several collaborators in different institutes;

- The implementation of a quick fix for a specific challenge may be detrimental to the performance of the quick fix used for another challenge. This feature implies that several iterations may be necessary before both challenges are met.

These points may look trivial but it should be reminded that it is tempting to select a pragmatic solution and/or a quick fix when under pressure. It takes strong nerves to step back and take the necessary time to perform the in-depth analysis of a specific challenge and this does not respect contractual time-lines.

In the author's opinion, a more appropriate approach for meeting challenges faced during full tokamak simulations is *systematic automation*. Automation may necessitate a greater time investment than a quick fix but the experience demonstrated that this investment is more often recovered than not. Automation also provides some degree of robustness in that the automated solution is more likely to be usable in other circumstances.

After the completion of the F4E grant and amendment, it was decided to pursue this work in a more relaxed atmosphere. The following improvements were implemented during this extension work:

- The DINA-CH&CRONOS restart mechanism was perfected in close collaboration with the DINA authors and the CRONOS authors. This mechanism allowed new simulations to be more reliably started in the middle of previous simulations.

  The restart feature of DINA-CH&CRONOS was not sufficiently reliable during the F4E grant to be used in full confidence. In retrospect, the work would have greatly benefited from this feature being fully operational at the beginning of the grant;

- The simulations developed during the F4E grant showed the formation of a current hole. During the grant, this challenge was addressed by hand modifications of the heating and current drive scenario. In the extension work, a current hole controller was developed,

tested, and implemented. It provided an automated solution for the prevention of the formation of a current hole.

The implementation of the current hole controller triggered an avalanche of positive effects. Firstly, the numerical reliability of DINA-CH&CRONOS significantly improved because the values of $q(\rho = 0)$ were prevented from exploding. This showed to be extremely beneficial to the DINA numerical scheme. This improvement enabled a refinement of the vertical stabilisation control scheme and allowed the implementation of a less aggressive vertical stabilisation control scheme. This exposes the fact that the previous vertical stabilisation control scheme was mostly regulating the plasma column vertical speed against numerical noise rather than physical disturbances. In turn, the refined vertical stabilisation control scheme enabled more precise gap control. This refinement was extremely beneficial to avoid such effects as the occasional upper X-point reconnection that was observed in simulations performed during the F4E grant.

This discussion demonstrates that the automation of the solution to one specific challenge may improve several other seemingly unrelated features.

- During the F4E grant, the L-H transition and H-L transition timings were set by hand thus often resulting in inconsistencies between the imposed confinement mode and the power injected within the plasma. Moreover, this generated inconsistencies between the imposed confinement mode and the prescribed density profile evolution.

  The L-H and H-L transition detection was automated in the extension work. This guaranteed the consistency of the full tokamak simulations when the heating and current drive scenarios were modified.

These developments significantly improved the full tokamak simulations performance and robustness.

There remains one outstanding challenge whose solution was not automated. The avoidance of the PF system vertical force limit violation was achieved by hand-tuning the PF system coil current reference waveforms. Although only occasional hand modifications were required, each new simulation necessitated the post-processing assessment of the vertical forces on the PF system coils. Limits violations could only be addressed by modifying the PF system coil current reference waveforms and performing a new simulation.

If full tokamak simulations using DINA-CH&CRONOS were to be performed again for other scenarios or for an updated version of the ITER hybrid and steady-state scenarios, it is the author's opinion that time should be allocated to address the following challenges:

- At present, the DINA-CH&CRONOS restart mechanism is satisfactory when used during relatively quiescent phases but lacks reliability when simulations are restarted in transient periods. Improving the DINA-CH&CRONOS restart mechanism may save considerable time and may enable more efficient analysis of specific phases of the simulated plasma pulses;

- In the presented simulations, the PF system coil current reference waveforms are hand-tuned to prevent the violation of the PF coils vertical force limitations. The automation of the solution to this challenge would be beneficial to the scenario development scheme flexibility and the robustness;

- DINA-CH, CRONOS, and their interface are remarkably reliable and robust. Numerical crashes rarely occur and when they do, they are often linked to extreme plasma behaviour such as the formation of a current hole formation or VDEs. However, unexplained and sometimes non-reproducible crashes occasionally occur. These crashes were overlooked in this work, mostly because they could be avoided by slight scenario modifications. Nonetheless, these crashes deserve some attention;

- In the presented simulations, the calculation of the heating and current drive deposition profiles is performed by CRONOS once every second of simulated pulse time. This approach is not entirely consistent, especially for the ramp-up and ramp-down phases in which the plasma equilibrium evolves quickly, but such spacing of the heating and current drive deposition profiles calculations was necessary in order to save simulation time.

  A significant improvement of the DINA-CH&CRONOS simulator could consist of parallelising the heating and current drive deposition profiles calculations. Letting DINA-CH&CRONOS without the source calculations evolve on one side while simultaneously calculating the updated heating and current drive deposition profiles in parallel would drastically increase the simulator speed. Not only may the gain in speed be significant, but the heating and current drive deposition profiles are likely to be updated at a higher rate thus improving consistency;

- The data decimation should be carefully tuned prior to the simulation in order to avoid over-decimation of fast phenomena and to prevent the under-decimation of slow phenomena, which could lead to computer memory issues.

This paragraph concludes by stating the three most important lessons learned during this work.

Firstly, one should remain aware that success is binary but the path to success may be perfectible. It is important to step back from time to time to reflect on the improvements from which the undertaken simulations may benefit.

Secondly, the author argues in favour of systematic automation of the solutions to the encountered challenges. Automation is, in the author's opinion, the most appropriate approach for addressing challenges in a robust manner. Moreover, automation passes on the acquired experience and prevents unnecessary work repetition.

Finally, the negative aspects necessarily associated with a discussion of the lessons learned should not overshadow the largely positive outcomes of this work. Most importantly, it should

be stated that DINA-CH&CRONOS is very close to be a self-describing simulator in which a scenario can be straightforwardly set up and executed on demand. In that sense, DINA-CH&CRONOS achieves its stated goal which consists of emulating the operation of tokamaks.

5.8   Conclusion

The ITER hybrid scenario and steady-state scenario were developed using the prescribed-boundary simulator CRONOS. These nominal scenarios were then implemented in the DINA-CH&CRONOS full tokamak simulator, in order to assess their feasibility given the ITER 2010 design and its associated PF system power supplies, vertical stabilisation power supplies, and heating and current drive systems. The feasibility of the hybrid and steady-state scenario operation is assessed in terms of currents and vertical forces sustained by the PF coils.

The full tokamak simulations of the ITER hybrid and steady-state scenarios were performed from low initiation plasma current, namely $I_p = 0.4$MA, and all the operational phases are simulated until plasma termination at about $I_p = 0.5$MA. These simulations demonstrated the feasibility of the ITER hybrid and steady-state scenarios given the physical assumptions inherent to the DINA-CH&CRONOS full tokamak simulator, and more specifically given the assumption that a high confinement enhancement factor may be achieved and maintained in ITER. These simulations also underlined the sensitivity of the q-profile evolution to the L-H transition timing and to the flat-top plasma shape.

The sensitivity of the hybrid and steady-state scenarios with respect to electron density peaking, prescribed pedestal pressure, confinement enhancement factor, and the plasma shape during flat-top have been assessed using CRONOS. The MHD stability of the hybrid and steady-state scenarios has been assessed with MISHKA concluding that both scenarios are stable with respect to MHD stability.

6 Conclusion

This Chapter summarises the present thesis and discusses perspectives and opportunities for further research.

6.1 Summary

This thesis studies the operation of the ITER advanced tokamak scenarios from the viewpoint of tokamak control.

Semi-empirical modelling of the tokamak, the plasma, and the heating and current drive systems is introduced in Chapter 2. The presented modelling takes a pragmatic engineering approach in that emphasis is put on fast and quantitatively accurate simulation of the tokamak evolution with respect to actuator signals.

The introduced semi-empirical models are combined in the DINA-CH&CRONOS full tokamak simulator. Because it models the coupled effects of electromagnetic evolution and kinetic evolution, DINA-CH&CRONOS is appropriate for the simulation of advanced tokamak scenarios. The validation of DINA-CH&CRONOS is discussed and it is concluded that it shows good quantitative accuracy with respect to experiments even though the range of validity of some modules is not precisely determined.

Use cases of the DINA-CH and DINA-CH&CRONOS full tokamak simulators are presented in Chapter 3. Firstly, the simulation of the magnetic probe responses to the PF system power supply ripple is estimated. Assessing the effect of the voltage ripple on the magnetic probe signals is particularly important for long tokamak pulses, because the noise in magnetic probe voltage signals is integrated over long durations and may lead to erroneous reconstruction of the magnetic field. It is concluded in this study that the effect of the PF system power supplies ripple on the magnetic probes signals is small.

Secondly, a novel current density profile control approach is introduced and its features are explored using DINA-CH&CRONOS. This approach consists of modulating the ECRH power

demand and modulating the loop voltage to generate a period-averaged offset of the current density. The selection of the respective phases of the loop voltage modulation and the ECRH power demand modulation determinates the radial location of the plasma current density offset. Current density control is likely to be, if not necessary, at least extremely useful in helping implementing desired q-profile structures in ITER advanced pulses. This work is therefore a contribution to the advanced tokamak operation research.

Finally, the implementation in DINA-CH&CRONOS of a current density profile controller in the framework of ITER operation is mentioned.

In Chapter 4, it is argued that ITER advanced operation may greatly benefit from optimal control techniques. ITER possesses a limited lifetime and long pulses are costly and risky. It is therefore important to optimise ITER operation while guaranteeing tokamak protection. Moreover, ITER may greatly benefit from the automation of the scenario development process. All these objectives can be achieved via the implementation of robust optimal control schemes.

Two different optimal control algorithms are introduced and discussed. Firstly, an open-loop-with-feedback algorithm is implemented in a tokamak-like framework. The implemented algorithm demonstrates a significant gain in performance while guaranteeing tokamak protection. The main drawback of the discussed open-loop-with-feedback approach is that it necessitates accurate on-the-fly simulation of the plasma evolution.

Secondly, a robust optimisation of the ITER ramp-up is developed and implemented in the DINA-CH&CRONOS framework. This is a demonstration of the application of formal optimal control techniques in the framework of tokamak operation. A significant gain in performance is observed while tokamak protection is guaranteed. The main drawback with this approach is that it is purely open-loop and thus cannot take advantage of the measured evolution of the tokamak.

Real-time optimisation (RTO) techniques are introduced and their possible implementation in the framework of tokamak operation is discussed. It is argued that RTO is not yet a sufficiently mature research field for tokamak optimal control, except perhaps the necessary conditions of optimality (NCO) tracking approach, under the condition that the optimal control problem be low-dimensional.

Model-parameter adaptation suffers from the drawback that multiple simulations of the tokamak evolution must be performed during the plasma pulse because the optimiser necessitates several iterations to converge. Convergence must be achieved in a time much shorter than the typical pulse length. The implementation of such a scheme on short pulse tokamaks like TCV may be difficult, but its implementation on ITER long pulses may be achievable.

NCO tracking does not necessitate on-the-fly simulation of tokamak evolution. However, it requires the measurement of the cost function and constraint sensitivities to the process inputs. Such measurements require the systematic stimulation of each process input. This

identification process may be long, especially if the number of process inputs is large. Moreover, NCO tracking necessitates that the identification of active constraints be given prior to the plasma pulse, which is a piece of information that may be challenging to obtain. NCO tracking may be appropriate for ITER advanced operation because the flat-top phase may be sufficiently long to measure the cost function and constraint sensitivities to the process inputs.

The modifier adaptation approach combines the drawbacks of model-parameter adaptation and NCO tracking in that it necessitates on-the-fly simulation of the tokamak evolution and requires the measurement of the cost function and constraints sensitivities to the process inputs.

This thesis concludes with full tokamak simulations of the ITER hybrid and steady-state scenarios.

CRONOS is firstly used to develop nominal hybrid and steady-state scenarios in collaboration with CEA. These scenarios are tuned in order to maximise the fusion gain, to guarantee MHD stability, and to extend the burn duration beyond 1000s in the hybrid scenario. The sensitivity of the hybrid scenario evolution to various physical assumptions is assessed and it is concluded that the q-profile evolution is highly sensitive to the L-H transition timing, to the value of the prescribed confinement enhancement factor, to the ECRH power deposited during ramp-up, and to a lesser extent to the density profile peaking and to the prescribed pedestal pressure.

The nominal scenarios are imported in the framework of DINA-CH&CRONOS. Several controllers are developed for the tracking and regulation of the nominal scenarios reference waveforms in the full tokamak simulations. A current hole controller is designed to prevent the formation of a current hole in the plasma centre.

The advanced scenarios are simulated using DINA-CH&CRONOS after adjustments necessary for successful operation. The most important adjustment consists of significantly advancing the L-H transition timing in order to freeze the drop of the q-profile at a higher value.

It is concluded that both the hybrid scenario and the steady-state scenario can be performed using the latest ITER design without violating the PF system operational limits. A hybrid scenario with $Q \cong 8$ and with a burn phase of the order of 1000s hybrid scenario is realised. A steady-state scenario with $Q \cong 5$ and without an ITB or a high pedestal pressure is also performed.

6.2 Perspective

Based on very simple examples, it was demonstrated that significant performance improvement could be obtained using optimal control. Testing and implementing optimal control techniques in simulations and in presently-operated tokamaks may require a significant effort,

but it is the author's opinion that such an effort should be made for ITER for the following reasons:

- Optimal control requires the definition of an optimal control problem, i.e. the explicit definition of a cost function and operational constraints. In that sense, the definition of an optimal control problem contributes to automate scenario development. This feature may greatly benefit ITER because it guarantees that the developed scenario remains within the operational limits while achieving close-to-optimal operation.

  This is especially important for ITER because it is unlikely that the future ITER operators and session leaders will all possess the necessary 'feeling' or pragmatic understanding of the tokamak to operate ITER close to its optimal performance while guaranteeing the tokamak integrity.

  This feature also enables the efficient transmission of acquired experience.

- Automated scenario development via optimal control techniques is likely to minimise the number of exploratory pulses required to achieve a certain target. This feature is important because the number of total pulses that may be implemented on ITER is restricted.

Less than one decade separates us from the operation of ITER. It is the author's opinion that a significant part this time should be dedicated to the further development of optimal control in the framework of tokamak operation.

The novel approach for current density profile modification exposed in this thesis is promising and necessitates experimental confirmation. Such confirmation could be easily achieved in tokamaks such as TCV. Further developments of this technique could specifically include the analysis of the radial profile of the current density offset with respect to the phase difference between the ECRH power demand modulation and the loop voltage modulation.

Simulations of the ITER advanced scenarios could benefit from more advanced control schemes. In this thesis, the emphasis was put on the completion of the advanced scenario simulations rather than on the development of robust and efficient controllers. This was motivated by the necessity of quickly completing the advanced scenario simulations in the framework of an F4E grant. The implementation of a current density control scheme could potentially benefit the ITER hybrid scenario simulation. The achievement of a steady-state could benefit from the presence of a loop voltage controller.

Discrete events such as the L-H transition and the H-L transition are disturbances that the control system may have difficulties to regulate. It is important to assess whether the ITER PF system is capable of handling such events, especially in the case of an unforeseen H-L transition during flat-top.

Acknowledgements

This thesis benefited from the valuable contributions of several persons whom the author would like to acknowledge.

First and foremost, I am grateful to my thesis supervisor, Dr Jo Lister. His expertise and experience both in plasma physics and in control engineering were the bases upon which this thesis relies. Working with him was also a great source of pleasure both scientifically and humanly. I have been extremely lucky to be able to work and spend time with him.

Let me thank Dr Sun Hee Kim for his knowledge and support. The development of the DINA-CH&CRONOS greatly owes to his work. I am particularly thankful for the time he devoted to helping me in a period that was extremely stressful for him. I am also grateful to Dr Jeronimo Garcia for his expertise, guidance, and kindness. A significant part of the study of the ITER hybrid and steady-state scenarios is to be credited to his work.

Dr Victor Lukash and Dr Rustam Khayrutdinov must be thanked for their expertise and support in the development and usage of the DINA code. Many thanks to Dr Jean-François Artaud, Dr Vincent Basiuk, Dr Frédéric Imbeaux, whose expertise in the functioning of CRONOS was a precious contribution to this work.

Dr Grégory François and Dr Philippe Müllhaupt significantly contributed to this thesis. Let me thank them for their expertise and their willingness to share their experience in control. Thanks to Justin Barton for his contribution in a fruitful collaboration.

I would like to address special thanks to Lucie Brocher. Lucie is the talented Master student with whom I had the opportunity to work in 2009 in the framework of her Master diploma. The study of the cross-modulation of ECRH power and loop voltage greatly owes to her work and dedication. Let me thank her for her motivation and her unfailing optimism.

Important contributions were provided by members of the consortium within which the simulations of the ITER hybrid and steady-state scenarios were performed. Let me specifically thank Prof Massimiliano Mattei, Dr Mario Cavinato, and Dr Vassili Parail for their contributions.

I am grateful to my colleagues from CRPP, in particular Dr Basil Duval, Dr Stefano Coda, Dr Olivier Sauter, Dr Jean-Marc Moret, and Dr Jonathan Graves. I would like to address special

A Calculation of fusion energy from a Deuterium-Tritium reaction

The amount of energy released during a fusion reaction is estimated by Einstein's formula $E = mc^2$, where E is the amount of energy released per fusion reaction and m is the mass difference between the reactants and the products. Different fusion reactions release different amounts of energy.

Let us calculate the energy released by the fusion of two light reactants. Firstly, the hydrogen isotope ^2_1H, also known as deuterium D, which possesses $Z = 1$ proton and $A = 2$ nucleons, i.e. $A - Z = 1$ neutron. Its mass is $m_D = 2.014\text{u}$ [2]. Secondly, let us assume that the second reactant is the hydrogen isotope ^3_1H, also known as tritium T. Its mass is $m_T = 3.016\text{u}$. One of the possible fusion reactions is

$$^2_1\text{H} + ^3_1\text{H} \rightarrow ^4_2\text{He} + n$$
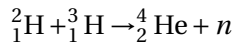
However, the mass of a ^4_2He isotope is $m_{He} \cong 4.003\text{u}$. The neutron mass is $m_n \cong 1.009\text{u}$. The mass difference between the reactants and the products is

$$m = m_D + m_T - m_{He} - m_n \cong +0.019\text{u} \cong 3.119 \cdot 10^{-29}\text{kg},$$

which corresponds to about 2% of the proton mass. This fusion reaction yields a produced energy of

$$E = mc^2 \cong 2.803 \cdot 10^{-12}\text{J} \cong 1.76 \cdot 10^7 \text{eV}.$$

This large amount of released energy is kinetic energy carried by the reaction products. We can thus rewrite the reaction equation in the following form:

$$^2_1\text{H} + ^3_1\text{H} \rightarrow ^4_2\text{He}(3.5\text{MeV}) + n(14.1\text{MeV}) \tag{A.1}$$

underlying the fact that the reactant are essentially immobile and the products share the released kinetic energy in inverse proportion to their mass because of momentum conservation.

Bibliography

[1] K. Schwarzschild, "On the equilibrium of the Sun's atmosphere," Nachrichten von der Königlichen Gesellschaft der Wissenschaften zu Göttingen. Math.-phys. Klasse, 195, p. 41-53, vol. 195, pp. 41–53, 1906.

[2] R. Weast, CRC handbook of chemistry and physics. Cleveland: CRC Press, 58th ed. ed., 1977.

[3] J. Riley and M. Tongudai, "The lithium content of sea water," Deep Sea Research and Oceanographic Abstracts, vol. 11, pp. 563–568, Aug. 1964.

[4] O. Serot, C. Wagemans, and J. Heyse, "New results on helium and tritium gas production from ternary fission," in AIP Conference Proceedings, pp. 857–860, 2005.

[5] M. Sawan and M. Abdou, "Physics and technology conditions for attaining tritium self-sufficiency for the DT fuel cycle," Fusion Engineering and Design, vol. 81, pp. 1131–1144, Feb. 2006.

[6] IAEA Power Reactor Information System, "Switzerland statistics 2011," 2012.

[7] B. Bumbacher, "Leibstadt Nuclear Power Plant Technical Description," tech. rep., Leibstadt Nuclear Power Plant, 2011.

[8] S. Française de Physique, La situation énergétique en France et dans le monde. EDP SCIENCES, 2012.

[9] V. P. Singh, R. K. Pai, D. D. Veerender, M. S. Vishnu, P. Vijayan, S. S. Managanvi, N. M. Badiger, and H. R. Bhat, "Estimation of biological half-life of tritium in coastal region of India.," Radiation protection dosimetry, vol. 142, pp. 153–9, Dec. 2010.

[10] P. J. Watt, "The critical need for closer ties between physics and industry," APS News, no. December, 2009.

[11] J. D. Lindl, P. Amendt, R. L. Berger, S. G. Glendinning, S. H. Glenzer, S. W. Haan, R. L. Kauffman, O. L. Landen, and L. J. Suter, "The physics basis for ignition using indirect-drive targets on the National Ignition Facility," Physics of Plasmas, vol. 11, p. 339, Feb. 2004.

Bibliography

[12] C. Alejaldre, J. Gozalo, J. Perez, F. Magaria, J. Diaz, J. Perez, A. Lopez-Fraguas, L. Garcia, V. Krivenski, R. Martin, A. Navarro, A. Perea, A. Rodriguez-Yunta, M. Ayza, and A. Varias, "TJ-II project; A flexible heliac stellarator," Fusion Technology; (USA), vol. 17:1, Jan. 1990.

[13] V. Erckmann, H.-J. Hartfuss, M. Kick, H. Renner, J. Sapper, F. Schauer, E. Speth, F. Wesner, F. Wagner, M. Wanner, A. Weller, and H. Wobig, "The W7-X project: scientific basis and technical realization," in 17th IEEE/NPSS Symposium Fusion Engineering (Cat. No.97CH36131), vol. 1, pp. 40–48, IEEE, 1997.

[14] S. V. Lebedev, D. J. Ampleford, S. N. Bland, S. C. Bott, J. P. Chittenden, J. Goyer, C. Jennings, M. G. Haines, G. N. Hall, D. A. Hammer, J. B. A. Palmer, S. A. Pikuz, T. A. Shelkovenko, and T. Christoudias, "Physics of wire array Z-pinch implosions: experiments at Imperial College," Plasma Physics and Controlled Fusion, vol. 47, pp. A91–A108, May 2005.

[15] M. Keilhacker, M. Kornherr, and K. H. Steuer, "Observation of collisionless plasma heating by strong shock waves," Zeitschrift für Physik, vol. 223, pp. 385–396, Aug. 1969.

[16] J. P. Freidberg, "Magnetohydrodynamic Stability of a Diffuse Screw Pinch," Physics of Fluids, vol. 13, p. 1812, July 1970.

[17] E. J. Lerner, S. K. Murali, D. Shannon, A. M. Blake, and F. V. Roessel, "Fusion reactions from >150keV ions in a dense plasma focus plasmoid," Physics of Plasmas, vol. 19, p. 032704, Mar. 2012.

[18] J. Wesson, Tokamaks. Oxford University Press, 2011.

[19] S. Coda, O. Sauter, M. A. Henderson, and T. P. Goodman, "Full bootstrap discharge sustainment in steady-state in the TCV tokamak," in 22nd IAEA Fusion Energy Conference, (Geneva), pp. EX/2–3, 2008.

[20] L. Spitzer, Physics of fully ionized gases, vol. 2nd rev. e. New York: Interscience Publication, 2nd rev. e ed., 1965.

[21] H. F. Dylla, "Glow discharge techniques for conditioning high-vacuum systems," Journal of Vacuum Science & Technology A: Vacuum, Surfaces, and Films, vol. 6, p. 1276, May 1988.

[22] S. Tanaka, K. Hanada, T. Minami, S. Ide, M. Iida, H. Tanaka, T. Maekawa, and Y. Terumichi, "Initiation of plasma current with the assistance of electron cyclotron waves in the WT-3 tokamak," Nuclear Fusion, vol. 33, pp. 505–513, Mar. 1993.

[23] E. Joffrin, "Advanced tokamak scenario developments for the next step," Plasma Physics and Controlled Fusion, vol. 49, pp. B629–B649, Dec. 2007.

[24] J. Doyle, K. Glover, P. P. Khargonekar, and B. A. Francis, "State-space solutions to standard H2 and H-infinity control problems," IEEE Trans. Auto. Control, vol. 34, no. 8, pp. 831–847, 1989.

[25] H. P. Furth, P. H. Rutherford, H. C. Wolfe, T. K. Chu, and H. W. Hendel, "Feedback Control Problems in Tokamaks," in <u>AIP Conference Proceedings</u>, vol. 1, pp. 74–79, 1970.

[26] R. Longchamp, <u>Commande numérique de systèmes dynamiques</u>. PPUR Presses polytechniques, 2010.

[27] E. Lazarus, G. Navratil, C. Greenfield, E. Strait, M. Austin, K. Burrell, T. Casper, D. Baker, J. DeBoo, E. Doyle, R. Durst, J. Ferron, C. Forest, P. Gohil, R. Groebner, W. Heidbrink, R.-M. Hong, W. Houlberg, A. Howald, C.-L. Hsieh, A. Hyatt, G. Jackson, J. Kim, L. Lao, C. Lasnier, A. Leonard, J. Lohr, R. La Haye, R. Maingi, R. Miller, M. Murakami, T. Osborne, L. Perkins, C. Petty, C. Rettig, T. Rhodes, B. Rice, S. Sabbagh, D. Schissel, J. Scoville, R. Snider, G. Staebler, B. Stallard, R. Stambaugh, H. St. John, R. Stockdale, P. Taylor, D. Thomas, A. Turnbull, M. Wade, R. Wood, and D. Whyte, "Higher Fusion Power Gain with Current and Pressure Profile Control in Strongly Shaped DIII-D Tokamak Plasmas," <u>Physical Review Letters</u>, vol. 77, pp. 2714–2717, Sept. 1996.

[28] O. Sauter, E. Westerhof, M. Mayoral, B. Alper, P. Belo, R. Buttery, A. Gondhalekar, T. Hellsten, T. Hender, D. Howell, T. Johnson, P. Lamalle, M. Mantsinen, F. Milani, M. Nave, F. Nguyen, A. Pecquet, S. Pinches, S. Podda, and J. Rapp, "Control of Neoclassical Tearing Modes by Sawtooth Control," <u>Physical Review Letters</u>, vol. 88, p. 105001, Feb. 2002.

[29] K. J. Å ström and R. M. Murray, "Feedback Systems: An Introduction for Scientists and Engineers," Jan. 2008.

[30] S. Skogestad and I. Postlethwaite, <u>Multivariable Feedback Control: Analysis and Design</u>. Wiley-Interscience, 2005.

[31] M. Keilhacker, A. Gibson, C. Gormezano, P. Lomas, P. Thomas, M. Watkins, P. Andrew, B. Balet, D. Borba, C. Challis, I. Coffey, G. Cottrell, H. D. Esch, N. Deliyanakis, A. Fasoli, C. Gowers, H. Guo, G. Huysmans, T. Jones, W. Kerner, R. König, M. Loughlin, A. Maas, F. Marcus, M. Nave, F. Rimini, G. Sadler, S. Sharapov, G. Sips, P. Smeulders, F. Söldner, A. Taroni, B. Tubbing, M. von Hellermann, D. Ward, and J. Team, "High fusion performance from deuterium-tritium plasmas in JET," <u>Nuclear Fusion</u>, vol. 39, pp. 209–234, Feb. 1999.

[32] J. D. Lawson, "Some Criteria for a Power Producing Thermonuclear Reactor," <u>Proceedings of the Physical Society. Section B</u>, vol. 70, pp. 6–10, Jan. 1957.

[33] M. Greenwald, J. Terry, S. Wolfe, S. Ejima, M. Bell, S. Kaye, and G. Neilson, "A new look at density limits in tokamaks," <u>Nuclear Fusion</u>, vol. 28, pp. 2199–2207, Dec. 1988.

[34] F. Troyon, R. Gruber, H. Saurenmann, S. Semenzato, and S. Succi, "MHD-Limits to Plasma Confinement," <u>Plasma Physics and Controlled Fusion</u>, vol. 26, pp. 209–215, Jan. 1984.

[35] F. Troyon and R. Gruber, "A semi-empirical scaling law for the β-limit in tokamaks," <u>Physics Letters A</u>, vol. 110, pp. 29–34, July 1985.

[36] R. J. Goldston, "Energy confinement scaling in Tokamaks: some implications of recent experiments with Ohmic and strong auxiliary heating," Plasma Physics and Controlled Fusion, vol. 26, pp. 87–103, Jan. 1984.

[37] M. Greenwald, R. Boivin, F. Bombarda, P. Bonoli, C. Fiore, D. Garnier, J. Goetz, S. Golovato, M. Graf, R. Granetz, S. Horne, A. Hubbard, I. Hutchinson, J. Irby, B. LaBombard, B. Lipschultz, E. Marmar, M. May, G. McCracken, P. O'Shea, J. Rice, J. Schachter, J. Snipes, P. Stek, Y. Takase, J. Terry, Y. Wang, R. Watterson, B. Welch, and S. Wolfe, "H mode confinement in Alcator C-Mod," Nuclear Fusion, vol. 37, pp. 793–807, June 1997.

[38] I. P. B. Editors, I. P. E. G. C. an Co-Chairs, I. J. C. T. Unit, and Physics, "ITER Physics Basis: Overview and summary," Nuclear Fusion, vol. 39, pp. 2137–2174, Dec. 1999.

[39] M. Shimada, D. Campbell, V. Mukhovatov, M. Fujiwara, N. Kirneva, K. Lackner, M. Nagami, V. Pustovitov, N. Uckan, J. Wesley, N. Asakura, A. Costley, A. Donné, E. Doyle, A. Fasoli, C. Gormezano, Y. Gribov, O. Gruber, T. Hender, W. Houlberg, S. Ide, Y. Kamada, A. Leonard, B. Lipschultz, A. Loarte, K. Miyamoto, T. Osborne, A. Polevoi, and A. Sips, "Chapter 1: Overview and summary," Nuclear Fusion, vol. 47, pp. S1–S17, June 2007.

[40] R. D. Middlebrook and S. Cuk, "A general unified approach to modelling switching-converter power stages," Power Electronics Specialists Conference, pp. 18–34, 1976.

[41] R. Middlebrook, "Modelling and analysis methods for DC-to-DC switching converters," in Conference record of the papers presented at the 1977 IEEE IAS International Semiconductor Power Converter Conference, Walt Disney World Contemporary Hotel, Lake Buena Vista, Fl., 28-31 March, 1977, (New York), pp. 90–111, Institute of Electrical and Electronics Engineers, 1977.

[42] Y. S. Lee, "A Systematic and Unified Approach to Modeling Switches in Switch-Mode Power Supplies," IEEE Transactions on Industrial Electronics, vol. IE-32, pp. 445–448, Nov. 1985.

[43] Y. Gribov, "Data for study of ITER plasma magnetic control - ITER_D_33_NHXN v3.4," tech. rep., ITER Internation Team, 2010.

[44] Y. Gribov, "Engineering limits and other data related to analysis of ITER plasma equilibria, poloidal field scenarios, and plasma control - ITER_D_247JZD issue 1," tech. rep., ITER International Team, 2006.

[45] E. B. Rosa, "Calculation of the self-inductance of single-layer coils," Bulletin of the Bureau of Standards, vol. 2, no. 2, pp. 161–187 BS Sci. 31, 1906.

[46] H. Nagaoka, "The Inductance Coefficients of Solenoids," Journal of the College of Science, Imperial University, vol. XXVII, no. 6, 1909.

[47] F. W. Grover, Inductance Calculations. Dover Publications, 1946.

[48] L. Rayleigh, "The absolute measurement of inductance," <u>Absolute Meas.</u>, vol. II, no. II, p. 322, 1905.

[49] J. Maxwell, <u>A treatise in Electricity and Magnetism</u>. Clarendon Press Oxford, 1873.

[50] A. A. Vlasov, "The vibrational properties of an electron gas," <u>Soviet Physics Uspekhi</u>, vol. 10, pp. 721–733, June 1968.

[51] W. W. Lee, "Gyrokinetic approach in particle simulation," <u>Physics of Fluids</u>, vol. 26, p. 556, Feb. 1983.

[52] S. I. Braginskii, "Transport Processes in a Plasma," <u>Reviews of Plasma Physics</u>, vol. 1, p. 205, 1965.

[53] J. P. Freidberg, <u>Ideal Magnetohydrodynamics</u>. Springer, 1987.

[54] V. D. Shafranov, "On Magnetohydrodynamical Equilibrium Configurations," <u>Soviet Journal of Experimental and Theoretical Physics</u>, vol. 6, p. 545, 1958.

[55] S. Jardin, N. Pomphrey, and J. Delucia, "Dynamic modeling of transport and positional control of tokamaks," <u>Journal of Computational Physics</u>, vol. 66, pp. 481–507, Oct. 1986.

[56] J. D. Jackson, <u>Classical Electrodynamics, 2nd Edition</u>. Wiley, 1975.

[57] W. D. D'haeseleer, W. N. Hitchon, J. D. Callen, and J. L. Shohet, <u>Flux Coordinates and Magnetic Field Structure</u>. Springer, 1991.

[58] S. H. Kim, <u>Full tokamak discharge simulation and kinetic plasma profile control for ITER</u>. PhD thesis, EPFL, 2009.

[59] F. Hinton and R. Hazeltine, "Theory of plasma transport in toroidal confinement systems," <u>Reviews of Modern Physics</u>, vol. 48, pp. 239–308, Apr. 1976.

[60] O. Sauter, C. Angioni, and Y. R. Lin-Liu, "Neoclassical conductivity and bootstrap current formulas for general axisymmetric equilibria and arbitrary collisionality regime," <u>Physics of Plasmas</u>, vol. 6, p. 2834, July 1999.

[61] M. Rosenbluth, W. MacDonald, and D. Judd, "Fokker-Planck Equation for an Inverse-Square Force," <u>Physical Review</u>, vol. 107, pp. 1–6, July 1957.

[62] V. Krivenski, I. Fidone, G. Giruzzi, G. Granata, R. Meyer, and E. Mazzucato, "Improving current generation in a tokamak by electron cyclotron waves," <u>Nuclear Fusion</u>, vol. 25, pp. 127–133, Feb. 1985.

[63] G. Lister, D. E. Post, and R. Goldston, "Computer simulation of neutral beam injection into Tokamaks using Monte Carlo technique," in <u>3rd Symposium on Plasma Heating in Toroidal Devices</u>, vol. -1, (Varenna, Italy), pp. 303 – 307, 1976.

[64] G. Lister, "A fully 3D neutral beam injection code using Monte Carlo methods," tech. rep., Max-Planck Institut für Plasmaphysik, Garching, 1985.

[65] J. Rome, J. Callen, and J. Clarke, "Neutral-beam injection into a tokamak, part I: fast-ion spatial distribution for tangential injection," <u>Nuclear Fusion</u>, vol. 14, pp. 141–151, Apr. 1974.

[66] Y. Feng, "Formulation and application of the neutral particle beam deposition code SINBAD," tech. rep., Max-Planck Institut für Plasmaphysik, Garching, 1993.

[67] Y. Feng, B. Wolle, and K. Hübner, "New, simplified technique for calculating particle source rates due to neutral beam injection into tokamaks," <u>Computer Physics Communications</u>, vol. 88, pp. 161–172, Aug. 1995.

[68] J. G. Cordey, "A review of Non-Inductive current drive theory," <u>Plasma Physics and Controlled Fusion</u>, vol. 26, pp. 123–132, Jan. 1984.

[69] T. Hellsten and L. Villard, "Power deposition for ion cyclotron heating in large tokamaks," <u>Nuclear Fusion</u>, vol. 28, pp. 285–295, Feb. 1988.

[70] T. Hellsten and L.-G. Eriksson, "A modelling scheme for the direct electron heating profiles during ion cyclotron resonance heating," <u>Nuclear Fusion</u>, vol. 29, pp. 2165–2173, Dec. 1989.

[71] P. T. Bonoli and R. C. Englade, "Simulation model for lower hybrid current drive," <u>Physics of Fluids</u>, vol. 29, p. 2937, Sept. 1986.

[72] C. F. Kennel, "Velocity Space Diffusion from Weak Plasma Turbulence in a Magnetic Field," <u>Physics of Fluids</u>, vol. 9, p. 2377, Dec. 1966.

[73] B. A. Trubnikov, "Particle Interactions in a Fully Ionized Plasma," <u>Reviews of Plasma Physics</u>, vol. 1, p. 105, 1965.

[74] R. Khayrutdinov and V. Lukash, "Studies of Plasma Equilibrium and Transport in a Tokamak Fusion Device with the Inverse-Variable Technique," <u>Journal of Computational Physics</u>, vol. 109, pp. 193–201, Dec. 1993.

[75] R. R. Khayrutdinov, J. B. Lister, V. E. Lukash, and J. P. Wainwright, "Comparing DINA code simulations with TCV experimental plasma equilibrium responses," <u>Plasma Physics and Controlled Fusion</u>, vol. 43, pp. 321–342, Mar. 2001.

[76] J.-Y. Favez, R. R. Khayrutdinov, J. B. Lister, and V. E. Lukash, "Comparing TCV experimental VDE responses with DINA code simulations," <u>Plasma Physics and Controlled Fusion</u>, vol. 44, pp. 171–193, Feb. 2002.

[77] J.-F. Artaud, F. Imbeaux, T. Aniel, V. Basiuk, L.-G. Eriksson, G. Giruzzi, G. T. Hoang, G. Huysmans, E. Joffrin, Y. Peysson, M. Schneider, and P. Thomas, "Predictive integrated modelling for ITER scenarios," in <u>32nd EPS Conference on Plasma Physics</u>, vol. 29, (Tarragona), pp. ECA Vol. 29C, P–1.035, 2005.

[78] M. Erba, T. Aniel, V. Basiuk, A. Becoulet, and X. Litaudon, "Validation of a new mixed Bohm/gyro-Bohm model for electron and ion heat transport against the ITER, Tore Supra and START database discharges," Nuclear Fusion, vol. 38, pp. 1013–1028, July 1998.

[79] V. Erckmann and U. Gasparino, "Electron cyclotron resonance heating and current drive in toroidal fusion plasmas," Plasma Physics and Controlled Fusion, vol. 36, pp. 1869–1962, Dec. 1994.

[80] L.-G. Eriksson, T. Hellsten, and U. Willen, "Comparison of time dependent simulations with experiments in ion cyclotron heated plasmas," Nuclear Fusion, vol. 33, pp. 1037–1048, July 1993.

[81] L. Villard, K. Appert, R. Gruber, and J. Vaclavik, "Global waves in cold plasmas," Computer Physics Reports, vol. 4, pp. 95–135, Aug. 1986.

[82] F. Imbeaux and Y. Peysson, "Ray-tracing and Fokker–Planck modelling of the effect of plasma current on the propagation and absorption of lower hybrid waves," Plasma Physics and Controlled Fusion, vol. 47, pp. 2041–2065, Nov. 2005.

[83] J.-F. Artaud and S. H. Kim, "A new free-boundary equilibrium evolution code, FREEBIE," in 39th European Physical Society Conference on Plasma Physics, (Stockholm, Sweden), p. P4.023, 2012.

[84] J. Urban, J.-F. Artaud, K. Besseghir, J. B. Lister, J. Garcia, F. Imbeaux, S. H. Kim, E. Nardon, and R. Nouailletas, "Free-boundary equilibrium transport simulations of ITER scenarios under control," in 39th European Physical Society Conference on Plasma Physics, (Stockholm, Sweden), p. P1.019, 2012.

[85] P. Hertout, C. Boulbe, E. Nardon, J. Blum, S. Brémond, J. Bucalossi, B. Faugeras, V. Grandgirard, and P. Moreau, "The CEDRES++ equilibrium code and its application to ITER, JT-60SA and Tore Supra," Fusion Engineering and Design, vol. 86, pp. 1045–1048, Oct. 2011.

[86] J. B. Lister, K. Besseghir, J.-F. Artaud, R. R. Khayrutdinov, S. H. Kim, and V. E. Lukash, "Development of the DINA-CH Full Tokamak Simulator," in 38th European Physical Society Conference on Plasma Physics, (Strasbourg, France), p. P1.105, 2011.

[87] J. Crotinger, L. LoDestro, L. Pearlstein, A. Tarditi, T. Casper, and E. Hooper, "CORSICA: A comprehensive simulation of toroidal magnetic-fusion devices. Final report to the LDRD Program," Mar. 1997.

[88] S. H. Kim, J. F. Artaud, V. Basiuk, V. Dokuka, R. R. Khayrutdinov, J. B. Lister, and V. E. Lukash, "Full tokamak discharge simulation of ITER by combining DINA-CH and CRONOS," Plasma Physics and Controlled Fusion, vol. 51, p. 105007, Oct. 2009.

[89] I. Benfatto, P. Mondino, A. Roshal, A. Coletti, D. Hrabal, A. Maschio, R. Piovan, S. Tenconi, S. Bulgakov, and V. Kuchinski, "AC/DC converters for the ITER Poloidal Field system," in Proceedings of 16th International Symposium on Fusion Engineering, vol. 1, pp. 658–661, IEEE, 1995.

[90] E. Gaio, R. Piovan, V. Toigo, and L. Benfatto, "Bypass operation of the ITER AC/DC converters for reactive power reduction," in 17th IEEE/NPSS Symposium Fusion Engineering (Cat. No.97CH36131), vol. 2, pp. 1141–1144, IEEE, 1998.

[91] D. Fasel, "Private communications," tech. rep., Centre de Recherches en Physique des Plasmas - EPFL, 2009.

[92] K. Besseghir, J. B. Lister, S. H. Kim, P. Moreau, F. Saint-Laurent, V. Dokuka, R. R. Khayrutdinov, and V. E. Lukash, "Identification of the ITER plasma equilibrium using modulation," in European Physical Society Conference on Plasma Physics, (Sofia, Bulgaria), p. P4.162, 2009.

[93] S. von Goeler, W. Stodiek, and N. Sauthoff, "Studies of Internal Disruptions and m=1 Oscillations in Tokamak Discharges with Soft—X-Ray Tecniques," Physical Review Letters, vol. 33, pp. 1201–1203, Nov. 1974.

[94] B. Coppi, "Instabilities due to Temperature Gradients in Complex Magnetic Field Configurations," Physics of Fluids, vol. 10, p. 582, Mar. 1967.

[95] T. Wijnands, D. V. Houtte, G. Martin, X. Litaudon, and P. Froissard, "Feedback control of the current profile on Tore Supra," Nuclear Fusion, vol. 37, pp. 777–791, June 1997.

[96] D. Moreau, F. Crisanti, X. Litaudon, D. Mazon, P. D. Vries, R. Felton, E. Joffrin, L. Laborde, M. Lennholm, A. Murari, V. Pericoli-Ridolfini, M. Riva, T. Tala, G. Tresset, L. Zabeo, K. Zastrow, and c. t. t. E.-J. Workprogramme, "Real-time control of the q -profile in JET for steady state advanced tokamak operation," Nuclear Fusion, vol. 43, pp. 870–882, Sept. 2003.

[97] J. E. Barton, M. D. Boyer, S. Wenyu, E. Schuster, T. C. Luce, J. R. Ferron, M. L. Walker, D. A. Humphreys, B. G. Penaflor, and R. D. Johnson, "First-principles model-based robust control of the current profile evolution in the DIII-D tokamak," tech. rep., Lehigh University, 2011.

[98] F. Felici and O. Sauter, "Non-linear model-based optimization of actuator trajectories for tokamak plasma profile control," Plasma Physics and Controlled Fusion, vol. 54, no. 2, p. 025002, 2012.

[99] S. H. Kim and J. B. Lister, "A potentially robust plasma profile control approach for ITER using real-time estimation of linearized profile response models," Plasma Physics and Controlled Fusion, vol. 52, no. 7, p. 074002, 2012.

[100] H. Wheeler, "Formulas for the Skin Effect," Proceedings of the IRE, vol. 30, pp. 412–424, Sept. 1942.

[101] K. Besseghir, L. Brocher, J. B. Lister, R. R. Khayrutdinov, V. E. Lukash, and J.-F. Artaud, "Cross-modulation of loop voltage and ECH power in ITER," in 37th European Physical Society Conference on Plasma Physics, (Dublin, Ireland), p. P2.175, 2010.

[102] J. E. Barton, E. Schuster, K. Besseghir, and J. Lister, "Towards First-principles Control-oriented Modeling of the Magnetic and Kinetic Plasma Profile Evolutions in ITER," Bulletin of the American Physical Society, vol. Volume 57,, Oct. 2012.

[103] M. A. Brdys and P. Tatjewski, Iterative Algorithms For Multilayer Optimizing Control. Imperial College Press, 2005.

[104] B. Chachuat, B. Srinivasan, and D. Bonvin, "Adaptation strategies for real-time optimization," Computers & Chemical Engineering, vol. 33, pp. 1557–1567, Oct. 2009.

[105] L. Pontryagin, Mathematical Theory of Optimal Processes. Harwood Academic (Medical, Reference and Social Sc, 1962.

[106] B. C. Chachuat, Nonlinear and dynamic optimization: from theory to practice. EPFL, 2009.

[107] Y. Ou, C. Xu, E. Schuster, T. C. Luce, J. R. Ferron, M. L. Walker, and D. a. Humphreys, "Design and simulation of extremum-seeking open-loop optimal control of current profile in the DIII-D tokamak," Plasma Physics and Controlled Fusion, vol. 50, p. 115001, Nov. 2008.

[108] K. Besseghir, J. B. Lister, and P. Müllhaupt, "Maintaining optimal ITER scenario trajectories," in European Physical Society Conference on Plasma Physics, (Dublin, Ireland), 2010.

[109] F. Crisanti, R. Albanese, G. Ambrosino, M. Ariola, J. Lister, M. Mattei, F. Milani, A. Pironti, F. Sartori, and F. Villone, "Upgrade of the present JET shape and vertical stability controller," Fusion Engineering and Design, vol. 66-68, pp. 803–807, Sept. 2003.

[110] K. Besseghir and J. B. Lister, "Scenario optimisation for ITER," in European Physical Society Conference on Plasma Physics, (Strasbourg, France), 2011.

[111] B. Chachuat, A. Marchetti, and D. Bonvin, "Process optimization via constraints adaptation," Journal of Process Control, vol. 18, pp. 244–257, Mar. 2008.

[112] G. François, B. Srinivasan, and D. Bonvin, "Use of measurements for enforcing the necessary conditions of optimality in the presence of constraints and uncertainty," Journal of Process Control, vol. 15, pp. 701–712, Sept. 2005.

Bibliography

[113] O. Gruber, R. C. Wolf, R. Dux, C. Fuchs, S. Günter, A. Kallenbach, K. Lackner, M. Maraschek, P. J. McCarthy, H. Meister, G. Pereverzev, F. Ryter, J. Schweinzer, U. Seidel, S. Sesnic, A. Stäbler, and J. Stober, "Stationary H-Mode Discharges with Internal Transport Barrier on ASDEX Upgrade," Physical Review Letters, vol. 83, pp. 1787–1790, Aug. 1999.

[114] R. C. Wolf, O. Gruber, M. Maraschek, R. Dux, C. Fuchs, S. Günter, A. Herrmann, A. Kallenbach, K. Lackner, P. J. McCarthy, H. Meister, G. Pereverzev, J. Schweinzer, U. Seidel, and t. A. U. Team, "Stationary advanced scenarios with internal transport barrier on ASDEX Upgrade," Plasma Physics and Controlled Fusion, vol. 41, pp. B93–B107, Dec. 1999.

[115] A. Staebler, A. Sips, M. Brambilla, R. Bilato, R. Dux, O. Gruber, J. Hobirk, L. Horton, C. Maggi, A. Manini, M. Maraschek, A. Mück, Y.-S. Na, R. Neu, G. Tardini, M. Wade, and A. U. Team, "The improved H-mode at ASDEX Upgrade: a candidate for an ITER hybrid scenario," Nuclear Fusion, vol. 45, pp. 617–625, July 2005.

[116] T. Luce, M. Wade, P. Politzer, S. Allen, M. Austin, D. Baker, B. Bray, D. Brennan, K. Burrell, T. Casper, M. Chu, J. DeBoo, E. Doyle, J. Ferron, A. Garofalo, P. Gohil, I. Gorelov, C. Greenfield, R. Groebner, W. Heidbrink, C.-L. Hsieh, A. Hyatt, R. Jayakumar, J. Kinsey, R. L. Haye, L. Lao, C. Lasnier, E. Lazarus, A. Leonard, Y. Lin-Liu, J. Lohr, M. Mahdavi, M. Makowski, M. Murakami, C. Petty, R. Pinsker, R. Prater, C. Rettig, T. Rhodes, B. Rice, E. Strait, T. Taylor, D. Thomas, A. Turnbull, J. Watkins, W. West, and K.-L. Wong, "Long pulse high performance discharges in the DIII-D tokamak," Nuclear Fusion, vol. 41, pp. 1585–1599, Nov. 2001.

[117] T. Luce, M. Wade, J. Ferron, A. Hyatt, A. Kellman, J. Kinsey, R. L. Haye, C. Lasnier, M. Murakami, P. Politzer, and J. Scoville, "Stationary high-performance discharges in the DIII-D tokamak," Nuclear Fusion, vol. 43, pp. 321–329, May 2003.

[118] E. Joffrin, C. Challis, J. Citrin, J. Garcia, J. Hobirk, I. Jenkins, J. Lonnroth, D. C. McDonald, P. Maget, P. Mantica, M. Beurskens, M. Brix, P. Buratti, F. Crisanti, L. Frassinetti, C. Giroud, F. Imbeaux, M. Piovesan, F. Rimini, G. Sergienko, A. C. C. Sips, T. Tala, and I. Voitsekhovitch, "High confinement hybrid scenario in JET and its significance for ITER," in 23rd IAEA Fusion Energy Conference, (Daejeon, South Korea), p. EXC1/1, 2010.

[119] J. Hobirk, F. Imbeaux, F. Crisanti, P. Buratti, C. D. Challis, E. Joffrin, B. Alper, Y. Andrew, P. Beaumont, M. Beurskens, A. Boboc, A. Botrugno, M. Brix, G. Calabro', I. Coffey, S. Conroy, O. Ford, D. Frigione, J. Garcia, C. Giroud, N. C. Hawkes, D. Howell, I. Jenkins, D. Keeling, M. Kempenaars, H. Leggate, P. Lotte, E. de la Luna, G. P. Maddison, P. Mantica, C. Mazzotta, D. C. McDonald, A. Meigs, I. Nunes, E. Rachlew, F. Rimini, M. Schneider, A. C. C. Sips, J. K. Stober, W. Studholme, T. Tala, M. Tsalas, I. Voitsekhovitch, and P. C. de Vries, "Improved confinement in JET hybrid discharges," Plasma Physics and Controlled Fusion, vol. 54, p. 095001, Sept. 2012.

[120] A. Isayama, Y. Kamada, N. Hayashi, T. Suzuki, T. Oikawa, T. Fujita, T. Fukuda, S. Ide, H. Takenaga, K. Ushigusa, T. Ozeki, Y. Ikeda, N. Umeda, H. Yamada, M. Isobe, Y. Narushima, K. Ikeda, S. Sakakibara, K. Yamazaki, K. Nagasaki, and t. J.-. Team, "Achievement of high fusion triple product, steady-state sustainment and real-time NTM stabilization in high- betap ELMy H-mode discharges in JT-60U," Nuclear Fusion, vol. 43, pp. 1272–1278, Oct. 2003.

[121] O. Sauter, M. Henderson, F. Hofmann, T. Goodman, S. Alberti, C. Angioni, K. Appert, R. Behn, P. Blanchard, P. Bosshard, R. Chavan, S. Coda, B. Duval, D. Fasel, A. Favre, I. Furno, P. Gorgerat, J.-P. Hogge, P.-F. Isoz, B. Joye, P. Lavanchy, J. Lister, X. Llobet, J.-C. Magnin, P. Mandrin, A. Manini, B. Marlétaz, P. Marmillod, Y. Martin, J.-M. Mayor, A. Martynov, J. Mlynar, J.-M. Moret, C. Nieswand, P. Nikkola, P. Paris, A. Perez, Z. Pietrzyk, R. Pitts, A. Pochelon, G. Pochon, A. Refke, H. Reimerdes, J. Rommers, E. Scavino, G. Tonetti, M. Tran, F. Troyon, and H. Weisen, "Steady-State Fully Noninductive Current Driven by Electron Cyclotron Waves in a Magnetically Confined Plasma," Physical Review Letters, vol. 84, pp. 3322–3325, Apr. 2000.

[122] S. Coda, T. P. Goodman, M. A. Henderson, O. Sauter, R. Behn, A. Bottino, Y. Camenen, E. Fable, A. Martynov, P. Nikkola, A. Scarabosio, G. Zhuang, and C. Zucca, "High-bootstrap, noninductively sustained electron internal transport barriers in the Tokamak a Configuration Variable," Physics of Plasmas, vol. 12, p. 056124, May 2005.

[123] H. Zushi, S. Itoh, K. Hanada, K. Nakamura, M. Sakamoto, E. Jotaki, M. Hasegawa, Y. Pan, S. Kulkarni, A. Iyomasa, S. Kawasaki, H. Nakashima, N. Yoshida, K. Tokunaga, T. Fujiwara, M. Miyamoto, H. Nakano, M. Yuno, A. Murakami, S. Nakamura, N. Sakamoto, K. Shinoda, S. Yamazoe, H. Akanishi, K. Kuramoto, Y. Matsuo, A. Iwamae, T. Fuijimoto, A. Komori, T. Morisaki, H. Suzuki, S. Masuzaki, Y. Hirooka, Y. Nakashima, and O. Mitarai, "Overview of steady state tokamak plasma experiments in TRIAM-1M," Nuclear Fusion, vol. 43, pp. 1600–1609, Dec. 2003.

[124] D. van Houtte, G. Martin, A. Bécoulet, J. Bucalossi, G. Giruzzi, G. Hoang, T. Loarer, B. Saoutic, and o. b. o. t. T. S. Team, "Recent fully non-inductive operation results in Tore Supra with 6 min, 1 GJ plasma discharges," Nuclear Fusion, vol. 44, pp. L11–L15, May 2004.

[125] ITER Physics Expert Groups on Confinement and Transport and Confinement Modelling and Database, "Chapter 2 : Plasma confinement and transport," Nuclear Fusion, vol. 39, no. 12, p. 2175, 1999.

[126] C. Kessel, G. Giruzzi, A. Sips, R. Budny, J. Artaud, V. Basiuk, F. Imbeaux, E. Joffrin, M. Schneider, M. Murakami, T. Luce, H. St John, T. Oikawa, N. Hayashi, T. Takizuka, T. Ozeki, Y.-S. Na, J. Park, J. Garcia, and A. Tucillo, "Simulation of the hybrid and steady state advanced operating modes in ITER," Nuclear Fusion, vol. 47, pp. 1274–1284, Sept. 2007.

[127] S. H. Kim, T. A. Casper, D. J. Campbell, J. A. Snipes, R. Bulmer, L. L. LoDestro, W. H. Meyer, and L. D. Pearlstein, "CORSICA simulations of ITER advanced operation scenarios," in European Physical Society Conference on Plasma Physics, p. P5.089, 2012.

[128] T. C. Luce, C. D. Challis, S. Ide, E. Joffrin, Y. Kamada, P. A. Politzer, J. Schweinzer, A. C. C. Sips, J. Stober, G. Giruzzi, C. E. Kessel, M. Murakami, Y.-S. Na, J. M. Park, A. R. Polevoi, R. V. Budny, J. Citrin, J. Garcia, N. Hayashi, J. Hobirk, B. F. Hudson, F. Imbeaux, A. Isayama, D. C. McDonald, V. V. Parail, T. W. Petrie, C. C. Petty, T. Suzuki, and M. R. Wade, "Development of advanced inductive scenarios for ITER," in 23rd IAEA Fusion Energy Conference, (Daejeon, South Korea), pp. ITR/1–5, 2010.

[129] J. Citrin, J. F. Artaud, J. Garcia, G. M. D. Hogeweij, and F. Imbeaux, "Impact of heating and current drive mix on the ITER hybrid scenario," Nuclear Fusion, vol. 50, no. 11, p. 115007, 2010.

[130] J. E. Kinsey, G. M. Staebler, and R. E. Waltz, "Predicting core and edge transport barriers in tokamaks using the GLF23 drift-wave transport model," Physics of Plasmas, vol. 12, p. 052503, Apr. 2005.

[131] P. B. Snyder, R. J. Groebner, J. W. Hughes, T. H. Osborne, M. Beurskens, A. W. Leonard, H. R. Wilson, and X. Q. Xu, "A first-principles predictive model of the pedestal height and width: development, testing and ITER optimization with the EPED model," Nuclear Fusion, vol. 51, no. 10, p. 103016, 2011.

[132] M. Greenwald, C. Angioni, J. W. Hughes, and H. Weisen, "Density profile peaking in low collisionality H-modes: comparison of Alcator C-Mod data to ASDEX Upgrade/JET scalings," Nuclear Fusion, vol. 47, no. 9, pp. L26–L29, 2007.

[133] G. T. A. Huysmans, S. E. Sharapov, A. B. Mikhailovskii, and W. Kerner, "Modeling of diamagnetic stabilization of ideal magnetohydrodynamic instabilities associated with the transport barrier," Physics of Plasmas, vol. 8, p. 4292, Oct. 2001.

[134] J. Citrin, J. Hobirk, M. Schneider, J. F. Artaud, C. Bourdelle, K. Crombe, G. M. D. Hogeweij, F. Imbeaux, E. Joffrin, F. Koechl, and J. Stober, "Predictive analysis of q -profile influence on transport in JET and ASDEX Upgrade hybrid scenarios," Plasma Physics and Controlled Fusion, vol. 54, p. 065008, June 2012.

[135] F. Koechl, V. V. Parail, M. Mattei, R. Ambrosino, G. Corrigan, L. Garzotti, C. Labate, D. C. McDonald, G. Saibene, and R. Sartori, "Self-consistent predictive modelling of 15MA inductive scenarios in ITER," in European Physical Society Conference on Plasma Physics, (Strasbourg, France), p. P2.107, 2011.

[136] F. Imbeaux, J. Citrin, J. Hobirk, G. M. D. Hogeweij, F. Koechl, V. M. Leonov, and S. Miyamoto, "Current ramps in tokamaks: from present experiments to ITER scenarios," Nuclear Fusion, vol. 51, no. 8, p. 083026, 2011.

[137] Y. R. Martin and T. Takizuka, "Power requirement for accessing the H-mode in ITER," Journal of Physics: Conference Series, vol. 123, no. 1, p. 012033, 2008.

[138] J. Garcia, "No Title," Plasma Physics and Controlled Fusion, 2013.

[139] J. García, G. Giruzzi, J. Artaud, V. Basiuk, J. Decker, F. Imbeaux, Y. Peysson, and M. Schneider, "Critical Threshold Behavior for Steady-State Internal Transport Barriers in Burning Plasmas," Physical Review Letters, vol. 100, p. 255004, June 2008.

[140] M. Murakami, J. M. Park, G. Giruzzi, J. Garcia, P. Bonoli, R. V. Budny, E. J. Doyle, A. Fukuyama, N. Hayashi, M. Honda, A. Hubbard, S. Ide, F. Imbeaux, E. F. Jaeger, T. C. Luce, Y.-S. Na, T. Oikawa, T. H. Osborne, V. V. Parail, A. R. Polevoi, R. Prater, A. C. C. Sips, J. A. Snipes, H. E. S. John, P. B. Snyder, and I. Voitsekhovitch, "Integrated modelling of steady-state scenarios and heating and current drive mixes for ITER," Nuclear Fusion, vol. 51, no. 10, p. 103006, 2001.

[141] R. Albanese and F. Villone, "The linearized CREATE-L plasma response model for the control of current, position and shape in tokamaks," Nuclear Fusion, vol. 38, no. 5, pp. 723–738, 1998.

[142] A. Kavin, "Private communications."

[143] K. Miyamoto, Fundamentals of plasma physics and controlled fusion. 1997.

Contact details

Karim Besseghir
Rue du Bluard 2
CH-1110 Morges
+41 79 321 57 46
k.besseghir@gmail.com

Education

2013 (exp.)	PhD in Plasma Physics, EPFL, Switzerland.
2007-2008	MSc in Physics with distinction (grade 82/100), Imperial College London, UK.
2004-2007	BSc in Physics (grade 5.57/6), EPFL, Switzerland.
2001-2004	Baccalaureat with distinction (grade 48.5/54), Chamblandes, Pully, Switzerland.

Professional experience and projects

2009-2013   **EPFL, Centre de Recherches en Physique des Plasmas (CRPP)**: PhD candidate in Plasma Physics, Lausanne, Switzerland. Part of this work consisted of the assessment and the implementation of optimal control techniques in the framework of tokamak operation. This thesis also focused on the usage and development of a tokamak simulator for the simulation of ITER advanced scenarios.
This work involved collaborations with several institutes in Europe and in the United States, as well as the participation in an international consortium of research institutes to which a grant was awarded for the modelling of ITER scenarios.

2008-2009   **Kookiiz.com**: Associate for the setting up and development of an online social platform. My contribution helped start the project from the technical and the administrative viewpoints. This start-up raised interest from a major Swiss media group for further collaboration.

2008   **Imperial College London, UK**: Master project in quantum physics. This work resulted in a publication in a peer-reviewed journal.

Competences

General   Strong background in physics, control engineering, and modelling. Working knowledge of accounting and finance (EPFL certificate and self-education). Experience with international projects and teamwork.

Languages   **French** – native language.
English – fluent (C2), with a Cambridge Proficiency Certificate.
German – working knowledge (B2). 2 months in Berlin's Goethe Institut in 2008.

Informatics   Matlab, Simulink, Excel, Word, PowerPoint, Visio, LaTeX, Wordpress, HTML, working knowledge of C++, Linux usage.

Other activities

2002-2012   **Budokwai Pully judo club**: Benevolent vice-president of the Budokwai judo club in Pully, Switzerland. This work consisted of the organisation of several public events and judo championships. It also involved the creation and maintenance of the club's website, as well as regular interactions with the town hall of Pully and other sports clubs.

Personal information

General   27 years old (9th December 1985), single. Swiss citizenship.

Hobbies   Judo (black belt, 2nd dan), ski, scuba diving, lead singer in a band, organisation of concerts, captain of an amateur football team, organisation of championships.

List of publications

First author K. Besseghir, J. Garcia, J.-F. Artaud, F. Imbeaux, R.R. Khayrutdinov, J.B. Lister, V.E. Lukash, and P. Maget, "Achieving and sustaining advanced scenarios in ITER modelled by CRONOS and DINA-CH," submitted to Plasma Physics and Controlled Fusion.

K. Besseghir, J.B. Lister, "Scenario optimisation for ITER," in 38th European Physical Society Conference on Plasma Physics, (Strasbourg, France), P1.104, 2011.

K. Besseghir, J.B. Lister, "Development of the DINA-CH full tokamak simulator and on-line scenario optimisation for ITER", in Joint Annual Meeting of the Swiss Physical Society and the Austrian Physical Society, (Lausanne, Switzerland), ID505, 2011.

K. Besseghir, J.B. Lister, Ph. Müllhaupt, "Maintaining optimal ITER scenario trajectories," in 37th European Physical Society Conference on Plasma Physics, (Dublin, Ireland), P2.174, 2010.

K. Besseghir, J.B. Lister, S.H. Kim, Ph. Moreau, F. Saint-Laurent, V. Dokouka, R.R. Khayrutdinov, V.E. Lukash, "Identification of the ITER plasma equilibrium using modulation," in 36th European Physical Society Conference on Plasma Physics, (Sofia, Bulgaria), P4.162, 2009.

Co-author V. Parail, R. Albanese, R. Ambrosino, J.-F. Artaud, K. Besseghir, M. Cavinato, G. Corrigan, J. Garcia, L. Garzotti, Y. Gribov, F. Imbeaux, F. Koechl, C.V. Labate, J.B. Lister, X. Litaudon, A. Loarte, P. Maget, M. Mattei, D. McDonald, E. Nardon, G. Saibene, R. Sartori, and J. Urban, "Self-consistent simulation of plasma scenarios for ITER using a combination of 1.5D transport codes and free boundary equilibrium codes," submitted to Nuclear Fusion.

J.E. Barton, E. Schuster, K. Besseghir, and J.B. Lister, "Towards first-principles control-oriented modelling of the magnetic and kinetic plasma profile evolutions in ITER," Bulletin of the American Physical Society, vol. 57, 2012.

J. Urban, J.-F. Artaud, K. Besseghir, J.B. Lister, J. Garcia, F. Imbeaux, S.H. Kim, E. Nardon, R. Nouailletas, "Free-boundary equilibrium transport simulations of ITER scenarios under control," in 39th European Physical Society Conference on Plasma Physics, (Stockholm, Sweden), P1.019, 2012.

K. Besseghir, J.B. Lister, J.-F. Artaud, J. Garcia, F. Imbeaux, R.R. Khayrutdinov, V.E. Lukash, "Advanced ITER scenarios with the DINA-CH&CRONOS simulator," in 39th European Physical Society Conference on Plasma Physics, (Stockholm, Sweden), P4.054, 2012.

J.B. Lister, K. Besseghir, J.-F. Artaud, R.R. Khayrutdinov, S.H. Kim, V.E. Lukash, "Development of the DINA-CH full tokamak simulator," in 38th European Physical Society Conference on Plasma Physics, (Strasbourg, France), P1.105, 2011.

K. Besseghir, L. Brocher, J.B. Lister, "Cross-modulation of loop voltage and ECH power in ITER," in 37th European Physical Society Conference on Plasma Physics, (Dublin, Ireland), P2.175, 2010.

C.M. Bender, K. Besseghir, H.F. Jones, and X. Yin, "Small-ε behaviour of the non-Hermitian PT-symmetric Hamiltonian $H = p^2 + x^2(ix)^\varepsilon$," Journal of Physics A: Mathematical and Theoretical, vol. 42, 355301, 2009.